FZR-444

Paulo Alexandre Vieira Crespo

Optimization of In-Beam Positron Emission Tomography for Monitoring Heavy Ion Tumor Therapy

Forschungszentrum
Rossendorf

Paulo Alexandre Vieira Crespo

Optimization of In-Beam
Positron Emission Tomography
for Monitoring Heavy Ion
Tumor Therapy

Forschungszentrum
Rossendorf

Optimization of
In-Beam Positron Emission Tomography
for Monitoring
Heavy Ion Tumor Therapy

Vom Fachbereich Physik

der Technischen Universität Darmstadt

zur Erlangung des Grades

eines Doktors der Naturwissenschaften

(Dr. rer. nat.)

genehmigte Dissertation von

Dipl.-Phys.-Eng. Paulo Alexandre Vieira Crespo

aus Beira, Mozambique

Darmstadt 2005
D 17

Para a Mã. Para o Pá.

To you Mom, to you Dad.

E para ti, Lena.

Index

List of Figures

List of Tables

List of Acronyms and Abbreviations

2D / 3D	2 Dimension(al) / 3 Dimension(al)
ADC	Analog to Digital Converter
APD(A)	Avalanche Photodiode (Array)
ASINS	Andrzej Sołtan Institute for Nuclear Studies, Swierk-Otwock, Poland
BASTEI	Beta Activity Measurements at the Therapy with Energetic Ions
BGO	Bismuth Germanate, $Bi_4Ge_3O_{12}$
BNC	Berkeley Nucleonics Corporation, San Rafael, CA, USA
CAEN	Costruzioni Apparecchiature Elettroniche Nucleari, Viareggio, Italy
CAGE	CAMAC Acquisition through GPIB and Ethernet
CAMAC	Computer Automated Measurement and Control
CERN	European Organization for Nuclear Research, Geneva , Switzerland, originally named Conseil Européene pour la Recherche Nucléaire
CFD	Constant Fraction Discriminator
CSP	Charge Sensitive Preamplifier
CT	Computed Tomography/Tomogram
CVD	Chemical Vapour Deposition
DAQ	Data Acquisition
DC	Direct Current
DKFZ	Deutsches Krebsforschungszentrum, Heidelberg, Germany
DOI-PET	Depth of Interaction Positron Emission Tomography
DNA	Deoxyribonucleic Acid
ENC	Equivalent Noise Charge
FBP	Filtered Backprojection
FOTEC	Forschungs- und Technologietransfer GmbH, Wiener-Neustadt, Austria
FOV	Field of View
FWHM	Full Width at Half Maximum
FZR	Forschungszentrum Rossendorf, Dresden, Germany
GPIB	General Purpose Interface Bus
GSI	Gesellschaft für Schwerionenforschung, Darmstadt, Germany
GSO	Gadolinium oxyorthosilicate, Gd_2SiO_5
HIMAC	Heavy Ion Medical Accelerator in Chiba, Japan
HPGe	High Purity Germanium (detector)

ICRU	International Commission on Radiation Units and Measurements, Inc., Bethesda, MD, USA
IMRT	Intensity Modulated Radiation Therapy
LBNL	Lawrence Berkeley National Laboratory, Berkeley, CA, USA
LED	Light Emitting Diode
LEM	Local Effect Model
LET	Linear Energy Transfer
LGSO	Cerium-doped Lutetium and Gadolinium Oxyorthosilicate, $Lu_{2(1-x)}Gd_{2x}SiO_5{:}Ce^{3+}$
LINAC	Linear Accelerator
LOR	Line of Response
LPS	Cerium-doped Lutetium Pyrosilicate, $Lu_2Si_2O_7{:}Ce$
LSO	Cerium-doped Lutetium Oxyorthosilicate, $Lu_2SiO_5{:}Ce^{3+}$
LuAP	Cerium-doped Lutetium Aluminium Perovskite, $LuAlO_3{:}Ce^{3+}$
LYSO	Cerium-doped Lutetium and Yttrium Oxyorthosilicate, $Lu_{2(1-x)}Y_{2x}SiO_5{:}Ce^{3+}$
MCA	Multichannel Analyzer
MCP-PMT	Microchannel Plate Photomultiplier Tube
MCS	Multiple Coulomb Scattering
MLEM	Maximum Likelihood Expectation Maximization
NPTC	Northeast Proton Treatment Center, Boston, MA, USA
OAR	Organ at Risk
OER	Oxygen Enhancement Ratio
OSEM	Ordered Subsets Expectation Maximization
PEM	Positron Emission Mammography
PET	Positron Emission Tomography
PIN	P-doped, Intrinsic region, N-doped (photodiode)
PMMA	Polymethylmethacralate, Lucite, $C_5O_2H_8$ ($\rho = 1.18$ g/cm^3)
PMT	Photomultiplier Tube
PSI	Paul Scherrer Institute, Villigen, Switzerland
RBE	Relative Biological Effectiveness
RF	Radiofrequency
RTR	Randoms-to-Trues Ratio
SCA	Single Channel Analyzer
SIS	Schwerionensynchrotron, heavy ion synchrotron at GSI Darmstadt
SPA	Spectroscopy Amplifier
TAC	Time to Amplitude Converter
TOF-PET	Time of Flight Positron Emission Tomography
YAP	Yttrium Aluminum Perovskite, $YAlO_3$

Zusammenfassung

In-beam Positronen Emissions Tomographie (in-beam PET) ist zur Zeit die einzige Methode für eine in-situ Kontrolle der Ionentherapie mit geladenen Hadronen. Bei solch einer Therapie werden die klinischen Auswirkungen einer Abweichung von der Bestrahlungsplanung durch Sicherheitssäume um den Tumor und geeignete Einstrahlrichtungen kompensiert. Darüber hinaus erlaubt die in-beam PET Methode Reichweiteabweichungen und anatomische Veränderungen während der fraktionierten Bestrahlung nachzuweisen. Mittels in-beam PET detektierter Abweichungen ist es möglich, die Differenz zwischen geplanter und applizierter Dosis abzuschätzen.

Erstmals in der klinischen Strahlentherapie wurde in-beam PET vom Forschungszentrum Rossendorf (FZR), Dresden an der Gesellschaft für Schwerionenforschung (GSI) in Darmstadt implementiert. Der eingebaute Tomograph ist für kleine Tumoren optimiert und besteht aus zwei sphärischen Detektorköpfen. Dadurch treten im Falle großer Bestrahlungsfelder unkorrigierbare Artefakte auf, welche die Bildauswertung stören. In dieser Arbeit zeigt eine Simulation, die mit einem 3D-Rekonstruktionsprogramm gekoppelt ist, dass die Verminderung des Öffnungswinkels einer zylinderförmigen Doppelkopf Kamera der ausschlaggebende Faktor ist, um eine optimale Qualität der in-beam PET-Bilder zu erhalten. Das Ergebnis der Studie sind zwei bevorzugte Detektoranordnungen: ein geschlossener Ring oder ein Doppelkopf Tomograph mit kleinen, einander gegenüber liegenden Öffnungen für den Eintritt des Therapiestrahls und den Austritt leichter Targetfragmente. Die Integration beider Detektoranordnungen in eine isozentrisch rotierende Ionenstrahlführung (*Gantry*) ist durchführbar, wenn der in-beam PET-Scanner an die Ionenstrahlführung gekoppelt wird. Es ist auch möglich, einen in-beam PET-Scanner mit den erwähnten Detektoranordnungen an therapeutischen Anlagen mit einer horizontalen Strahlführung zu implementieren. Die vorgeschlagenen Detektorkonfigurationen waren hinsichtlich ihrer Bild gebenden Eigenschaften am Teilchstrahl zu untersuchen - dies ist eine Schlussfolgerung auf die an der Schwerionentherapie-Anlage des Lawrence Berkeley Laboratory eingetretene Situation. Dort konnte in-beam PET nicht in die klinische Nutzung überführt werden, weil es, höchstwahrscheinlich bedingt durch den mit der passiven Formierung des Bestrahlungsfeldes einhergehenden Fluss an Sekundärteilchen, zu einer Aktivierung der Szintillations-Detektoren aus Bismut-Germanat kam. Die Untergrundereignisse aus dieser Kristall-Aktivierung verhinderten das Registrieren von in-beam PET Daten mit einem für die Bildgebung ausreichenden Signal-Rausch-Verhähltnis. Deswegen mussten Detektoren basierend auf dem in den 1990er Jahren gefunden Szintillator LSO (Lutetiumoxyorthosilikat), der bereits verbreiteten Eingang in die PET Tracer Bildgebung gefunden hat, auf ihre Eignung für die Bildgebung am Teilchenstrahl untersucht werden. Jeder Detektor besteht aus 32 LSO-Kristallen, welche mit einer Lawinen-Photodioden-Matrix (*avalanche photodiode array*, APDA) optisch gekoppelt sind. Wegen ihrer Kompaktheit und ihrer Unempfindlichkeit gegenüber Magnetfeldern wurden die APDA anstelle von Photomultipliern (*photomultiplier tube*, PMT) als Szintillations-Detektoren gewählt. Ein magnetisch unempfindlicher Detektor ist notwendig, wenn der in-beam PET-Scanner nahe dem letzten Magneten der Strahlführung montiert ist. Dies gilt besonders für die geplante isozentrisch rotierende Ionenstrahlführung an der Heidelberger Ionen-Therapie-Anlage, die sich bereits in der Bauphase befindet. Um beide Dektektoren im Koinzidenzmodus sowohl *offline*, als auch synchronisiert mit der

medizinischen Strahlführung der GSI auslesen zu können, wurde ein Mehrkanal-Listmode-Datenerfassungssystem aufgebaut. Eine Mess-Position, bei der der Winkel zwischen den zwei LSO/APDA Detektoren und dem Isozentrum sehr klein war, zeigte gute Ergebnisse für die in-beam PET-Bildgebung. Solche Kleinwinkel-Messungen sind durchgeführt worden, wobei beide Detektoren in Strahlrichtung vor oder hinter dem Target positioniert waren. Dabei hat sich gezeigt, dass die Detektoren eine gute Lösung für die in dieser Arbeit vorgeschlagenen, verbesserten in-beam PET-Scanner sind. Eine weitere Bestätigung dieses Ergebnisses folgt aus γ-Spektren, die mit einem Germanium-Detektor aufgenommen wurden. Nach dem Einsatz des Szintillators bei Patientenbestrahlungen war keine Aktivierung des LSO-Szintillators nachweisbar.

Obwohl ein geschlossener Ring oder ein Doppelkopf Tomograph mit kleinen Öffnungen verbesserte in-beam PET-Bilder ermöglichen, stellt die niedrige Zählrate beim in-beam PET ein zweites Problem bezüglich der Bildqualität dar. Es wird durch einen erhöhten Untergrund an zufälligen Koinzidenzereignissen während der Strahlextraktion hervorgerufen. Noch wichtiger ist, dass neue Beschleunigerentwicklungen dieses Problem weiter erhöhen werden, bis zu einem Grad, bei dem in-beam PET-Datenaufnahme unmöglich wird, wenn das bisher angewandte Prinzip der Datenerfassung weiter benutzt wird. Es sind zwei Methoden zur Unterdrückung solcher Zufallsereignisse geprüft worden. Beide haben die Synchronisation der detektierten Ereignisse mit der vom Beschleuniger vorgegeben Zeit-Mikrostruktur des Teilchenstrahles zur Grundlage. Eine Methode erreicht diese Synchronisierung durch einen schnellen Teilchendetektor, der vor dem Isozentrum im Strahlweg positioniert ist. Dies ermöglicht, Photonenkoinzidenzen, die während der Extraktion der Ionenpakete detektiert werden, für die Bildrekonstruktion zu verwerfen. Eine zweite Methode besteht in der Synchronisation jeder Photonenkoinzidenz mit dem Hochfrequenz-Signal des Beschleunigers. Die Bildstatistik wurde durch diesen Methoden fast um den Faktor zwei verbessert. Dies zeigt, dass die Methoden und deren Datenerfassungstechnik eine Lösung für zukünftige in-beam Positronen Emissions Tomographen darstellen, unabhängig davon, ob es sich bei dem Therapiebeschleuniger um ein Synchrotron oder Zyklotron handelt.

Overview

Summary

In-beam positron emission tomography (in-beam PET) is currently the only method for an in-situ monitoring of highly tumor-conformed charged hadron therapy. In such therapy, the clinical effect of deviations from treatment planning is highly minimized by implementing safety margins around the tumor and selecting proper beam portals. Nevertheless, in-beam PET is able to detect eventual, undesirable range deviations and anatomical modifications during fractionated irradiation, to verify the accuracy of the beam portal delivered and to provide the radiotherapist with an estimation of the difference in dosage if the treatment delivered differs from the planned one.

With unprecedented success in clinical radiotherapy, the in-beam PET implemented by the team from the Forschungszentrum Rossendorf (FZR), Dresden, at the Gesellschaft für Schwer-ionenforschung (GSI), Darmstadt, was optimized for the initially expected, small-sized tumors. For large irradiation fields, though, uncorrectable limited-angle reconstruction artifacts arise due to the dual-head, spherical camera geometry, disturbing image evaluation in such cases. In a first study within this work, a set of simulation and fully-3D reconstruction routines shows that minimizing the opening angle of a cylindrical camera is determinant for an optimum quality of the in-beam PET images. The study yields two favorite detector geometries: a closed ring or a dual-head tomograph with narrow gaps. The implementation of either detector geometry onto an isocentric, ion beam delivery (gantry) is feasible by mounting the PET scanner at the beam nozzle. The implementation of an in-beam PET scanner with the mentioned detector geometries at therapeutic sites with a fixed, horizontal beam line is also feasible. Nevertheless, knowing that previous in-beam PET research in Berkeley was abandoned due to detector activation (Bismuth Germanate, BGO), arising most probably from passive beam shaping contaminations, the proposed detector configurations had to be tested in-beam. For that, BGO was substituted with a state-of-the-art scintillator (lutetium oxyorthosilicate, LSO) and two position sensitive detectors were built. Each detector contains 32 pixels, consisting of LSO finger-like crystals coupled to avalanche photodiode arrays (APDA). In order to readout the two detectors operated in coincidence, either in standalone mode or at the GSI medical beam line, a multi-channel, zero-suppressing free, list mode data acquisition system was built. The APDA were chosen for scintillation detection instead of photomultiplier tubes (PMT) due to their higher compactness and magnetic field resistance. A magnetic field resistant detector is necessary if the in-beam PET scanner is operated close to the last beam bending magnet, due to its fringe magnetic field. This is the case at the isocentric, ion beam delivery planned for the dedicated, heavy ion hospital facility under construction in Heidelberg, Germany. In-beam imaging with the LSO/APDA detectors positioned at small target angles, both upbeam and downbeam from the target, was successful. This proves that the detectors provide a solution for the proposed next-generation, improved in-beam PET scanners. Further confirming this result are germanium-detector-based, spectroscopic γ-ray measurements: no scintillator activation is observed in patient irradiation conditions.

Although a closed ring or a dual-head tomograph with narrow gaps is expected to provide

improved in-beam PET images, low count rates in in-beam PET represent a second problem
to image quality. More importantly, new accelerator developments will further enhance this
problem to the point of making impossible in-beam PET data taking if the present acquisition
system is used. For these reasons, two random-suppression methods allowing to collect in-beam
PET events even during particle extraction were tested. Image counts raised almost twofold.
This proves that the methods and associated data acquisition technique provide a solution for
next-generation, in-beam positron emission tomographs installed at synchrotron or cyclotron
radiotherapy facilities.

Objectives of this dissertation

The objectives pursued with the present work are the optimization of in-beam positron emis-
sion tomography applied for the monitoring of heavy ion tumor irradiation. This optimization
requires, in a first step, identifying present or future limitations of in-beam PET. Present
limitations are those already existing at the in-beam PET installed at the GSI facility. Fu-
ture limitations are those expected to arise at in-beam PET to be installed onto heavy ion
tumor treatment facilities under planning or construction elsewhere. In a second step, the
understanding of the sources of those limitations is necessary. Based on this knowledge sev-
eral mathematical and technological innovative solutions are proposed, or extended from its
present status, constructed and verified, either by simulation or experimentally. In some cases,
discriminated below and throughout this dissertation, the understanding of the source of the
limitation is brought from reasearch work performed previously, or during the course of these
studies, by a second party. In these situations this work focuses on providing an overcoming
solution, based on that knowledge, as well as verifying it.

The most important limitation of in-beam PET, firstly addressed in this work, is the problem of
image artifacts arising from limited angle tomography. In order to study the origin of the several
artifacts and to be able to propose a detector configuration that minimizes them, two software
tools were needed. These were a tomograph simulation, capable of handling several detector
configurations, and a flexible reconstruction routine able of reading and treating mathematically
the ouput of this simulation. Reconstruction routines provided by conventional PET applied
to data sets of very low statistics yield images of poor quality. More importantly, they require
the tomograph to be space invariant, a requisite only met by closed ring detector geometries.
On the other hand, the reconstruction routine developed for the in-beam tomograph at GSI is
based on a fixed histogram size. The size of this histogram is given by the product of the number
of detectors on both heads. This limits its application to tomographs with larger heads due to
two reasons. First, the histogram size increases almost two orders of magnitude as one moves
from the dual-head tomograph installed at GSI to a typical closed ring PET scanner. A fixed
histogram strategy, if implemented, would be too demanding in terms of computer memory
and processing time. Second, the implementation of larger detector heads allows one valid
event to trigger two detectors in the same head, which cannot be considered by such histogram
strategy. Therefore, the development of a reconstruction routine that extends the mathematical
data treatment already implemented for the in-beam tomograph at GSI was necessary. This
extended reconstruction routine, applied onto larger tomographs, allows to study the source of
artifacts in limited angle tomography. In addition, it provides a reconstruction solution for a
future closed ring or dual-head, in-beam tomograph with smaller gaps (larger heads).

The optimum detector geometry for in-beam PET poses integration challenges when brought
onto heavy ion treatment sites. On one side such tomograph must be as flexible as possible
in order to avoid collisions with the patient, its table and couch and with the beam delivery
system. This favors a small volume, dual-head tomograph solution. On the other side, in-beam

PET images obtained with a limited angle tomograph loose quality in respect to those sampled with closed ring ones. Technical solutions for implementing in-beam PET at future therapeutic sites, with these variables properly considered, were also necessary not only for rotating beam deliveries as well as for fixed, horizontal beam lines. During the course of this work a technical solution for implementing a dual-head, in-beam positron emission tomograph onto a rotating beam delivery was developed at GSI by a second party. In addition to self developed integration proposals, this work analyzes the advantages and disadvantages of the design of GSI and, in addition, extends it by proposing the installation of a closed-ring tomograph.

Besides the limitations arising from limited angle tomography, in-beam PET images are also affected by low statistics data sets. Data taking during particle extraction is presently vetoed due to the presence of a high noise background which overlaps the annihilation signal. A correlation existing between the moment of arrival of background events with the arrival of the carbon ions, synchronized with the accelerator radiofrequency signal, was found and exploited by other members of this in-beam PET team. A technical solution applying this knowledge was necessary in order to allow in-beam PET data taking during particle extractions. Such solution was required for two reasons: (i) for increasing the statistics of the acquired images, and (ii) for implementing in-beam PET at future facilities using optimized synchrotron or cyclotron accelerators. This is because recent developments in accelerator technology result in beam extraction times occupying close to 100 % of the accelerator duty cycle.

Finally, the detector and data acquisition technology installed at the in-beam PET at GSI is based on the solutions available at the time of its installation. Not only state-of-the-art technology has outperformed the efficiency of the tomograph once installed, as well as the special requirements of in-beam PET have been better understood. This must lead to dedicated in-beam PET solutions that differ from conventional tracer imaging technology. With this objective set, proposing and testing modern γ-ray detectors and data acquisition strategies directly optimized for in-beam PET was also a need. A new detector solution was also necessary in order to overcome the limitation of the current detectors if operated in close vicinity to fringe magnetic fields. Such fields, generated by the last beam bending magnet, will be present if in-beam PET is installed onto isocentric, rotating beam deliveries.

Outline

This dissertation, *Optimization of In-Beam Positron Emission Tomography for Monitoring Heavy Ion Tumor Therapy*, lies within the framework of the Heavy Ion Tumor Therapy Collaboration. In order to introduce the term *in-beam PET* into its context, chapter 1 summarizes the motivations inherent to conformal radiotherapy and the present clinical results of charged particle radiotherapy. The physical and radiobiological rationale for carbon ions are then presented and its clinical impact is brought up by including, from the literature, treatment planning comparisons of carbon ions both with photons and with protons. Concerning heavier ions, a summary of previous, pioneering trials elucidates why carbon ions are advantageous. Finally, the principles and capabilites of in-beam positron emission tomography are described, together with the technical solution implemented by the team from FZR at the facility in GSI in order to monitor the carbon ion patient irradiation.

The aim of chapter 2 was to optimize the detector geometry for in-beam PET. A fully 3D, maximum likelihood expectation maximization algorithm applicable to several closed ring or dual-head tomographs shows the possible sources of image artifacts in limited-angle tomography. The analysis of β^+-activity distributions simulated from real-treatment situations and detected with several detector arrangements allows to conclude that a dual-head tomograph

with narrow gaps yields in-beam PET images with sufficient quality for monitoring head and neck treatments. For monitoring larger irradiation fields, e.g. treatments in the pelvis region, a closed ring tomograph was seen to be highly desirable. In the last section of this chapter a study of the space availability for patient and bed, tomograph and beam portal, proves viable the implementation of a closed ring detector geometry for in-beam PET.

Chapter 3 analyzes three proposals for in-beam PET integration into space-constrained treatment rooms due to the presence of an isocentric, rotating beam delivery. They are: PET at the patient couch, PET on a separate gantry and PET at the beam nozzle. It concludes that the configuration with PET at the beam nozzle, developed at GSI, not only satisfies most integration requisites but also offers the possibility of integrating a closed ring tomograph, therefore greatly benefiting the quality of forthcoming in-beam PET images. The integration of in-beam PET onto fixed, horizontal beam lines is also studied.

In chapter 4 the operation parameters of two state-of-the-art scintillation detection devices are optimized. The detectors consist of finger-like LSO crystals coupled to APDA. The substitution of PMT by APDA provides the magnetic field resistance and compactness needed for the next-generation, in-beam PET detectors, as described. The energy and time resolutions measured, better than those obtained with the presently installed detectors, are directly related to the quality of PET images. Further studies presented in this chapter provide quantitative efficiency and acceptance results used in the normalized images and depth-profiles presented in the following two chapters.

The in-beam imaging capability of these LSO/APDA detectors operated under or after harsh irradiation conditions are described in chapter 5. In one experiment the detectors were positioned up and downbeam from a target irradiated with a fluence equivalent to $1\,000$ typical daily therapeutic fractions. A line source positioned between the detectors was imaged, allowing parameters like time, energy and spatial resolution to be compared before, during and after irradiating the target. A second experiment imaged the β^+-activity distribution generated by a monoenergetic beam in a target of Lucite. In addition, a third experiment exposed a scintillator block of LSO to the flux of light particles leaving two single-portal patient treatments. Germanium-detector-based, spectroscopic γ-ray measurements showed no scintillator activation. Due to the small amount of ^{176}Lu, a natural radioactive isotope, in LSO, the influence of the natural background activity density of LSO onto an LSO-based tomograph was estimated. It is seen that, in order not to compromise the quality of the low-statistics in-beam PET images, modern, digital data acquisition techniques are necessary in order to reduced the coincidence time resolution of the detectors. Finally, the impact of recent developments in ultra-fast timing detectors, potentially allowing the implementation of the time-of-flight technique onto commercial PET scanners, was extrapolated to in-beam PET. Very promising results can be achieved for tomographs with a coincidence time resolution below 200 ps FWHM.

In chapter 6 two random-suppression methods allowing to collect in-beam PET events even during particle extraction were tested, raising image counts almost twofold and providing a data acquisition solution for next-generation, in-beam positron emission tomographs installed at synchrotron and cyclotron beam lines. The two LSO/APDA detectors were used and the 2D images and depth profiles obtained during particle extraction clearly show the feasibility of both methods proposed.

The conclusions from this dissertation, together with future work suggestions, are presented in chapter 7.

Chapter 1

Radiotherapy with Carbon Ions

1.1 Motivation

Cancer is one of the major causes of death in modern society, ranking second after heart and circulatory diseases. At the time of diagnostics, about 58 % of tumors have not spread to distant locations, i.e. have not formed metastases (Fig. 1.1). Tumors at this localized stage can potentially be cured by local interventions - surgery, radiation therapy or a combination of both. About 22 % of all cancer patients are cured by surgery. Presently available radiotherapeutic methods can cure 12 %, while another 6 % receives a combination of surgery and radiotherapy.
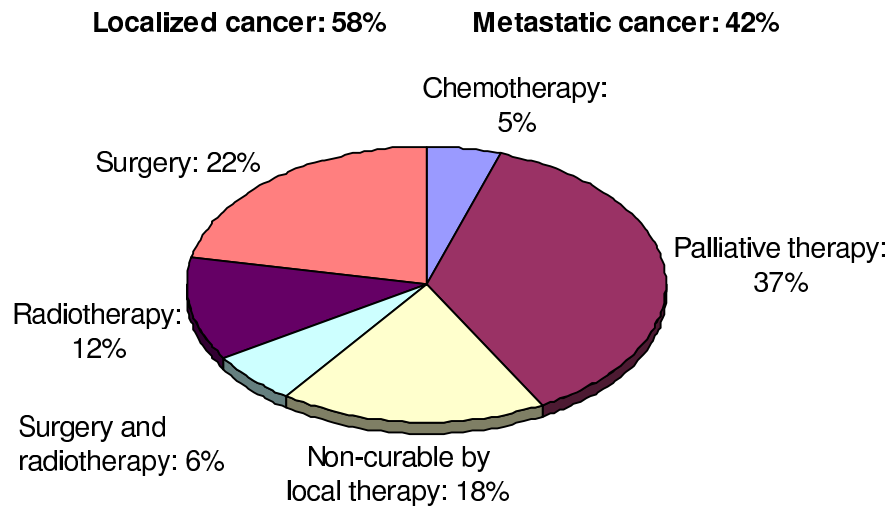
Figure 1.1: Presently used cancer treatment methods, after [GSI99a].

However, current local or loco-regional tumor treatment modalities in the European Union fail for 18 % of all cancer patients, which represents about 280 000 deaths per year [Sch96c]. This is due to the impossibility of removing the tumor in total or applying a radiation dose high enough to sterilize all cancer cells [Sch03b]. If not all, a great part of these patients could be cured successfully if localized tumor treatment techniques, like radiotherapy, would be improved. The heavy ion tumor therapy pilot project, currently running at the Gesellschaft für Schwerionenforschung[1] (GSI) Darmstadt, is among the best examples of this improvement: since December 1997 over 250 patients with radioresistant tumors in the head and neck region as well as in the pelvis were treated with high energy carbon ions yielding very promising clinical results [Deb00, Sch02b, Sch03b]. The aim of the pilot project is to exploit the physical

---
[1] Laboratory for Heavy Ion Research

and radiobiological advantages of carbon ions for high precision radiotherapy [Kra90], allowing radioresistant tumors growing in close vicinity to organs at risk (OAR) to be irradiated. In a first stage, only slow-growing, non-metastasic tumors of the head, neck or spinal chord are selected, namely

- skull base tumors: chordoma, chondrosarcoma, malignant schwannoma atypical meningeoma, adenoidcystic carcinoma, and

- tumors close to the spinal chord: sacral chordoma, chondrosarcoma, and soft tissue sarcoma.

An example of the first clinical results is shown in Fig. 1.2. Further results show that carbon ion irradiation is feasible and safe with no severe acute radiation-induced toxicity [Sch02a].

Figure 1.2: First results from the clinical study showing the course of disease of a female patient before (left) and six weeks after therapy at GSI (right), from [GSI99b]. As a result of the strong recession of the tumor located in the base of the skull region, the symptons of paralysis have almost completely disappeared.

A compilation of therapy results from this study as well as from other hadron therapy facilities is shown in Table 1.1, together with results achieved with conventional photon therapy. Although tumors other than chondromas and chondrosarcomas are handled at GSI, they occur more seldom so the study is ongoing with preliminary results discussed elsewhere [Sch04, Sch03c].

The trend in clinical effectiveness by using charged particles can clearly be seen. In order to arrive at this motivating stage, over 50 years have passed since physical and radiobiological research with ion beams was initiated at the Lawrence Berkeley National Laboratory (LBNL) in 1947, only one year after R. Wilson had proposed the use of ion beams for therapy due to their superior depth dose distribution [Wil46]. An historical evolution is described in [Kra00]. The improved results nowadays achieved at the treatment facility at GSI are due to the following scientific and technological developments:

- excellent 3-D beam conformity through an active beam delivery system by means of the intensity controlled rasterscan technique [Hab93],

- inverse treatment planning [Krä00] based on the GSI-developed radiobiological model, the local effect model LEM [Sch96d] and

- the use of positron emission tomography (PET) for in-situ monitoring the particle localization [Eng04b].

Table 1.1: Hadron therapy results from multi-center studies according to [Kra00]. GSI results after [Sch03b].

Indication	End-point	Results photons	Results hadrons	Res. GSI
Nasopharyngeal carcinoma (advanced stage)	5y-S	45-50 %	63 %	
Chordoma	LCR	30 %	65 %	87 %
Chondrosarcoma	LCR	33 %	88 %	100 %
Blastomatous glioma	AST	12 months	16.9 months	
Malignant meningioma	PFSR	30 %	85 %	
Uveal melanoma	5y-S	95 % loss of eye	96 % maintenance of vision	
Tumors of the paranasal sinuses	LCR	21 %	63 %	
Pancreatic carcinoma	AST	6.5 months	7.8 months	
Liver tumors	5y-S	23 %	100 % (HIMAC)	
Cervix uteri (stage IIIB)	LCR	66 %	73 % (neutron boost)	
Urinary bladder carcinoma	DS	30 %	50 % (neutron boost)	
Prostate (C, D1)	LCR	31-68 %	89 % (neutrons)	
Salivary glands	LCR	24-28 %	61 %	
Soft tissue carcinoma	5y-S	31-75 %	52-83 %	

LCR:	Local Control Rate	PFSR:	Progression Free Survival Rate
DS:	Down Staging	AST:	Average Survival Time
5y-S:	5-year Survival rate	HIMAC:	Heavy Ion Medical Accelerator in Chiba, Japan

Based on this pilot project and incentivated by its promising results, the institutions that take part in it[1] have made a proposal for a dedicated hospital-based ion beam facility for cancer therapy to be built in Heidelberg, Germany. This facility, expected to be operational in 2006, will have a treatment throughput of 1000 patients per year with a wider spectrum of treatable tumors. It will, furthermore, provide beams ranging from proton to oxygen ions thus enabling further clinical studies to be performed.

1.2 Physical Rationale for Carbon Ions

Beams of heavy charged particles like protons or heavy ions[2], like carbon, represent the optimum tool for the treatment of deep seated, inoperable and radioresistant tumors growing in close vicinity to organs at risk [Wil46, Kra90]. In contrast to conventional photon therapy, the dose deposited by heavy charged particles increases with the penetration depth, culminating in a sharp maximum at the end of the particle range - the Bragg peak (section 1.2.1). In order to achieve a precise tumor-conform irradiation, the Bragg maximum can be shifted in depth by energy variation and distributed laterally through magnetic deflection of the particle beam (section 1.2.2). In addition to these excellent physical selectivity, the biological efficiency concerning cell killing increases towards the end of the trajectory of the carbon ion. Therefore, the increase in dose at the Bragg peak is further enhanced by an increase in biological effi-

---

[1] The Radiologische Universitätsklinik Heidelberg (project coordinator), the Deutsches Krebsforschungszentrum Heidelberg (DKFZ) and the Gesellschaft für Schwerionenforschung Darmstadt (GSI) in cooperation with the Forschungszentrum Rossendorf (FZR), Dresden.

[2] Ions heavier than protons are called *heavy* in radiobiology [Kra00], as opposed to nuclear physics terminology, due to their increased biological effectiveness (section 1.3).

ciency (section 1.3). Finally, nuclear fragmentation reactions between the ^{12}C projectiles and atomic nuclei in the target volume create a small amount of β^+ emitters, mostly ^{11}C, ^{15}O and ^{10}C, which allow an in-situ dose localization control by using positron emission tomography techniques (section 1.4).

1.2.1 Passage of charged particles through matter

The depth dose profile exhibited by heavy charged particles is due to its ways of interacting with matter.

Electronic energy loss

Moderately relativistic[1], charged particles other than electrons lose energy in matter primarily by ionization. The mean rate of energy loss, or stopping power, is given by the Bethe-Bloch equation [Hag02, Leo94]

$$-\frac{dE}{dx} = K z_{eff}^2 \frac{Z}{A} \frac{1}{\beta^2} \left[\frac{1}{2} \ln \frac{2 m_e c^2 \beta^2 \gamma^2 T_{max}}{I^2} - \beta^2 - \frac{\delta}{2} \right] \tag{1.1}$$

with T_{max} the maximum kinetic energy which can be imparted to a free electron in a single collision and the other variables defined in Table 1.2.

Table 1.2: Variables and values of the Bethe-Bloch equation according to [Hag02].

Symbol	Definition	Units or value
$\frac{dE}{dx}$	energy loss	$\mathrm{MeV\,g^{-1}\,cm^2}$
A	atomic mass of medium	$\mathrm{g\,mol^{-1}}$
N_A	Avogadro's number	$6.022\,136\,7(36) \times 10^{23}\,\mathrm{mol^{-1}}$
$\frac{K}{A}$	$4\pi N_A r_e^2 m_e c^2 / A$	$0.307\,075\ \mathrm{MeV\,g^{-1}\,cm^2}$ for $A = 1\ \mathrm{g\,mol^{-1}}$
z_{eff}	effective charge of incident particle	
Z	atomic number of medium	
$m_e c^2$	electron rest energy	$0.510\,999\,06(15)\ \mathrm{MeV}$
I	mean excitation energy	eV
δ	density effect correction	

The values for the mean excitation energy I adopted by the International Commission on Radiation Units and Measurements (ICRU) for the chemical elements [ICR84] are now in wide use. Within the range of therapeutic relevant energies, below several hundreds of AMeV for carbon ions, $T_{max} = 2 m_e c^2 \beta^2 \gamma^2$ and the stopping power scales down with $\sim 1/\beta^2$ with increasing energy. The relativistic term $\delta/2$ in the Bethe-Bloch equation (density effect) is negligible and radiative processes do not take place.

Fig. 1.3 shows the stopping power for positive muons in copper for a wide range of projectile energies so that the limits of validity of the Bethe-Bloch equation can be seen. These limits depend both on the effective atomic number of the absorber and the mass of the particle slowing down [Hag02].

At lower energies corrections for tightly-bound atomic electrons (shell correction) and other effects must be made. Among these is the Barkas effect which explains the higher stopping power observed for positive charged particles, e.g. the μ, π and proton, in respect to their

---

[1] Particles with a velocity ranging between 10 % and 99 % of the speed of light, approximately.
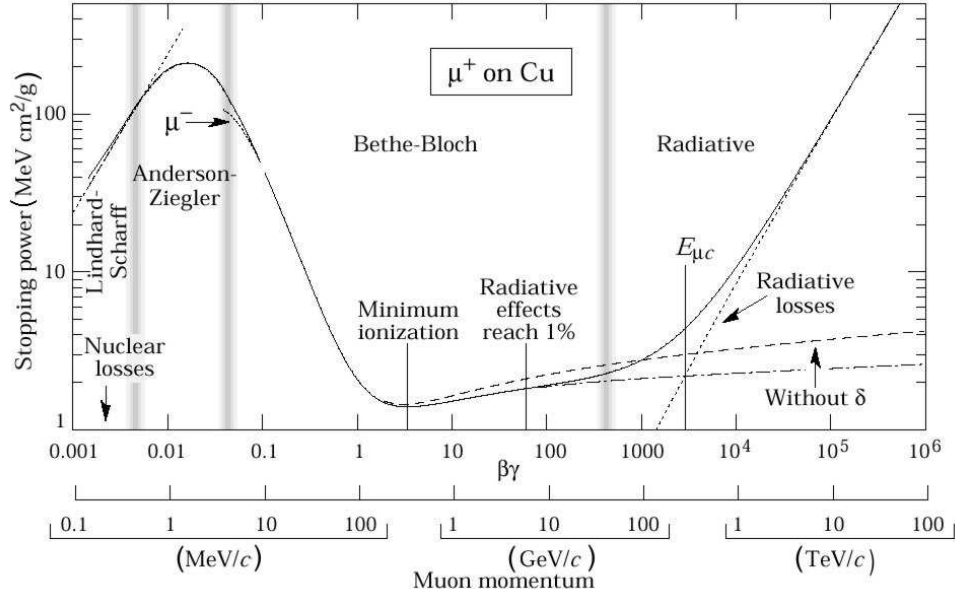
Figure 1.3: Stopping power for positive muons in copper as a function of $\beta\gamma = p/Mc$, after [Hag02]. Data below the break at $\beta\gamma \sim 0.1$ are taken from ICRU 49 [ICR93] and at higher energies from [Iva98]. For $0.01 < \beta < 0.05$ there is no satisfactory theory. For protons, empirical fitting formulae were developed by Andersen and Ziegler. For $\beta \leq 0.01$ (more or less the velocity of the outer atomic electrons), Lindhard has been able to describe the stopping power, which is proportional to β. At even lower energies, non-ionizing nuclear recoil dominates the total energy loss [Zie85]. The "μ^-" curve illustrates the Barkas effect described in the text.

negative counterpart [Zie99] due to the polarization of target electrons onto and away from the positive or negative projectile, respectively. A detailed discussion of low-energy corrections to the Bethe-Bloch formula is given in [ICR93]. Of main importance for heavier ions is the fact that at lower velocities a positive projectile starts collecting electrons from the surrounding target material, thus decreasing its effective charge z_{eff}. The correlation between the velocity of the projectile β and z_{eff} is given by the Barkas formula [Bar56]

$$z_{eff} = z(1 - e^{-125\,\beta z^{2/3}}).\tag{1.2}$$

The dominant part in the Bethe-Bloch valid regime is the $1/\beta^2$ factor and the z_{eff} dependence. The $1/\beta^2$ factor yields an increase in energy loss with decreasing energy: $1/\beta^2 \sim 1/E$. This can be seen in Fig. 1.4 for several ions, with the stopping power displayed with units of linear energy transfer ($LET_\infty = LET$), a measure of the energy deposited in the target by all electrons ejected by the passing particle. If LET_{100} would be used, for example, then only those electrons ejected with energies inferior to $100\,eV$ would be considered (restricted stopping power).

When the energy loss of a charged hadron is plotted versus its penetration depth, its maximum - the Bragg peak - is located at the end of the track. Fig. 1.5 shows this effect for carbon ions in water with different energies and with the energy loss converted to units of relative dose.

In radiobiology and therapy the absorbed dose D, with unit Gray (Gy), is defined as the energy deposited in the target per mass unit [ICR70], i.e. $1\,Gy = 1\,J\,kg^{-1}$. If a thin volume - thin compared to the energy loss of a particle - is irradiated by a parallel beam of particles with fluence F the dose imparted into this volume is

$$D\,[Gy] = 1.6 \cdot 10^{-9} \cdot \frac{dE}{dx}\left[\frac{keV}{\mu m}\right] \cdot F\left[\frac{1}{cm^2}\right] \cdot \frac{1}{\rho}\left[\frac{cm^3}{g}\right].\tag{1.3}$$
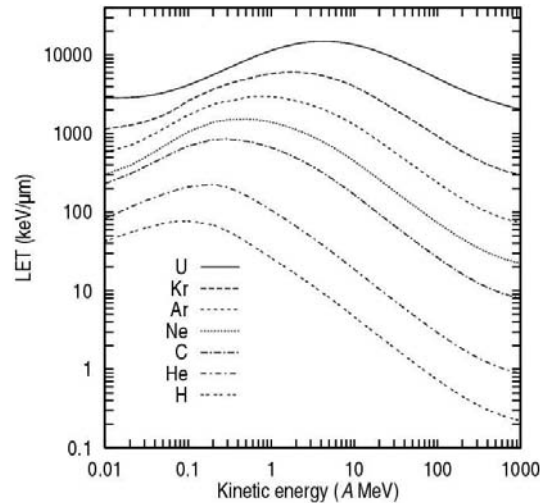
Figure 1.4: Energy loss in water for several particles, after [Sch91]. The curves were calculated with the computer code ATIMA (atomic interactions with matter).
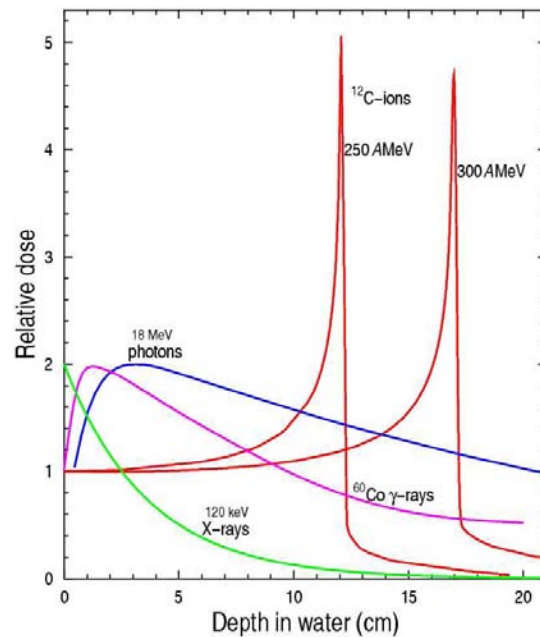
Figure 1.5: Depth dose profiles for photons and carbon ions with different energies, after [Kra00].

The low energy loss of charged particles at higher energies, shown in Figs. 1.3 and 1.4, yields the nearly constant dose plateau in the entrance channel in Fig. 1.5. Such depth-dose profile is optimum for the treatment of deep-seated tumors, as first noted by R. Wilson in 1946 [Wil46].

Multiple scattering and range straggling

A charged particle traversing a medium is deflected by many small-angle scatters. Although the strong interactions also contribute to this phenomenon, most deflections are due to Coulomb scattering with target nuclei, hence the effect is called multiple Coulomb scattering (MCS). As confirmed by proton measurements [Got93], the theory of Molière [Mol48] describes precisely

the Coulomb scattering distribution. It is roughly Gaussian for small deflection angles and it shows larger tails like Rutherford scattering for larger ones. For small angles θ it is sufficient to use a Gaussian approximation with an angular width given by [Hig75, Hig79, Lyn91a]

$$\sigma_\theta = \frac{13.6 \, MeV}{\beta pc} \, z \, \sqrt{x/X_0} \left[1 \, + \, 0.038 \ln\left(\frac{x}{X_0}\right) \right], \qquad (1.4)$$

with p, βc and z the momentum, velocity and charge of the projectile and x/X_0 the thickness of the scattering medium in radiation lengths[1]. For very heavy ions MCS has been compared with various theoretical distributions [Won90]. A compilation of results of MCS of heavy charged particles pertinent to therapy applications is presented in [Lit68].

The effects of MCS on the lateral broadening of beams of protons and carbon ions are shown in the top graph of Fig. 1.6. The lateral spreading of a photon beam is also shown for comparison. It can be clearly seen that protons exceed the lateral spreading of the photon beam after 7 cm penetration, whereas the deflection of the carbon beam is less than 1 mm up to a penetration depth of 20 cm. Beam lateral spreading plays an important role in treatment planning, mostly when high doses are needed (tumor) in close vicinity to low dose regions (healthy tissue, organs at risk). Examples of treatment planning comparisons between carbon ions and photons as well as protons and photons are given in sections 1.2.2 and 1.2.3, respectively.
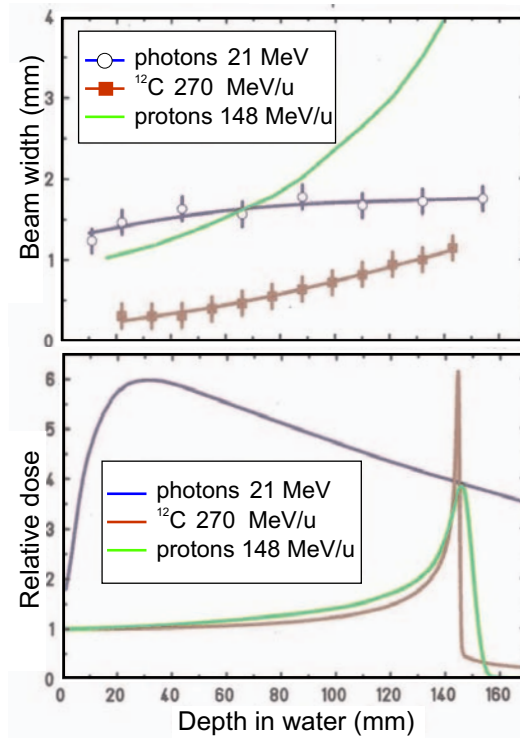
Figure 1.6: Lateral spreading of a photon, carbon and proton beam in water (top) and the corresponding relative depth-dose profiles (bottom), after [Web96]. Despite the initial difference in beam widths, a lower lateral scattering among the charged species is verified for carbon ions.

The dose-profiles on the bottom graph in Fig. 1.6 show a sharper Bragg peak at 14.5 cm for carbon ions versus protons due to the lower range straggling of heavier projectiles. The range R of a beam of monoenergetic charged particles with energy E is defined as the penetration

---

[1]   Mean distance over which a high-energy electron loses all but $1/e$ of its energy by bremsstrahlung [Hag02].

depth at which half of its initial particles have already stopped. If the ionization energy loss were a continuous process a sharp fall-off of the beam would occur at

$$R = \int_E^0 \frac{1}{dE/dx} \, dE, \tag{1.5}$$

which is not the case because the ionization process is stochastic and, furthermore, different MCS processes yield different paths for the beam constituents. Therefore, the calculated value R represents the mean range with a Gaussian distribution with the form [Boh15, Ahl80]

$$G(x) = \frac{1}{\sqrt{2\pi}\sigma_x} \exp\frac{(x-R)^2}{2\sigma_x^2} \tag{1.6}$$

where x is in the beam direction and

$$\sigma_x^2 = 4\pi \frac{Z_{eff}^2}{Z^2} N\Delta x \left[\frac{1-\beta^2/2}{1-\beta^2}\right]. \tag{1.7}$$

In water this width can be approximated to [Chu99]

$$\sigma_x = 0.0120 \, \frac{R^{0.961}}{\sqrt{A}}. \tag{1.8}$$

This formula is valid in the range $2\,\text{cm} \leq \text{R} \leq 40\,\text{cm}$. The value of σ_x (cm) is almost proportional to R and is inversely proportional to $\sqrt{A}$. For example, for a range of 20 cm in water $\sigma_x = 0.2$ cm for protons, 0.1 cm for helium, 0.06 cm for carbon and 0.046 cm for neon ions. However, in practice range profiles are determined rather by the density distribution of the penetrated tissue than by the intrinsic projectile straggling. For small penetration depths ($\text{R} < 10$ cm in the case of carbon ions delivered with active scanning - section 1.2.2), the half width of the Bragg maximum frequently has to be increased artificially with a passive absorber (ripple filter) in order to reduce the overall treatment time since, if the Bragg peak is too sharp, too many energy steps would be needed in order to fill the the target volume [Web96, Kra00].

Nuclear fragmentation

Heavy-ion nuclear reactions can be classically divided into three large classes: central collisions, peripheral collisions and various Coulomb force induced processes also named distant or barrier processes [Kau61, Nör80]. The impact parameter[1] b is responsible for this classification. At beam energies corresponding to approximately the Coulomb barrier[2] both barrier processes and central collisions take place, the latter forming only compound nuclei at these low energies. If b is relatively large the Coulomb barrier is not penetrated, giving rise to barrier processes like Rutherford scattering, Coulomb excitation [Alk56], nucleon transfer by tunneling [Rey56] and other combinations of these processes [Bre56]. The effects of Rutherford scattering (the only elastic collision) on the beam lateral broadening were described in the previous section (MCS). At smaller b the projectile can penetrate the Coulomb barrier but at the moment of contact with the target it has very little kinetic energy. A compound system is formed (fusion) which decays at some subsequent time[3]. The angular cross sections for emitted products of barrier processes peak at some angle for each bombarding energy and the peaks move to smaller angles with increasing energy [McI60].

---

[1] Distance b between the trajectories of the centers of two colliding nuclei (Fig. 1.7).

[2] Value of the Coulomb potential when the two nuclei are at a distance corresponding to the sum of their radii: $V_{Coul} = \frac{1}{4\pi\epsilon_0}\frac{Z_1 Z_2 e^2}{r}$, with $r = 1.4 \times [A_1^{1/3} + A_2^{1/3}]$.

[3] This regime is used to search for super heavy nuclei. At GSI and LBNL cold fusion is used, whereas the Joint Institute for Nuclear Research (JINR), in Dubna, Russia, uses hot fusion methods [Hof00].

When the beam energy is well above the Coulomb repulsion between projectile and target, nuclear fragmentation gradually takes place and the contribution of elastic scattering decreases [Won94]. This is the case with the incoming energies for therapy with carbon ions (85 to 430 AMeV). Because of its high-energy the projectile comes in contact with the target nucleus and, as a consequence of the geometry of the reaction in this energy regime (Fig. 1.7), central or near central collisions account for about 10 % of all nuclear fragmentation events [Sih93, Oli79]. At these energies, central collisions are characterized by multifragmentation, i.e. the blow-up of the reaction partners into many fragments distributed over a wide range of angles [Oli79]. Peripheral collisions, therefore, constitute the major source of events of nuclear fragmentation.
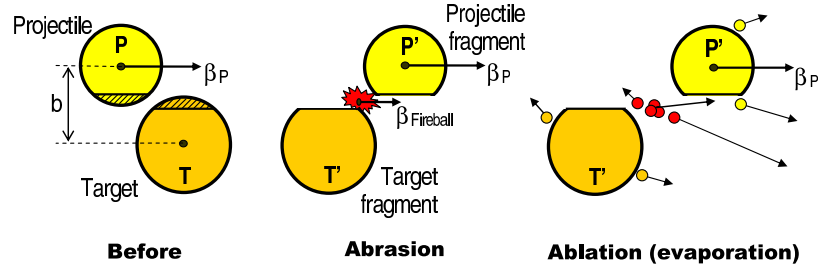
Figure 1.7: Scheme of a peripheral nuclear collision according to the abrasion-ablation model.

Most peripheral collision models today are based on the concept of nuclear abrasion-ablation [Oli79] depicted in Fig. 1.7. The target and projectile overlap only partially and, depending on the impact parameter and the sizes of the nuclei, a fireball is formed (abrasion, $\sim 10^{-23}$ s) with all overlapping nucleons (participants). Due to the high velocity of the reaction, the remaining projectile and target nucleons can be considered not to take part in the reaction (spectators). Consequently, the fireball travels along the beam direction with less kinetic energy per nucleon (it contains nucleons both from projectile and target), whereas the projectile fragment remains large and travels almost with the same velocity of the original projectile. In a second step ($\sim 10^{-21}$ to 10^{-16} s) the excitation energy in the fragments and fireball is released by evaporation (ablation) of nucleons. When the energy of the excited products falls below the nucleon separation threshold the emission of γ-rays takes place (chapter 6).

Peripheral collisions result in fewer particles (compared to central collisions) observed in the forward cone of laboratory angles [Gun04a, Gun04b]. They include both charge-changing (projectile loses one or more protons) as well as non-charge-changing (loss of one or more neutrons) reactions. Both reactions have utmost importance on the physical dose distribution. Charge-changing reactions produce lower-Z particles which have longer ranges and deliver an unwanted dose beyond the Bragg peak of the original projectile. Non-charge-changing reactions produce lower-A isotopes which stop before the original projectile (range scales with A/Z^2 at same velocity).

In order to correctly account for the dose contribution of all intervening particles, fragmentation measurements were performed in Berkeley for neon [Sch89] and at GSI for carbon ions [Sch96a, Sch96b] among other species. Fig. 1.8 shows the results for several projectiles. The bottom row of Fig. 1.8 shows that the fragmentation of ^{16}O yields more C^{6+} nuclides than N^{7+}. This is due to selection rules that prevent the abundance of the different fragments from decreasing monotonously with atomic number [Kra00]. In the same row it is possible to see a slight inversion of the number of fragments for higher penetration depths, corresponding to fragmentation reactions of the fragments themselves into further lower-Z particles. This contributes to the high yield of low-Z fragments shown in the middle row (curve with $Z \leq 4$).
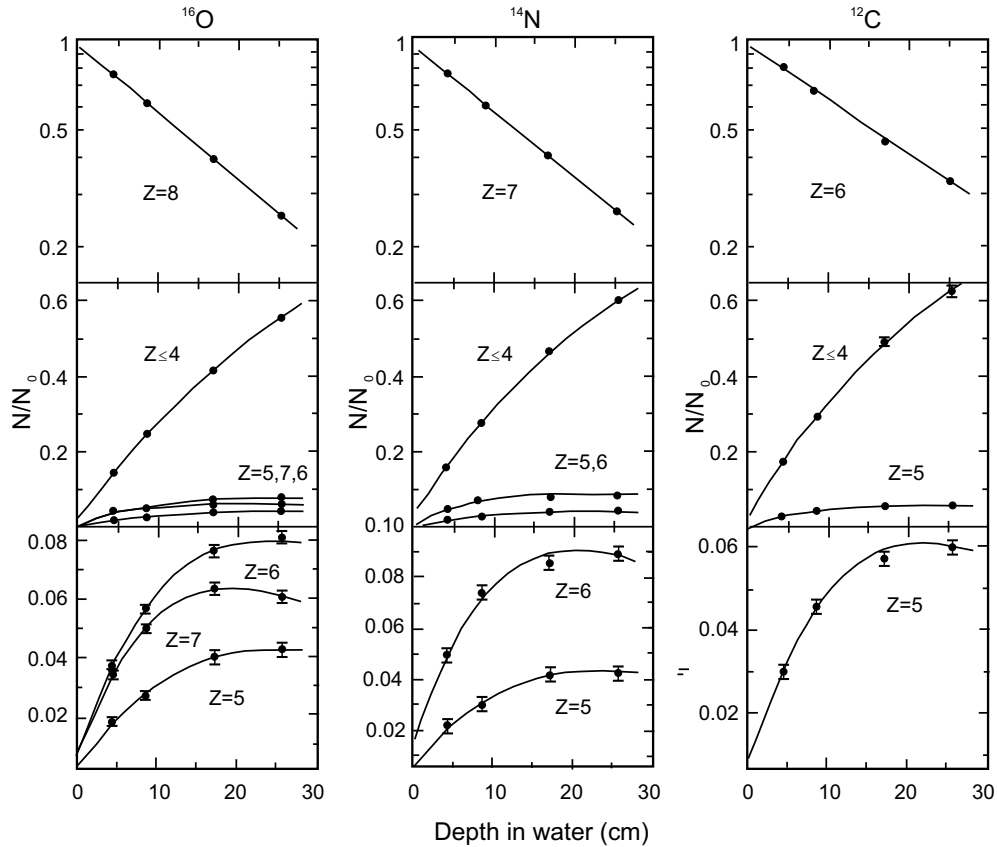
Figure 1.8: Fragmentation measurements for oxygen, neon and carbon ions with $670\,A$MeV, after [Sch96b]. Top row shows the attenuation of the original projectiles. The middle and bottom rows show the buildup of lower-Z fragments.

In general, beam fragmentation tends to deteriorate the sharp dose contours by enhancing lateral and longitudinal scattering. This is a minor problem at the entrance channel - high energies - but becomes more important at the tail of the Bragg peak. Fragmentation products restrict the use of an absorber material (section 1.2.2) in the beam. Fig. 1.8 also shows an increase in the number of fragments with increasing projectile size and charge. For heavier ions, the undesirable amount of fragments produced is further enhanced (e.g. neon, section 1.2.3).

The knowledge of the fluences F of the several nuclear fragmenation projectiles N_z reaching the target volume at $\mathbf{r}$ with density ρ is necessary in order to calculate the total dose:

$$D_{eq}(\mathbf{r}) = \sum_{z=1}^{N_z} \int_0^E F(z, E, \mathbf{r}) \cdot LET(z, E) \cdot RBE(z, E) \cdot \frac{1}{\rho(\mathbf{r})} \, dE. \qquad (1.9)$$

D_{eq} denotes the equivalent dose since the physical dose deposited at each location $\mathbf{r}$ is weighted by its relative biological effectiveness RBE (section 1.3).

Finally, nuclear fragmentation may result in radioactive projectile and target fragments de-exciting by β^+ decay. A tremendous advantage to radiotherapy is opened by using imaging techniques like positron emission tomography (PET) to measure this β^+ activity, since it is highly correlated with the incoming beam (section 1.4).

1.2.2 Advantages in comparison to photons

The main physical advantage in radiotherapy when heavy charged particles are compared to photons arises from the different depth-dose profiles of the two species, as shown in Fig. 1.5. The profile exhibited by photons is due to the physics processes through which electromagnetic radiation interacts with matter, namely

- photoeffect: the photon is absorbed and an atomic electron ejected;

- incoherent (Compton, inelastic) scattering: the photon is scattered and an atomic electron ejected, this is the main process at radiotherapeutical relevant energies;

- coherent (Rayleigh, elastic) scattering: the photon is deflected from its trajectory but the target atom is neither ionized nor excited;

- pair production: disintegration of a photon into an electron-positron pair due to an interaction with the nuclear field, or with the field of the atomic electrons; and

- photonuclear absorption: nuclear absorption, usually followed by emission of a neutron or other particle.

Fig 1.9 exemplifies how the individual processes are depending on the photon energy for a carbon target. Although for water, tissue and denser organic material the cross sections are different, the ratio between the different processes does not change dramatically. Therefore, it can be seen that within the typical energy ranges for photon radiotherapy (~ 4 to 50 MV) the main physical process contributing to the dose is the Compton effect. For diagnostic imaging (X-rays), much lower energies are used and the photoeffect plays also an important role.

Although the number of penetrating photons in an incoming beam decreases exponentially with the target depth, the photon depth-dose profile in Fig. 1.5 first shows a slight increase and only after an energy-dependent peak it starts falling exponentially. This is due to the fact that
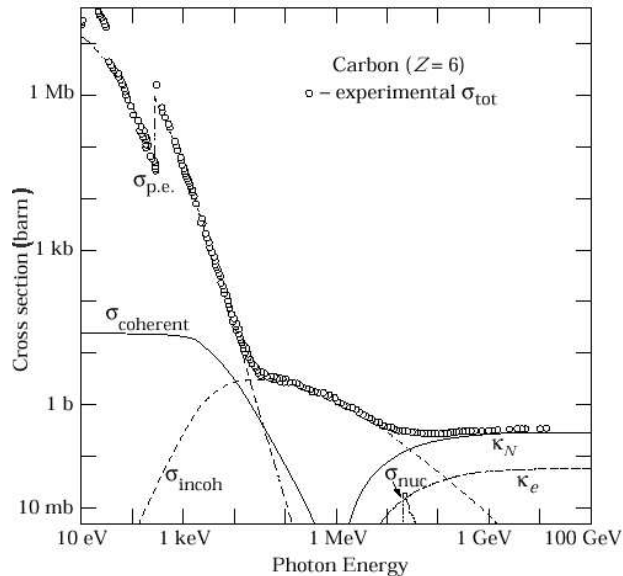
Figure 1.9: Cross sections for photon interactions in carbon, after [Gro98b], with $\sigma_{p.e.} = $ photoeffect, $\sigma_{coherent} = $ coherent scattering, $\sigma_{incoh} = $ incoherent scattering, $K_N = $ pair production (nuclear field), $K_e = $ pair production (electron field) and $\sigma_{nuc} = $ photonuclear absorption.

the Compton released electrons are strongly forwardly peaked so that the energy transferred into the target is transported a few centimeters deeper into the direction of the beam (build up). For this reason dose calculations for photon therapy do not use the photon attenuation coefficient but the photon energy-absorption coefficient (absorbed dose).

Another physical disavantage of radiotherapy with electromagnetic radiation when compared to carbon ions is the higher beam lateral broadening with photons. Lateral scattering of charged particles was discussed in section 1.2.1 and its consequences onto treatment planning with carbon ions and with protons are presented in sections 1.2.2 and 1.2.3, respectively.

Beam shaping: the importance of the rasterscan technique

One important advantage besides the depth-dose profile of charged hadrons in regard to photons is the possibility to drive a charged beam by using magnetic deflection. Despite being a technical challenge due to the high energies required to make a charged beam penetrate deep enough into tissue and bone (e.g. a 400 AMeV ^{12}C beam penetrates 27.3 cm in water), this principle avoids all the passive shaping components in the path of the beam described below.

Beam shaping for photons: Although a method for active shaping of scanned high-energy photon beams has been proposed [Sve98], only passive beam shaping, depicted in Fig. 1.10, has been used to date for simplicity reasons. X-rays (characteristic and bremsstrahlung) are produced by hitting high energy electrons (after the accelerating waveguide) in the radiator target. The photons are emitted primarily in the forward direction, but also laterally and backwards. At the primary collimator - a block of high density metal e.g. tungsten - laterally-produced X-rays are attenuated. A uniform intensity across the beam is later produced at the beam flattening filter. The ionization chambers provide a current proportional to the absorbed dose rate of the treatment beam in the patient (or a tissue-equivalent phantom). Feedback systems automatically adjust the electron beam current in the accelerating waveguide and beam steering current, to ensure constant treatment beam output and uniformity. Finally, the wedge filter can be used to modify the intensity of the X-ray photon beam in one plane to shape the isodose distribution around a target volume. Older linear accelerators (LINAC) may have manual wedge filters of varying thicknesses. Some LINAC use a dynamic wedge or *flying jaw* technique to give the effect of a wedged beam using precise computer control of jaw movement. In newer systems, able to deliver intensity modulated radiotherapy (IMRT), a
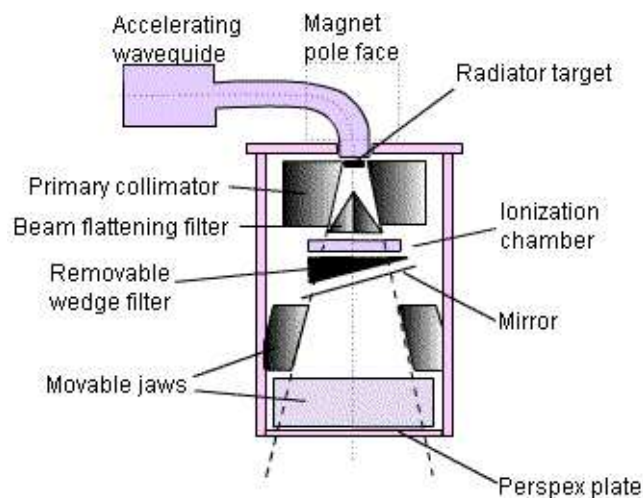
Figure 1.10: Diagram of a photon treatment head, after [Lin05].

dynamic multileaf collimator consisting of 20 or more thin collimator plates is used to obtain irregularly-shaped fields that conform to the target volume.

Passive beam shaping for hadrons: Both passive and active beam shaping have been implemented in charged hadron radiotherapy. The width of the Bragg peak and the lateral dimensions of a particle beam are usually much smaller than the tumor volume to be treated. Therefore, the beam has to be spread in lateral and longitudinal direction in order to fill the target volume as precisely as possible. Tumor conformity is an issue in order not to damage healthy tissue, but special care must also be taken in order to avoid cold spots (local regions with lower dose) in the target since an underkill there corresponds to a tumor regrowth center.

Fig. 1.11 depicts the principle of passive shaping for heavy ions. The accelerator produces a beam of fixed energy which is laterally spread at the scattering system. At this stage the dose profile corresponds to a pristine Bragg-peak. To overlay the dose over the whole extension of the tumor a range modulator together with a range shifter degrade the spatial resolution of the pristine peak and assure that the overlay of several Bragg-peaks produces a so-called spread-out Bragg peak (SOBP). A compensator, manufactured for each patient[1], is responsible for finally adapting the beam shape to the tumor volume avoiding dose delivered at the several OAR. A detailed review of beam shaping systems is given in [Kra00].
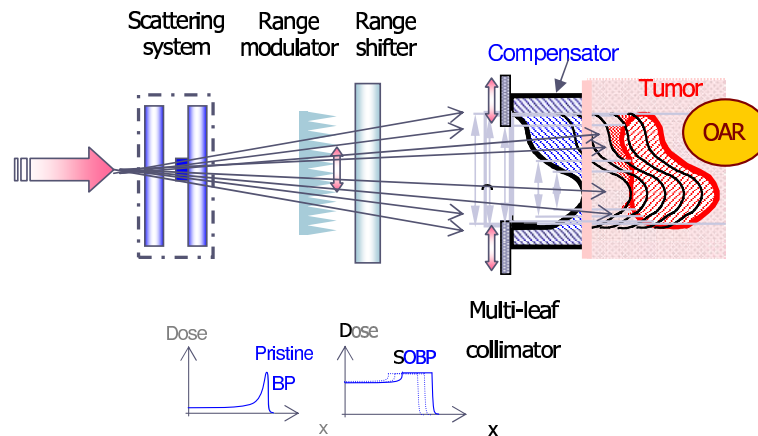
Figure 1.11: The principle of passive beam shaping, after [Reg02].

Besides requiring a compensator being built for every patient and being limited in volume conformity, passive shaping also needs higher beam intensities, when compared to active shaping described below, because a major part of the primary beam is wasted in apertures and blocking devices. This, furthermore, produces a large amount of mostly forwardly scattered neutrons and neutron-induced contaminations with its biological and technological drawbacks like, for example, the activation of nearby imaging devices (section 1.4).

Active beam shaping: Excellent 3D beam conformity through an active beam delivery system has been achieved at GSI by means of the intensity controlled rasterscan technique [Hab93]. The target volume is dissected into layers of equal particle energies (Fig. 1.12) and a small pencil beam moves in each layer along a continuous path from one pixel to the next one[2] by making use of the depicted fast magnetic system. The particle fluence is measured for each pixel and

---

[1] An individual range modulator may also be necessary.

[2] This is the rasterscan principle. The voxelscan principle (also called spot scanning, section 1.2.3) applied at the Paul Scherrer Institute (PSI) in Switzerland shuts off the proton beam between each pixel [Ped95]. There, depth conformity is achieved by means of a range shifter, i.e. the scatterers, collimator and compensator of Fig. 1.11 are avoided.

the beam is switched to the next pixel when the intensity for one position has been reached. If the irradiation of one energy slice is complete the beam is switched off and the next, higher energy is requested from the accelerator. With an accelerator duty cycle of approximately 40 % (2 s spill extraction with a macropulse period of 5 s, detailed in section 1.4.2 and chapter 6), the GSI scanning system is able to deliver, from macropulse to macropulse, carbon beams ranging from 80 to 430 AMeV with 252 energy steps, corresponding to ranges in water between 2 and 30 cm, respectively. In addition, the beam intensity and diameter can be changed in the same mode. This is usefull because larger tumors can be treated faster with a larger beam spot while small tumors or tumors very close to critical structures can be handled with smaller beam sizes.
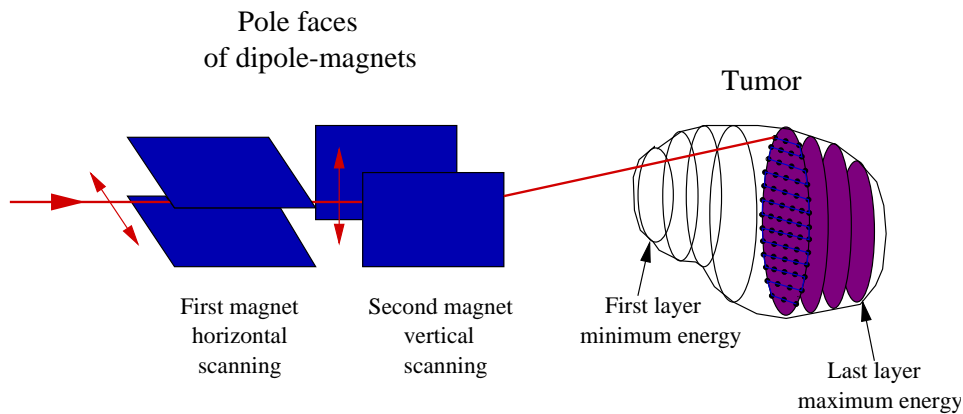
Figure 1.12: The principle of the raster scanning technique, after [Hab93].

Not shown in the picture but also of great importance is the beam diagnosis system implemented between the last steering magnet and the patient. Two multiwire proportional chambers (MWPC) constantly verify the beam position while three ionization chambers read continously the beam intensity being delivered [Bad97]. This information is fed into the magnet control unit so that in the case of an unexpected deviation an interlock (beam switched off) is achieved within half a millisecond [Hab93].

Treatment planning comparison: carbon ions versus IMRT

To compensate for the unfavorable, exponentially-decaying dose profile of photons in radiotherapy the patient is irradiated from several directions (portals) in order to accumulate a higher dose in the tumor and spare the surrounding healthy tissue. Nevertheless, even with state-of-the-art photon radiotherapy techniques like IMRT it can be seen that the degree of tumor conformity is much higher for ions, as exemplified in Fig. 1.13 for a head tumor and described in more detail in [Sch03a] for spinal chordomas. The high conformity achieved with carbon ions is due not only to the physical and radiobiological characteristics of the ions, but also to the excellent beam delivery described above.

1.2.3   Advantages in comparison to other charged particles

In the previous section the physical advantages of charged hadron therapy were compared with electromagnetic radiation. Within the spectrum of charged particles, though, the question of which one performs better is not so easy to answer since all present an inverse depth-dose profile and all can be steered by magnetic scanning.

Carbon beam, 2 portals   **IMRT, 9 portals**
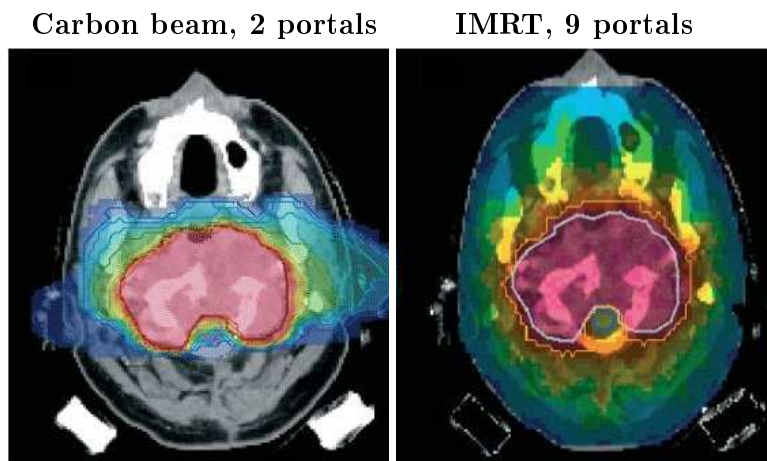
Figure 1.13: Comparison of dose conformity with carbon ions versus IMRT for the same patient, from [Wey03], courtesy of Oliver Jäkel, PhD. The 10 color levels indicate iso-dose lines starting from 5 % (blue) to 95 % (red) of the maximum dose. A significantly higher dose is delivered to normal tissue with IMRT. Also, a much better conformity is achieved at the brain-stem (organ at risk) in the case of the carbon treatment.

Protons

The first use of protons in therapy was performed at the Berkeley 184-inch synchrocyclotron [Tob52] in 1952, for pituitary[1] treatments. Rotational therapy (twisting the head about the pituitary as a center of rotation) was used with a high energy beam in order to avoid stopping the beam due to the uncertainty in the tissue-thickness along the beam track. The first Bragg-peak therapy was performed in 1956 at Uppsala with a 230 MeV synchrocyclotron [Lar63]. In 1965 the 170 MeV synchrocyclotron at Harvard was converted into a dedicated medical facility and became the site for the longest running program in radiosurgery and therapy with protons. To date, over 30 000 patients have been treated at these and other newer facilities, with protons being the most used charged particle cancer treatment modality due to the lesser complexity of a proton radiotherapy facility [Kra00].

Although the answer to which modality performs better cannot be complete without addressing radiobiology (section 1.3), a physical advantage of carbon ions over protons was already pointed out in section 1.2.1, i.e. ions suffer less Coulomb scattering from target atomic nuclei due to its larger mass and therefore momentum, thus enabling sharper gradients to be delineated. However, nuclear fragmentation of the projectile, which does not happen with protons, enhances the dose beyond the Bragg peak (Fig 1.6). For this reason, despite the low physical dose, and due to possible range uncertainties induced by anatomical density irregularities along the beam path, treatment planning with carbon ions should be careful when stopping the beam just before any critical structure.

Two treatment planning comparisons between passively shaped protons and actively scanned carbons ions are discussed in [Jäk02]. Important conclusions regarding dose conformity can be drawn. For example, for a patient with a clivuschordoma the dose in the target volume is more homogeneous when delivered with carbon ions, with a maximum/minimum ratio of 99 % / 69 % versus 102 % / 51 % for passive conformed protons. In summary, dosage of OAR is reduced and irregular tumors can be much better delineated with active delivered carbon beams. This work

---

[1] The pituitary is a small, pea-sized gland located at the base of the brain [Pit05]. It functions as a master gland, sending signals to the thyroid gland, adrenal glands, ovaries and testes.

is of great clinical impact due to the high number of facilities treating patients with passive shaped protons worldwide. But it does not provide a direct answer to which species performs better on the clinical level because of the disavantage of passive shaping considered in the proton treatment planning. Therefore, Fig 1.14 shows two treatment plannings for the same patient comparing the conformity achieved with spot scanned protons (PSI) and IMRT [Lom99]. Cold spot analysis, for example, indicates that the proton plans generally provide better coverage of the target. The same applies to healthy tissue and OAR irradiation. The example shown in the figure, though, shows better conformity achieved with photons around the brain stem. It must be noted that the proton treatments did not use inverse planning and that the spot scanning technique still has some material in the beam path (section 1.2.2), meaning again that the proton conformity is not at its optimum. A comparison with Fig 1.13, despite being different patients with different tumors, reveals a better sparing of the brainstem (an OAR) with carbon beams.
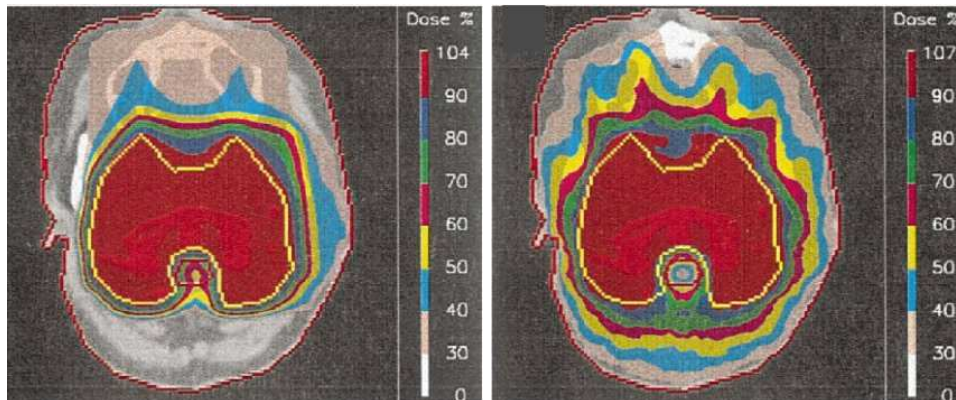
Figure 1.14: Comparison of dose conformity for spot-scanned protons (left) versus IMRT (right) for the same patient, from [Lom99]. The proton treatment consists of 2 portals without inverse planning, whereas the IMRT plan is based on 9 beam portals. A higher dose is delivered to normal tissue with IMRT but with better conformity achieved at the brainstem (organ at risk).

In conclusion, there is clear evidence that better conformity and target homogeneity is achieved with heavier ions (e.g. carbon) in comparison to protons. But it seems that there is a lack of clinical data to prove the benefit of these improvements, i.e. no direct comparison between heavy ions and protons has yet been performed which includes clinical outcomes. The heavy ion radiotherapy facility in construction in Heidelberg, planned to deliver ions ranging from hydrogen to oxygen, can provide an answer to this quest.

Heavier Ions

The possibility of using carbon, neon and silicon beams for radiotherapy was investigated from 1977 to 1992 at LBNL [Pet94]. Radiobiological studies indicated that the ratio of the effective dose in the peak to the effective dose in the entrance or plateau region was higher for carbon than for neon. This finding suggests that carbon ions are optimal because they deliver lower doses to normal tissues upstream from the tumor. But the oxygen enhancement ratio[1] (OER) was shown to be lower for neon and silicon than for carbon ions, which implies that, at least theoretically, ions with higher atomic number should be more effective therapeutically because most tumors are hypoxic. For this reason, argon ions were initially used for patient

---

[1] Ratio of hypoxic to aerated doses needed to achieve the same biological effect, i.e. cell killing (section 1.3). High OER implies that, in hypoxic conditions, a higher dose must be delivered in order to produce the same cell killing obtained in oxic conditions [Hal94].

treatment. After a few treatments, the beam was shifted to silicon and finally to neon ions in order to reduced side effects. Energies between 450 and 670 AMeV were selected for the neon radiotherapy research trials at the Bevatron facility at LBNL, with the most commonly used being 585 AMeV [Pre97].

By the time the Bevatron facility was closed due to budget reasons in 1993, 299 patients had received at least 10 Gy with neon ions as part of their treatment. In comparison to conventional photon therapy, improved control and survival rates were achieved for patients with paranasal sinus tumors, some salivary gland tumors, biliary tract carcinomas, some soft tissue and bone sarcomas and advanced prostate carcinomas. In some cases the mentioned rates were twice as high as with photons. But the outcome of treatment of other types of tumors, such as some brain tumors, melanomas, advanced or recurrent head and neck squamous-cell carcinoma, non-small-cell lung cancer and esophageal, gastric and pancreatic malignacies was not better than with conventional therapy. Furthermore, significant late effects on normal tissues were induced [Lyn91b]. It must be stated that most of the selected patients had advanced disease for which no other form of curative therapy existed.

The tremendous, pioneering work at LBNL allowed to study the response to ion beams of a variety of tumors and evaluate the corresponding acute and late toxicity. But the use of carbon ions seems to obviate the complications of heavier ions. They provide better equivalent dose localization, more sparing of normal tissues and optimal high-LET deposition.

1.3 Radiobiological Rationale for Carbon Ions

Because radiation can cause damage to the normal tissue in front of, and surrounding a deep-seated tumor, limitations to dose escalation in the tumor arise in order to avoid complications in the healthy tissue. This poses a more serious problem in radioresistant tumors where higher doses in the tumor are necessary in order to sterilize all cancer cells [Sch03b].

With carbon ions, in addition to their excellent physical selectivity (section 1.2), the biological efficiency concerning cell killing increases towards the end of the trajectory of the ion [Sch96d]. Therefore, the increase in physical dose at the Bragg peak is further enhanced by an increase in biological efficiency thus increasing the peak-to-plateau ratio of the equivalent dose.

1.3.1 Radiation chemistry, ionization density and DNA damage

Radiation damage along a particle track is caused by direct and indirect mechanisms. Both are induced by the particle itself and, to a much greater extent, by the electrons ejected as the particle passes by[1]. In direct mechanisms the DNA molecules are ionized, therefore damaged, by these ionizing particles. In indirect mechanisms the damage to the DNA is induced by free radicals[2], produced by the ionizing particles, which diffuse and react with the DNA. In indirect action the energy transferred by the ionizing particle produces free radicals R· such as e_{aq}^-, ·OH, and H· (cells contain more than 70 % water). Of these, ·OH is believed to be the most effective in causing damage because it is an oxydizing agent and can extract an hydrogen atom from DNA [Hal94]. But the damage induced by indirect action is only stable in the presence of oxygen in the cellular medium. This experimental fact is not clearly understood. A possible explanation assumes that the cellular oxygen forms a stable organic peroxide with the free radical RO_2· that attaches to the DNA lesion, preventing the damaged DNA to repair

---

[1] In the case of indirectly ionizing radiation (photons, neutrons) only the ejected electrons contribute to the ionization of the medium.

[2] Highly reactive, neutral, chemical species containing one unpaired electron in the outer shell.

itself. As a consequence, cells deprived from oxygen (hypoxic) suffer less permanent damage from indirect action than those in an oxygenated medium. Since $\sim 2/3$ of the damage induced by sparsely ionizing radiation (photons, protons) follows this mechanism, it is clear that high-LET particles (LET $> 30\,\text{keV}/\mu\text{m}$), which mostly induce damage via direct action, offer a clear advantage to treat hypoxic tumors[1].

The reason why high-LET particles induce damage mostly by direct action at the end of their track is that their ionization density is much higher there (Fig. 1.15). At the begining of their trajectory even high-LET projectiles ionize the medium sparsely due to their high velocities. The DNA double-helix ($\sim 2\,\text{nm}$ diameter) might suffer single, even double strand breaks that it can repair. But at the end of its track a high, compact ionization density is deposited by carbon ions that induces clusters of DNA lesions in both helix strands that the cell cannot repair. Since the damage is done by direct action upon the DNA the presence or absence of cellular oxygen is irrelevant. Therefore, the DNA has permanently lost its information and mitosis (cell division) is no longer possible, i.e. the tumor cannot proliferate and local control is achieved.
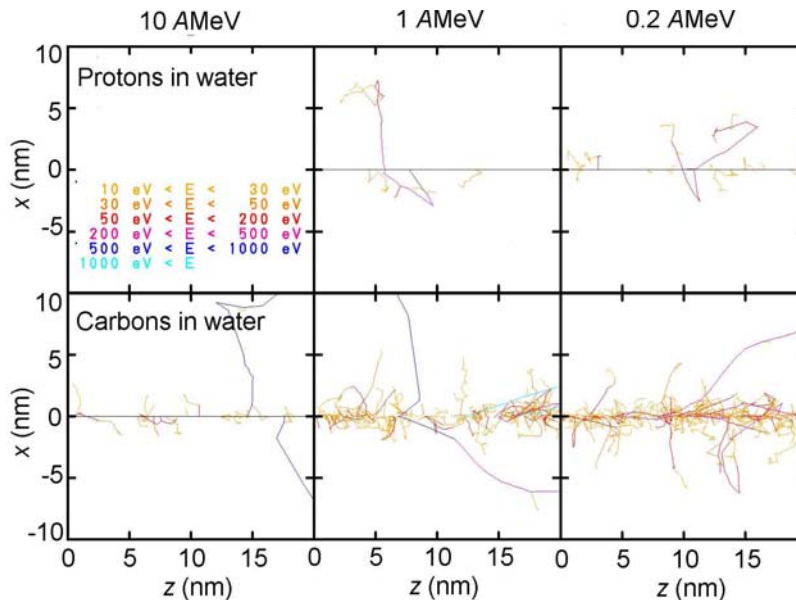
Figure 1.15: Track structure comparison (Monte-Carlo) between protons and carbon ions, after [Krä94]. The projectile moves along the Z-axis ejecting target atomic electrons. At high energies both projectiles behave similarly. Only at the carbon Bragg peak a high, compact ionization density can be seen around the track.

1.3.2   Relative biological effectiveness

Because the same physical dose delivered with sparsely ionizing or with high-LET radiation results in different cell damage (section 1.3.1), radiobiology uses the relative biological effectiveness RBE to normalize any physical dose with that delivered with X-rays that would result in the same cell killing (isoeffect):

$$RBE_{part} = \frac{D_{photons}}{D_{part}}\bigg|_{isoeffect}. \tag{1.10}$$

---

[1] Normally large tumors with central cores that lack oxygen because the blood supply has been reduced by the proliferating tumor cells.

For carbon, RBE values between three and five are verified at the Bragg peak for most radioresistant tumors. Fig. 1.16 shows how the match between the RBE maximum and the Bragg peak enhance the peak-to-plateau ratio of the effective dose.
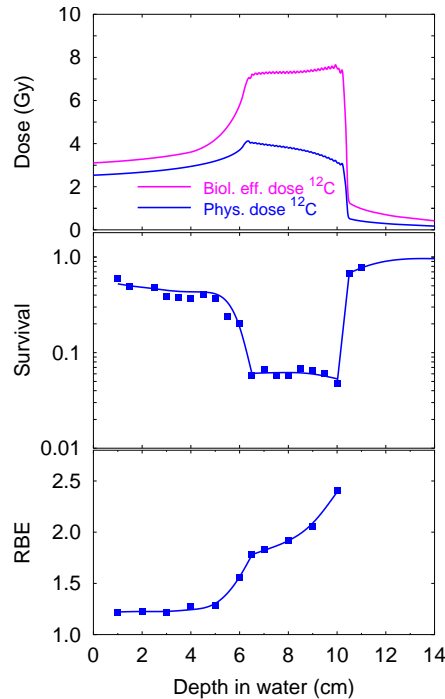
Figure 1.16: Correlation between dose, cell survival and RBE, after [Wey03]. The carbon ion physical dose (top, sum of several Bragg peaks) is multiplied with the RBE (bottom) yielding a flat biologically effective dose at the tumor (top, effective dose). Measured survival rates of chinese hamster ovary (CHO) cells are overlayed onto the curve predicted with the local effect model [Sch96d].

For protons, RBE is normally taken to be 1.1 along most of their track, so no enhancement of the physical dose takes place. In the last micrometers of their track a rise in the proton RBE is verified but with no clinical usefulness. For ions like neon and heavier, their extremely high LET at the Bragg peak (Fig. 1.4) produces an overkill of cells there yielding no biological enhancement. In this case the maximum of the RBE occurs even before the Bragg peak, which has therapeutical disavantages.

It must be stated that the RBE depends on tissue and tumor type, particle species, beam intensity, beam energy (thus LET) and physical dose [Kra99]. For this reason, more than 100 000 cell cultures (viruses, bacteria and mammalian cells) were irradiated at GSI before the first patient irradiation in order to fine-tune the LEM [Sch96d] used in the treatment planning [Krä00]. Furthermore, the ejection of atomic electrons by the passage of fast ions was also measured [Rei98] in order to provide a precise input for track structure calculations [Krä94].

1.4 In-beam PET for In-Situ Monitoring the Beam Localization

The properties of carbon ion beams make it a sharp knife that has to be used with extreme precaution so that tissue exposure to a high dose within the high-RBE Bragg peak is restricted to the tumor volume only. For this reason, imaging techniques allowing to monitor the beam localization as it penetrates the target are highly desired. To date, two methods first proposed at LBNL [Tob77, Lla88] are possible, both making use of positron emission tomography

(PET). The most straightforward one uses β^+-decaying radioactive projectiles. This approach has been followed at the passive-shaping, carbon radiotherapy facility HIMAC, where a first irradiation with ^{11}C or ^{10}C ions is delivered to the patient in order to perform accurate range measurements [Ura01]. Because the production rate of the secondary beam from the stable ^{12}C ion has an efficiency of 1 % to 0.1 %, respectively, with very expensive consequences arising from shielding and radiation protection, the following irradiation fractions are performed with ^{12}C. With this method, the patient is scanned in a commercial PET system following the radioactive beam irradiation. Activity densities of 10^3 - 10^5 Bq Gy^{-1} are achieved within the irradiated volume, depending on the half-life of the isotope. The method offers the advantage of providing a high activity suitable for high-statistics, artifact-free (from the point of view of the positron tomograph) PET imaging. It delivers important clinical information by verifying the correspondence between the planned and delivered treatments. But it has two main drawbacks: (1) the activity created in the tumor and surrounding healthy tissue is washed out by the blood circulation during the patient irradiation, transport to the PET room and during the PET scan itself, leading to image blurring and false different intensities in highly versus poorly perfused tissue and, more importantly, (2) anatomical changes occurring during the course of any a-posteriori fractionated irradiation (section 1.4.2) will no longer be detected, together with the impossibility of verifying the portal positioning during those irradiation.

The second imaging method allowing to monitor the beam localization makes use of nuclear fragmentation (section 1.2.1) between stable beam projectiles and target nuclei. This is the method implemented at GSI [Eng05a], with a specially adapted positron scanner measuring the activity created during patient irradiation [Eng04b], and therefore named *in-beam PET*.

1.4.1   Auto-activation and target activation

As the beam penetrates the target, both projectile and target fragments may become radioactive (auto and target activation, respectively) and de-excite by β^+ decay. After deposition of the auto-activated particles and because of the similar range with the original projectile (section 1.2.1) a peak of activity close to the Bragg peak of the original projectile is formed. Target projectiles remain in the site of collision and their activation produces a radioactive trace along the beam path [Tob71, Eng92]. The results from both processes occurring in a phantom of plexiglas[1] can be seen in Fig. 1.17 for carbon ions. The dominant auto-activation mechanism is the loss of one neutron by the projectile, leading to an activity peak at the site of deposition of the ^{11}C created in flight (≤ 8 % before the Bragg peak of ^{12}C, depending on the site of creation of the ^{11}C). This allows to control the location of the distal edge of the beam. The similarity between the sum of all β^+-decaying components and the dose deposited by the stopping beam should be noticed.

The activated fragments in the depth-profile in Fig. 1.17 (top, left axis) will decay with different lifetimes and the corresponding annihilation photons will be emitted in all directions. Consequently, the deposited activity could be fully registered only if (1) a detector with a solid angle of 4π and 100 % efficiency for 511 keV photons could be installed around the target, which is not feasible, and (2) the imaging time T_{imag} would satisfy both $T_{imag} \geq 3 \cdot \tau(^{11}\mathrm{C}) = 88$ min[2] (unfeasible in radiotherapeutic applications) and $T_{imag} \ll T_{1/2}(washout) \sim 4$ min [Tom03], which is impossible. The term washout denotes the transport of part of the deposited activity onto other regions of the body by the blood circulation. The limitations imposed by (1) and (2) are further discussed and optimized in chapters 2 and 6, respectively.

---

[1] Lucite, polymethylmethacralate (PMMA), $C_5O_2H_8$, with $\rho = 1.18$ g cm^{-3}.
[2] The isotope produced with the longest half-life is ^{11}C. The symbol $\tau(^{11}\mathrm{C})$ denotes its lifetime and $3 \cdot \tau(^{11}\mathrm{C})$ corresponds to its decay by 95 %.
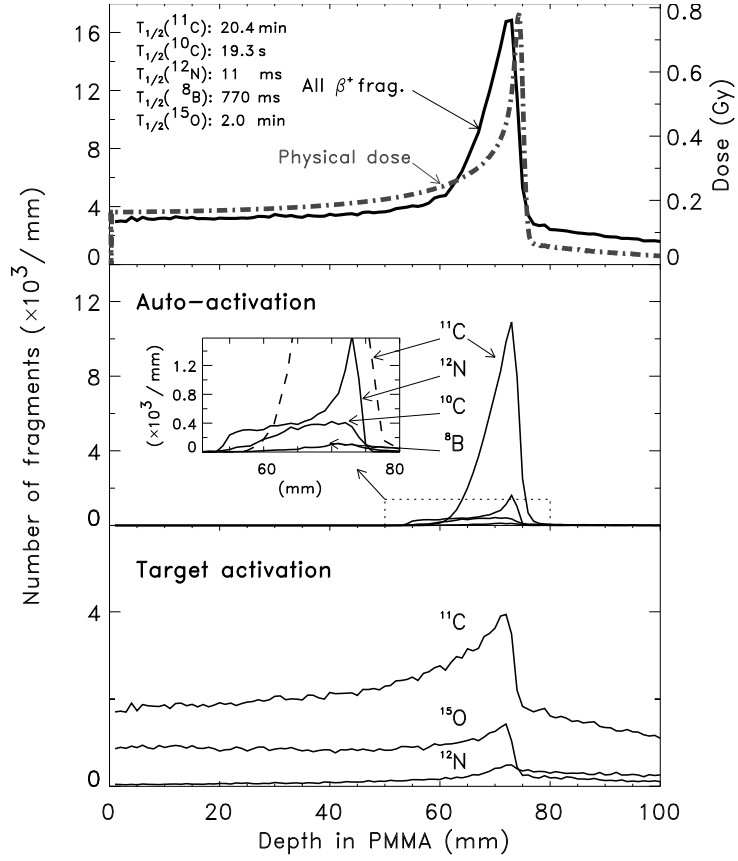
Figure 1.17: Depth-dose distribution of ^{12}C (top, right axis) correlated with auto (middle) and target activation (bottom) in plexiglas. The PosGen Monte-Carlo code [Has96, Pön04] was used to simulate the stopping of 5 million incoming projectiles with 200.28 AMeV and forming a pencil-like beam with a cross section of 1 cm FWHM.

Auto-activation occurs also with projectiles heavier than carbon, as summarized in Table 1.3 for ions with potential use in radiotherapy (except neon).

Table 1.3: Positron emitters induced by several stable projectiles and relevant for in-beam PET. The maximum fragment to projectile range ratio is denoted R_{fr}/R_{pr}.

Beam	Emitter	R_{fr}/R_{pr} (%)	$E_{\beta^+ endpt.}$ (MeV)	$T_{1/2}$
^{14}N^{7+}	^{13}N^{7+}	92	1.2	10 min
	^{11}C^{6+}	107	1.0	20.3 min
^{16}O^{8+}	^{15}O^{8+}	94	1.7	2.05 min
	^{13}N^{7+}	106	1.2	10 min
^{20}Ne^{10+}	^{19}Ne^{10+}	95	2.2	17 s
	^{17}F^{9+}	105	1.7	64 s

Target activation with protons, photons and neutrons

Auto-activation does not take place in sufficient quantity (or does not take place at all) for ions with atomic number lower than carbon, nor with photon or neutron radiotherapy. But several attempts have been made in order to retrieve imaging information from target activation in

this regime, with studies ongoing in the case of protons [Par05a] and photons [Bra03, Eng05b].

Protons: Dose monitoring of proton depth-dose profiles poses a problem due to the poor spatial correlation between the dose and the activity profiles, which do not show an unitary relation [Oel96]. Furthermore, at the end of their trajectory the beam energy lies below the nuclear cross section threshold of ~ 10 - 20 MeV, yielding a distal edge positioned before that of the dose-profile. Nevertheless, lateral deposition can be well localized and range deviations of pristine Bragg-peaks have been resolved within 1 mm [Par05a], mostly due to the three times higher activity induced when compared with ^{12}C irradiation with the same dose and range [Par02b].

Photons: High-energy photons above ~ 20 MeV interact with tissue nuclei through photonuclear reactions producing ^{11}C, ^{13}N and ^{15}O [Hug79]. The reactions rate is proportional to the photon fluence and thus approximatelly also to the absorbed dose [Jan02, Eng05b].

Neutrons: PET can be used to control the patient beam positioning during fast neutron therapy when the scan is performed right after the therapy session [Vyn89] and high neutron energies are used (at least p(40)+Be, i.e. 40 MeV protons impinging on a berilium target) due to the ~ 20 MeV threshold for producing ^{11}C and ^{15}O.

1.4.2   In-beam PET in clinical routine at GSI

Considering the short half lives of both auto and target activated fragments, the rather low activity density created at the fractionated carbon irradiation at GSI (~ 200 Bq Gy^{-1} cm^{-3}, with typical fields having $D_{phys} \sim 0.5$ Gy) and the rapid washout of a large part of the produced activity with $T_{1/2}(washout) \sim 4$ min [Tom03], an in-beam PET scanner was the solution of choice [Eng04b]. But previous in-beam PET research in Berkeley did not result in clinical routine due to the activation of the BGO-based[1] detectors. This arised most probably from passive beam shaping contaminations [Lla88]. For this reason, special care was taken by the FZR team before the installation of the dual-head tomograph at the GSI pilot project [Paw96]. Due to the rasterscan technique (section 1.2.2), pencil-like beams are delivered to the target at GSI resulting in much less, but not negligible, particle spread downbeam from the target [Sch96b, Gun04a, Gun04b]. After proper data-taking handling, described below, successful in-beam imaging with BGO-based detectors was achieved.

The positron tomograph BASTEI

The positron tomograph BASTEI (<u>B</u>eta <u>A</u>ctivity Mea<u>s</u>urements at the <u>T</u>herapy with <u>E</u>nergetic <u>I</u>ons) installed at the GSI tumor therapy unit consists of two detectors heads with 42×21 cm^2 front area each. Each head was built with detector blocks of BGO coupled to photomultiplier tubes (PMT) from the ECAT® EXACT™ tomograph from CTI PET Systems Inc. A dual-head tomograph was chosen (Fig. 1.18) in order to avoid interference with the horizontal beam line and with patient positioning. A total of 8×4 scintillation block detectors were implemented in each head, with each detector block consisting of 8×8 BGO crystals with 54×54 mm^2 front surface each (center-to-center) and 2 cm depth, read with an Anger scheme[2] by four PMT.

The data acquisition had to be slighty modified in order to account for the macrostructure of the beam delivery (Fig. 1.19). Because of the high random rate registered during beam extractions, only events registered during the pauses between beam extractions, i.e. beam injection and acceleration, are taken into account by the reconstruction algorithm (chapter 6). To do this, a

---

[1] Bismuth Germanate, Bi$_4$Ge$_3$O$_{12}$.
[2] The scintillation light is distributed to more than one PMT, with the fraction of light collected by each PMT yielding the hit crystal [Ang58].
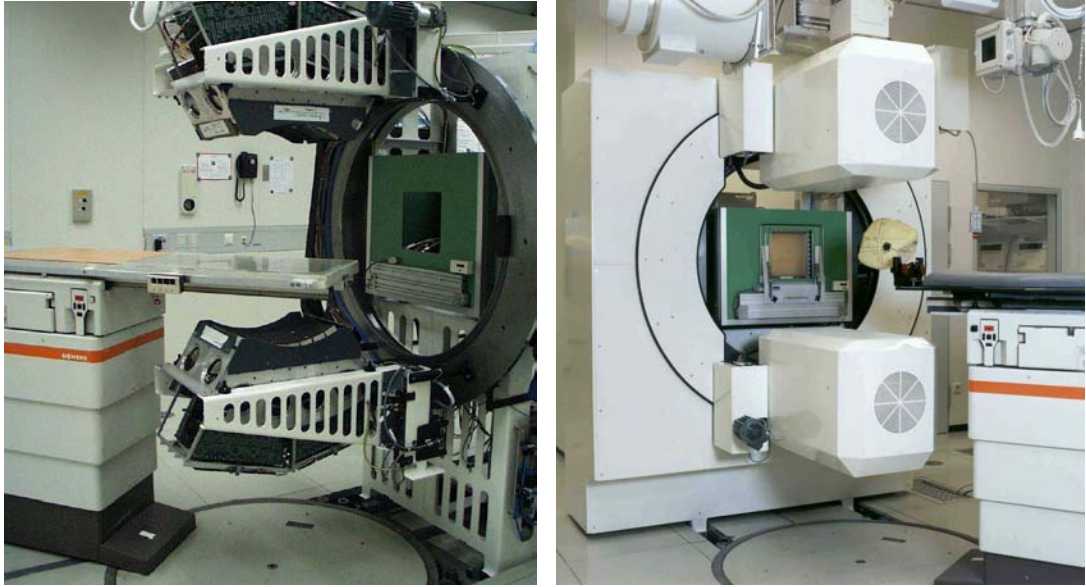
Figure 1.18: The PET scanner installed at GSI without (left) and with (right) the protection housing. The patient couch rotates about the isocenter and the two PET heads are positioned above and below it.

bit, containing the accelerator status information (extraction = 1, no extraction = 0), had to be introduced into the in-beam PET data words [Eng04b].
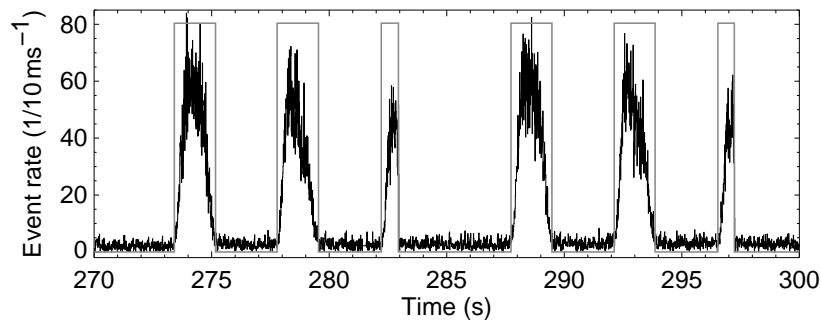
Figure 1.19: Correlation between the beam delivery and the number of detected coincidences during an in-beam PET scan. The rectangular graph denotes the extraction signal: low during beam acceleration (no particle delivered, data reconstructed), high during the beam macropulses (data discarded for reconstruction).

Clinical routine with BASTEI

All fractionated irradiation with carbon ions have been recorded on-line by means of the in-beam tomograph described above, allowing a comparison to be made between the expected versus the observed β^+ distribution after each irradiation [Eng00]. The PET data, acquired and saved in list mode format, are submitted to a dedicated, attenuation-correcting, maximum likelihood expectation maximization algorithm MLEM [Lau99] with a correction for single-Compton events occurring in the object [Pön03b] which allows to reconstruct the measured β^+ activity in the patient. Visualization is done by merging the in-beam PET images with the patient CT by using stereotactic coordinates [Pön03b]. The deposited activity distributions do
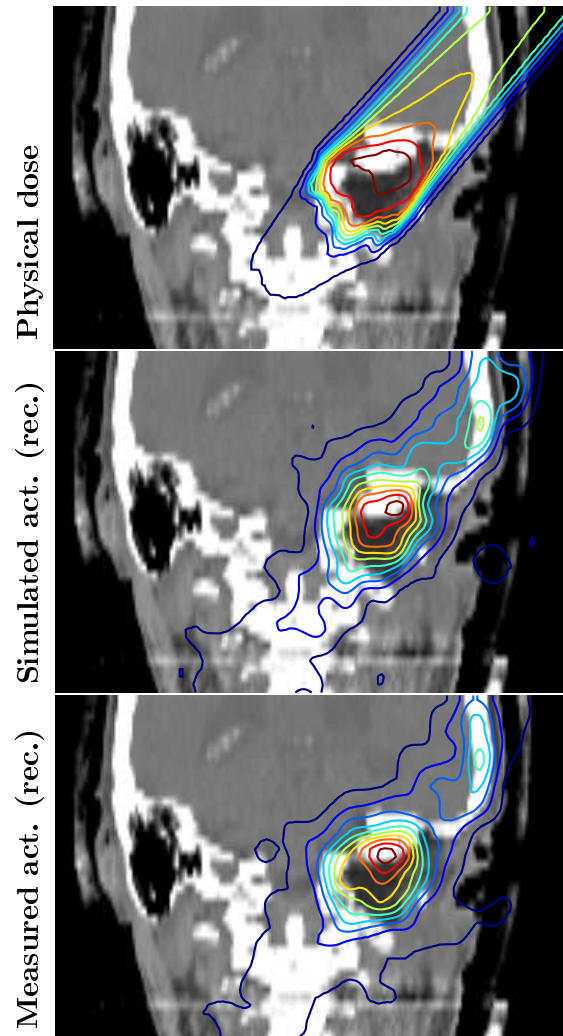
Figure 1.20: Dose distribution (top) versus β^+ distributions expected (middle) and measured (bottom) after tumor irradiation. Isodose lines are plotted from 5 % (dark-blue contour line) to 95 % (magenta) of the maximum dose in intervals of 10 %. The activity distributions were obtained after 50 iterations with the MLEM described in [Lau99, Pön03b]. Note the sparing of the brain stem in all images, positioned after the distal edge of the beam.

not match exactly the dose applied to the patient due to [Paw97, Eng04b]:

- the different nature of both processes: dose deposition arises mainly from interactions with target atomic electrons whereas the activity distributions are generated by nuclear fragmentation reactions (section 1.4.1); and

- the washout effect: activity deposited in highly perfused tissue vanishes before that deposited in less blood perfused regions like bone or large, hypoxic tumors [Kau02, Tom03].

In addition, the reconstructed images of the deposited activity distributions are further distorted because

- a dual head PET scanner provides a space-dependent detector efficiency which results in a position dependent image intensity. This is not possible to correct due to the non-uniform spatial resolution degradation induced by the gap between the two PET heads (chapter 2); and
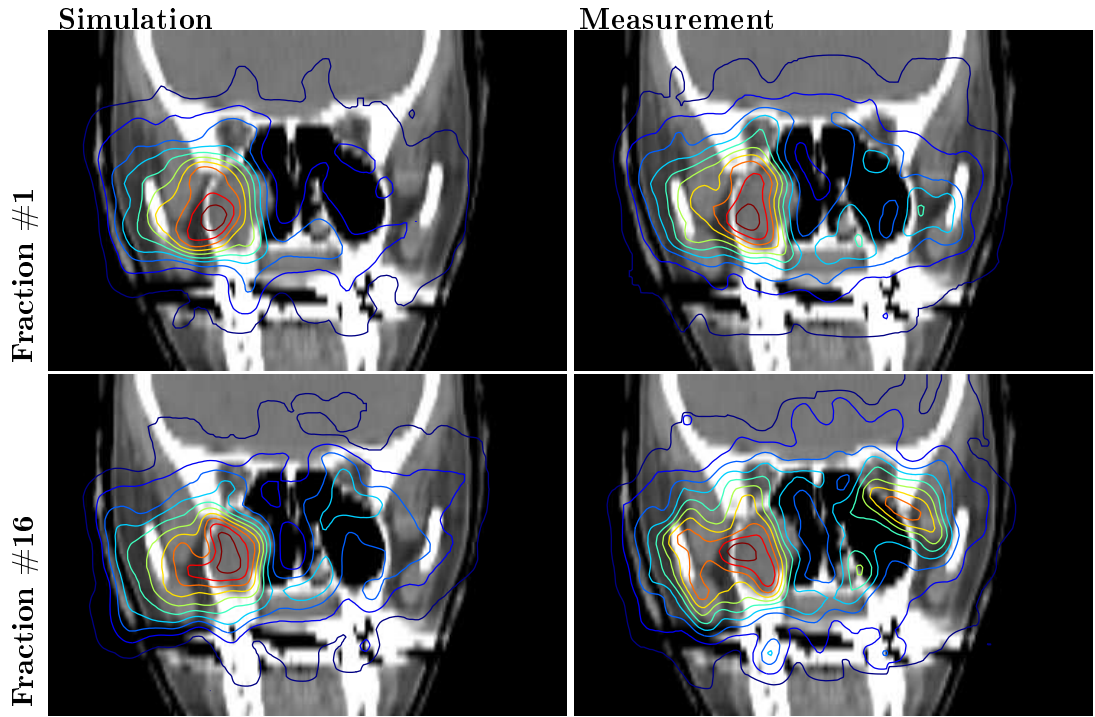
Figure 1.21: Detection of anatomical modifications with in-beam PET during the course of fractionated radiotherapy. The expected β^+ distribution for the first field, first fraction (top left), is compared with the corresponding measured activity (top right). A good correlation is observed betwen simulated and measured contours at the beam distal edge (high gradients lead to sharp images). The measured activity during the 16th fraction (bottom right) shows a small activity focus on the left side of the cavity (right on the image). This was interpreted, and confirmed with a CT scan, as an over-range of the carbon ions due to a shrinking of the tumor in the right paranasal sinus. No clinical impact was induced as no organs at risk were exposed (text has details).

- the low cross-section for β^+ activity production, the short acquisition times, the small solid angle coverage of the positron camera and the event loss rate due to the accelerator duty cycle of $\sim 2/5$ (duration of beam extraction over spill repetition time, Fig. 1.19) result in very low statistics data sets which render the images very noisy (chapter 6).

In order to overcome the mismatch between predicted dose images and the measured β^+ activity images (Fig. 1.20), a Monte Carlo code [Has96, Pön04] which takes into account the treatment plan and the course of the irradiation is used which allows to compare, for each delivered field, the expected and the measured β^+ distribution in the patient. The careful analysis of the resulting images allows important information to be retrieved concerning the quality of the performed irradiation. The clinical experience gained from in-beam PET monitoring [Eng00] the carbon ion radiotherapy treatments within this pilot project proved the capability of PET to detect, and trigger the immediate correction if needed, unpredictable and undesirable deviations in the distribution of the delivered dose with respect to the planned one [Eng04b]. Because deviations in the particle ranges may occur due to (1) physical limitations of the beam model in treatment planning, (2) very small shifts of the delivered portal and (3) local, anatomical modifications of density in the target volume relative to the planning CT (e.g. tumor volume reduction or filling of cavities with mucus over the fractionated irradiation) the team of medical physicists chooses entry portals where these seldom occurring deviations induce no clinical impact by simulating them beforehand [Jäk01]. Nevertheless, mean deviations of 6 % of the prescribed dose can occur[1] in radiation sensitive OAR such as the spinal

---

[1] Mean deviation calculated assuming the errors occur systematically the same way during all fractions, which is highly improbable. This deviation becomes more important if the number of treatment fractions is reduced.

chord [Kar03], which reveals the importance of in-beam PET monitoring. In summary, despite occurring very seldomly and, as mentioned, with no clinical implications to date, these deviations can be detected on the basis of in-beam PET images and local deviations from the planned dose can be quantified [Par02a, Eng04a].

An example is shown in Fig. 1.21, which presents one case in which this analysis identifyed patient morphologic changes during the course of the treatment sessions. Consequences to the delivered dose could be locally quantified [Par02a, Par04]. The left images show the expected β^+ distributions for the first field, first fraction (top) and for the 16th fraction (bottom). The beam enters the patient from the right (left in the image) and stops at the edge of the paranasal sinus. The right images show the corresponding measured distributions. A remarkable match can be seen between simulated and measured contours at the beam distal edge (high gradients lead to sharp images) in the first fraction. During the 16th fraction a small activity focus could be seen on the left side of the cavity (right on the image), which was first interpreted, and later confirmed with a CT scan, as an over-range of the carbon ions due to a shrinking of the tumor present in the right paranasal sinus. In this case the over-range was not of clinical significance since the organic structures exposed to it did not include an OAR, together with the fact that the displayed images correspond to a slice 20.16 mm below the isocenter, where the maximum dose was delivered and, thus, present contours of smaller doses. Although this example shows deviations with no clinical significance, it proves well the ability of in-beam PET to monitor the quality of carbon ion tumor irradiation.

1.5   Summary

At GSI Darmstadt a heavy ion therapy unit that exploits the radiotherapeutic advantages of carbon ion beams has treated over 250 patients to date with very promising clinical results.

The main advantages of heavy charged particles in respect to photons in radiotherapy are twofold: (1) the inverse depth-dose profile allowing higher doses at the tumor while sparing proximal healthy tissue and (2) the possibility to drive a charged beam by magnetic deflection, avoiding all material in the beam path and providing optimum tumor conformity.

The main advantages of carbon ions in respect to the spectrum of charged particles in radiotherapy are threefold: (1) the lateral and range straggling decrease with the square root of the atomic number of the projectile, allowing best beam conformity while the tail after the Bragg peak, due to fragmentation projectiles, is still quite small; (2) the relative biological effectiveness of carbon ions increases at their Bragg peak, which enhances the biological dose at the tumor, thus allowing a control of otherwise radioresistant tumors and (3) in-beam PET offers a non-invasive, in-situ, non-dose-proportional monitoring of the beam localization during therapeutic irradiation .

After the physics processes inherent to positron activity production were described, the technological solutions implemented for the first time by the team from FZ Rossendorf were presented, followed by two head and neck treatment examples that underline the clinical importance of in-beam PET in monitoring tumor irradiation with carbon ions. The following chapters try to further optimize several technological aspects of in-beam PET introduced in this chapter, presenting in addition studies leading to the implementation of in-beam PET onto isocentric, rotating ion beam deliveries (gantries) as well as fixed, horizontal beam lines.

Chapter 2

Optimizing the Detector Geometry of In-Beam PET

2.1 Motivation

The first attempts in operating an in-beam positron tomograph at the Lawrence Berkeley National Laboratory (LBNL) had to be abandoned due to detector activation arising most probably from passive beam shaping contaminations [Lla88]. To avoid this with good security margins, and because of the patient positioning restrictions imposed by the fixed, horizontal beam line at the GSI pilot project, together with the fact that first-planned treatments consisted of small-sized tumors only, a dual-head positron camera was installed (Fig 1.18). This was done after careful research that garanteed the imaging capabilities of the selected tomograph [Paw96], including a synchronization of in-beam PET data with the macrostructured particle extraction delivered by the synchrotron (section 1.4.2). To cope with such limited-angle tomograph a dedicated, attenuation correcting, maximum likelihood expectation maximization algorithm MLEM [Lau99] with a correction for single-Compton events occurring in the object [Pön03a, Pön03b] was developed. All these developments contributed to the success of in-beam PET for monitoring, in clinical routine, the carbon ion irradiation at the GSI pilot project [Eng04b].

With the clinical results achieved prompting the construction of a dedicated hospital facility where in-beam PET is expected to monitor more delicate therapeutic situations, optimizing the detector geometry after having learned the unavoidable limitations of the presently installed tomograph becomes a priority. The first challenge was to develop a simulation and a reconstruction routine capable of handling a higher number of coincidence channels than the reconstruction installed at GSI. There, each head of the tomograph contains $2\,048$ detector elements resulting in about 4.2 million coincidence channels. If the ECAT® EXACT™ HR$^+$ tomograph (CTI PET Systems Inc.) is considered, containing 32 complete detector rings, the number of single detectors raises to $18\,432$. Since in-beam PET is characterized by data-sets of low statistics, rebinning the 3D collected data into 2D sets disturbs the spatial information of the few lines-of-response (LOR) existing, which vetoes the application of already existing rebinning algorithms. Because of the enormous amount of crystal combinations possibilities, close to 170 million, dynamic memory allocation is necessary together with a factorization scheme that allows the reconstruction to handle only non-empty coincidence channels [Cre02]. Therefore, a set of routines was developed in order to simulate and reconstruct in real 3D the mentioned full-ring tomograph. Furthermore, the routine sets are able to handle dual-head tomographs with different opening angles so that, whatever tomograph geometry is found to be optimum, reconstruction restrictions will not pose a problem to next-generation, in-beam PET scanners at future heavy ion clinics.

2.2   Reconstruction of PET List Mode Data

Image reconstruction algorithms are usually divided into two categories: analytic and iterative methods. Analytic methods assume that the measured data approximate line integrals through the radioisotope distribution and use the widely accepted filtered backprojection (FBP) technique [Bro76]. Although this is not an exact method (mathematically an infinite number of projections is assumed, when only a finite number of projections are acquired), the results are precise enough for most medical applications. A major advantage is the speed of reconstruction achieved: current scanners process, with this method, a stack of 2D slices forming a 3D image in only a few minutes. The major disadvantage, besides noise and poorer spatial resolution when compared to iterative methods, lies on the fact that this method requires the detector response to be space-invariant. This requirement is only satisfied by positron cameras that cover completely their field of view (FOV), i.e. ring-shaped or rotating dual-head cameras. Iterative methods, despite of their large amount of computing time and power required, yield better images for they are based on exact mathematical models. In fact, in high resolution PET and when areas with low tracer uptake are in close vicinity to hot spots, e.g. in liver tumors, iterative reconstruction methods are of special interest, as FBP frequently yields non-conclusive results in these special cases. A further advantage of algebraic techniques is that the physics involved with imaging, including attenuation and scatter, can be included into the reconstruction algorithm. For the present study case, analytic methods were ruled out to start with as the space-invariant requirement is not fulfilled by dual, fixed-head PET camera geometries. Thus, the maximum likelihood expectation maximization algorithm, already applied to the BASTEI camera [Lau99] and described by Shepp and Vardi in great physical and mathematical detail [She82], was also applied to detector geometries similar to that of the ECAT EXACT HR$^+$ scanner from CTI PET Systems, Inc.

2.2.1   The maximum likelihood expectation maximization algorithm

The maximum likelihood expectation maximization method describes the process of imaging as

$$y_j = \sum_i a_{ij} x_i, \tag{2.1}$$

with x_i the activity of the ith voxel contributing with weight a_{ij} to the jth coincidence channel. However, the inversion of matrix $\boldsymbol{A} = \{a_{ij}\}$ in Eq. 2.1 which would lead to a direct solution for $\mathbf{x}$ is impossible since the problem is ill-posed for several reasons: (1) the matrix elements a_{ij} are not exactly known, since they depend on x_i (due to Compton scattering), (2) there may be not enough projections acquired to provide a sufficient number of equations and, even if the number of equations were sufficient, (3) the statistical nature of the radioactive decay and its detection would introduce ambiguities into the system of equations. Therefore, an iterative procedure must be applied. This procedure can be deduced by considering that the probability of observing a measured coincidence channel distribution $\boldsymbol{y} = \boldsymbol{y}_{meas}$, given a hypothetical activity distribution $\boldsymbol{x}_{hyp}$, can be maximized by applying the likelihood function to these variables. The probability of success, i.e. detecting the activity of one voxel x_i in a particular coincidence channel y_j, is much smaller than the total number of possibilities, which makes the detection process Poisson-like. Because a pair of photons interacting in a pair of detectors will not be detected in any other channel (neglecting Compton effect in the crystals), the variables are then Poissonian and independent. This allows the Poisson distribution to be applied, being that $\mathrm{P}(\boldsymbol{y}_{meas} \,|\, \boldsymbol{x}_{hyp})$ is the probability to be maximized via the likelihood function. Manipulation of that function proves that the likelihood is concave (convergence

exists) and by appling a maximization expectation algorithm Eq. 2.2 can be obtained:

$$x_i^{(n)} = x_i^{(n-1)} \sum_j a_{ij} \frac{y_j}{\sum_k a_{kj} x_k^{(n-1)}}. \tag{2.2}$$

Eq. 2.2 represents the maximum likelihood expectation maximization (MLEM) algorithm, with $n = 1 \ldots$ iteration number, $i = 1 \ldots$ number of voxels in image, $k = 1 \ldots$ number of voxels in image, and $j = 1 \ldots$ number of coincidence channels. The vector $\boldsymbol{x}^{(0)}$ is the starting homogeneous image. The matrix elements a_{ij} are difficult to compute and to store due the enormous size of $\boldsymbol{A}$[1], so they are calculated in each reconstruction step by using an approximation.

2.2.2 Routine stability and optimization

The algorithm described in the previous section was applied to the ECAT EXACT HR$^+$ scanner detector geometry. A simulation was developed that creates list mode data sets that can be read by this routine. The simulation can consider full ring detector arrangements, as well as any camera with two gaps (Fig. 2.1) with sizes given by an integer number of missing detector blocks. Although the size of the simulated detector pixels can be changed by the user with the simulation and reconstruction codes proceeding automatically, all results presented here refer to detector pixels with 5 mm in the axial direction (Z_{PET}) and approximately 4.5 mm in the transaxial direction. The radial depth of the scintillator material was changed between 0, 20 and 30 mm, corresponding to a simulation of the geometrical acceptance of the tomograph only (0 mm) as well as to the efficiency of coincidence detection, as detailed in the next sections.
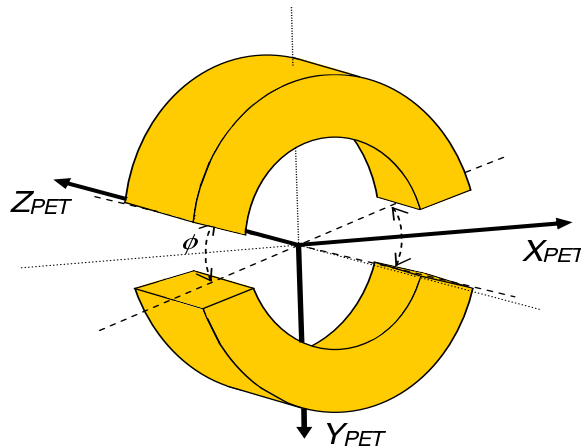
Figure 2.1: Scheme of the dual-head positron camera studied. The gap between the two detector heads defines the angle ϕ at the isocenter, with $\phi = 0°$ representing a closed ring camera.

Reconstruction artifacts from discrete sampling and its correction

Although the annihilated photons are emitted isotropically, their sampling is discrete with a step imposed by the detector size. The on-line calculation of the a_{ij} coefficients considers, for each coincidence channel with a non-zero value, the line that connects the two corresponding detectors. This line approximation, if taken singularly, will introduce artifacts in the image, leading to the appearence of false grains in image points corresponding to crossings of detectors centers. Due to the sensitivity of the MLEM algorithm to high spatial frequencies, these points will be maximized and lead to false, unstable images if no further action is taken. Fig. 2.2 depicts this problem in the left and middle images, and its solution in the right image.

---

[1] The dimensions of matrix $\boldsymbol{A}$ is on the order of 65000×65000 for a single plane of a typical scanner.
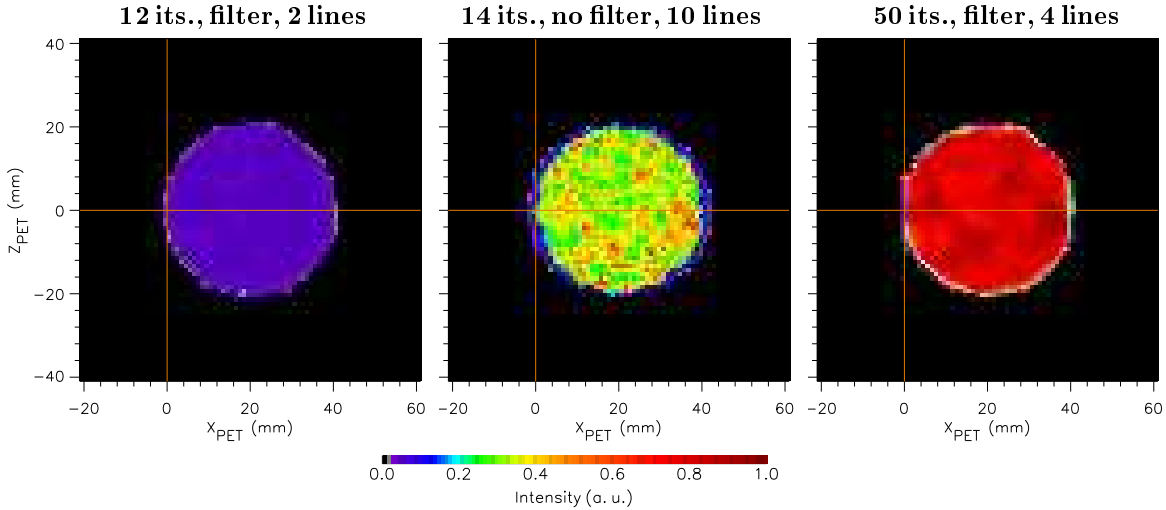
Figure 2.2: Removal of the granularity effect due to detector size. The images show reconstructed datasets from a simulated sphere of activity with 20 mm radius and center shifted by 20 mm along X_{PET}. A closed ring camera was considered. The left image was obtained with a spatial filter applied between each iteration and with 2 lines filling each LOR. In the middle image no filter was applied and 10 lines filled each LOR. Finally, routine stability was achieved when the spatial filter is applied even with 4 lines only filling each LOR. All images were solid angle corrected.

A common approach in iterative algorithms where the matrix **A** is not available is the simulation of several lines within each LOR connecting two detectors. This reduces the algorithm time performance but brings stable images if the number of lines is high enough. The number of simulated lines per LOR can be reduced by applying a spatial filter (median of each voxel with its 26 neighbours) to the object image between each iteration, thus increasing the performance of the algorithm in terms of time with no compromise in image stability and quality (Fig. 2.2).

2.3   Detection Efficiency with Several Detector Arrangements

The arrangement of the detectors in a tomograph and its intrinsic geometry, e.g. scintillator depth, result in different coincidence detection efficiencies that need to be known before a tomograph is chosen for the Heidelberg heavy ion clinics and, therefore, are presented in section 2.3.1. In addition, this knowledge is necessary in order to correct, in each iteration step of the reconstruction algorithm, each image voxel with its corresponding solid angle value, given in section 2.3.2. Furthermore, the effect of low-statistics images in regions with very small solid angle values is also presented.

2.3.1   Quantification of detection efficiencies

Fig. 2.3 shows the dependence of the coincidence detection efficiency of several tomographs with a sphere of activity with radius ranging from 1 to 200 mm centered in their FOV. The top graph depicts the geometrical coincidence detection efficiency. By allowing the annihilation photons to penetrate into the scintillator material the coincidence detection efficiency was obtained for tomographs with crystals of lutetium oxyortholsilicate (LSO) with a radial length of 30 mm (middle graph) and 20 mm (bottom graph). Besides taking into account the different tomograph opening angles ϕ (cf. Fig. 2.1), each graph plots two sets of curves with one corresponding to a tomograph with the dimensions of a tyical PET scanner, with an axial FOV of 16 cm and a radius of approximately 41 cm, whereas the second set of curves in each
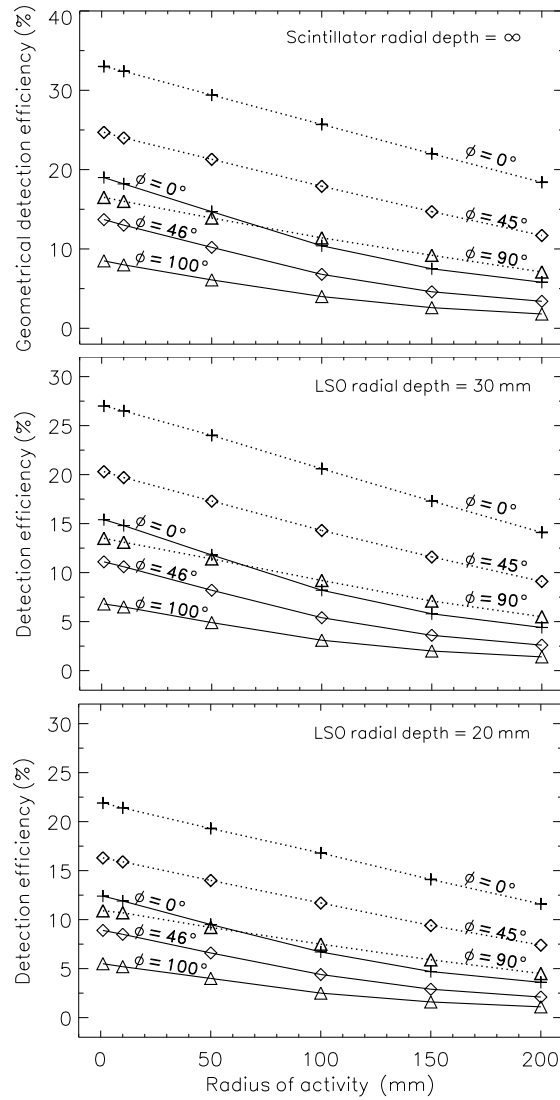
Figure 2.3: Coincidence detection efficiencies for several detector arrangements with different scintillator thicknesses and with a sphere of activity located at the isocenter. The dotted lines denote a larger tomograph with 45.8 cm inner radius and 32 cm axial length versus the 41.2 cm and 16 cm considered with the solid lines, respectively.

graph regards a possible scanner configuration better suited for in-beam PET, with doubled axial FOV and a radius of approximately 46 cm and, consequently, higher coincidence detection efficiency.

2.3.2 Geometrical solid angle

In order to be able to study the performance of several tomographs, each with different opening angles ϕ, the knowledge of their coincidence detection efficiency is necessary. Fig. 2.4 plots the solid angle distribution, i.e. the geometrical coincidence detection efficiency without taking into account the penetration of the photons in the detectors, for several tomographs: a closed-ring ($\phi = 0°$), a dual-head, small-gaps ($\phi = 46°$) and a dual-head, wide-gaps ($\phi = 100°$) tomograph with dimensions approximately equal to the ECAT EXACT HR$^+$ scanner, i.e. 16 cm axial FOV and 41 cm radius. All reconstructed images shown in the present chapter were weighted between each iteration step with the corresponding solid angle distribution shown in Fig. 2.4.
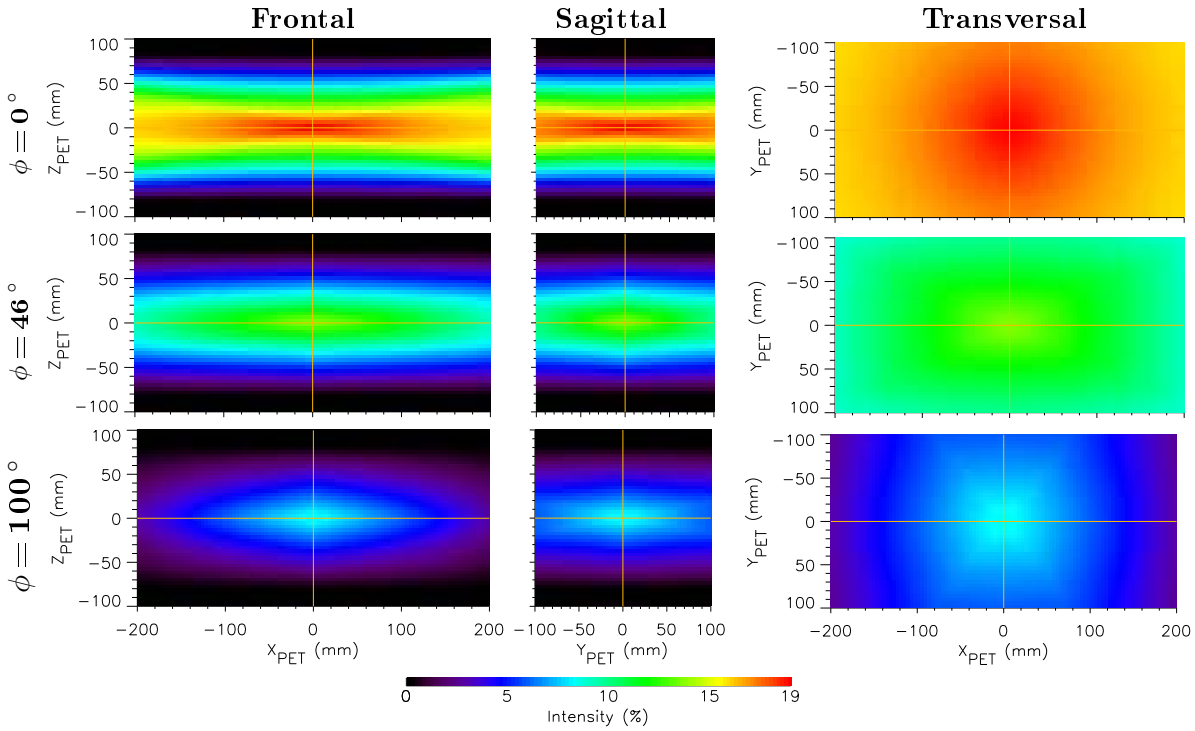
Figure 2.4: Geometrical solid angle distributions in a closed ring ($\phi = 0°$), a dual-head, small-gaps ($\phi = 46°$) and a dual-head, wide-gaps ($\phi = 100°$) tomograph.

As presented in Fig. 2.5, a smooth coincidence detection efficiency extending through the complete image space sampled is highly desirable in order to equally correct noisy images. Fig. 2.5 shows that equal noise oscillations sampled in a given signal are under- and over-amplified when a correction with a low coincidence detection efficiency in respect to the central, maximum value, has to be applied. This behaviour is observed in section 2.6 where its influence on simulated, real-treatment images is shown: a false, high-intensity activity arises in the beam entrance channel for images sampled with tomographs with higher coincidence detection efficiency gradients.
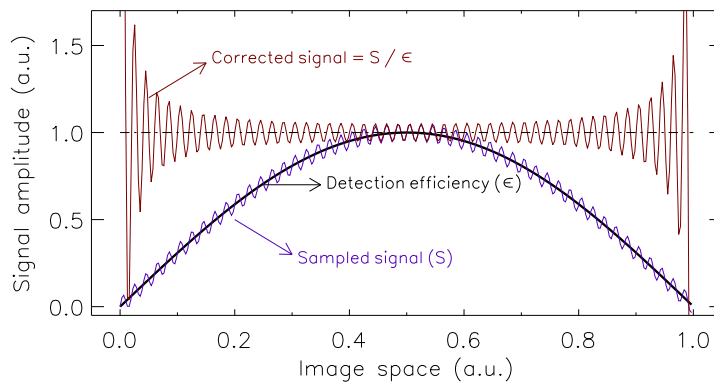
Figure 2.5: Importance of a smooth detection efficiency in noisy samples. An under- and over-amplification effect arising in noisy samples corrected with a too low detection efficiency value is shown. The average of the corrected signal is unity, as expected. But the maximum likelihood expectation maximization algorithm, being very sensitive to noise, amplifies the false noise peaks.

2.4 Degradation of Spatial Resolution with Dual-Head Scanners

Fig. 2.6 compares the spatial resolution obtained with a simulated closed ring detector geometry ($\phi = 0°$) to that obtained with a dual-head tomograph with $\phi = 100°$. Several point sources were simulated at different locations inside the FOV of tomographs with 20 mm radial depth of scintillator. The Fig. shows a 2D image and the corresponding line profile for one such point source reconstructed after 50 iterations. It can be seen that an image spread appears along the axis with missing detectors (Y_{PET}) for the dual-head geometry, which translates into a lower spatial resolution obtained along this axis. This degradation is quantified in Table 2.1 for the three axes of the tomographs at several point source locations. The values in the table included from the BASTEI tomograph were measured with ^{22}Na sources [Lau99] and cannot be directly compared with the simulated values due to several reasons: (1) the simulation does not include Compton scattering neither in the object nor in the detectors and contains singular point sources whereas the measured values contain both physical processes mentioned in addition to the intrinsic volume of the source, and (2) the values measured with BASTEI suffer from an increased spatial resolution degradation [Mos93] arising from the light sharing readout implemented at the detector level [Mos94], i.e. four photomultiplier tubes (PMT) read the 8×8 pixels of each scintillator block in modified Anger readout [Ang58].
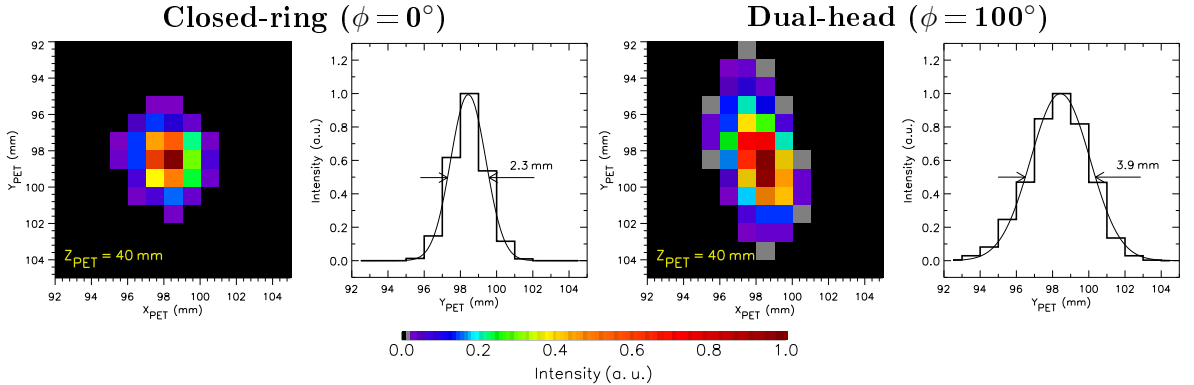
Figure 2.6: Degradation of spatial resolution from a closed ring to a dual-head tomograph.

Table 2.1: Degradation of spatial resolution from a closed ring to a dual-head tomograph.

Point source location			Closed ring FWHM (mm)			Dual-head $\phi = 100°$ FWHM (mm)			BASTEI FWHM (mm)		
X_{PET} (cm)	Y_{PET} (cm)	Z_{PET} (cm)	X	Y	Z	X	Y	Z	X	Y	Z
0	0	0	1.8	1.9	1.9	1.8	2.3	1.8	5	7.5	5
10	0	4	1.9	2.0	1.8	2.0	3.1	2.0	5	11	5
10	5	4	2.0	2.0	1.9	2.0	3.6	1.8	5	13	5
10	10	4	2.1	2.3	1.8	2.2	3.9	1.8	5	22.5	5

But the approximately twofold degradation of the spatial resolution in the axis with missing detectors, observed with isolated point sources, is not the main disadvantage of fixed, dual-head tomographs. The reduction of signal intensity due to this spatial spread, not shown in Fig. 2.6, represents a more important artifact to be be minimized (sections 2.5 and 2.6).

2.5 Imaging with Dual-Head Tomographs

Rare but possible patient anatomical modifications during the course of the fractionated irradiation at the GSI heavy ion therapy unit do not include only the example shown in section 1.4.2,

where in-beam PET detected a non-critical reduction of the tumor volume (Fig. 1.21). In head and neck irradiation, the filling of one or more of the sinus cavities with mucus or due to an inflammation of the surrounding tissue may also be detected by in-beam PET: when the beam crosses this filled cavity it generates there an unexpected excess of β^+ activity due to the non-empty traversed path. When such alterations of the tissue density occur the main task of in-beam PET is to detect whether a possible reduction of the beam range occurs with, consequently, an under-dosage of tumor tissue downbeam. Although occurring seldom, clinical in-beam PET allows an alert to be made to the radiotherapist in such situations. Typically, an anti-mucus drug administered to the patient is enough to solve the problem. More delicate and very rare situations may require a new CT of the patient and eventually the calculation
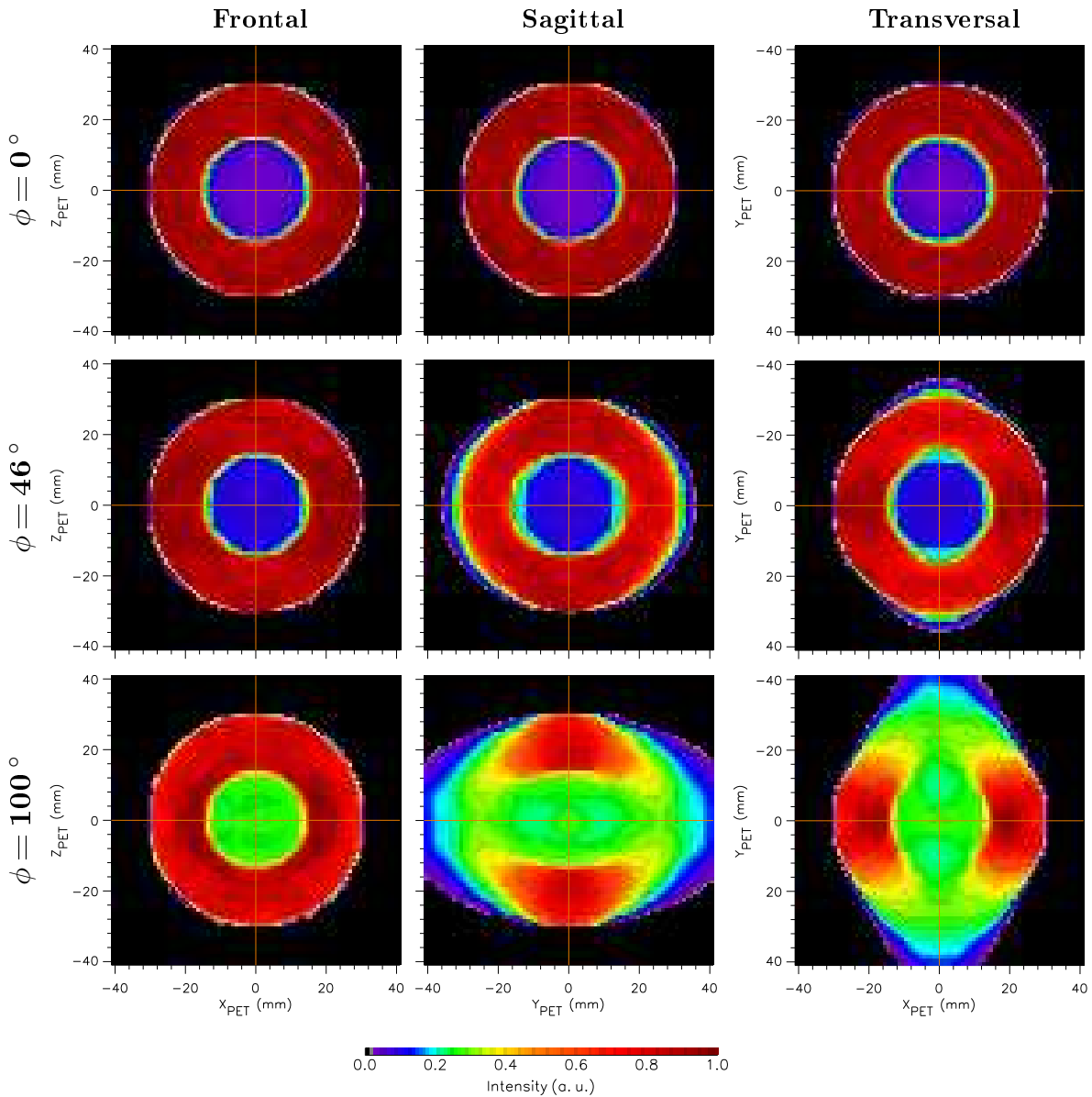
Figure 2.7: Reconstruction of a hollow sphere homogeneously filled with activity (100 million annihilations). The sphere was positioned at the isocenter of three different tomographs. The closed-ring detector configuration registered 16 million events, whereas the dual-head geometries detected 11 million ($\phi = 46\,^\circ$) and 6 million ($\phi = 100\,^\circ$) events.

of a new irradiation plan. Therefore, it is extremelly important that the in-beam PET images preserve the maximum information when the annihilation activity surrounds empty activity regions (air-filled cavities). In order to approximate such a situation and study the effect of the camera geometry onto in-beam PET images, the detection of the activity from a hollow sphere was simulated with three different positron cameras.

2.5.1 Precise activity volume: hollow sphere

Fig. 2.7 shows the reconstructed images of a hollow sphere positioned at the isocenter of three different tomographs: a closed-ring and two dual-head tomographs with different opening angles ϕ (cf. Fig. 2.1). A very high number of annihilations, 100 million (1 MBq cm^{-3}), was simulated in each case in order to exclude possible low statistics artifacts. The images were obtained after 50 iterations with the MLEM algorithm, with a solid angle correction applied to the intermediate image between each iteration step. It can be seen that, as expected, the three views obtained with a closed-ring tomograph are very similar to the originally simulated hollow-sphere, with the activity in the hollow region at the isocenter being as low as approximately 5 % of the maximum, homogeneous activity (although no activity at all was expected here). If a dual-head tomograph with $\phi = 46°$ is considered, corresponding to a length of 34 cm along the Y_{PET} axis without detector coverage, a slight image elongation is observed along this axis, affecting therefore the saggital and transversal views of the image. When the detector gap along the Y_{PET} axis is increased to 63 cm, corresponding to an angle $\phi = 100°$, both the sagittal and transversal views of the image present an extended elongation with, consequently, high loss of image intensity. Furthermore, the frontal view shows an activity in the hollow region at the isocenter of approximately 30 % of the image maximum, therefore disturbing image evaluation in cases where non-expected activity is present in empty cavities.

Based on these sets of images, a dual-head tomograph with small gaps, i.e. $\phi = 46°$, seems to bring an optimum detector configuration for an in-beam PET tomograph since it seems not to induce strong image deterioration nor loss of signal intensity, while offering the advantage of allowing an entrance and escape portal for the incoming beam and outgoing light-particle flux [Gun04a, Gun04b], respectively. Nevertheless, the dimensions of the simulated hollow-sphere, with an outer diameter of 6 cm only, allow this conclusion to be applied to small tumors only. In order to study the same image deterioration effects onto activities positioned further away from the isocenter, the hollow sphere was shifted by 3 cm along the Y_{PET} axis, with results presented in the next section.

2.5.2 Importance of detector geometry over collected statistics

Besides a shift of 3 cm along the Y_{PET} axis, the activity density of the hollow-sphere simulated in the present section was decreased by 2 orders of magnitude, down to 10 kBq cm^{-3} (1 million simulated annihilations), in respect to the case presented in the previous section. This allows to study the performance of the different detector configurations when a low-statistics annihilation activity is further apart from the isocenter. Fig. 2.8 shows the images obtained in the same conditions presented above: after applying 50 iterations to the simulated data with the MLEM algorithm, with a solid angle correction implemented between each iteration step.

It can be seen that the images obtained with a closed ring detector configuration become noisier, as expected due to the lower statistics data sets, but with no influence observed neither in the shape of the activity contours nor in the signal intensity inside the inner empty cavity. In the dual-head, small-gaps detector configuration ($\phi = 46°$), the frontal view presents almost the same results obtained with a closed-ring detector configuration. The saggital and transversal
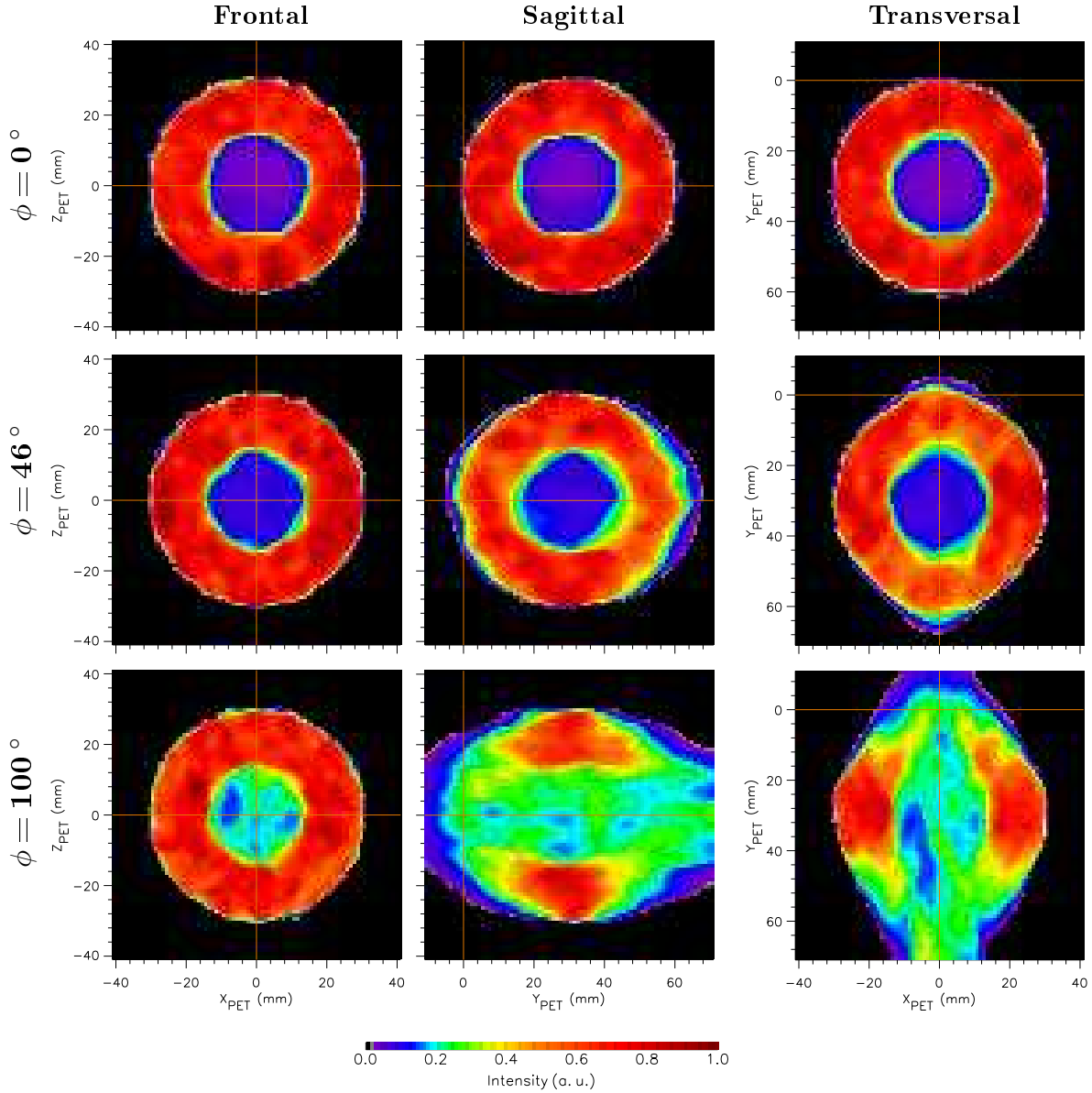
Figure 2.8: Reconstruction of a hollow sphere with low statistics (1 million annihilations simulated) with the center of the sphere shifted 30 mm along Y_{PET}. The number of detected coincidences were approximately 3.2×10^5, 2.3×10^5 and 1.4×10^5 for the detector configuration with $\phi = 0°$, $\phi = 46°$ and $\phi = 100°$, respectively.

image views, however, do present some small loss of signal intensity at the edges of the image along the Y_{PET} axis, with a consequent slight image intensification in the middle of the hollow sphere at $Y_{PET} \sim 30$ mm. This fact, brought to an extreme with the dual-head, wide-gaps detector configuration ($\phi = 100°$), is also observed with the realistic patient-treatment images simulated in the next section.

Besides the mentioned loss of signal intensity, the comparison of Fig. 2.8 with Fig. 2.7 allows to conclude that the geometry of the detector configuration plays a much more important role in in-beam PET than the number of collected events, i.e. a low-statistics image acquired with a closed-ring tomograph (Fig. 2.8, top row) contains more information than a high-statistics image sampled with a dual-head detector configuration (Fig. 2.7, middle and bottom rows).

2.6 Tomograph Optimization with Realistic Patient Images

In order to be able to evaluate the quality of the images from several camera configurations in real therapeutic situations, β^+-activity distributions calculated from real treatments were connected to the simulation routine. For that, the PosGen Monte-Carlo code [Has96, Pön04], which generates a β^+-activity distribution for a given carbon ion irradiation field based on the computed tomogram (CT) of the patient and on a particular delivered irradiation, was slightly modified: the spatial coordinates of the generated β^+-activity distribution were saved before taking into account the positron annihilation and the detection of the corresponding γ-rays with the BASTEI tomograph. This generated β^+-activity distribution was then the input of the routine that simulates the three tomograph detector configurations under study. Table 2.2 summarizes the simulation and reconstruction details of sections 2.6.1 and 2.6.2. It can be seen that the activity of the simulated images is one order of magnitude higher than the estimated target activity produced in both treatments considered. This was done in order to study the influence of the detector geometry onto their reconstructed images without influences from low statistics data sets. A low statistics simulation, corresponding to treatment-like data sets, was performed for the head and neck irradiation and results are shown for two tomograph geometries.

Table 2.2: Measured and simulated target activity for the two treatments studied.

Treatment considered	Head and neck	Pelvis
Coincidences detected with BASTEI[a]	1.13×10^5	4.76×10^5
Measuring time (s)	712	860
Effective measuring time[b] (s)	551	529
Estimated average target activity[c] (kBq)	4.1	18
Simulated target activity[d] (kBq)	35	180

[a] Measured in the pauses between beam extraction only.
[b] Measuring time weighted with the accelerator duty cycle delivered.
[c] Assuming an integrated coincidence detection efficiency of 5 %.
[d] High statistics data sets. Low statistics (text) denote one order of magnitude less.

2.6.1 Head and neck irradiation

High statistics simulated data sets

Fig. 2.9 depicts a typical portal for a head and neck irradiation with carbon ions. The images in the top row show the delivered physical dose generating a given β^+-activity distribution, shown in the bottom row. Both the physical dose and the β^+-activity distribution are superimposed onto the CT of the patient. In the case shown, the beam enters the patient from the left (right in the frontal and transversal images) forming an angle of $14°$ clockwise with the X_{CT} axis, as can be seen in the frontal view. The transversal view allows to see that the patient head is tilted to the left (right in the image). As expected, a good agreement between the generated β^+-activity distribution and the anatomical structures of the patient, e.g. the sinus cavities, is observed, with an enhanced activity concentration generated in higher density target structures like bone. This last detail is further increased in real patient images due to biological mechanisms like washout, diffusion or transport of the β^+-activity by the blood circulation or by highly perfused tissues. These metabolic processes were not included in the images shown since the PosGen Monte-Carlo code does not simulate them yet.

By simulating the detection of the β^+ activity distribution displayed in the bottom images of
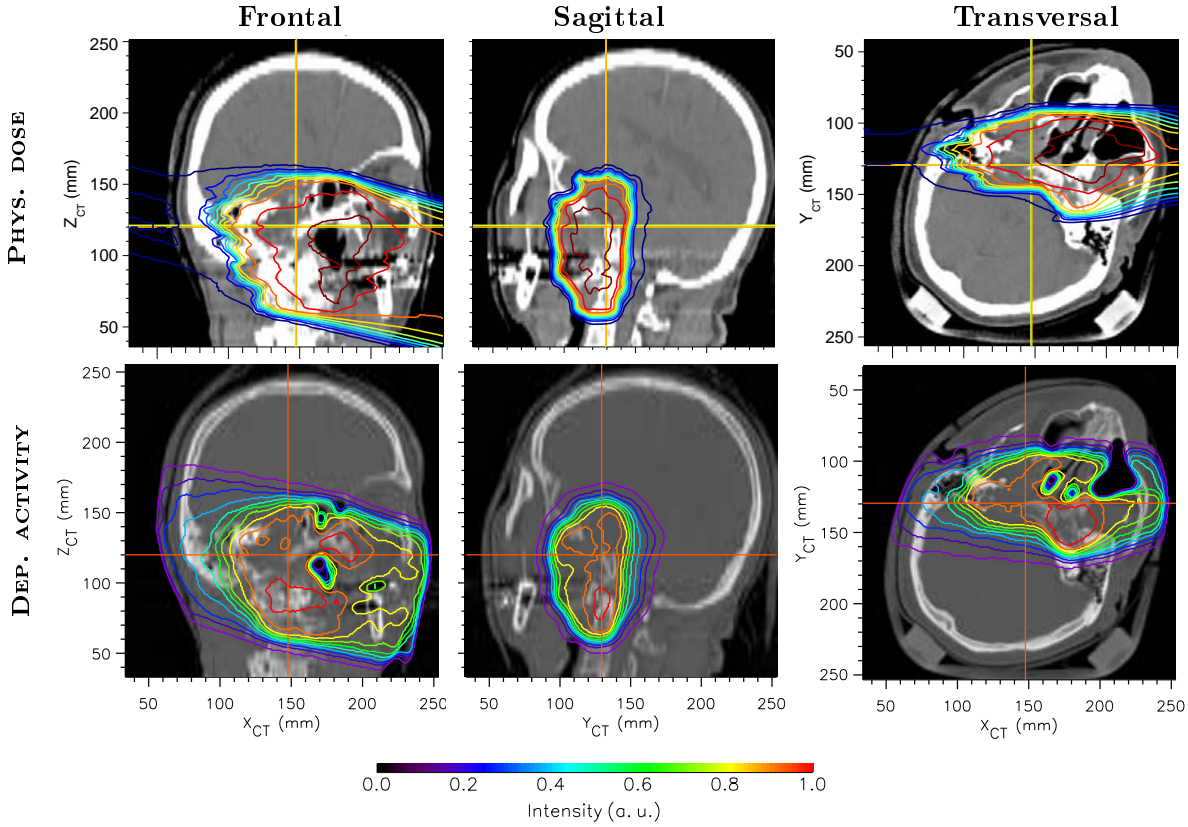
Figure 2.9: Head and neck irradiation: physical dose and generated β^+ activity distribution. Iso-dose (top) and iso-activity (bottom) contours are superimposed onto the patient CT.

Fig. 2.9 with the three different detector geometries under study the reconstructed images of Fig. 2.10 were obtained. For the closed-ring detector geometry the simulated positron camera was rotated around the Y_{PET} axis by 6° anti-clockwise, i.e. the X_{CT} and X_{PET} axes form an angle of 6°, with the beam direction and the X_{PET} axis forming an angle of 20°. In the case of both dual-head detector configurations the simulated positron camera was rotated 14° clockwise so that the beam crosses the camera through its midplane, along the X_{PET} axis.

The images obtained with the closed ring tomograph are remarkably similar to the β^+-activity distribution displayed in Fig. 2.9. This was expected since, despite the rotation of the camera in respect to the beam direction, the FOV of the camera covers all the irradiated volume. It can be seen that important characteristics for clinical in-beam PET are well conserved: (1) a sharp activity gradient is observed at the distal edge of the irradiation field in the frontal and transversal views (distal contours with values between 90 % down to 40 % of the maximum activity, approximately), which allows to monitor the range of the treatment field; (2) a good overlap exists between the patient empty cavities, like the maxillary and ethmoid sinuses and the mouth cavity, with the minima of the β^+ activity (frontal and transversal views); (3) the activity maxima are localized in the same bone structures obtained with the PosGen code (all views); and (4) the outline of the activity contours matches well that obtained with the PosGen simulation in all image views.

The reconstructed images obtained with a dual-head tomograph with narrow gaps ($\phi = 46\,°$) are similar to the closed-ring ones in what concerns variables (1), (2) and (4) mentioned above. However, a shift in the activity contour with maximum intensity is observed, which is thought to arise from the asymmetric loss of image intensity at locations not equally distant from the
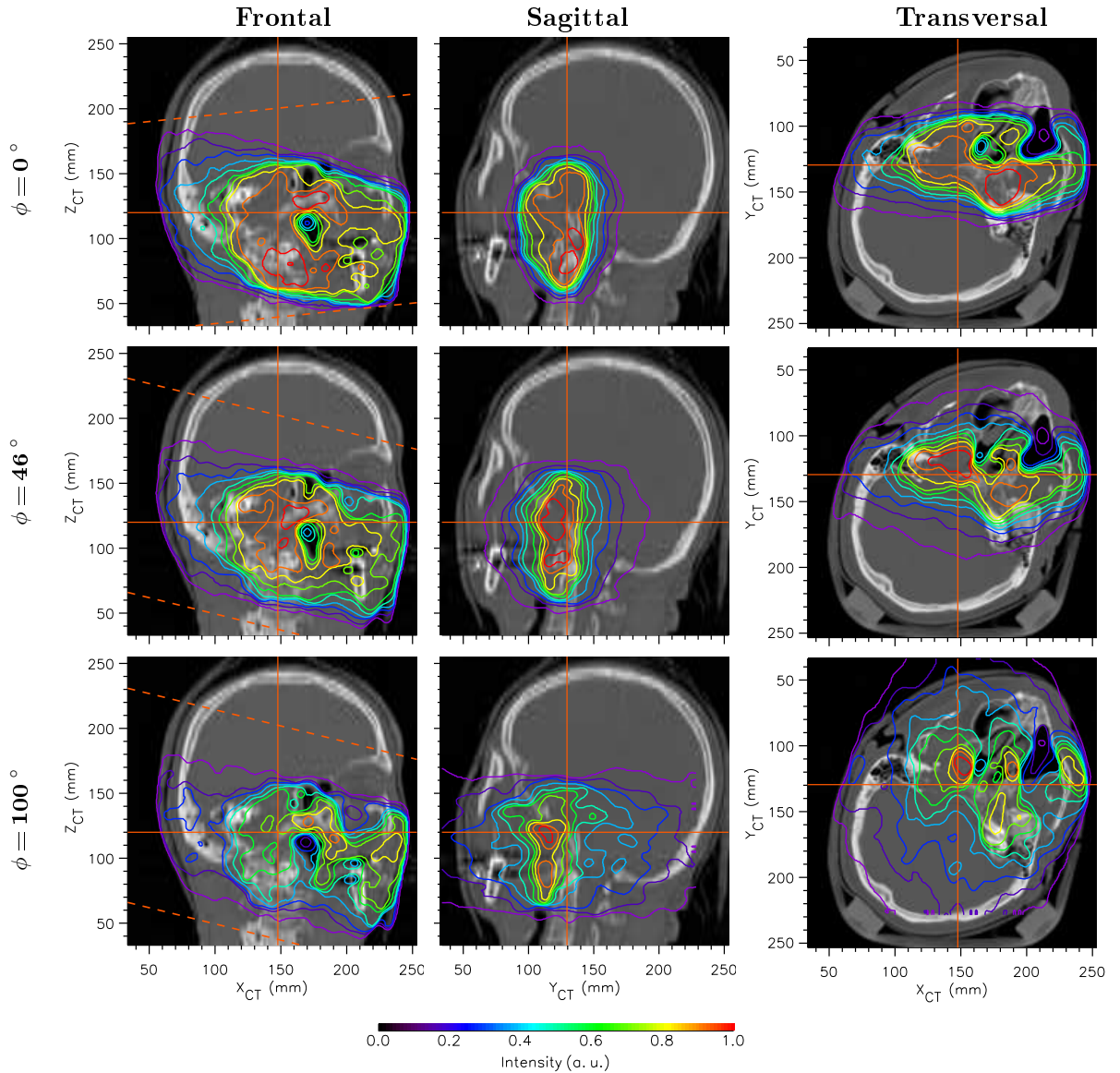
Figure 2.10: Head and neck irradiation: reconstruction with different tomographs. The dashed lines in the frontal views depict the margins of the tomograph considered (top view).

isocenter, as detailed in Fig. 2.8. Nevertheless, the quality of the reconstructed images shown seems to be quite high for monitoring tumor irradiation.

In what concerns the dual-head tomograph with wide gaps, $\phi = 100\,^\circ$, the reconstructed images show the expected object elongation along the Y_{PET} axis (overlapping the Y_{CT} axis). In addition, the frontal and transversal views show the effect detailed in Fig. 2.5, where a noisy activity signal corrected with too low solid angle values gives rise to a false increase in signal intensity. It must be stated that these images cannot be directly compared to those obtained with the BASTEI tomograph. Besides the different detector geometries, spherical in BASTEI versus cylindrical in the present studies, the reconstruction routine developed for BASTEI uses a dedicated penalization algorithm for image coordinates located too far apart from the isocenter, therefore maintaining image proportionality in regions surrounding the isocenter, where the tumor is located. Nevertheless, the present images do show that items (1) and (2) mentioned above are still valid, meaning that monitoring the irradiation range and possible patient morphological alterations is still possible with accuracy with the present images.
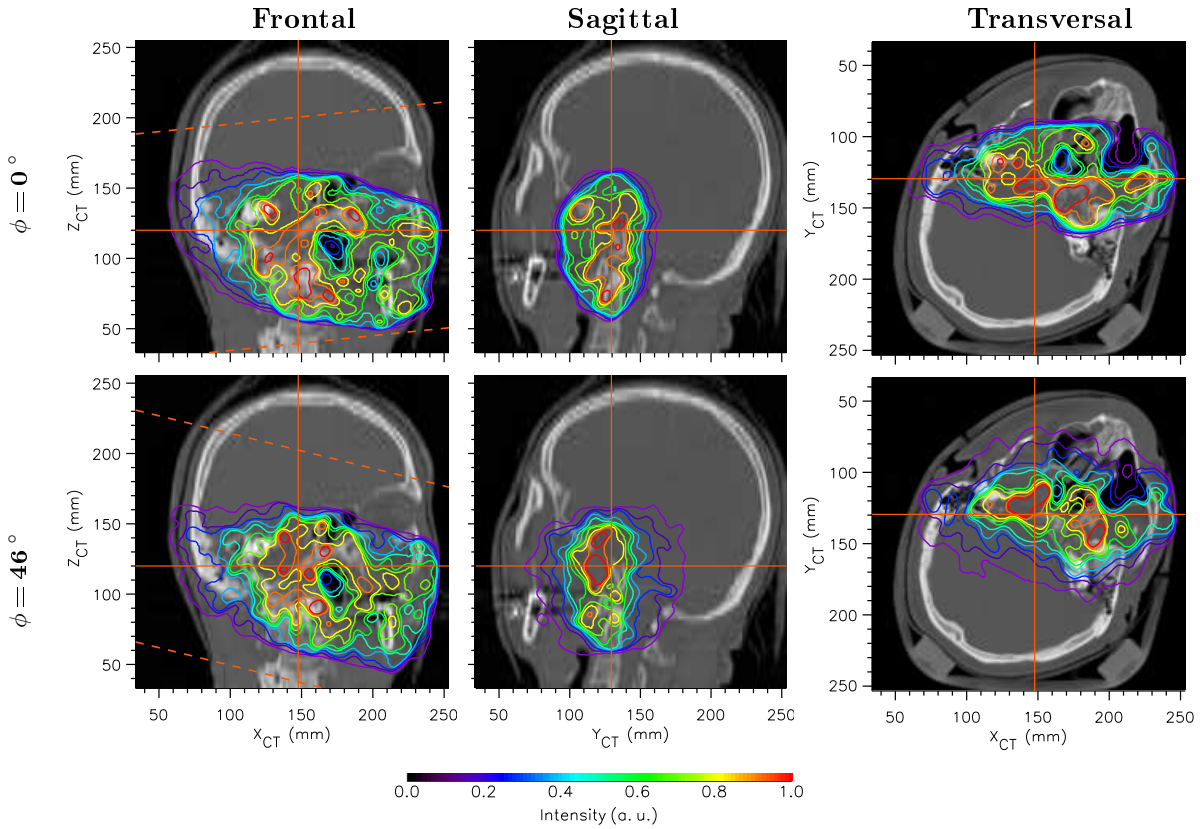
Figure 2.11: Head and neck irradiation: study with low statistics data sets. A total of 2.5 million simulated annihilations yielded 2.4×10^5 and 1.75×10^5 events detected with the closed ring and the dual-head tomographs, respectively. The dashed lines in the frontal views depict the margins of the tomograph considered (top view).
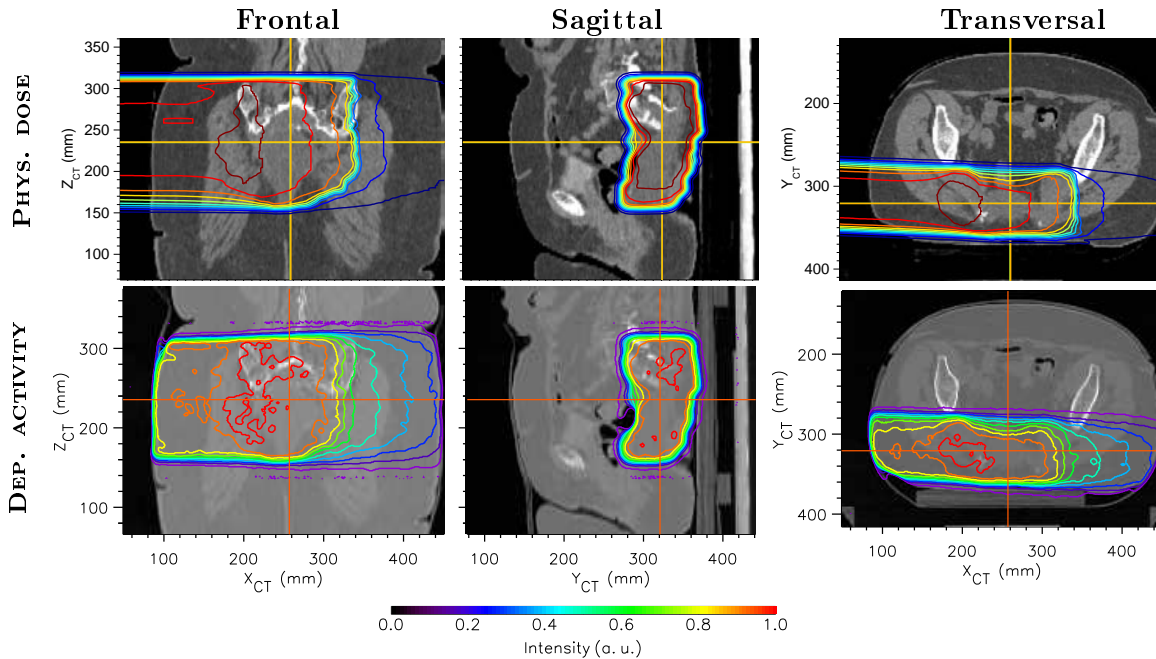
Figure 2.12: Pelvis irradiation: physical dose and generated β^+ activity. Iso-dose (top) and iso-activity (bottom) contours are superimposed onto the patient CT.

Low statistics simulated data sets

Fig. 2.11 shows that, for the closed-ring and dual-head, small-gaps tomographs, the conclusions obtained with the higher statistics data sets in Fig. 2.10 are still valid if more realistic, low statistics simulations are taken into account. Despite the higher noise (granularity) of the images in respect to the high statistics images of Fig. 2.10, mostly observed for the maximum β^+-activity contours, the agreement of the remaining iso-activity lines with the simulated, deposited activity is still valid, namely the sharp activity gradient at the distal edge of the irradiation field, the overlap with empty patient cavities and the overall agreement of the outline of the activity contours with the predicted contours.

In summary, it is evident that a closed-ring tomograph conserves all important characteristics from clinical in-beam PET. For the irradiation of head and neck tumors a dual-head tomograph with small gaps ($\phi = 46\,^\circ$) maintains most of the characteristics of in-beam PET needed for clinical use meaning that, should the installation of a closed-ring detector geometry be not feasible, the dual-head geometry with $\phi = 46\,^\circ$ should be preferred in respect to the geometry with $\phi = 100\,^\circ$. The feasibility of implementing a closed-ring tomograph is studied in section 2.7.

2.6.2   Pelvis irradiation

Spinal chordomas cannot be treated with an effective dose using conventional radiation therapy without exceeding the tolerance dose of the spinal cord while ensuring sufficient target coverage at the same time [Sch03a]. For this reason, several patients suffering from the mentioned tumors have been irradiated with carbon ions at the GSI pilot facility, within a treatment complemented with fractionated irradiation with photon intensity modulated radiation therapy (IMRT). Fig. 2.12 depicts one fraction of a carbon ion pelvis irradiation as mentioned. In addition to continue treating spinal chordomas, the dedicated facility in Heidelberg will also exploit the advantages of heavy ions to treat patients suffering from prostate cancer [Nik04]. In both cases, and in other tumors outside the head and neck region that are planned to be addressed at a later stage, monitoring the heavy ion irradiation with in-beam PET brings usefull information to the radiotherapist due to the close proximity of organs at risk (OAR) to the target volume. In the sagittal view of Fig. 2.12 it can be seen that the colon of the patient, a radiosensitive organ, lies adjacent to the target volume. The present section studies the influence of the detector geometry onto in-beam PET images in this situation.

By simulating the detection of the β^+-activity distribution shown in the bottom row of Fig. 2.12 with several tomographs the reconstructed images of Fig. 2.13 were obtained. For the closed-ring configuration ($\phi = 0\,^\circ$) two detector arrangements were considered: a large coverage ring with 24 cm axial FOV, 45.6 cm inner radius and rotated 18° clockwise around its Y_{PET} axis, thus allowing a collision-free beam delivery (top row); and an ECAT EXACT HR$^+$-like geometry with the tomograph rotated 25° clockwise around its Y_{PET} axis (second row) for the same reason. Clearly, the large coverage closed-ring configuration yields the best images and in section 2.7 its implementation feasibility is discussed. Nevertheless, although the smaller closed-ring tomograph considered does not cover the proximal and distal irradiated volume completely, the images corresponding to the covered regions do resemble remarkably well the generated β^+-activity. It can be seen that the reconstructed distal edges of the activity allow to monitor the range of the irradiation by direct comparison with the simulated activity contours (frontal and transversal views) and, in addition, the sharp activity gradient observed in the saggital view allows a precise monitoring of the irradiation close to the colon of the patient, in this case.

Although the FOV of both dual-head tomographs ($\phi = 46\,^\circ$ and $\phi = 100\,^\circ$) cover the irradi-
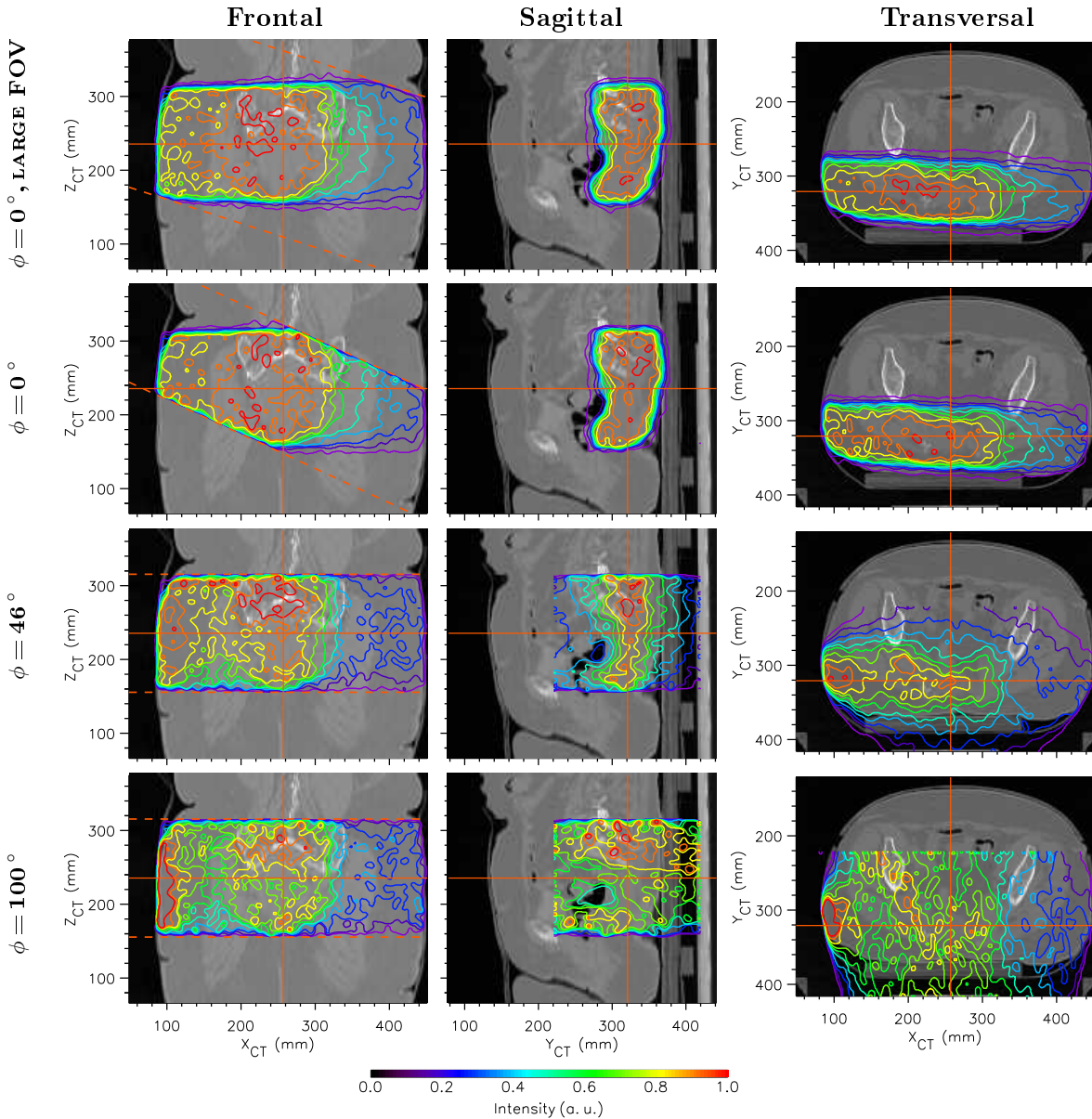
Figure 2.13: Pelvis irradiation: reconstruction with different tomographs. The dashed lines in the frontal views depict the margins of the tomograph considered (top view). The top row shows images obtained with a simulated tomograph with an axial FOV (a) of 24 cm and radius (R_{PET}) of 45.8 cm; in the remaining an ECAT EXACT HR$^+$-like scanner was considered: $a = 16$ cm and $R_{PET} = 41$ cm.

ated volume completely, their reconstructed images contain clearly less information as that obtained with a rotated closed-ring tomograph due to the image degradation arising from the gap between the detector heads (section 2.5).

In summary, for large irradiation fields occuring during tumor treatments in the pelvis region, in-beam PET benefits the most from a closed ring tomograph. It was seen that even a cheaper solution, like a commercially avaliable, conventional nuclear medicine scanner with approximately 16 cm axial FOV, yields better image quality as any fixed, dual-head tomograph, despite the incomplete coverage of the irradiated region in the case of the closed-ring geometry. The best images were obtained with a large FOV tomograph and the next section studies the feasibility of its implementation.

2.7 Feasibility of a Closed-Ring In-Beam PET Scanner

Due to the higher image quality obtained with a closed-ring tomograph, particularly with large irradiation fields, the present section investigates the possibility of implementing such an in-beam PET scanner for heavy ion tumor irradiation. The top images in Fig. 2.14 depict a worst-case irradiation scenario: a beam portal with maximum beam width and delivered perpendicularly to the patient. Assuming a rotation of the tomograph around its Y_{PET} axis, as depicted in the top-right image, the maximum beam radius R_b that does not collide with the in-beam PET detectors is given by

$$R_b = \sqrt{R_{PET}^2 + (a/2)^2} \cdot \cos\left[\arcsin\left(\frac{D}{2 \cdot \sqrt{R_{PET}^2 + (a/2)^2}}\right) + 2 \cdot \arctan\left(\frac{a}{2 \cdot R_{PET}}\right)\right], \quad (2.3)$$

with R_{PET} the inner radius of the tomograph, D the diameter of a cylinder-shaped volume reserved for the patient and couch and a the axial FOV of the tomograph. The graphs in the bottom of Fig. 2.14 depict both the correlation between R_b and a, from Eq. 2.3, for two tomographs with different R_{PET} (solid curves, left Y axis), as well the correspondence between d_n and a (dashed curves, right Y axis). It can be seen that a tomograph with e.g. $R_{PET} = 45.8$ cm and $a = 24$ cm (Fig. 2.13, top row) can be implemented with a patient table not wider than 65 cm (the maximum width at the GSI facility) provided that the center of the tomograph is aligned with the central axis of the patient table and that the distance between
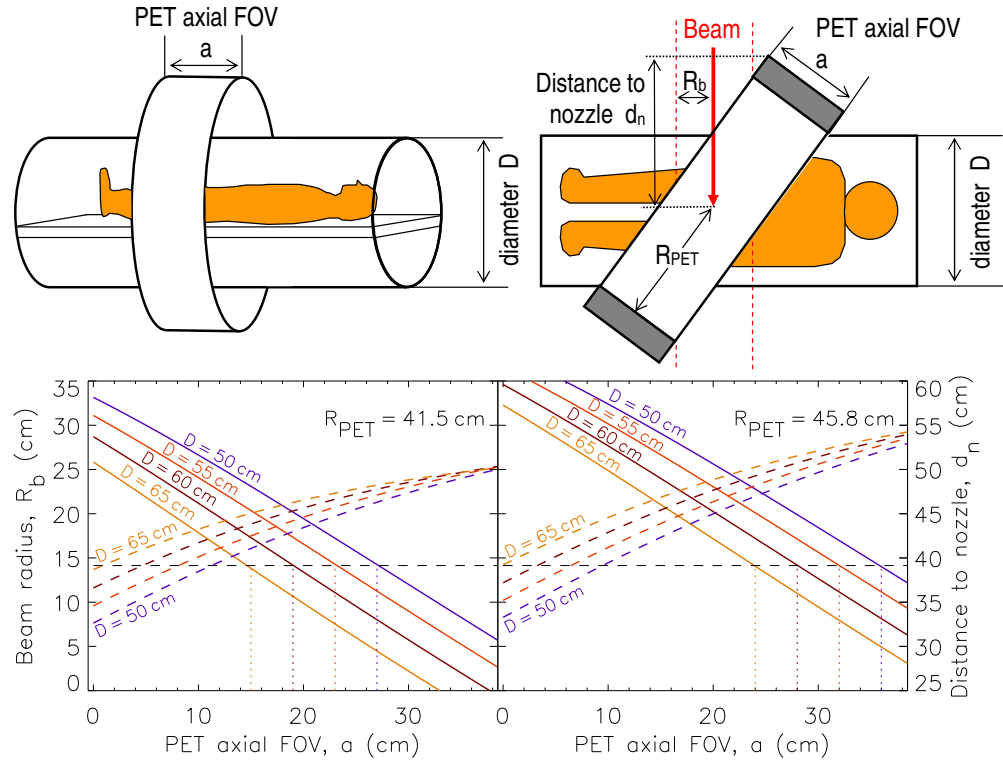
Figure 2.14: Feasibility of a closed-ring, in-beam PET tomograph with inner radius R_{PET}. The correlation between the maximum allowed beam radius R_b (left Y axis) and the axial FOV of the tomograph a is plotted with solid lines. The dashed lines plot the distance of the isocenter to the nozzle d_n (right Y axis) versus a for a scanner with 5 cm radial depth. The dashed line at $R_b = 14.14$ cm denotes the radius of a circle containing the maximum beam window deliverable at the GSI facility (20×20 cm^2).

the nozzle and the isocenter is not smaller than 50 cm. This last result assumes an in-beam PET scanner with a radial depth of 5 cm, a technological challenge since these 5 cm should include the detectors, front-end electronics and cabling as well as the support structure. Nevertheless, an existing solution has been developed for the PEM dual-head tomograph [Var05] which satisfies these restrictions[1].

2.8   Summary and Outlook

A fully 3D, maximum likelihood expectation maximization algorithm applicable to several closed-ring or dual-head tomographs was developed. It complements the reconstruction routine previously developed for the limited angle in-beam positron tomograph installed at the GSI tumor therapy facility. The combination of the new routine with a software package simulating different detector arrangements, also developed within this work, allowed the degradation of PET images obtained with dual-head tomographs to be quantified. It was seen that a smooth spatial distribution of the coincidence detection efficiency of a tomograph is highly desirable in order to reduce artifacts arising at the edges of the efficiency-corrected images, namely a false increase of image intensity if no image penalization is applied. Another image artifact arising with dual-head tomographs is the degradation of the spatial resolution of the image in the axis along the detector gap, leading to signal loss along that axis.

The evaluation of images obtained from simulated, real patient treatments for a head and neck and a pelvis irradiation revealed that a dual-head tomograph with an opening angle of approximately 46° yields satisfactory results in the case of the head and neck irradiation (smaller target volume). As expected, the best image quality was obtained with a closed-ring tomograph. Even with an incomplete coverage of the irradiated volume in the case of the pelvis treatment, the reconstructed β^+-activity distributions are remarkably similar to that generated in the patient. For this reason, the feasibility of implementing a closed-ring, in-beam PET scanner was investigated. It was seen that, considering the dimensions of the patient table and maximum beam window at the GSI facility, the installation of such a tomograph is possible, provided that the isocenter of the tomograph is aligned with the central axis of the patient table during the measurements. This last detail means that the isocenter of the target volume may not correspond to the isocenter of the in-beam PET scanner. As seen, this does not impose a loss of image quality for a closed ring tomograph and offers, in fact, two advantages: (1) increased simplicity, in respect to a target-isocenter fixed solution, in the process of bringing the tomograph into the measuring position and, (2) availability of radiotherapy monitoring by means of in-beam PET to all patients with a maximum width of 65 cm, independently of the location of their tumor. Item (2) cannot be satisfied with a dual-head tomograph since both isocenters, those of the tomograph and of the target volume, must overlap during the irradiation due to the image degradation seen at locations far from the isocenter of the tomograph. The integration of an in-beam PET scanner onto a rotating beam delivery is discussed in chapter 3.

Finally, it must be stated that the reconstruction routines developed provide a working solution for whatever tomograph found to be optimum for next-generation, in-beam PET systems. Nevertheless, their merging with modern, faster algorithms, e.g the ordered subsets expectation maximization (OSEM), typically reducing the number of iterations from 50 to only a few, is highly desirable in order to significantly decrease the data processing time.

---

[1] The prototype LSO/APDA PEM detectors, with a radial depth of approximately 4 cm, include two APDA per scintillator (DOI-PET), the corresponding fast readout electronics and cabling as well as the mechanical support structure.

Chapter 3

Integrating In-beam PET into Horizontal and Isocentric Ion Beam Deliveries

3.1 Motivation

The clinical results achieved by the pilot project at the tumor therapy unit at the Gesellschaft für Schwerionenforschung (GSI) in Darmstadt have prompted the construction of a dedicated, hospital-based facility [Hea98] providing much higher patient throughput by implementing three treatment rooms (beam deliveries). One of these will be equipped with an isocentric beam delivery (gantry) offering almost no restrictions in beam portal selection, i.e. close to fully 3D beam entrance coverage. This was seen to bring clinical advantages for treating more delicate therapeutic situations [Jäk00]. For this reason, an in-beam positron tomograph is planned to be installed in this treatment room. This fact has prompted research activites in order to (1) satisfy the technical restrictions imposed by medical needs and by all operating equipment to be installed at this isocentric beam line and (2) optimize this next-generation, in-beam tomograph by studying and minimizing the limitations of the presently operating in-beam scanner BASTEI.

Concerning in-beam PET integration, i.e. item (1) above, the technical restrictions are six-fold: (1) fast accessibility of the medical personnel to the patient at all times (this chapter); (2) collision-free solution concerning in-beam PET, beam nozzle and patient and couch (this chapter); (3) collision-free solution concerning in-beam PET and the incoming and outgoing [Gun04a, Gun04b] particle flux (sections 2.7 and 5.3); (4) volume minimized tomograph due to integration reasons (chapter 4); (5) magnetic field insensitive detectors due to the close proximity, at different distances and changing beam energies, of the last beam bending magnet (section 4.2.2); and (6) state-of-the-art detectors providing optimum γ-ray detection efficiency as well as energy and time resolutions for an efficient suppression of the high-yield, in-beam induced event background (chapter 6). In what regards the optimization of the tomograph itself, i.e. item (2) in the previous paragraph, the studies in chapter 2 showed that a closed ring detector geometry yields the best quality of in-beam PET images, followed by a small-aperture, dual head tomograph. For this reason, the implementation of these two tomograph configurations onto an isocentric ion beam delivery (gantry) are studied in the present chapter.

3.2 The Collision Table Between Gantry and Patient Table

A study analyzing the treatment of tumors under more delicate therapeutic situations, due to the close proximity of organs at risk (OAR), revealed that an isocentric beam delivery (gantry) offering almost no restrictions in beam portal selection brings important clinical advantages [Jäk00]. It was seen that all positions of the ion gantry and patient table that do

not lead to a physical collision between them constitute a desired beam portal. In Fig. 3.1 the coordinate system used[1] is described, together with a so-called collision table which correlates gantry and patient table angles, allowing to know at a glance whether a given combination of gantry and table angles yields a physical collision between them or constitutes an allowed beam portal. It can be seen that the collision areas signed correspond to beam portals where the irradiation would arrive to the patient in an approximate caudo-cranial direction (from the feet up) and would not be included, consequently, in a feasible treatment plan. All gantry-table angle combinations not signed are free for patient irradiation.
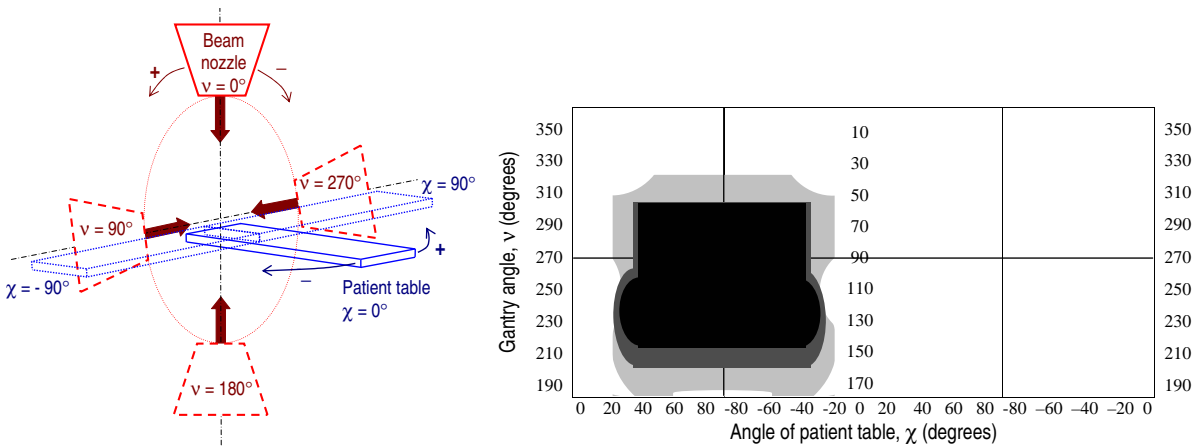
Figure 3.1: Coordinate system for the beam nozzle and patient table angles (left), according to the IEC[1] coordinate convention [Joy74], and corresponding collision table (right). The middle quadrants in the collision table correspond to gantry angles ν between 0 and 180°, as shown in the corresponding ordinate axis plotted at the center. The outer quadrants (first and fourth) correspond to ν between 180 and 360° (ordinate axis at the edges). The black and dark gray areas in the collision table correspond to nozzle and patient table angle combinations resulting in a physical collision between both. The different areas arise from different sizes of the patient table and couch considered. If a linear accelerator-based facility is considered the light gray area results [Jäk00].

In the following sections the integration of an in-beam PET scanner into the treatment room equipped with the ion gantry is studied. For every integration possibility analyzed a collision table was constructed, marking those angle combinations that lead to either some physical collision of the PET scanner with any other instrument, or a collision of the incoming/outgoing beam with the material of the PET scanner. The best integration design should not increase the collision area signed in Fig. 3.1.

3.3   PET at the Patient Couch

In this configuration, illustrated in Fig. 3.2, the tomograph is installed with its rotation axis parallel to the patient table. The dual-head PET scanner moves along the couch and can be positioned around the region being irradiated, with the aperture between the two detector heads allowing the beam to pass through without touching the γ-ray detectors (not shown in the right image in Fig. 3.2). This configuration can provide a full coverage of the volume under observation if the detector heads are allowed to rotate around its axial direction (Z_{PET} in

---

[1] Every beam input direction corresponds to a combination of patient table and beam gantry angles. Herein the angles are stated according to the International Electrotechnical Commmision (IEC) coordinate convention [Joy74].
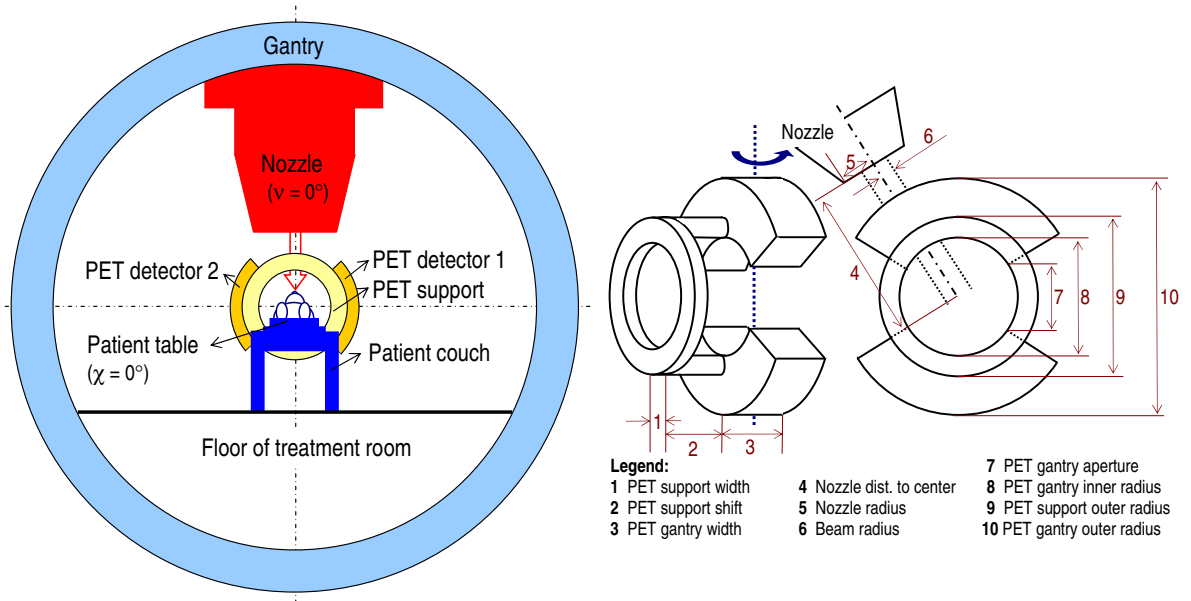
Figure 3.2: PET at the patient couch. A dual-head positron scanner is fixed to the patient couch with its axis parallel to that of the patient table. The detector heads rotate, based on their support ring, allowing the aperture between them to be positioned along the beam (not shown in the right image).

Fig. 2.1) provided that the rotation movement is correlated with the beam delivery macropulses so that no detector lies in the beam path during particle extraction. Such solution requires most probably complex stability issues to guarantee that the moving detector heads do not shift the isocenter of the in-beam positron tomograph. Another possibility to provide full coverage of the irradiated region arises by tilting a closed-ring tomograph, as proposed in section 2.7. This is feasible in the present configuration provided that the tomograph is allowed to rotate
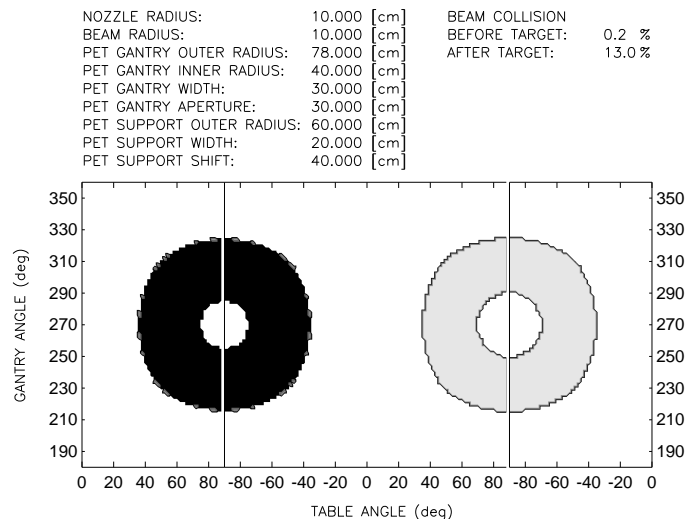
Figure 3.3: Collision table for the configuration with PET at the patient couch. Calculated both for a closed ring as well as a dual-head tomograph. The dark area denotes a physical collision between the nozzle and the support ring of the PET scanner. It lies within the caudo-cranial portals that are not used. The gray area signs a collision of the particle flux leaving the patient, downbeam, with the support ring (text has details).

about the axis signed with the dotted line in Fig. 3.2. Fig. 3.3 shows the collision table resulting from the implementation of either a closed ring or a dual-head tomograph at the patient couch. The dimensions of all components signed in its legend were optimized in order to achieve the minimum collision area. It can be seen that 13 % of all possible portals would result in an irradiation, after the target, of the support ring holding the detectors. This collision area was calculated conservatively, assuming a straight forward propagation of the particle flux downbeam and with a beam radius of 10 cm, as detailed in the Fig. More importantly, the forbidden portals lie exactly in the cranio-caudal direction (from the head down), a favorite and important region of input portals for head and neck irradiation [Jäk00].

In summary, the most important disadvantage of the present configuration is the forbidden irradiation area in the cranio-caudal direction arising from the interaction of the particle flux leaving the patient [Gun04a, Gun04b] with the support of the PET scanner.

3.4   PET on a Separate Gantry

If the PET scanner is fixed on a separate gantry, positioned inside the treatment room and opposite to the patient couch [Eng03] as depicted in Fig. 3.4, than all portals corresponding to the free area in Fig. 3.1 become available. This means that all irradiation fields are possible from the point of view of PET, so that the fobidden portals in the collision table result only from physical collisions between the nozzle and the patient table or couch, as shown in Fig. 3.1. This solution, implementable only with a dual-head tomograph, requires the patient to be positioned for irradiation in a first step, followed by the movement of the PET scanner onto its measuring position in a second step and, finally, the rotation of the ion gantry untill the desired angle ν is reached, i.e. the only extra procedure in respect to the present irradiation at GSI arrives from the moving of the ion gantry. Nevertheless, the positioning of the positron tomograph requires an extra coordination of several synchronous movements signed with the marked block
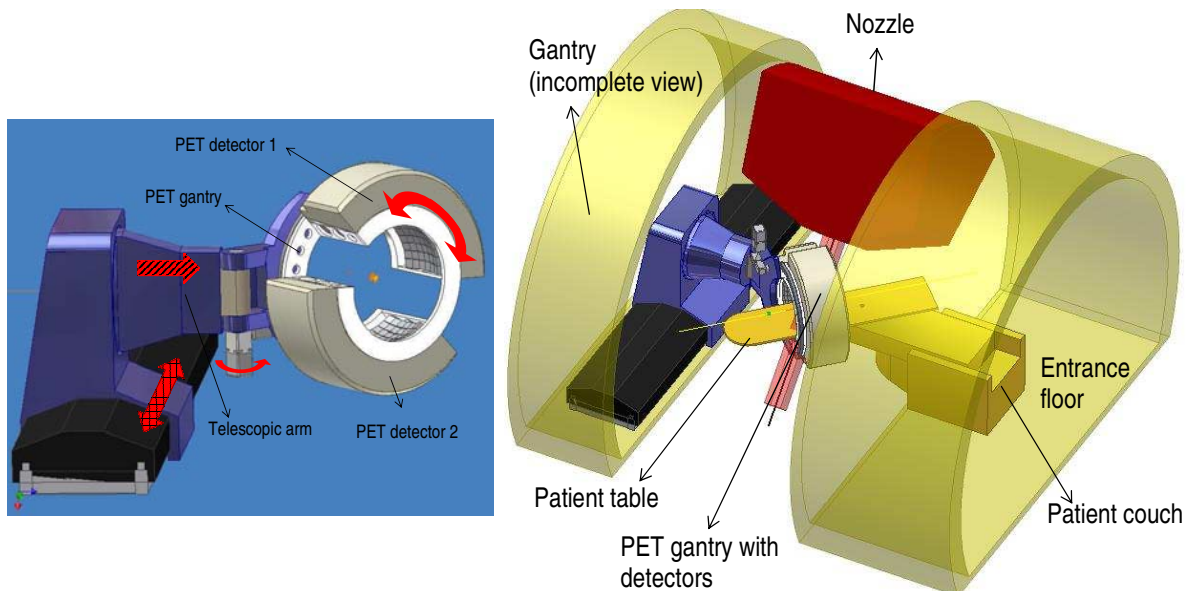
Figure 3.4: PET on a separate gantry. A dual-head positron scanner is fixed on a separate gantry, positioned inside the treatment room and opposite to the patient couch. The patient is first positioned for treatment, followed by the positioning of the dual-head scanner with movements indicated with the block arrows in the left image (text has details).

arrows in Fig. 3.4. These are (1) the extension of the telescopic arm (hashed arrow) in parallel with (2) a dislocation of the arm structure perpendicularly to the movement of arm extension (squared arrow). The synchronization of these movements can be implemented either at the machine level or require human intervention. In either case, a physical collision between the positron gantry and the patient or table during this positioning procedure is not excluded in the case of machine or human error. Such collision possibility is highly minimized with the present PET scanner positioning scheme at the GSI horizontal, fixed beam line. This item constitutes the main disadvantage of the present configuration, together with the time required to bring the PET scanner into its measuring position and, more importantly, the time needed to gain access or release the patient being treated in the case of an emergency.

3.5 PET at the Beam Nozzle

This configuration was developed at GSI for a dual-head tomograph [Kop04]. A support ring, rotating around the nozzle, holds two mechanical arms which position the PET detector heads at the isocenter (Fig. 3.5). During patient positioning the detector heads lie behind (following the beam direction) the support ring (not shown), enabling full patient access at the isocenter. This PET positioning mechanism offers the advantage that, in the case of an emergency during irradiation, the arms open and return the detector heads to their back position without any physical collision being possible neither with the patient or table nor with the nozzle or beam. Therefore, an immediate access to, or release of the patient is possible. In addition, by rotating the two detector heads around an axis perpendicular to the beam direction, shown with the block arrow and dotted line in Fig. 3.5, the implementation of a closed-ring tomograph becomes feasible for all irradiation portals, i.e. the collision table of Fig. 3.1 is valid. This closed-ring tomograph is still divided in two detector heads but without an aperture between them.
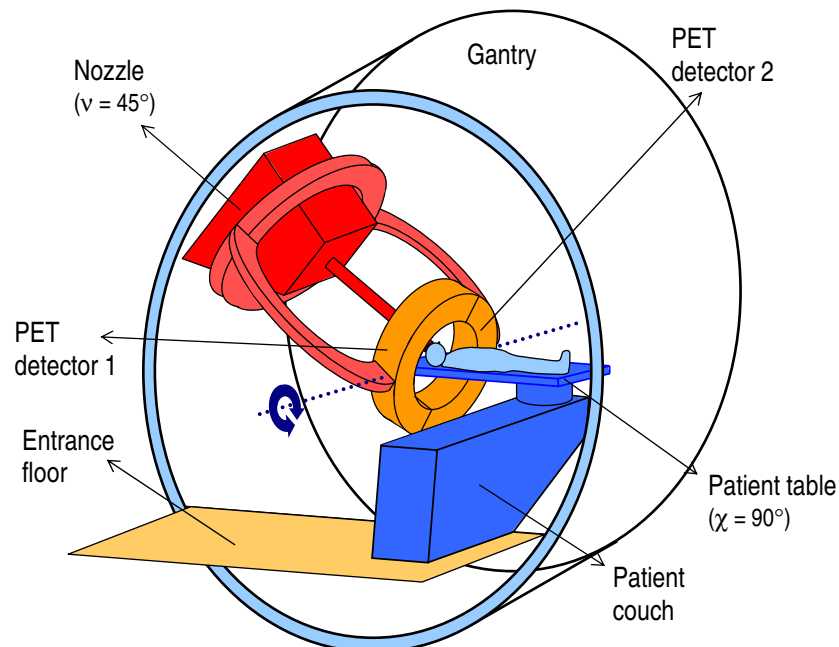
Figure 3.5: PET at the beam nozzle. A support ring rotating around the nozzle holds two arms that position each of the PET detector heads at the isocenter. By rotating the two detector heads around an axis perpendicular to the beam direction (block arrow and dotted line) the implementation of a closed ring tomograph becomes feasible for all irradiation portals.

In summary, the present configuration seems to satisfy all requisites for in-beam PET: a fast access of the medical personnel to the patient at all times; a collision-free solution concerning the PET scanner, the nozzle and the patient and couch with, in addition, no possible interference of the in-beam PET detectors with the beam; and, very important for the quality of in-beam PET images, the implementation of a closed ring detector geometry becomes feasible. On the other hand, some disavantages are brought up by bringing the PET detectors close to the last beam bending magnet, in addition to operating them at different magnetic field strengths during patient irradiation. These issues and their solution are addressed in chapter 4.

3.6   PET at a Fixed, Horizontal Beam Line

Fig. 3.6 displays a solution for implementing a closed-ring, in-beam PET at a fixed, horizontal beam line. It is similar to the present implementation of BASTEI in the sense that the mechanical structure holding the two PET detector heads moves along the beam nozzle, bringing the tomograph into the measuring position and back. The main difference lies in the capability of rotating each detector head about a vertical axis (white arrows in the right image of Fig. 3.6), therefore allowing the tomograph to be placed at the isocenter in a tilted position with respect to the incoming beam. This rotation, together with the vertical movement of each of the mechanical arms holding the two detector heads, allows a closed ring positron tomograph to be installed if the dimensions considered in section 2.7 for the in-beam PET detectors, patient table and distance to nozzle are taken into account.

Should the installation of a closed-ring, in-beam PET be not feasible, a dual-head tomograph with small gaps, installed with the system depicted in Fig. 3.7, is also possible. This tomograph should be built in a way to allow a closed-ring detector configuration to be used whenever possible. Either with a closed-ring or with a dual-head tomograph, the positioning system depicted in Figs. 3.6 and 3.7 offers the advantage of a fast, collision-free access to the patient at all times. For that, the heads just need to be moved apart vertically in the case of an emergency.
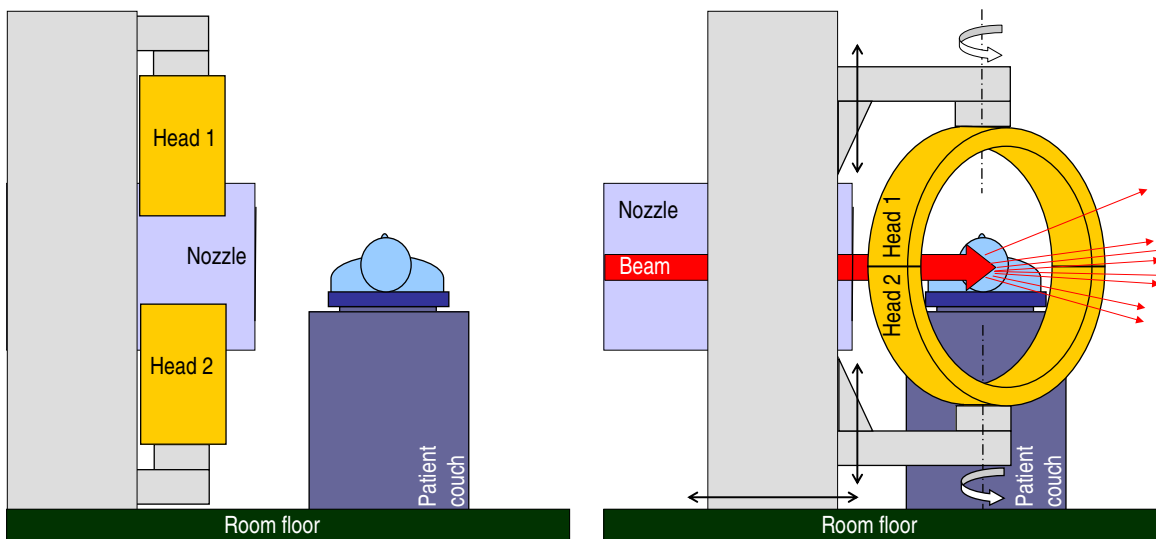
Figure 3.6: Closed ring, in-beam PET at a fixed, horizontal beam line. The left image shows the two detector heads in the park position, whereas in the right the heads are positioned for data taking during irradiation, with the couch at an angle $\chi = 90°$.
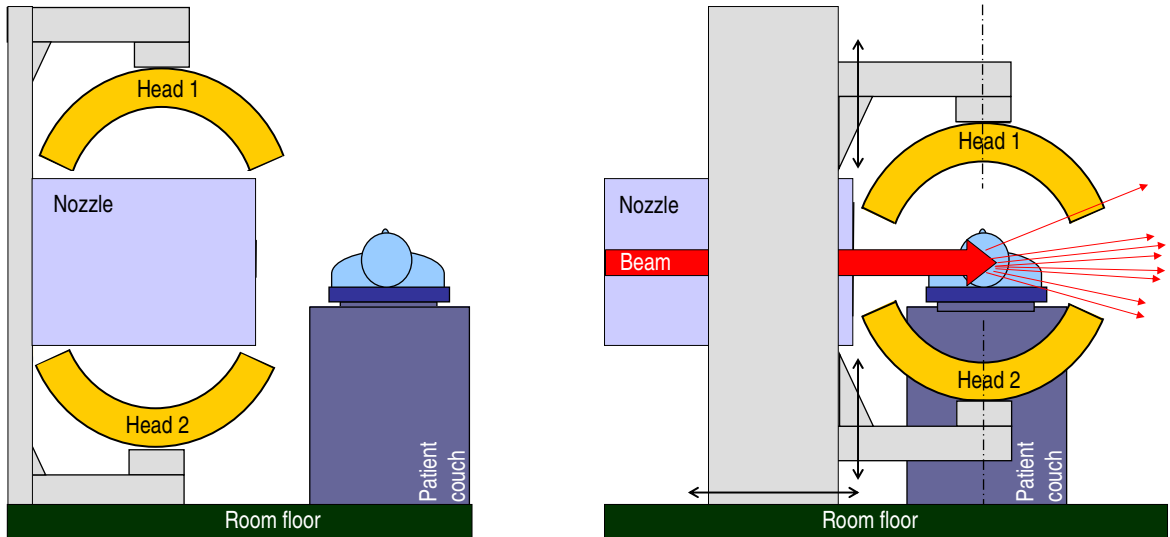
Figure 3.7: Dual-head, small-gaps in-beam PET at a fixed, horizontal beam line. The left image shows the two detector heads in a possible park position, whereas in the right the heads are positioned for data taking during irradiation, with the couch at an angle $\chi = 90°$.

3.7 Summary and Outlook

An isocentric, ion beam delivery (gantry) offering almost no restrictions in beam portal selection, i.e. close to full 3D beam entrance coverage, was previously seen to bring clinical advantages for treating more delicate therapeutic situations [Jäk00]. In order to monitor these precise irradiation fields, in-beam PET with the highest possible image quality is a requisite. In the present chapter three configurations for installing an in-beam positron tomograph onto an isocentric, ion beam delivery were studied. Several technical restrictions arise when addressing the installation issue, and any of them must be respected, namely: (1) fast accessibility of the medical personnel to the patient at all times; (2) collision-free solution concerning in-beam PET, beam nozzle and patient and couch; (3) collision-free solution concerning in-beam PET and the incoming and outgoing particle flux [Gun04a, Gun04b]; (4) volume minimized tomograph due to integration reasons; (5) magnetic field insensitive detectors due to the close proximity, at different distances and changing beam energies, of the last beam bending magnet; and (6) state-of-the-art detectors providing optimum γ-ray detection efficiency as well as energy and time resolutions. Items (4), (5) and (6) are discussed and optimized in the next three chapters.

In order to evaluate the feasibility of three in-beam PET implementation configurations in what regards items (2) and (3) above, a collision table scheme previously defined was used. This scheme shows that an in-beam PET configuration with either a closed-ring or a dual-head tomograph installed at the patient couch results in a forbidden irradiation of a great part of necessary cranio-caudal portals. This is due to the interference of the particle flux leaving the target with the PET support material, which may cause its activation and, therefore, would veto this installation due to radiation protection issues.

A second configuration analyzed consisted in installing a dual-head positron tomograph on a separate gantry, with this gantry being positioned inside the treatment room, opposite to the patient couch [Eng03]. It was seen that this configuration provides a solution regarding items

(2) and (3) during in-beam PET measurements, therefore allowing any portal to be delivered. But it was also seen that, due to the complex PET positioning system, it fails to satisfy requisite (1).

A third configuration, developed at GSI for a dual-head tomograph [Kop04], installs the PET scanner and all its support and driver machinery at the beam nozzle. This solution seems to satisfy all the requisites mentioned. In addition, it was seen that this configuration further allows a closed-ring detector geometry to be implemented, which brings an important enhancement of the quality of in-beam PET images (chapter 2). Nevertheles, there are disadvantages of bringing the PET detectors close to the last beam bending magnet. These are addressed and a solution is proposed in chapter 4. In summary, it seems that the implementation of a closed-ring tomograph fully installed on the beam nozzle brings the best answer for in-beam PET at a rotating, isocentric ion beam delivery.

In what concerns in-beam PET at a fixed, horizontal beam line, a solution complementing that installed at BASTEI elucidates the feasibility of installing both a closed-ring as well as a dual-head, small-gaps positron tomograph at such beam lines.

Chapter 4

Detector Development: LSO Scintillator coupled to APD Arrays

4.1 Motivation

The in-beam positron emission tomograph BASTEI[1], under clinical operation since December 1997 at the german heavy ion tumor therapy facility at GSI Darmstadt [Eng04b], is based on the positron emission tomography (PET) technology for tracer imaging available at the time of installation. Consequently, its radiation detectors, scanner geometry and data acquisition and processing are suboptimal with respect to the requirements of next-generation, in-beam PET systems for therapy monitoring at future heavy ion clinics, namely high detection efficiency for annihilation radiation[2], a fast scintillator enabling the smallest time resolution for the suppression of random coincidences (chapter 6), good energy resolution for rejecting Compton photons scattered in the patient, insensitivity against influences from the therapy beam (chapter 5), hardness against hadronic radiation (chapter 5), magnetic field insensitivity, compactness and flexibility for positioning the patient at the beam delivery (chapter 3) and a fast signal processing and data acquisition able of separating the events acquired during the high rates registered during particle extractions (chapter 6).

The new scanner to be installed at the dedicated heavy ion facility in Heidelberg [Hea98] is to be operated close to the last beam bending magnet, which is not the case at the present fixed horizontal beam line in Darmstadt. For this reason, and because a reduction of the volume of the tomograph is highly desirable due to integration reasons[3], the compact, magnetic field resistant avalanche photodiode arrays (APDA) become the detector of choice for scintillation readout, instead of the bulky, presently used photomultiplier tubes (PMT). In addition, the γ-ray detection material BGO is planned to be substituted with a state-of-the-art, commercially available scintillator that better satisfies the requisites mentioned. One possible candidate is cerium-doped lutetium oxyorthosilicate (Lu_2SiO_5:Ce^{3+}, LSO).

In the present chapter the physical and technological properties of the APDA scintillation detector, the LSO scintillator itself and the γ-ray detector resulting from the coupling of the two (LSO/APDA) are described, together with the optimization procedures endured before the construction of the detector. Finally, the imaging properties of two LSO/APDA detectors, assembled at the Forschungszentrum Rossendorf, are presented. The detectors are fully char-

---

[1] <u>B</u>eta <u>a</u>ctivity mea<u>s</u>urements at the <u>t</u>herapy with <u>e</u>nergetic <u>i</u>ons.

[2] The presently installed scintillator, Bismuth Germanate ($Bi_4Ge_3O_{12}$, BGO), has a rather high intrinsic detection efficiency, therefore satisfying this requisite quite well.

[3] This next-generation, in-beam PET must be accomodated in a cylindrical room with a diameter of 5 meters (chapter 3) together with the last beam bending magnet, the several detectors of the therapy-online-monitor system, the patient couch, the X-ray tubes and lasers for patient positioning verification and the mechanical structures holding all these devices.

acterized in single-mode operation and in coincidence with each other forming a very small positron tomograph.

4.2   Detection of γ-rays in Nuclear Medicine Imaging

Radiolabeled nuclear imaging techniques include high resolution ($< 100\ \mu$m) *ex vivo* and *in vitro* autoradiographic techniques using film, phosphor storage plates or real time autoradiographic systems [Cha98], and *in vivo* methods using radionuclides that produce photons of appropriate energy (γ-rays, annihilation photons or characteristic X-rays with energies in the range of 25 - 511 keV) during decay [Che04b]. The *in vivo* methods are further divided into single photon imaging, utilizing radionuclides with single or multiple, uncorrelated γ-ray emissions detected by gamma camera[1] systems [Sho84] and PET, where β^+-decaying radionuclides emit an energetic positron that annihilates into two, almost back-to-back 511 keV γ-rays after the positron thermalizes in the surrounding medium and annihilates itself with an atomic electron. A non-complete collinearity of the γ-rays emitted takes place and was measured to be $\leq 0.5°$ FWHM[2] in water. It arises due to the momenta of both the thermalized positron and the atomic electron at the moment of annihilation [Phe75]. Because of this almost back-to-back photon emission and detection in a PET system, called electronic collimation, no physical collimation is required and, therefore, its sensitivity is much higher (10^2 - 10^3) than in a SPECT system. However, single-photon emitting radionuclides are generally more readily available than positron-emitting nuclides, as many of the latter have short half-lives [Che04b].

With a photon energy of 511 keV in PET, and a photon-energy range typically ≤ 400 keV in single-photon imaging, with the 140 keV γ-ray from ^{99m}Tc used most frequently [vE02], an efficient detection must rely on a conversion medium in which the incident γ-rays have a reasonable probability of interacting (section 4.2.1) and on a detector to read the output of the conversion medium (section 4.2.2).

4.2.1   Scintillators for γ-ray conversion

Ionization detectors that use a gas as the sensitive volume are poor detectors for counting both γ-rays and X-rays because of their low interaction probability and their weak capability to measure the energies of individual photons. Therefore, scintillator materials used in nuclear medicine are generally either inorganic substances in the form of solid crystals or organic substances both dissolved in liquid solution or dissolved in a solvent subsequently polymerized, i.e. forming a solid solution. Inorganic scintillators are employed in most of the current medical diagnostic imaging modalities using X-rays or γ-rays [Web90]. This is explained by the comparatively good detection efficiency of inorganic scintillators for hard radiation in respect to organic scintillators or solid detectors, i.e. silicon or germanium-based semiconductor detectors exposed directly to the photons.

Table 4.1 shows the main properties of the most important scintillators used, or under study and development, for γ-ray detection in radionuclide medical imaging. Its compilation was based mostly upon [vE02] and [Paw95], with information also from the references given in the Table and from [Cry00, Gro98a, Kno89]. The scintillator density ρ is multiplied by the fourth power of its effective atomic number Z_{eff} since the absorption by photoelectric effect per unit length is proportional to ρZ_{eff}^{3-4} [vE02]. For 511 keV quanta the chance of photoeletric effect at $Z = 80$ is less than 50 %, the other 50 % being the Compton effect, proportional to ρ. Depending

---

[1] If the gamma camera is rotated around the patient and used with tomographic acquisition and reconstruction techniques, the term SPECT (single photon emission computed tomography) arises.

[2] Full width at half maximum.

Table 4.1: Scintillators for γ-ray detection in radionuclide medical imaging.

Scintillator	Density ρ (g cm^{-3})	ρZ_{eff}^4 ($\times 10^6$ g cm^{-3})	Atten. length[a] (mm)	Photo effect fr.[a] (%)	Hygroscopic	Yield (ph./keV)	Decay const. (ns)	Peak emission (nm)	$\Delta E/E$[b] (%, FWHM)	dE/dx per mip[c] (MeV/cm)	After-glow (%/ms)	Medical application	Reference(s)
NaI:Tl	3.67	24.5	29.1	17	Yes	41	230	410	5.6	4.8	0.3-5/6	SPECT	[Hof48, Sho84]
CsI:Na	4.51	38	22.9	21	Yes	40	630	420	7.4	5.6	0.5-5/6	XII	[Hel00]
CsI:Tl	4.51	38	22.9	21	Slightly	66	$>800^d$	420	6.6 / 4.3^e	5.6	0.5-5/6	SPECT, PET, CT	[vE02, Gar00]
CsF	4.64	37	20.0	23	Very	2 / 2.8	3 / 5	390		6.0^g		TOF-PET	[Mos83]
BaF$_2$	4.89	42	20.5	17	Slightly	2^f / 8.2^s	0.7^f / 620^s	220^f / 310^s	10	6.6		TOF-PET	[Lav83]
BGO (Bi$_4$Ge$_3$O$_{12}$)	7.13	227	10.1	40	No	9	300	480	9.0	9.2	0.005/3	PET	[Web73]
LSO (Lu$_2$SiO$_5$:Ce)	7.4	143	11.4	32	No	26	40	420	7.9	9.7^g	<0.1/6	PET	[Mel92, Mel91]
LYSO $\frac{Lu}{Y}$ (Lu$_{1.8}$Y$_{0.2}$SiO$_5$:Ce) $\frac{90}{10}$	7.1	127	11.5		No	26^h	41	420	7-9	7.8^g	<0.1/6	PET	[Coo00, Pid03]
(LuYSiO$_5$:Ce) $\frac{50}{50}$	6.0	75	16.7	21	No	26^h		420	7-9	7.1^g	<0.1/6	PET	[Kim02, Mos99b]
LuAP (LuAlO$_3$:Ce)	8.3	148	10.5	30	No	12	18	365	~15	11.0^g		PET	[Min94, Mos95]
LPS (Lu$_2$Si$_2$O$_7$:Ce)	6.2	103	14.1	29	No	30	30	380	~10	8.3^g		DOI-PET	[Pau00]
LGSO (Lu$_{0.4}$Gd$_{1.6}$SiO$_5$:Ce)	6.5	79	14.3	26	No	16	65	440	8	8.6^g		PET	[Shi04]
GSO (Gd$_2$SiO$_5$:Ce)	6.7	84	14.1	25	No	8	60	440	7.8	8.7^g		PET	[Tak83, vE02]
YAP (YAlO$_3$)	5.5	7	21.3	4.2	No	21	30	350	4.3	7.8^g		PET	
LaCl$_3$:Ce	3.86	23.2	27.8	14	Yes	46	25(65%)	353	3.3	5.2^g		SPECT	[vL00]
LaBr$_3$:Ce	5.3	25.6	21.3	13	Yes	61	35(90%)	358	2.9	6.9^g		SPECT	[vL01]
CeBr$_3$	5.2	26.6	21.5	14	Yes	68	17	370	3.4	5.9^g		TOF-PET	[Sha04]
LXe (liquid xenon)	3.06	26	30.4	21	-	11 / 26^j	27(30%) / 45(70%)^j	165	22/16^i	3.9^g		DOI-PET	[Che83]
PbWO$_4$	8.2	268	8.9	43	No	0.2	15	440-500		13.0			[Sch92, Cry00]
Plastic (vinyltoluene)	1.03	<0.005	444	-	No	<12	1-3	375-435	-				[Paw95, Bir64]
Ideal (PET, PMT)	>6	>245	<12	>30	No	>8	<500	300-500	<10	-			[Der82, Mos00]
Ideal (PET, APD)						$\gg 8$		400-900					
Ideal (TOF-PET)						$\gg 8$	<40						

[a] At 511 keV.
[b] At 662 keV, PMT readout.
[c] Minimum ionizing particle.
[d] Smaller than 6 μs.
[e] At 662 keV, PMT and silicon drift detector (SDD) readout.

[f] Fast decay component.
[g] Extrapolation from $Z_{eff}/A \times \rho$, based on NaI.
[h] PMT readout, 33 ph./keV with APD readout.
[i] At 511 keV, with 22% in [Che04a], 16% in [Cre00] (ionization mode).
[j] Arises from e$^-$/ion$^+$ recombination, vanishes under electric field.

[s] Slow decay component.
SPECT: Single photon emission computed tomography.
XII: X-ray image intensifier.
TOF-PET: PET with time-of-flight information.
DOI-PET: PET with depth-of-interaction information.

on the kind of scintillator and on the crystal size, detection of both the Compton electron and the Compton-scattered photon in the same crystal or detector may significantly contribute to the intensity of the full-energy peak, as demonstrated for example in positron emission mammography (PEM) dedicated systems using LSO scintillators coupled to APDA [San04]. In PET applications a scintillator with small attenuation length is necessary in order to minimize the crystal radial length, typically on the order of three times the attenuation length. This, in turn, minimizes the parallax error responsible for radial degradation of the images at voxels away from the isocenter of the tomograph [Hum03]. The photoeffect fraction, together with the photopeak energy resolution, are indeed important for a high full-energy peak intensity and, consequently, for a high detection efficiency of events valid for reconstruction, a low contribution of photons Compton-scattered in the patient, that show up as a continuous blur in the images, and a high true-to-random coincidence ratio since random events are more affected by Compton photons than true events [Mue02]. The photon yield and the decay constant of the scintillator play their role in minimizing the coincidence-time resolution $2\,\Delta t$ achievable by the system. A small time resolution is mandatory for achieving the lowest random coincidence rate C_r possible since $C_r = 2\,\Delta t\,C_i\,C_j$, where C_i and C_j are the singles count rates in detectors i and j forming the line of response (LOR) ij. Furthermore, a small scintillation decay time is also necessary for minimizing dead time, i.e. the time in which a coincidence cannot be registered because the PET system is busy handling a previous coincident event. Several parts of the system contribute to the dead time and the detector is one of them. Besides its influence on energy resolution, a high light yield is also important for achieving optimum spatial resolution at the detector in systems using scintillation-light sharing methods to reduce the number of readout electronic channels [Cas86, dG94, Wie94].

Additional prerequisites for an in-beam PET scintillator

In addition to the main scintillator properties described in the previous paragraph for nuclear medicine imaging with PET, the requirements of in-beam PET include also a radiation hard crystal that does not become activated, leading to γ-ray lines in the 511 keV region (experimental results in chapter 5). This is necessary due to the light particle flux consisting mainly of neutrons and protons, but also with slightly heavier particles, that has been measured to leave the irradiated patient downbeam, peaked in the forward direction [Gun04a, Gun04b].

All crystal scintillators suffer from radiation damage [Zhu98] when exposed to large radiation doses. The most common damage phenomenon is the appearence of radiation-induced absorption bands caused by color center formation. The absortion bands reduce the light attenuation length of the crystals and, consequently, its light output. Other effects include an increase in phosphorescence (afterglow), which leads to an increase in readout noise, and a reduced intrinsic scintillation light yield due to damage of the scintillation mechanism. Damage may recover both under room temperature, leading to a dose rate dependence [Zhu97], as well as after thermal annealing or optical bleaching[1]. The effects usually can only be observed clearly in thick ($>$ 5 cm) crystals [Bob84] and are dependent on the type of radiation [Kob83]. A material is usually called radiation hard if no measurable effects occur at a dose of 10 kGy. Examples of radiation hard materials are $CdWO_4$, GSO and BaF_2 [Maj85]. In general, doped alkali halide scintillators such as NaI:Tl and CsI:Tl are rather susceptible to radiation damage, with NaI:Tl recovering the damage non spontaneously and CsI:Tl suffering permanent damage [Bob84].

The radiation resistance of scintillators commonly used in PET, like BGO and LSO, have been

---

[1] Thermal annealing and optical bleaching consist in applying a heat treatment ($\sim 500\,^\circ$C) or exposure to light in the visible/ultra-violet spectrum ($\sim 1\,\mathrm{mW/cm^{-2}}$), respectively, to the damaged crystal in order to rearrange its constituent atoms and crystal defects to a configuration similar to that existing before the irradiation, thus restoring to some degree its light transmission properties.

measured both for low-energy γ-rays, high-energy protons and fast neutrons for BGO [Kob83], as well as for X-ray exposure for LSO [Coo99]. For BGO, the studies with hadrons show a conservative value of 150 Gy as the maximum dose before 1 % transmittance is lost after 20 radiation lengths. Furthermore, long lived excited states are produced in the crystal after a hadron dose of 10 kGy only, with disintegration rates of $10^2\,\mathrm{s}^{-1}\,\mathrm{g}^{-1}$ and $35\,\mathrm{s}^{-1}\,\mathrm{g}^{-1}$ corresponding to γ-ray lines above 500 keV and 1 MeV, respectively. In the case of pure LSO, an increase in absorbance of scintillating light of $\sim 10\,\%$ and $37\,\%$ at 400 nm was measured after an exposure of 1 minute and 30 minutes, respectively, to an X-ray dose rate of 120 Gy min^{-1}. This behaviour was attributed to the enhancement of oxygen related defects and was not observed in cerium-doped LSO due to its activator-based scintillation mechanism [Kno89]. Cerium doped LSO is a fairly radiation hard scintillator up to 100 kGy [Mos02].

Scintillators commonly used in nuclear medicine

By far the most commonly used scintillator for nuclear medicine applications is the thallium-activated sodium iodide crystal NaI:Tl, used in combination with a PMT readout (section 4.2.2) mostly in single-photon emission systems but also in high resolution PET scanners [Ada01]. Other scintillators most suitable for PET at the current time are BGO, LSO, LuAP, LPS, GSO and YAP (Table 4.1). The most widely used in commercial PET scanners is BGO. It presents a high detection efficiency for 511 keV photons (a 3 cm long crystal has almost 3 attenuation lengths) and high photoeffect fraction, together with a relatively low production cost. The main disadvantages of BGO are its rather long decay time of 300 ns and low light yield in respect to other scintillators such as LSO, leading to worse time and energy resolutions, respectively. One of the most suitable scintillator material for PET is LSO. It presents a high ρZ_{eff}^4, a high light yield, short decay time and relatively good mechanical properties necessary for high-throughput manufacturing. Due to its short decay constant a time resolution of 1.2 ns has already been achieved in a commercial PET scanner [Con03], with BGO-based tomographs presenting typically 12 ns. Therefore, renewed interest in profiting from the time-of-flight information in LSO-based tomographs has arisen [Mos04], with a commercial solution already on the market [Con03]. As mentioned before in this section, a commercial PEM system based on LSO scintillators coupled to APDA is under construction [San04]. Due to a scintillation readout on both sides of the LSO crystals, this system, expected to provide a time resolution of the order of 500 ps FWHM, will allow DOI-PET to be implemented in mammography applications. For completeness, it must be stated that several groups have been actively developing new PET methods and techniques using noble elements, like liquid xenon (LXe), in scintillation and ionization correlated modes [Cre00] in order to solve the problem of parallax error in PET [Che83, Col00].

4.2.2 Detectors for scintillation light collection

Current commercial PET scanners generally use detector modules readout in Anger logic, i.e. one scintillator detector block is implemented with saw cuts defining *individual* pixels and the scintillation light is read by several PMT [Mos94]. The analog ratios among the PMT signals yields the coordinate of the hit crystal [Ang58]. This reduces the number of electronic readout channels by a factor given by the ratio between the number of individual crystals and PMT but, on the other hand, increases the detector dead-time per front area unit[1] by the same amount and introduces a spatial resolution degradation of typically 2 mm added in quadrature to other factors influencing the spatial resolution of the tomograph [Mos93]. The reasons for using PMT for scintillation light readout are their much higher gain and better noise characteristics

---

[1] The detector dead-time per unit area is a figure of merit commonly used to describe the effective detector dead-time due to the scintillator decay time together with the readout scheme implemented [Mos94].

in respect to other more compact light detectors such as silicon-based APDA [Pic04]. Other photodetectors providing sufficiently high gain bandwidth for use in PET applications are multi-anode PMT [Suz93], metal channel dynode PMT [Kyu94], hybrid PMT[1] [Dat97], micro channel plate PMT (MCP-PMT) [Fie03], visible light photon counters[2] (VLPC) [Pet89] and Geiger-mode APD[3] [Buh03]. The latter has been gaining increasing importance due to its low-cost, compactness, room-temperature operation capability, insensibility to magnetic field and hadrons and good timing characteristics in low-light environments, with pixel recovery times of about 20 ns. However, due to current fabrication limitations, the light pulses readout by Geiger-APD must be limited to 2×10^3 photons per mm^2, which is still a too low dynamic range for PET applications. Multi-anode PMT, such as the 8×8 pixel, flat-panel PMT H8500 from Hamamatsu [Fie03], as well as MCP-PMT, such as the 8×8 pixel 85011-501 from Burle [Fie03], have recently made substantial progress towards delivering devices with high packing fractions of 90 and 70 %, respectively, high gain of 10^6, excellent single-photon timing characteristics of 300 and 130 ps FWHM, respectively, and acceptable pixel-to-pixel uniformity with efficiency drops of 10 - 20 % at the edges. However, their quantum efficiencies lie below that of normal PMT by 20 and 30 %, respectively. Finally, multi-anode PMT cannot be used under magnetic fields, whereas MCP-PMT offer high magnetic field insensitivity.

Additional prerequisites for an in-beam PET detector

From the list of detector characteristics outlined in the previous paragraph, two must be underlined for a detector suitable for the next-generation in-beam PET: compactness and magnetic field insensitivity; and other two must be added for solid state detectors: radiation hardness and small nuclear counter effect[4].

As detailed in chapter 3, this next-generation tomograph will have to adapt itself into different measuring positions in respect to the patient and patient-couch, the X-ray and laser patient positioning system, the detectors of the therapy on-line monitor and to the last portion of the rotating beam line (nozzle). This fact justifies efforts on reducing detector volume and, therefore, on the need for detector compactness. Concerning magnetic field insensitivity, Fig. 4.1 shows the calculated fringe magnetic field after the last beam bending magnet of the rotating gantry (nozzle). Depending on the irradiation portal selected, each PET detector will have to be positioned at different places in respect to the last magnet and, therefore, will have to operate under different magnetic field intensity and orientation from measurement to measurement. Furthermore, the magnetic induction is changing during the irradiation due to the variation of beam energy. This poses strong restrictions on the use of PMT, even with mu-metal shielding, since a decrease in gain between 10 and 15 % was measured with a magnetic field intensity of 2 mT only (20 Gauss) when the magnetic field was oriented along the longitudinal axis of the PMT [Bou00]. This decrease was measured with the ETL 9126FLB17 PMT, a linear focus dynode structure PMT with 11 amplification stages, and the PMT was covered with a mu-metal sheet extended to 30 mm beyond the photocathode. If the mu-metal sheet screening finished at the edge of the photocathode a decrease in gain of 50 % was already observed at a field intensity if 1 mT (10 Gauss). In addition to these facts, the park position of the PET scanner lies in close proximity to the last beam magnet. This may induce permanent malfunctioning or performance degradation onto the detectors. For these reasons, a magnetic field insensitive

---

[1] Also named hybrid photodiode or hybrid PD.

[2] Typically operated at liquid helium temperatures: 6.5 K.

[3] Also named silicon photomultiplier (SiPM) or Geiger photodiode (GPD).

[4] The nuclear counter effect is a quantification of the electrical signal generated by the passage of ionizing radiation through an APD. It is expressed as the effective thickness of a diode with gain 1 that generates the same signal as the APD under evaluation.
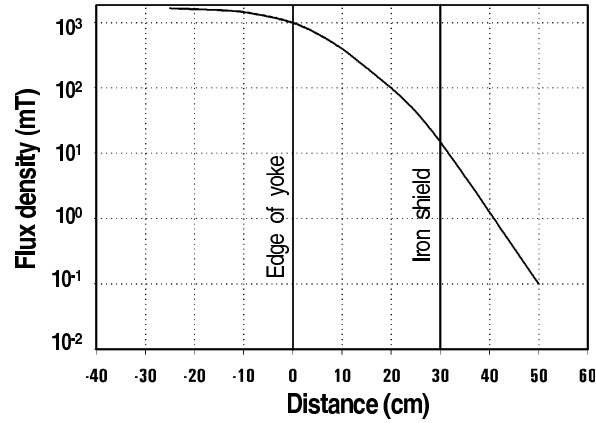
Figure 4.1: Calculated fringe magnetic field after the last beam bending magnet [Hab01].

device is the optimum detector for the next-generation in-beam tomograph.

In what concerns radiation hardness and small nuclear counter effect, these are needed due to the light particle flux that was measured to leave the patient downbeam [Gun04a, Gun04b]. Althought the flux is mainly forwardly peaked and no detectors are expected to be positioned within an angle of $\pm 20°$ in respect to the beam direction along the isocenter (chapter 3), the irradiation of large fields does bring the forwardly peaked light-particle flux in close proximity to the PET detectors. Therefore, radiation hard detectors with small nuclear counter effect are desirable.

Semiconductor photodetectors with internal amplification

The photograph in Fig. 4.2 compares the 8×4 pixel APDA S8550 from Hamamatsu with a PMT having typical dimensions of those used in commercial positron tomographs. In addition to the reduction in detector volume, the very small path of the charge carriers within each pixel of the APDA results in a detection efficiency, gain and timing characteristics insensitive to magnetic fields[1]. This makes a silicon-based APDA a good candidate detector for the next-generation in-beam PET.

The most commonly used semiconductor detector materials are silicon and germanium, with

Figure 4.2: Photograph showing a 4×8 pixels avalanche photodiode array (left), a 1 Euro coin (middle) and a photomultiplier tube with 1 inch front window (right).

---

[1] Measured up to 4 T with a single-pixel APD with similar internal structure [Org02].

one electron-hole pair (e-h) produced per 3.6 and 2.8 eV of radiation energy absorbed, respectively. This is a low value compared to the ionization energy in a gas (about 30 eV) or to the approximately 300 eV necessary to extract an electron from a photocathode. Due to the small energy required to produce an e-h pair, semiconductors present a high quantum efficiency of about 70 % for light with 400 nm wavelength, which contrasts with a quantum efficiency of the order of 25 % for PMT. Gallium arsenide (GaAs), with an ionization energy of 4.1 eV, is perhaps a future alternative to silicon; presently, it seems to be an expensive and not fully mastered technology of potentially better radiation hardness [Smi96]. Similar detectors have been manufactured with diamond (13 eV/e-h) too, yielding ultra-fast, extremely radiation hard and magnetic field insensitive detectors bringing great advantages into single-particle detection or beam monitoring applications [Ber01]. Concerning photon detection with diamond, though, a quantum efficiency below 10^{-4} % has been measured with a chemical vapor deposition (CVD) detector for photon energies corresponding to wavelengths between 300 and 1 200 nm [Pac00].

Semiconductor detectors have a number of problems that have limited their use in clinical practice in the past. For example, silicon and germanium conduct a significant amount of thermally induced electrical current at room temperature. Statistical oscillations in this background noise current interfere with the radiation-induced current pulses. Hence, these detectors are operated either at temperatures well below room temperature or under reverse polarization voltages high enough to produce electron multiplication within the detector, i.e. with internal gain. The principle of operation of a silicon semiconductor detector with internal amplification is shown in Fig. 4.3. The figure depicts a device optimized for the detection of short wavelength light
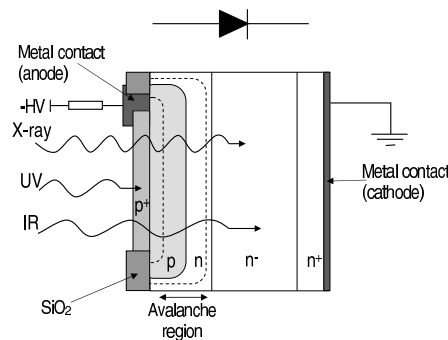
Figure 4.3: Schematic cross-section of one pixel of an APD. The high electric field at the p-n junction provides there enough energy to the drifting electrons to collide with other electrons and create more e-h pairs. This avalanche process, optimized for ultra violet photons in the figure, results in the internal gain of the APD.

(blue to ultra violet), i.e. a device where the p^+-doped layer, laying before the amplification region composed by the p-n junction, is made small [Wil83]. This reduces the sensitivity to light in the infra-red region of the spectrum as well as to the more penetrating X-rays since these photons interact with the detector at deeper depths, generating there electrons that will not cross the amplification region during their trajectory to the cathode (the diode is reversely polarized, i.e. a positive voltage is applied at the cathode). The generated holes will drift to the anode and pass the high electric field p-n junction, but they do not achieve enough velocity to induce multiplication. Short wavelength light will interact very close to the surface and all electrons generated there have to pass the amplification region on their way to the cathode, resulting in the creation of more e-h pairs (avalanche) that will be collected in the corresponding electrodes. One immediate advantage of such an APD optimized for short wavelength detection is that the resulting nuclear counter effect is heavily minimized: the extremely small

extension of the p$^+$-doped region, with typically less than 10 μm thickness [Dei00], results in a correspondingly small effective path for ionizing radiation. Minimum ionizing particles create about 100 e-h pairs per μm in silicon, but only those generated before the amplification region will be able to start an avalanche. The nuclear counter effect of an APD from Hamamatsu with very similar structure as the S8550 was measured to be as low as 5.6 μm[1].

Radiation damage can occur via two main mechanisms: surface and bulk damage. Surface damage results from defects in the front layer of the APD, increasing the surface dark current and reducing the quantum efficiency. The total dark current I_d in an APD is given by $I_d = I_{ds} + I_{db}M$, with M the internal gain of the APD and I_{ds} and I_{db} the surface and bulk dark currents, repectively. The effect of the surface dark current plays a minor role when compared to the bulk dark current, which suffers multiplication. Bulk damage results from displacements of atoms from their lattice sites along the bulk of the APD, increasing the bulk dark current and potentially changing the APD gain for a given bias voltage. Several APD from Hamamatsu with a pixel area of 5×5 mm^2 and with internal structure very similar to the individual pixels of the S8550 [Dei00] were irradiated with a fluence of 9×10^{12} protons per cm^2, corresponding to 2×10^{13} neutrons per cm^2 [Huh93]. After an annealing period of 6 weeks the gain had decreased by 3 %, the quantum efficiency at wavelengths smaller than 600 nm showed no remarkable differences and the dark current had increased from 2.5 to 3990 nA [Dei00]. The fluence delivered corresponds to approximately 10 years of operation of the APD at the electromagnetic calorimeter of one of the experiments (compact magnetic solenoid) of the extremely high-luminosity large hadron collider at CERN. For comparison, the mean number of carbon ions delivered at GSI to treat the first 240 patients was about 3×10^{12}. The integrated yield of light secondaries emitted in the forward semi-hemisphere, measured in [Gun04a], is about 1.7 particles per primary ^{12}C. These particles include neutrons, protons, deuterons, tritons and helium. This results in a total fluence of light particles emitted in the forward semi-hemisphere of about 5×10^{12}. For a treatment room irradiating 1000 patients per year the corresponding yearly fluence is $\leq 2 \times 10^{13}$ light secondaries emitted in the forward semi-hemisphere. Assuming the yield to be spatially homogeneous, a detector with 1×1 cm^2 area and positioned at a distance of 1 m in the beam direction, after the target, will receive a light-particle fluence of about 3×10^8 particles cm^{-2}. This fluence is four to five orders of magnitude below that used to test the radiation hardness of the APD from Hamamatsu, described in [Huh93]. Therefore, the use of the S8550 APDA for in-beam PET is safe in what concerns its radiation hardness.

4.3 Characterization of the LSO Sample

Due to the adequate properties of both LSO as a scintillator and an APDA as a light detector for in-beam PET, a piece of LSO bought from CTI was used to prepare 64 finger-like crystals, each with $2.1 \times 2.1 \times 15$ mm^3, in order to couple them to two APDA with 8×4 pixels each. Before fixing the crystals to the APDA their scintillating properties were investigated, namely their light yield and energy resolution, with the results shown in the present section.

4.3.1 Setup

Fig. 4.4 shows the electronics setup implemented to measure the scintillating properties of a sub-set of all 64 crystals, with the sub-set uniformly sampled in respect to the position of the crystals in the original bole. The light yield of the crystals was measured both in the vertical as well as in the horizontal position, i.e. with the 2.1×2.1 mm^2 and the 2.1×15 mm^2 crystal faces coupled to the window of a XP2020Q calibrated PMT from Philips Photonics,

---

[1] These APD were optimized by Hamamatsu in order to be used at the electromagnetic calorimeter of the future compact magnetic solenoid detector under construction at CERN [Dei00].
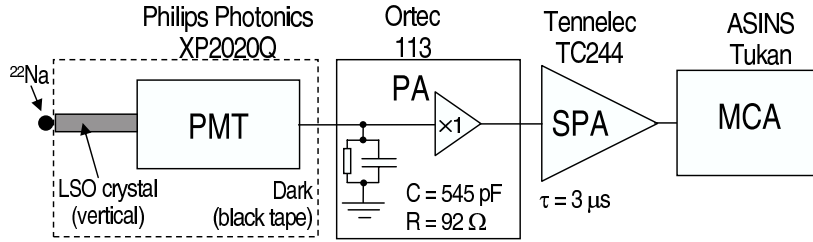
Figure 4.4: Electronics setup for characterizing the scintillation of the LSO crystals. PMT, PA, SPA and MCA denote a photomultiplier tube, a preamplifier, a spectroscopic amplifier and a multichannel analyzer, respectively.

respectively. Silicon oil was used as a coupling medium and the crystals were wrapped in several layers of teflon tape, except for the face touching the PMT. Crystal wrapping was done in a dark room in order not to induce afterglow in the scintillator. The PMT was operated at -1700 V and the signal from its anode was fed into a preamplifier (PA) model 113, from Ortec, connected with an input capacitor of 545 pF. A spectroscopic amplifier (SPA) TC244, from Tennelec, multiplied the PA signal by 1000 during the single photoelectron measurements and by 7.5 during the measurements with a ^{22}Na source. The shaping constant of the SPA was $3\,\mu$s during all measurements. Finally, the SPA signal was fed into the multichannel analyzer Tukan, from the Andrzej Soltan Institute of Nuclear Studies (ASINS) in Swierk, Poland.

4.3.2   Light yield and energy resolution

The peak position of the 511 keV γ-quanta from a ^{22}Na source (ch_{511}) was compared to the peak position of the single photoelectron spectrum (ch_{spe}) of the calibrated XP2020Q PMT
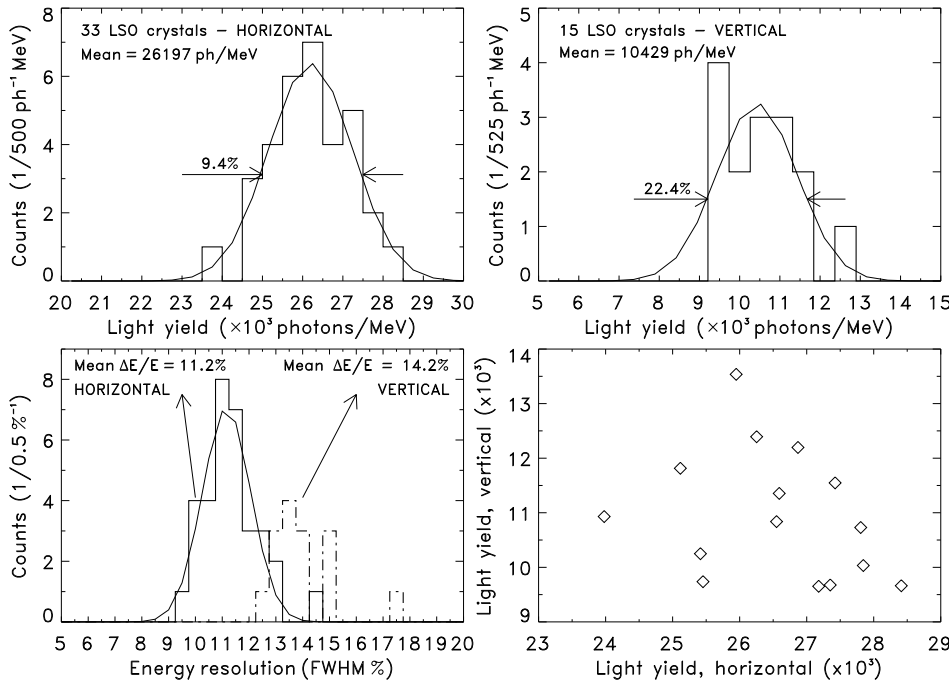
Figure 4.5: Light yield *L.Y.* and energy resolution of the LSO samples. The top row shows two histograms with the *L.Y.* of crystals measured in the horizontal and vertical positions (Fig. 4.4). The bottom left image shows the histograms with the energy resolutions obtained and the bottom right plot shows that there is no correlation between the *L.Y.* measured in the horizontal and vertical positions, which means the observed *L.Y.* dispersion is due to experimental error only.

from Philips Photonics. The light yield $L.Y.$ of each crystal, measured in photons per MeV, is calculated following

$$L.Y. = \frac{1}{\eta_{int}} \cdot \frac{1}{0.511} \cdot \frac{M_{spe}}{M_{511}} \cdot \frac{ch_{511}}{ch_{spe}}, \qquad (4.1)$$

with η_{int} being the integral quantum efficiency of the PMT with respect to the emission spectrum of LSO, with a value of 20 % [Kap00], $M_{spe} = 1000$ the gain of the spectroscopic amplifier when measuring the single photoelectron spectrum and $M_{511} = 7.5$ the gain of the amplifier when measuring the spectrum with the ^{22}Na source. Fig. 4.5 shows the results obtained with the crystals in the horizontal and vertical positions, i.e. parallel to the PMT window and perpendicular to it (Fig. 4.4), respectively. The lower light yield measured with the crystals in the vertical position was expected and is due to the longer path of the scintillation photons in the crystal before reaching the PMT window. A longer path results in a higher number of re-absorbed scintillation photons due to the incomplete transparency of LSO to its own produced light. The higher number of reflections necessary in the vertical position also plays a role in justifying the lower light yield. As a consequence of a lower light yield, the mean energy resolution measured with the crystals in the vertical position (14.2 %) also deteriorates in respect to the horizontal position (11.2 %). In order to investigate whether the light yield non-uniformity of 22.4 % FWHM in the vertical position, and 9.4 % FWHM in the horizontal, arises due to experimental deviations or from a bias in the original LSO bole, the light yields in the horizontal and vertical positions are plotted against each other in Fig. 4.5. No correlation is observed, meaning that the light yield dispersion must arise from experimental error and, more importantly, all LSO crystals present similar scintillation characteristics and could, therefore, be used for the construction of the two LSO/APDA detectors.

4.4 Characterization of the APD-Array

Before coupling the LSO crystals onto the pixels of the two APDA, the properties of the APDA were studied and optimized, namely the dependence and stability of its gain with the applied reverse voltage, the shaping at the amplifier that minimizes noise readout, the ratio of light to X-ray amplification at different internal gains, the number of primary e-h pairs generated with the light from the given crystals, the energy and time resolution achievable with a ^{22}Na source, and the crosstalk between adjacent pixels with electronic and light-sharing origins.

4.4.1 Setup for DC and pulse-mode readout

The S8550 was operated in a closed, grounded metal box and the readout electronics depicted in Fig. 4.6 was implemented. Inverse polarization of the diodes was achieved with the anode
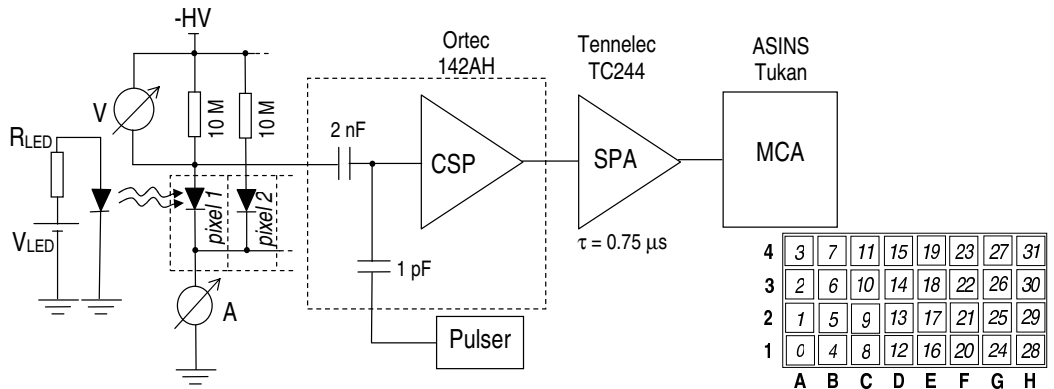
Figure 4.6: Electronics setup used for the characterization of the S8550 APDA in current and pulse modes. CSP, SPA and MCA denote a charge sensitive preamplifier, a spectroscopic amplifier and a multichannel analyzer, respectively. A front view of the APDA is shown at the bottom-right, together with the two pixel numbering schemes used: from A1 to H4 or from 0 to 31.

of each pixel connected through a resistor to the high voltage, and all cathodes connected to common ground. For the DC-gain characterization a blue LED illuminated the APD, with the current from the individual anodes read with a voltmeter at the extremes of the polarizing resistor. The current at the common cathode was read with an ampere-meter of negligible internal resistance. For pulsed light, X-ray and scintillation detection, the voltmeter and ampere-meter were substituted by the electronics depicted to the right of the 2 nF capacitor in Fig. 4.6, namely, a charge sensitive preamplifier 142AH from Ortec, compatible with detector capacities from of 0 to 100 pF [Ort05], a high precision pulser PB-5 from Berkeley Nucleonics Corp. (BNC), a spectroscopic amplifier TC244 from Tennelec and a Tukan MCA from ASINS.

4.4.2 Gain characterization

For each pixel, the dark current dependence on the applied high voltage was measured with a 10 MΩ voltmeter that read the voltage drop at the polarizing resistor. The gain curve was measured similarly, with a blue light emitting diode (LED) illuminating the APDA surface in DC mode and the signal current I_{signal} calculated according to

$$I_{signal} = I_{total} - I_{dark}, \tag{4.2}$$

with I_{total} being the total current measured with the LED turned on, and I_{dark} the current measured with the LED turned off. Two types of illumination conditions were studied: single-pixel illumination and homogeneous illumination of all pixels.

Single-pixel illumination

In order to guarantee the illumination of one single pixel only, a 0.5×0.5 mm^2 hole was made in a black tape stripe that covered the whole APDA. The hole was matched to the center of one pixel, with active area 1.6×1.6 mm^2. A scan was performed with the applied high voltage and both I_{total} and I_{dark} were measured. The results from this scan are plotted in Fig. 4.7. Two regimes are clearly observed. In regime I, the e-h cloud produced by the penetrating photons is not totally collected in the corresponding cathode or anode, respectively. This is
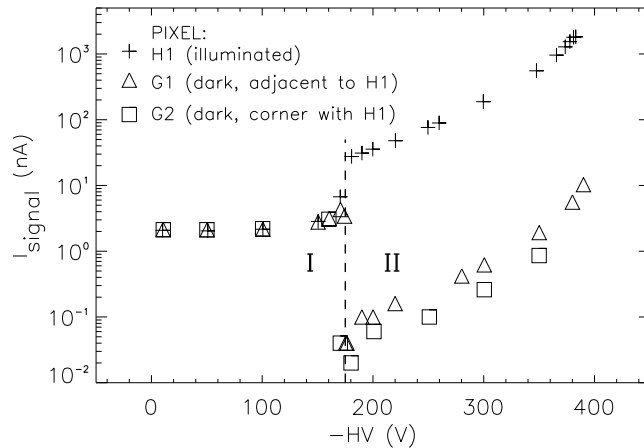
Figure 4.7: Dependence of I_{signal} on the applied voltage. In region I, before the pinch-off voltage is reached (vertical dashed line), dispersion of the e-h clouds takes place with consequent signal spread into adjacent, dark pixels. When the applied voltage is high enough to force the electric field lines to converge into the corresponding electrode only, region II is reached. There, the e-h clouds are forced to drift to the collecting electrodes and the crosstalk current drops abruptly to values below 1 %. The multiplication regime takes place at higher voltages.

because the electric field lines produced by the low applied voltage are strong enough to avoid e-h recombination and start the drift, but are insufficiently strong to hold each cloud together. Repulsion disperses the formed clouds, and the hole (h) cloud which should be collected at one single pixel (anode) will spread to adjacent dark channels. A sharp step in the signal of the illuminated pixel is observed at a polarization voltage of about 173 V, which corresponds to the transition to a second regime where the pixels are individualized. The physical phenomenon behind this fact is the convergence of the electric field lines to each pixel readout region, i.e. the applied voltage has reached a value strong enough to hold the hole cloud drifting together without losses. This interpretation is confirmed by the sharp decrease of the current of adjacent dark channels (electronic crosstalk) at exactly the same voltage (Fig. 4.7). As expected, this transition voltage is not a fixed number, even for a certain pixel, and it was observed to vary slightly with the illumination conditions (next paragraph).

Homogeneous APDA illumination

With the aim of finding a reference point to normalize the output current signal and, therefore, obtain the gain evolution with the applied voltage, the current output of one pixel having the LED homogeneously illuminating the APDA surface was measured, with the result plotted in Fig. 4.8. The two different regimes described in the previous paragraph can be observed, now
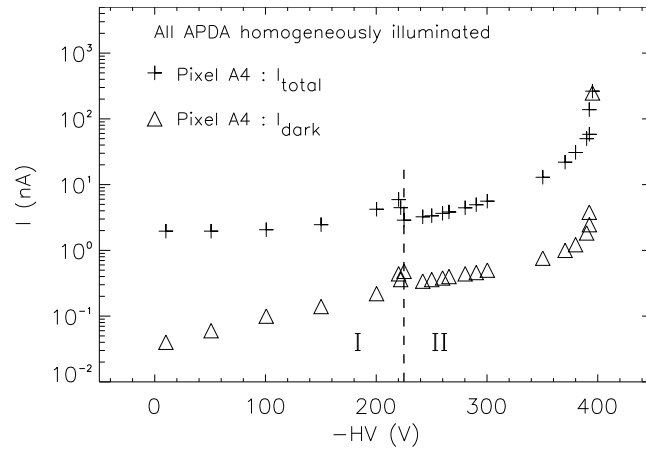
Figure 4.8: Dependence of I_{total} and I_{dark}, from a single pixel, on the applied voltage. All the APDA was homogeneously exposed to light in DC mode. Regimes I and II as in Fig. 4.7.

characterized by a sharp fall of both the total current and the dark current. This phenomenon can again be explained based on a *pixel decoupling* dependence on the applied voltage. Below the pinch-off voltage, about 210 V in this pixel, a continuous e-h cloud is created along the whole surface of the APDA, even between pixels, and the holes are being collected in the corresponding anodes. After pixelization at 210 V, the contribution from the dead areas between pixels ceases since the electric field lines, now fully connecting the anode to the cathode, do not allow signal collection from these regions. The fact that the dark current also feels this transition further confirms the described interpretation.

Gain normalization

As shown in Figs. 4.7 and 4.8, the evolution of the signal amplitude with the applied voltage strongly depends on the illumination conditions if the signal is read from the individual anodes. In oder to find a reference point with unitary gain in DC mode illumination, the current signal from all diodes was read. An ampere-meter with negligible internal resistance measured
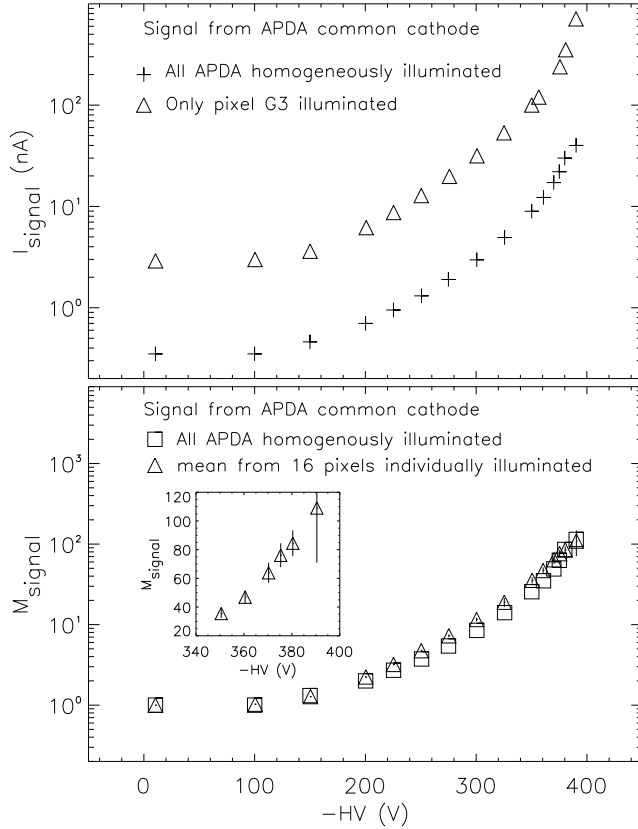
Figure 4.9: Common cathode measurements for gain normalization. The evolution of the current signal is independent on the illuminating condition (top). The different offsets (top) are due to different light intensities. The current signal yields a stable reference point for normalization of the gain (bottom). Error bars depict $\pm \sigma$ at each measured gain for the curve with the mean from 16 single-pixel measurements.

the current flowing between the common cathode of the APDA and ground (Fig. 4.6), thus eliminating the contribution from electronic crosstalk since the current contribution from all pixels is read at the same time. The top image in Fig. 4.9 depicts the obtained results. No regime change is observed, neither with single-pixel nor with full APDA illumination, since at any applied voltage all the cloud (in this case the electron cloud) is read, either from several pixels (before pixelization) or from one individualized pixel (after pixelization). Therefore, the initial flat plateau of both curves can be safely taken as a reference point with unity gain, yielding the gain curves depicted in the bottom image of Fig. 4.9. A measurement of the gain characteristics of several individual pixels resulted in a gain distribution about the mean value with $\sigma = 5$ at $M = 50$, or a σ of about 10 at $M = 80$, as highlighted in the inset.

Gain non-uniformity

In order to check the gain non-uniformity of the APDA from pixel to pixel, several spectra were acquired with a ^{55}Fe source and with the same reverse voltage. Fig. 4.10 shows results for two pixels. The standard deviation of the gain non-uniformity was found to be 4.3 % with the APDA operating at an internal gain of 61 (reverse voltage of -370.4 V).

Effective applied voltage

A 10 MΩ load resistor (Fig. 4.6) was applied to each pixel in order to keep the dark current low and, thus, increase the signal-to-noise ratio (SNR). Yet, a high load at the polarizing resistor may induce a voltage drop which can be significant if high dark currents take place or even
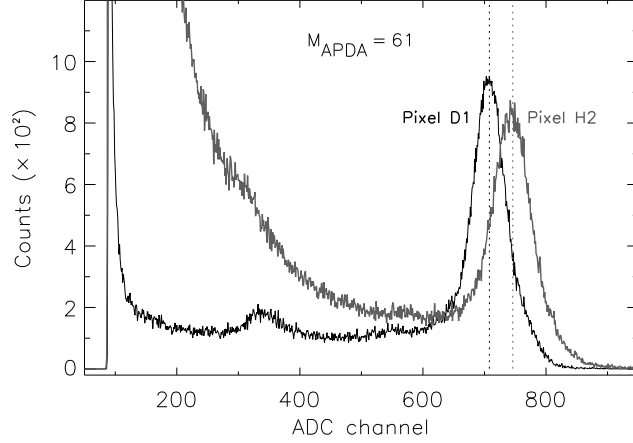
Figure 4.10: Gain non-uniformity measured between two pixels with an ^{55}Fe source. A different noise behaviour was also observed.
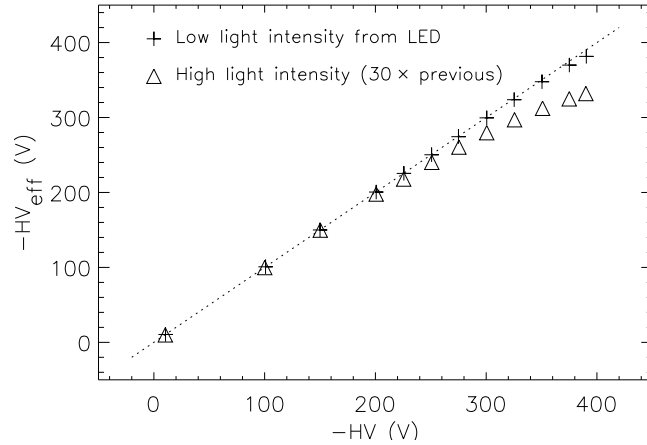
Figure 4.11: Effective voltage HV_{eff} at the APDA due to the polarizing resistor (10 MΩ), with $HV_{eff} = HV \text{-} V$ (Fig. 4.6). The light intensity was adjusted by changing V_{LED} in Fig. 4.6.

if high signal currents are being measured. Such voltage drop at the polarizing resistor would result in a lower effective polarizing voltage at the diodes inducing, consequently, lower gain. Fig 4.11 confirms that the effective applied voltage does not decrease significantly for the range of voltages and dark currents studied. It also shows how a too high photon luminosity would reduce the effective applied voltage at the APDA, with a consequent non-quantified decrease in gain. For the measurement of scintillation light pulses, described in the next section, the conditions are met for stable operation since the LED provided much higher luminosity than the very weak scintillation or X-ray pulses.

4.4.3 Scintillation and X-ray detection

The APDA gain characterization presented in the previous section is also valid in pulse mode readout and is the basis for the gain knowledge of the device. In the present section the remaining performance characteristics of the APDA for scintillation detection are presented. Whenever LED light is mentioned in this section it refers to pulsed blue light, i.e. the fixed voltage supply feeding the LED in DC mode in Fig. 4.6 (V_{LED}) was substituted with a precision pulser PB-5 from BNC, yielding pulses of light instead. Whenever pulser is mentioned it refers to the known amount of charge injected directly into the electronics readout ($Q_{inj} = U_{pulser} \cdot C_{test}$) through the 1 pF test capacitor of the preamplifier (Fig. 4.6).

Noise optimization

Figs. 4.12 and 4.13 show the results obtained by scanning the amplifier shaping time τ_{AMP} at a constant reverse voltage applied, and by scanning the applied reverse voltage with a constant amplifier shaping time, respectively. Noise is quantified in units of photon energy (FWHM, eV) as well as by the equivalent noise charge[1] (ENC) at the detector level (electrons, root mean square). The difference between the normalization to the X-ray gain or to the light gain is explained in the next paragraph. Measurements above an internal gain of about 73 (Fig. 4.13) were not possible because the APDA reached breakdown, with the dark current rising steeply.
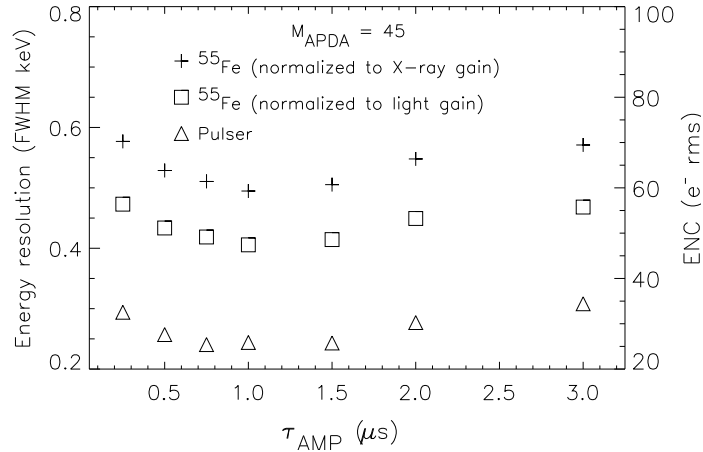
Figure 4.12: Noise dependence on the amplifier shaping time. The noise is quantified in units of photon energy (FWHM in keV, left ordinate), as well as by the equivalent noise charge (ENC) of the detector (number of electrons in root mean square, right ordinate).
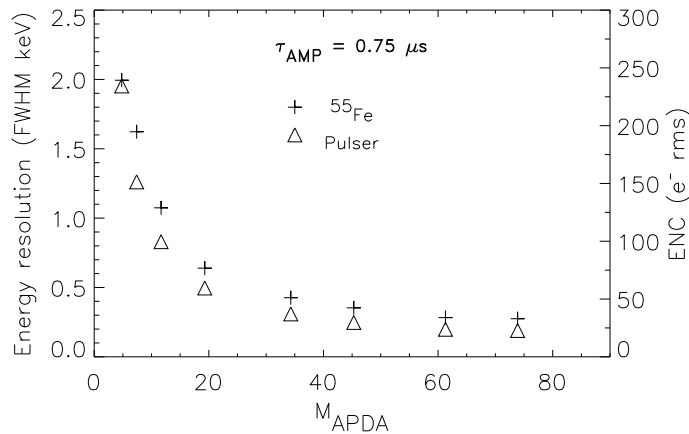
Figure 4.13: Noise dependence on the internal gain of the APDA. The noise is quantified in units of photon energy (FWHM in keV, left ordinate), as well as by the equivalent noise charge (ENC) of the detector (number of electrons in root mean square, right ordinate).

Ratio of the X-ray gain versus light gain and energy calibration

Due to its internal structure and the position of the p-n junction, optimized for the detection of light of short wavelength (Fig. 4.3), the S8550 presents different internal gains for pulsed

---

[1] Equivalent noise charge ENC is the quantity of charge which, appearing on the detector, would give an output pulse height with equivalent voltage measured in units of root mean square. For silicon-based detectors, ENC = FWHM (eV) / [2.35 × 3.6 (e-h eV^{-1})].

light and X-rays, with this difference increasing with the applied voltage due to the increasing extension of the avalanche region. In order to perform a precise energy calibration, the 59.5 keV X-ray peak of a ^{241}Am source was sampled with a PIN photodiode[1], together with a pulse of charge injected at the preamplifier test capacitor (Fig. 4.6). This allowed to calculate the equivalent energy delivered by the pulser [Mos01]. The gain curve obtained in the previous section (DC mode, Fig. 4.9, bottom) was then used to recalculate the pulser equivalent energies at all applied reverse voltages according to

$$ E_{pulser,\,M} = \frac{peak_{pulser,\,PIN}}{peak_{Am,\,PIN}} \cdot 59.5 \, keV \cdot M_{pulser} \cdot \frac{G_{APDA}}{G_{PIN}} \cdot \frac{1}{M_{APDA}}, \qquad (4.3) $$

with $E_{pulser,\,M}$ the pulser equivalent energy at a device internal gain M_{APDA}. The terms $peak_{pulser,PIN}$ and $peak_{Am,PIN}$ denote the peak positions of the pulser and the X-ray line from the ^{241}Am source measured with the PIN diode, respectively. The term M_{pulser} denotes the amplitude increased at the pulser when measuring with higher reverse voltages, and G_{APDA} and G_{PIN} are the gains set at the amplifier when measuring with the APDA and with the PIN diode, respectively. Fig. 4.14 shows the spectrum obtained with a ^{55}Fe source with the APDA operated at an internal gain of 45. The energy calibration used the method just described.
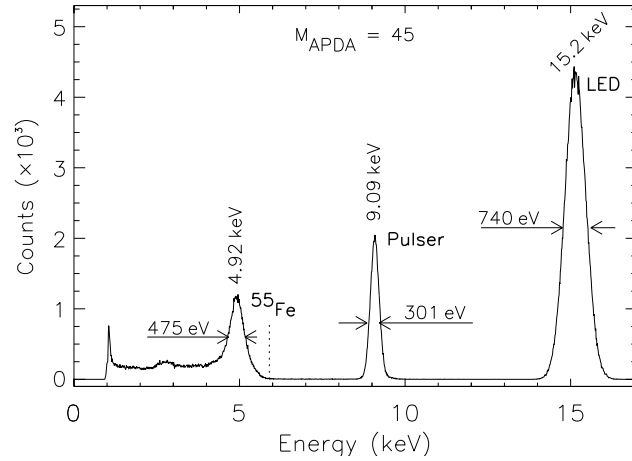
Figure 4.14: Spectrum acquired from a single APDA pixel exposed to a ^{55}Fe source, the light from a pulsed LED and a test pulser. The different APDA gain for X-ray and visible light is responsible for the shift to lower energy of the 5.9 keV X-ray peak.

Similar spectra acquired at different APDA internal gains show the light-to-pulser ratio constant, whereas the X-ray peaks shift increasingly to smaller amplitudes. This behaviour is summarized in Fig. 4.15 for different APDA gains. It has its origin on the deeper penetration depth of X-rays into the diode, creating e-h clouds already inside the avalanche region (Fig. 4.3). These electrons create a smaller signal in respect to those raised before the avalanche region as a consequence of their shorter path through the multiplication region.

A simpler and faster calibration method, but less precise due to the intrinsic inaccuracy of the value of the test capacitor of the preamplifier, makes direct use of the amount of charge Q_{inj} injected at the test capacitor: $Q_{inj} = U_{pulser} \cdot C_{test}$, with U_{pulser} the amplitude of the signal delivered by the pulser[2] and C_{test} the preamplifier test capacitor. In order to convert the injected charge into units of energy, the mean energy necessary to create an e-h pair in

---

[1] Photodiode fabricated with a longer, low-doped, high-resistivity intrinsic (I) region between the p-doped (P) and the n-doped (N) regions. The extended intrinsic region yields $M_{PIN}(\text{light}) = M_{PIN}(\text{X-ray}) = 1$.

[2] This signal must have a fast rise time t_r and long fall time t_f, approaching a step function from the point of view of the test capacitor. Typically $t_r \leq 10$ ns and t_f is of the order of 100 μs.
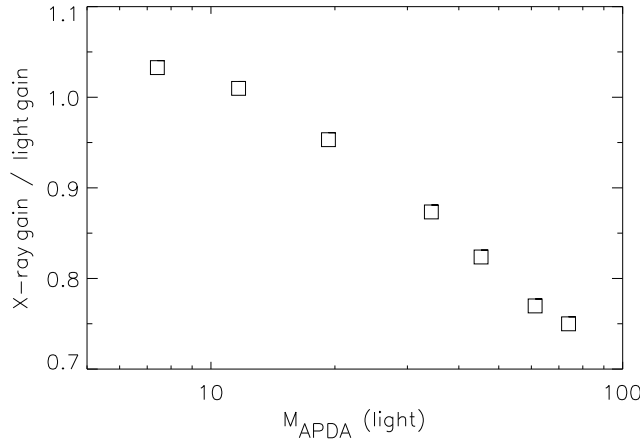
Figure 4.15: Ratio between X-ray and light gain $R_{X,light}$ for different APDA gains M_{APDA}.

silicon, 3.6 eV, is used. This method does not dependent on the gain of the device:

$$E_{pulser,M} = \frac{U_{pulser} \cdot C_{test}}{1.6 \cdot 10^{-19} \text{ C}} \cdot 3.6 \text{ eV}. \tag{4.4}$$

Number of primary electron-hole pairs and energy resolution

The value of the ratio *X-ray-to-light-gain* ($R_{X,light}$) described above is necessary in order to calculate the number of primary e-h pairs N_{e-h} generated in the APDA at a given internal gain with a given scintillation crystal. This parameter, in turn, is important in order to compare the performance of different semiconductor-based scintillation detectors since the number of primary e-h produced per energy unit is proportional both to the energy as well as the timing resolutions achievable with the device. Fig. 4.16 shows this measurement for one pixel of the S8550 APDA. The gain of the spectroscopic amplifier in both measurements was kept at a constant value of 200, therefore a value of 4900 e-h / MeV is obtained by applying:

$$N_{e-h}/\text{MeV} = \frac{5900 \text{ eV}}{3.6 \text{ eV}} \cdot \frac{peak_{22-Na}}{peak_{55-Fe}} \cdot R_{X,light} \cdot \frac{1}{0.511 \text{ MeV}}, \tag{4.5}$$

with 5900 eV being the energy of the X-ray from the ^{55}Fe source.
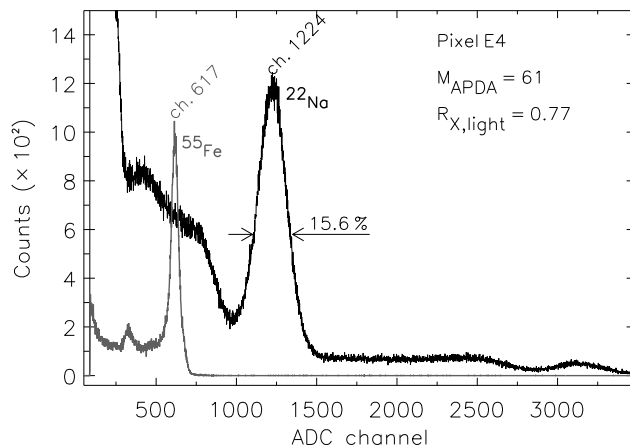
Figure 4.16: Single pixel spectra acquired with a ^{55}Fe and a ^{22}Na source, with the ^{22}Na γ-rays detected after conversion in a $2 \times 2 \times 10$ mm^3 LSO crystal mounted in the vertical position. The reverse voltage applied to the APDA corresponds to an internal amplification $M_{APDA} = 61$, to which corresponds an X-ray-to-light-gain ratio $R_{X,light} = 0.77$.

The same value can again be calculated by injecting a known amount of charge at the test capacitor of the preamplifier:

$$N_{e-h}/\text{MeV} = \frac{U_{pulser} \cdot C_{test}}{1.6 \cdot 10^{-19}\,\text{C}} \cdot \frac{peak_{22-Na}}{peak_{pulser}} \cdot \frac{1}{M_{APDA}} \cdot \frac{1}{0.511\,\text{MeV}}. \tag{4.6}$$

Although the value obtained for N_{e-h}/MeV with the S8550 is inferior to that of other devices from other manufacturers, such as the $8900\,\text{e-h/MeV}$ measured with the same crystal with a quadrant pixel APDA from Advanced Photonix Inc. [Kap02], the device from Hamamatsu offers the advantages of being readily available even if higher quantities are requested, easy to handle due to its expoxy resin covering the front surface (windowless) and being fabricated with technology specially developed to reduce the effects of hadronic radiation.

As expected, the energy resolution measured with an APDA is worse in respect to that obtained with a PMT, even for crystals of shorter length (Fig. 4.16 versus Fig. 4.5).

Inter-pixel crosstalk

Fig. 4.17 plots the signal crosstalk measured in DC mode at different reverse voltages for one pixel (left), and measured at a device gain of 61 for a single pixel illuminated in pulse mode. The illumination conditions in both cases were described at the begining of this section: a black tape stripe covered the whole APDA front surface except for the illuminated pixel, which was exposed to light through a hole in the tape with 0.5×0.5 mm^2 adjusted to its center. While the crosstalk between adjacent pixels is seen to be below 1 % in DC mode at all voltages above pinch-off (Fig. 4.17, left), the same value increases to about 5.7 % when pulses of light
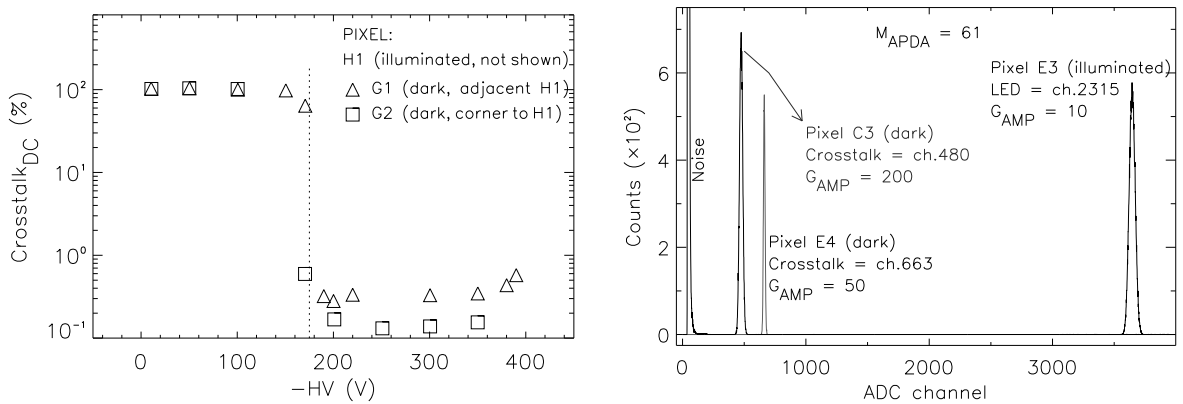
Figure 4.17: Electronic and light crosstalk in DC (left) and pulse (right) modes, measured by illuminating one pixel and reading the signal in the neighboring, dark ones.

Figure 4.18: Crosstalk values, in percent, with pixel E3 illuminated in pulse mode. The difference observed between pixels E2 and E4 lies on the two different APDA grounds, one connecting the two upper (3 and 4) and the other the two lower (1 and 2) rows of pixels.

are detected by the illuminated pixel at a device gain of 61 (Fig. 4.17, right, pixel E3 versus E4). An inter-pixel crosstalk of about 1 % is observed in Fig. 4.17, right, for non-adjacent pixels separated by one intermediate pixel (pixel E3 versus C3). Fig. 4.18 summarizes the crosstalk measurements with pixel E3 illuminated in pulse mode.

The asymmetry between the crosstalk values in DC and pulse mode was observed for other pixels as well and proves that the crosstalk measured in pulse mode is not due to light-sharing, since the illumination geometry was the same in both modes, but due to electronic crosstalk arising from the diode junction capacity and its ability to pick up a signal from current pulses propagating in its vicinity. Transient signal crosstalk induction was studied theoretically and observed experimentally in [Cre98] for charge carriers drifting in liquid xenon under an electric field, for example.

4.5   The Two LSO/APD-Array Detectors

The properties of the scintillator samples and the scintillation detector studied individually in sections 4.3 and 4.4 indicate that a low-noise signal readout electronics is required per pixel. In this section the steps taken in order to assemble the LSO/APDA detectors with minimum signal loss, both at the light collecting level due to loss of scintillation photons as well as at the signal processing due to the introduction of electronics noise, are presented.

4.5.1   Detector assembly

In Fig. 4.19 the assembly of the LSO single crystals onto the pixels of the S8550 is shown. Each pixel had all faces but one wrapped in teflon tape with $75\,\mu$m thickness, with the non-covered face fixed with silicon glue to each pixel of the APDA. The photographs in Fig. 4.19 show the crystals before covering their top surface with teflon tape.
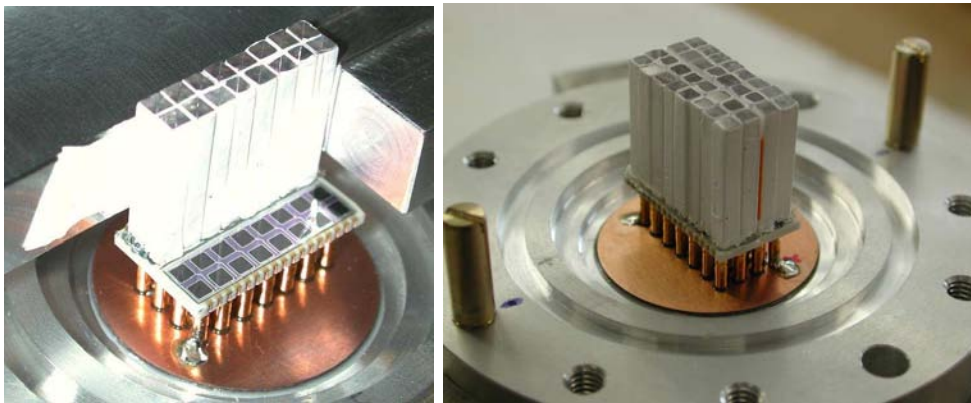
Figure 4.19: Assembly of the LSO single crystals onto the pixels of the S8550. The APDA pins are connected to a circular copper disk, seen below the device, with a diameter of 26 mm.

Silicon glue was used to fix the LSO crystals to the APDA after a seven days test that compared the light collected with glue and with high viscosity silicon oils up to a viscosity factor of 2 million. During the first day the oil creeps along the teflon tape and makes it transparent to light, resulting in a decrease in light collection of 2.5 % measured after 12 hours, together with a decrease in energy resolution of 1.9 % measured with an XP2020Q PMT and with a $2.1 \times 2.1 \times 15\,\mathrm{mm}^3$ crystal coupled to it in the vertical position. This effect does not take place if silicon glue is used since it solidifies in less than one hour. Furthermore, by using glue, crystal displacements during detector handling at a later stage are avoided.

4.5.2   Energy and timing signal splitting at the preamplifier

The LSO/APDA detectors were later covered with an aluminum box, shown in the left photograph of Fig. 4.20, that guaranteed complete darkness at the detector level. Also shown in both photographs are the ventilated aluminum boxes containing the 32 charge sensitive preamplifiers (CSP) that read each detector pixel individually. The CSP were developed at ASINS, in Swierk, Poland, for these specific detectors [Kap04]. Each CSP provides two outputs: a fast, negative-shape signal for timing applications and a slow, positive-shape signal for energy readout (Fig. 4.21). This splitting simplifies the electronics for signal processing at this study stage with two detectors only. It obviously does not provide a final solution if these detectors should be applied in a real tomograph with thousands of readout channels. The decision for signal splitting was based on the advantages of implementing an optimum, but slow, noise-
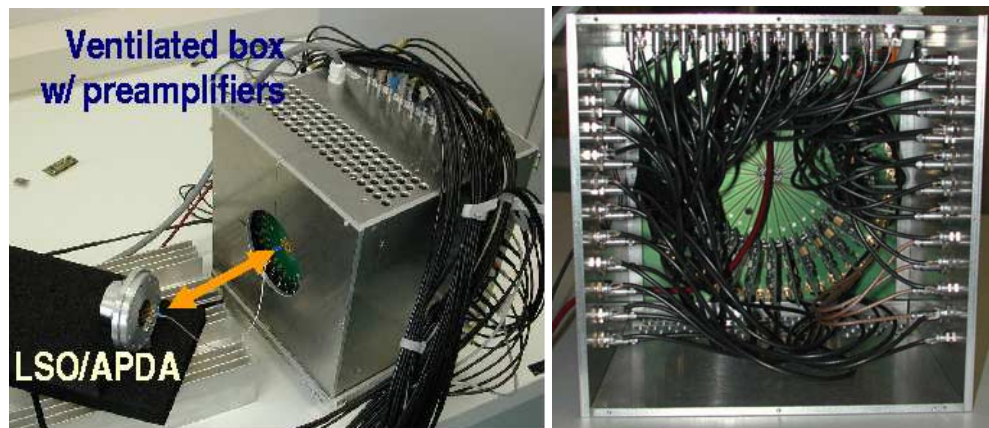
Figure 4.20: Front and back views of one detector head. The LSO/APDA detector (left) is enclosed in a light-proof, aluminum box. The detector connects to a motherboard containing 32 charge sensitive preamplifiers (CSP) through its back pins (arrow). The right photograph shows the back of the CSP box without the cover and the ventilator.
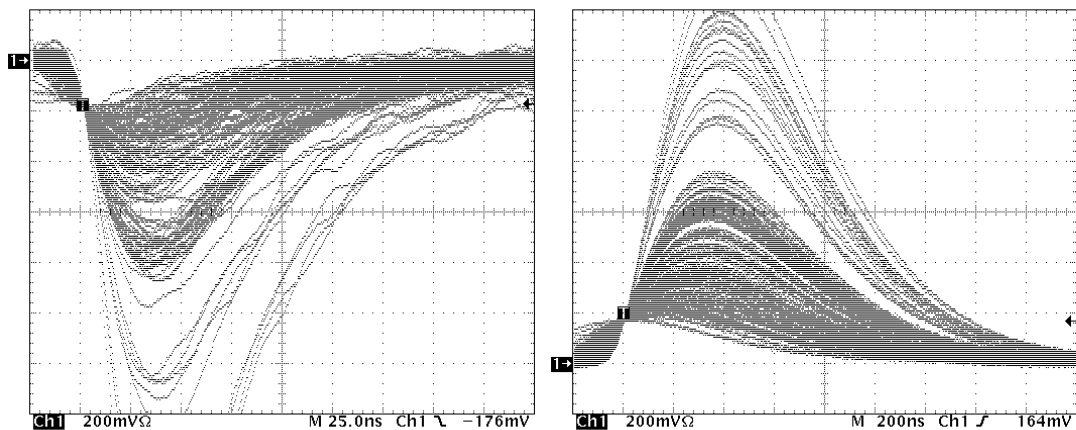
Figure 4.21: Fast (left) and slow (right) outputs from one pixel with a ^{22}Na source irradiating the whole detector. Several signals are superimposed, allowing the lines corresponding to the interaction of a 511 keV photon to be seen. The fast output was sampled after the preamplifier and a DC amplifier with gain 10. The slow output was sampled after the preamplifier and an amplifier with 0.5 μs shaping constant and gain $\geq$ 10. Both signals were read with a 50 Ω input resistance at the scope.
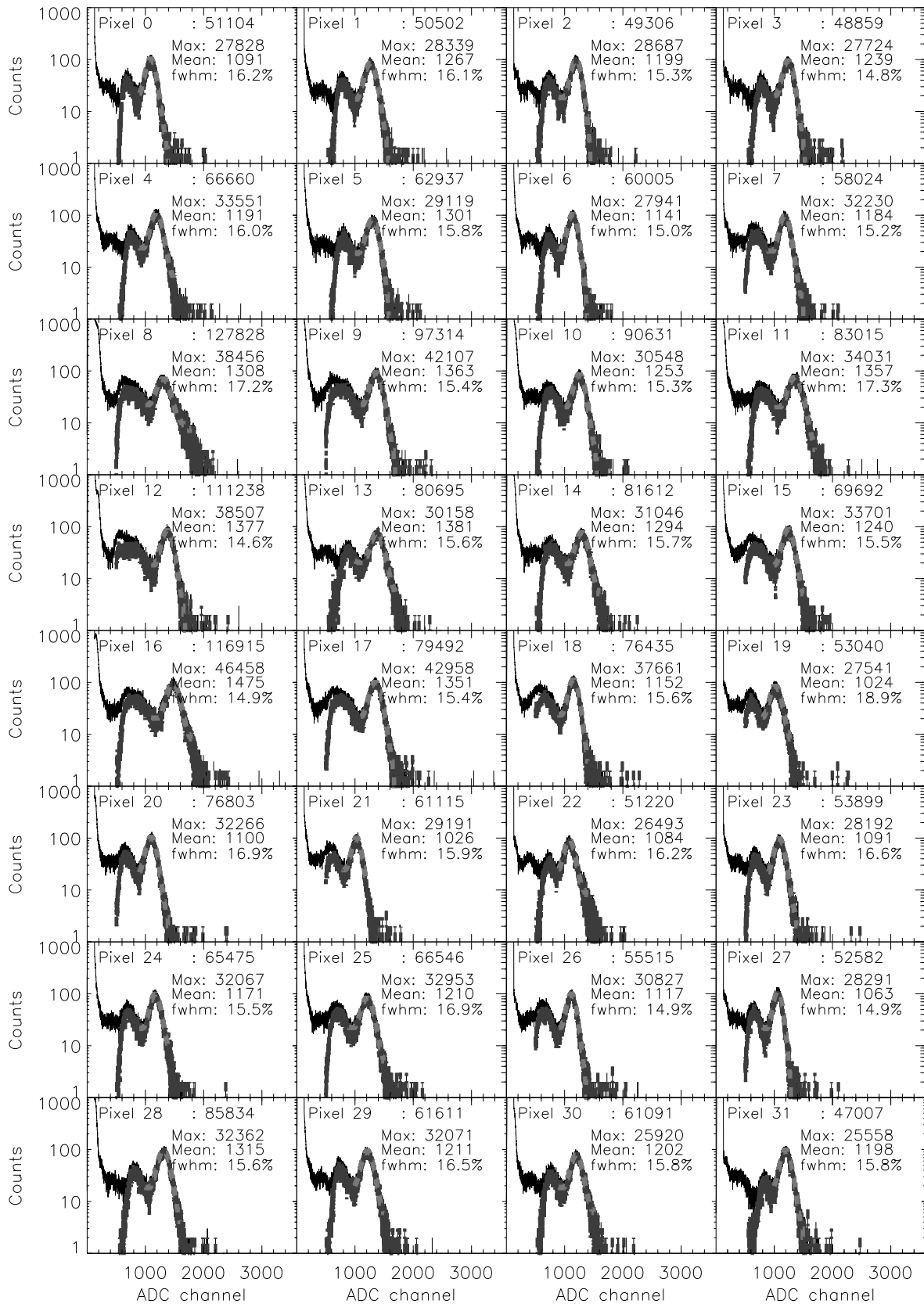
Figure 4.22: Energy calibration of detector 1 with a ^{68}Ge line source. Shown for each pixel: total counts above channel 128 (i.e. above noise), number of counts where a maximum energy deposition took place in that pixel, mean of the fit to the 511 keV full-energy peak and the corresponding FWHM. A low energy threshold was set between ADC channels 500 and 600, corresponding to about 250 keV. The gray line plots the spectrum with maximum events only.

reduction shaping constant at the energy signal, seen in section 4.4, together with a fast, but noisier, timing output optimized for the fast decay time of LSO.

4.6 Imaging Properties of the LSO/APD-Array Detectors

In this section the detector properties influencing the imaging performance of the two detectors are described. These are important parameters later used for image quantification in the following chapters 5 and 6. The electronics chain implemented to operate the two detectors in coincidence is detailed in section 5.2. In section 6.3 this electronics chain is further enhanced in order to allow the suppression of random events during in-beam PET measurements. Finally, appendix B describes the data acquisition system implemented for event readout. The results presented in this section concern measurements made with radioactive sources only.

4.6.1 Energy and time resolution

The mean energy resolution obtained both with a ^{68}Ge line source and a ^{22}Na point source for the 64 channels is $15.5 \pm 0.4\,\%$ FWHM. Fig. 4.22 shows the energy spectra of one detector obtained with a line source of ^{68}Ge scanned in the mid-plane between the detectors, with these operated in coincidence. The measured coincidence time resolution is $6.2 \pm 0.2\,$ns FWHM, slightly worse than the $3.0 \pm 0.2\,$ns FWHM extrapolated from a measurement against BaF$_2$ and obtained for one single pixel in [Kap03]. The slightly worse time performance was expected and arises from two factors: the longer LSO crystals used, 15 mm versus 10 mm in [Kap03], respectively, and, more importantly, the increased number of channels in these measurements which introduce a higher time spread at the electronics level.

4.6.2 Scanned line source measurements and image fill factor

For image reconstruction as well as to check the stability of the detectors the individual detection efficiency of the lines-of-response (LOR) between all detector crystals has to be known. In order to measure this, a ^{68}Ge line source has been moved centrally between the detectors in steps of 0.5 mm. Fig. 4.23 shows the results from two measurements performed at stabilized temperature, at different days and in different rooms. Stable results with identical profiles were obtained, together with similar standard deviations of the number of counts per LOR. The different mean numbers of counts per LOR obtained between the top and bottom results in Fig. 4.23 is expected due to two factors: the setups had different coincidence solid angles, with the distance between the detectors being 212 mm and 112 mm, respectively, and the acquisition times differed from 5 min/step versus 2 min/step, respectively. From this, a ratio of the mean counts per LOR can be predicted:

$$\frac{N_{212}}{N_{112}} = \frac{5\,min/(212\,mm)^2}{2\,min/(112\,mm)^2} = 0.698\,. \tag{4.7}$$

N_{212} and N_{112} denote the mean number of counts for scans with the detectors 212 mm and 112 mm apart, respectively (Fig. 4.23). The measured versus expected ratios agree to about 4 % if the measured numbers of counts are properly corrected against the acquisition dead time. This is necessary since during the measurements the dead time of the acquisition system decreases as one moves the source from the centre of the field-of-view (FOV) to the edges.

The images in the left column of Fig. 4.23 contain the solid angle dependence of each voxel in the image central plane, weighted by the different efficiencies of each LOR intersecting it, i.e. they are the basis for normalization of all further images backprojected into the central plane. These images allow to quantify the intensity of any mid-plane image in absolute terms, provided that
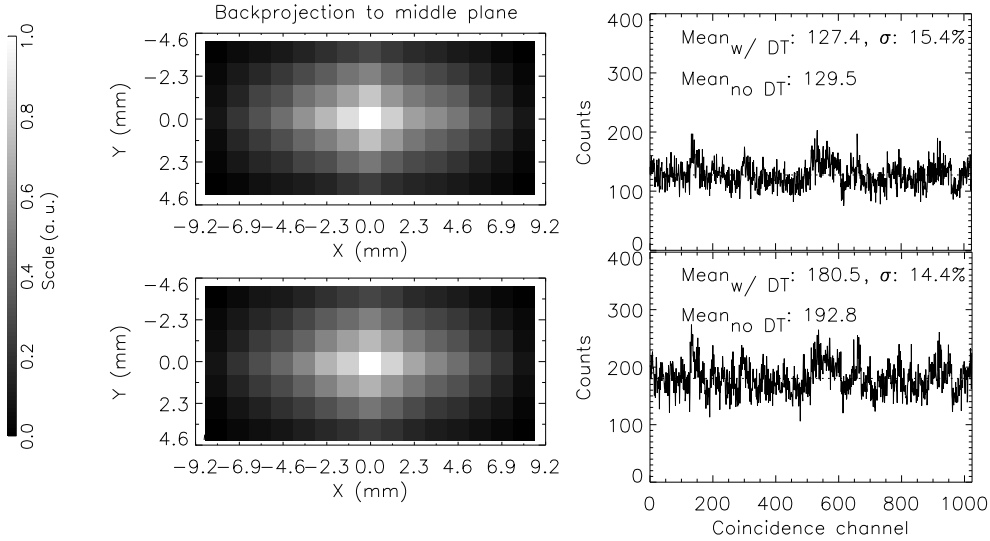
Figure 4.23: Results of the scanned line source measurements. The top row corresponds to a distance of 212 mm between the detectors, with 5 minutes acquisition/step, whereas the distance in the bottom row was 112 mm, with 2 minutes acquisition/step. Each coincidence channel (LOR) contains the number of events with energies within the photopeaks (FWHM) in both hit crystals. $Mean_{w/DT}$ and $Mean_{no\,DT}$ are the mean number of counts with and without dead time influence, respectively. The X and Y axes define the mid-plane between the detectors.

it was acquired with the same detector geometry and that the coincidence detection efficiency of the central voxel is known (section 4.6.3). For that, a multiplicative factor named image fill factor Π must also be known:

$$\Pi = \frac{\sum_{i,j}^{N_x,N_y} \cdot \Omega_{i,j}}{\sum_{i,j}^{N_x,N_y}}, \tag{4.8}$$

with N_x and N_y the number of image voxels in the X and Y directions, respectively, and $\Omega_{i,j}$ the solid angle of image voxel {i,j}. This image fill factor quantifies the mean difference between all image voxels shown in Fig. 4.23 and unity, with unity verified at the very central voxel (100 % relative intensity). Its value, used for image quantification in chapters 5 and 6, was calculated from Eq. 4.8 to be 30.5 % for the mid-plane images of Fig. 4.23. A similar procedure was applied to any other backprojection onto another plane between the two opposing detectors.

4.6.3 True coincidence detection efficiency

In order to estimate the true coincidence detection efficiency of two crystals forming a LOR the scanned line source measurement with detectors being 112 mm apart was considered (Fig. 4.23, bottom). Since the diameter of the ^{68}Ge rod source used is larger than the edge of the crystals, 3 mm versus 2.10 mm, respectively, a simulation was carried out in order to estimate the mean solid angle that sees the activity at the central plane as the line source is scanned, as depicted in Fig. 4.24.

Table 4.2 shows the parameters used to estimate the true coincidence detection efficiency within a LOR. The mean number of detected events per LOR, N_d, already includes the correction for the dead time of the data acquistion system. The mean solid angle, $\overline{\Omega_9}$, has been calculated from the ratio between the pairs of photons hitting the front surfaces of the opposing crystals (Fig. 4.24) and the total number of histories. The acquisition time, Δt, is weighted by 9 due
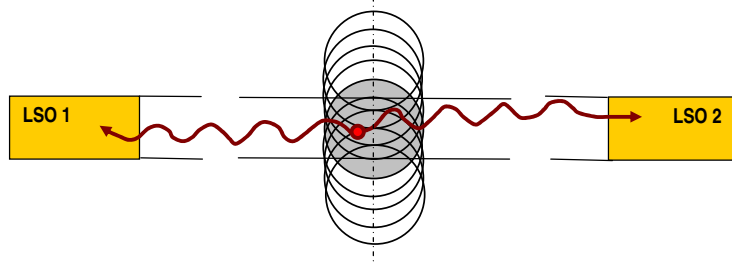
Figure 4.24: Geometry used to simulate the solid angle of a LOR between two opposing crystals. The line source, with 3 mm diameter, lies perpendicular to the image plane and is scanned with steps of 0.5 mm. For each position i of the source, ten million annihilation photon pairs were started. The ratio of photon pairs impinging on the detectors surfaces over the number of events started defines the solid angle Ω_i of each position.

Table 4.2: Parameters used for the true coincidence detection efficiency estimation.

Detected coincidences	N_d	192.8
Source activity (^{68}Ge) / 2 mm	A_{rod}	238.6 kBq
Mean solid angle (9 positions)	$\overline{\Omega_9}$	1.52×10^{-5}
Acquisition time (9 positions)	Δt	9×120 s
Expected coincidences	N_e	3917
Photons on detector surfaces	$(1 - \epsilon_{Al})^2$	88.9 %
Absorption in LSO	ϵ_{LSO}^2	53 %
Double photoelectric interaction	ϵ_{ph}^2	15 %
Within FWHM	ϵ_{fwhm}^2	57.8 %

to the fact that $\overline{\Omega_9}$ is the mean of 9 rod source steps:

$$\overline{\Omega_9} = \frac{1}{9} \sum_0^8 \Omega_i \,, \tag{4.9}$$

with Ω_i defined in Fig. 4.24. The expected number of coincidences is the product

$$N_e = A_{rod} \cdot \overline{\Omega_9} \cdot \Delta t, \tag{4.10}$$

and so the true coincidence detection efficiency ϵ_{LOR} is

$$\epsilon_{LOR} = N_d/N_e = 4.9 \,\%. \tag{4.11}$$

On the other hand, this efficiency can be calculated according to

$$\epsilon_{LOR} = (1 - \epsilon_{Al})^2 \cdot \epsilon_{LSO}^2 \cdot \epsilon_{ph}^2 \cdot \epsilon_{fwhm}^2 \,, \tag{4.12}$$

with $(1 - \epsilon_{Al})^2$ the fraction of photon pairs penetrating the 1.5 mm thick detector aluminium covers and reaching the surfaces of the crystals, ϵ_{LSO}^2 the part of photons absorbed in the LSO crystals, ϵ_{ph}^2 the probability that both annihilation photons interact by means of the photoelectric effect with LSO [Mos96] and ϵ_{fwhm}^2 the fraction of photon pairs falling within the FWHM in both peaks. Taking the values listed in Table 4.2 into Eq. 4.12 gives $\epsilon_{LOR} = 4.1 \,\%$, which is in a resonable correspondence with the value calculated with Eq. 4.11 if the rather simple model is taken into consideration.

4.6.4 Inter-pixel light crosstalk

An inter-pixel crosstalk of less than 10 % was observed between adjacent pixels. Fig. 4.25 shows the influence of the crosstalk signal from the detection of positron annihilation γ-rays in pixel A1, positioned at the corner edge of detector 1, onto the spectra of its directly adjacent pixels. It can be seen that almost all full-energy events occurring in pixel A1 generated a crosstalk signal in its edge-neighboring pixels A2 and B1. The low-energy peak observed in corner-neighbor pixel B2, with less counts and a mean energy well below 55 keV, was expected since the smaller surface contact between both pixels decreases the number of scintillation photons crossing between pixels.

The inter-pixel light crosstalk values measured do not play a major role for the detection of positron annihiliation since they amount to energy values close to the noise level and, therefore, any readout threshold will discard them. This is no longer the case if higher energy events are to be read since a 5 MeV signal ocurring in a given pixel, for example, will induce a 500 keV signal in its neighbors, as detailed in [Cre05d] and in section 6.9.3.
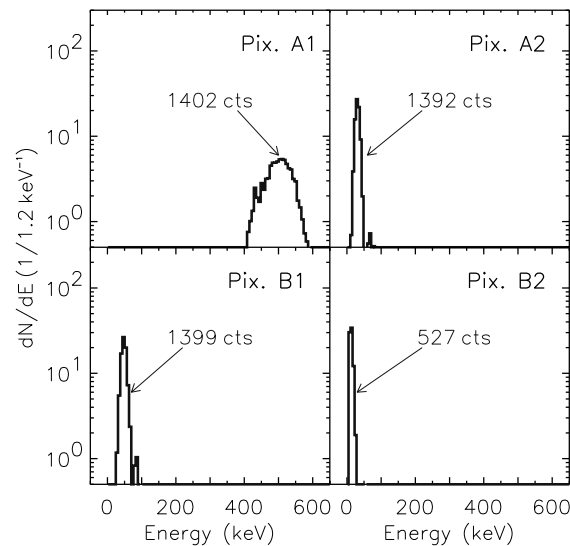
Figure 4.25: Light crosstalk within the pixels of the assembled detector. The γ-rays with 511 keV which deposit their full energy into pixel A1 leave a small crosstalk signal in their directly adjacent neighbor pixels A2 and B2. Corner-adjacent pixel B2 registers a smaller number of crosstalk signals with less amplitude, as expected due to geometrical reasons.

4.6.5 Temperature stabilization

Fig. 4.26 puts in evidence the need for a stabilized temperature. The top row shows one of the measurements of Fig. 4.23 but displayed with solid angle correction. The bottom row shows a measurement where the temperature was changed during the line source scan. The dramatic change in detector efficiency with the temperature is reflected in the strong inhomogeneity of the bottom image.

Fig. 4.27 shows the energy resolution degradation with changing temperature. As expected from the APDA gain temperature coefficient of $-2.4\,\%\,/\,\mathrm{K}$ [Mos03], the photopeak shifts to the left with higher temperature, yielding non acceptable energy resolution values. The effect on the coincidence time resolution is not seen since it is smaller than the time spread introduced by the independent signal processing hardware of the 64 timing channels. Temperature stability at the detector level was achieved approximately 40 minutes after turning on all electronics,
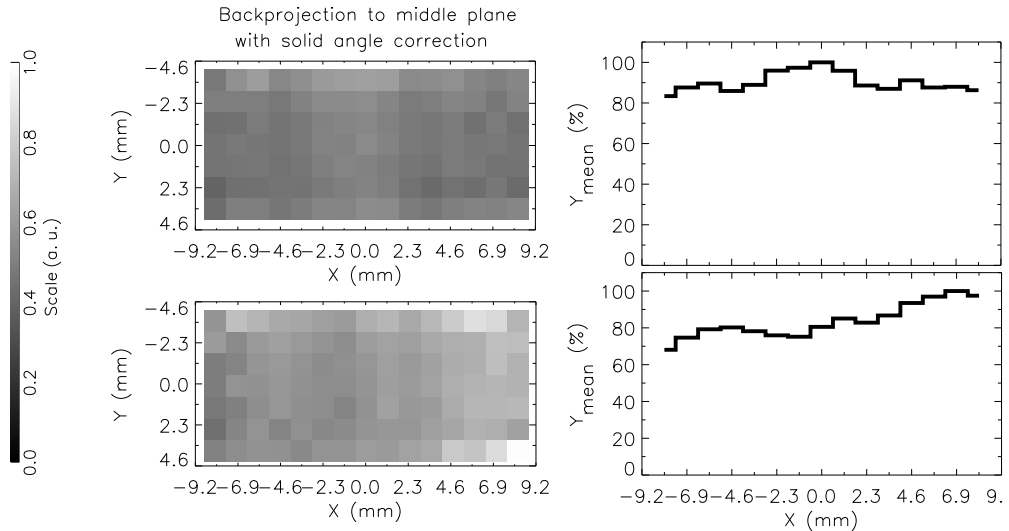
Figure 4.26: Influence of the temperature on the detector sensitivity. The plots on the left column were obtained by backprojecting the events acquired with a scanned line source onto the central plane between the detectors (112 mm distance, 2 min/step). Each image voxel is corrected for its solid angle weight. The right column shows the normalized projections of these images onto the X axis. The top measurement was performed with a stabilized temperature, whereas at the bottom a temperature change of about 5 K took place. Axes and intensity scale as in Fig. 4.23.
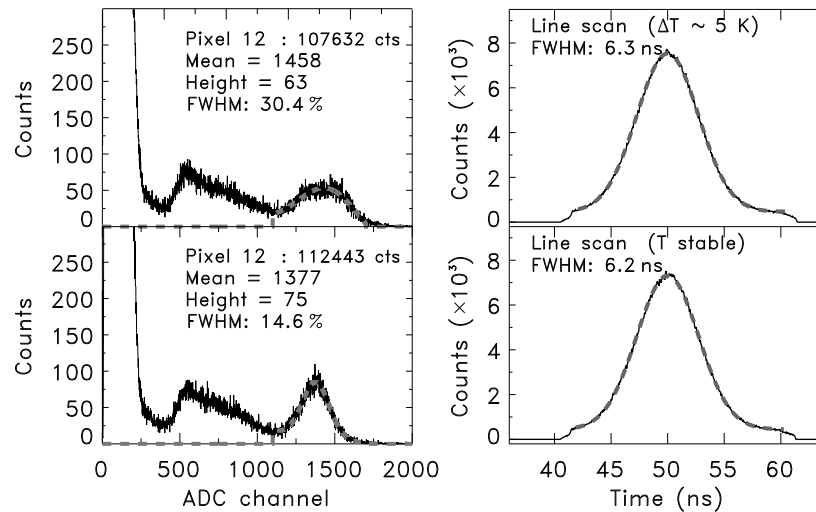
Figure 4.27: Influence of temperature drift on energy and time resolution. The top row shows the effect of a continuous temperature drift on the energy and time spectra. The bottom row shows spectra acquired with a stable temperature (measurement performed at equilibrium after the initial rise in temperature finished).

and with a normal air-conditioning room temperature control. This was verified by performing all day measurements without photopeak shifts observed. Both detector preamplifier boxes were ventilated with a small fan avoiding temperature gradients between the ambient and the detectors and preamplifiers.

4.7   Summary and Outlook

The next generation in-beam positron emission tomograph to be installed at the dedicated heavy ion facility in Heidelberg is to be operated close to the last magnet of the rotating medical beam line. Experimental results from the literature, combined with conservative calculations of the fringe magnetic field expected outside the mentioned magnet, show that the presently used photomultiplier tubes do not provide enough magnetic field resistance, even when covered with an optimum magnetic field shield such as mu-metal sheets. In addition, spatial restrictions arise due to the number of diagnostics instrumentation to be installed at the patient treatment site, which make a reduction of the in-beam PET detector volume very desirable. The substitution of PMT by state-of-the-art avalanche photodiode arrays APDA for scintillation light detection provides an answer to this two requisites. Their combination with recently commercially available, fast scintillators such as cerium-doped lutetium oxyorthosilicate LSO further enhance the performance of the next-generation in-beam PET detectors, namely better time and energy resolution can be achieved in respect to the presently installed detectors. These parameters are directly related to the quality of PET images. They are, furthermore, essential for in-beam PET readout during beam extractions in order to suppress the high yield of background events registered there, as presented in chapter 6.

Because of the advantages mentioned in the previous paragraph, two detectors each consisting of finger-like LSO crystals individually coupled to the 32 pixels of an APDA from Hamamatsu were assembled after the optimum parameters for signal maximization have been studied, namely the use of silicon glue for crystal coupling, teflon tape as a scintillation light reflector outside each crystal, high voltage value optimized for minimum signal noise and readout electronics adapted to the time and energy constraints of the detector. The measured energy and time resolutions of $15.5 \pm 0.4\,\%$ FWHM and $6.2 \pm 0.2\,\mathrm{ns}$ FWHM, respectively, are below those of the BGO/PMT-based tomograph presently installed at the therapy unit at the Gesellschaft für Schwerionenforschung at Darmstadt. Nevertheless, the electronics strategy implemented, with two shaping channels implemented per pixel optimized for energy and timing reading, is by no means feasible in a clinical tomography system with thousands of channels. This dual-channel strategy was adapted here only to make possible a straight-forward study of the performance of the detectors under irradiation conditions, as presented in chapters 5 and 6.

In addition to the assembly and readout optimization of the detectors, the last section in this chapter summarizes the imaging properties of the two LSO/APDA detectors operated in coincidence. Based on several flood source measurements performed with a line source, the solid angle of the image voxels in the mid-plane between the detectors was quantified and the coincidence detection efficiency for one LOR was calculated, providing the parameters for image quantification during the in-beam imaging experiments described in chapters 5 and 6. Ambient temperature was found to be an important parameter affecting the performance of the detectors and influencing their imaging sensitivity. Therefore, measures for temperature stabilization were taken. It was experimentally verified that stable measurements can be performed when equilibrium between the ventilated detector heads and the air-conditioned experimental room is reached, which takes place approximatelly 40 minutes after the detector power supplies are switched on.

The studies exposed in the present chapter provided the basic detector operation knowledge for the next two chapters.

Chapter 5

Feasibility of an LSO/APDA-Based Tomograph with Small Gaps

5.1 Motivation

Due to the promising clinical results achieved at the German heavy ion tumor therapy pilot project (chapter 1), a hospital-based facility is being constructed at the university clinics of Heidelberg, Germany, and additional facilities are being planned elsewhere [Sie04]. At the Heidelberg facility, for example, delicate therapeutic situations are expected to be treated with a rotating beam delivery (gantry, chapter 3) preferentially equipped with a dedicated in-beam PET system. Fig. 5.1 depicts this system, with a gap between the two detector heads considered in order to (1) provide an entrance for the primary beam, occupying a maximum area of 20×20 cm^2, and (2) an escape port for the flux of light fragments, mainly neutrons and protons [Gun04a, Gun04b], leaving the patient downbeam.

In chapter 2 it was shown that the detectors of such a PET system should cover a large solid angle, forming a double-head tomograph with small gaps in order to minize image artifacts. Furthermore, the detectors should be of small volume, minimal weight and resistant to magnetic fields due to the proximity to the beam bending magnets (chapter 3). The combination of crystals of cerium-doped lutetium oxyorthosilicate (Lu$_2$SiO$_5$:Ce^{3+}, LSO) and avalanche photodiode arrays (APDA), described in chapter 4, could solve these problems. While similar detectors have shown their applicability to tracer imaging [Pic01], their performance for in-beam PET was unknown. Therefore, an experimental study of the proposed detectors before a final design of the next-generation in-beam PET scanners was necessary. For this reason, the performance and in-beam imaging capabilities of the two position sensitive γ-ray detectors described in chapter 4, each consisting of a Hamamatsu APDA (S8550) with its pixels individually coupled to single LSO crystals, were investigated and summarized in [Cre04] and [Kap04], with a more detailed analysis presented here.

The two detectors were operated in coincidence at the medical beam line of the Gesellschaft für Schwerionenforschung (GSI) in Darmstadt, Germany. In a first set of experiments their imaging performance was tested before, during and after the irradiation of phantoms of polymethylmethacralate (PMMA) with a carbon ion beam with fluence equivalent to 1 000 typical daily therapeutic fractions. In these experiments the detectors were positioned both upbeam as well as downbeam from the irradiated target, forming small angles with the beam direction in order to investigate the performance of detectors laying at these critical points.

A second set of experiments, performed after the irradiation with high fluences, tested the in-beam imaging capability of these detectors in conditions that simulate the in-beam patient irradiation: The depth distribution of positron emitter radionuclides created in a phantom that stopped the high energy carbon ion beam were imaged by making use of the accelerator status information for selecting events acquired during the extraction pauses only.
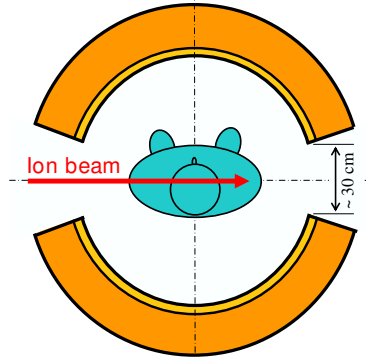
Figure 5.1: Scheme of the PET detector configuration under study for the next-generation, in-beam PET scanners.

Since previous in-beam PET research in Berkeley was abandoned due to detector activation (Bismuth Germanate, $Bi_4Ge_3O_{12}$, BGO) arising most probably from secondary particles caused by the passive beam shaping components [Lla88], the possible activation of the scintillator material LSO by the flux of light particles leaving the patient downbeam [Gun04a, Gun04b] was investigated. For that, two patients with single irradiation portals were selected and a small matrix of crystals was placed in their masks downbeam, following the beam direction with maximum penetration depth in order to meet the expected maximum light particle flux leaving the irradiated patient. High resolution spectroscopic measurements of the crystals irradiated in the described way were then performed and compared with measurements made before the irradiation.

The influence of the natural background activity density of LSO onto the random coincidences background expected for a tomograph with the geometry proposed in this chapter is also addressed. Natural lutetium contains 2.6 % of the isotope ^{176}Lu, which decays with a half-life of about 3.8×10^{10} years by β^- emission, followed by a γ-ray cascade. This results in an LSO background activity density of 240 Bq cm^{-3} [Hub02]. Calculations show that suppressing this background is essential in order not to compromise the images taken by LSO-based, in-beam PET scanners. Nevertheless, randoms subtraction techniques fail for in-beam PET measurements during particle extraction, which are mandatory for the next-generation tomographs to be operated under optimized accelerator particle delivery (chapter 6). Therefore, a modern readout scheme, capable of decreasing the coincidence time resolution obtained with conventional nuclear electronics, is proposed. Alternatively, a recently developed scintillator with reduced background but less detection efficiency in respect to LSO is also considered.

Finally, the impact of recent developments in ultra-fast timing detectors, potentially allowing the implementation of the time-of-flight (TOF) technique onto commercial PET scanners, is extrapolated to in-beam PET. It is shown that TOF techniques gain much importance for dual-head, in-beam PET scanners due to the capability of the TOF information to reduce the image elongation that characterizes limited-angle tomography. Equally important, both for closed-ring as well as for dual-head, in-beam positron tomographs, is the immense decrease in data processing time if the TOF information is used [Cre05a], making in-beam PET images available even during the irradiation for tomographs with a coincidence time resolution below 200 ps FWHM.

In summary, the studies presented in this chapter, performed under high beam fluences and, therefore, providing high count rates for the PET measurements, are conclusive in what regards the capability of performing in-beam PET imaging with detectors positioned at small angles with the beam direction.

5.2 Electronics Setup for In-Beam Imaging

In order to assess whether photon detectors consisting of LSO crystals coupled to APDA are a feasible solution for this next generation of in-beam PET, the two LSO/APDA detectors described in the previous chapter were operated in coincidence at the GSI medical beam line. Each detector consists of 32 LSO crystals ($2.1 \times 2.1 \times 15$ mm^3 each) coupled individually to the 4×8 pixels of a Hamamatsu S8550 APDA with silicon glue (chapter 4). Fig. 5.2 shows the fast-
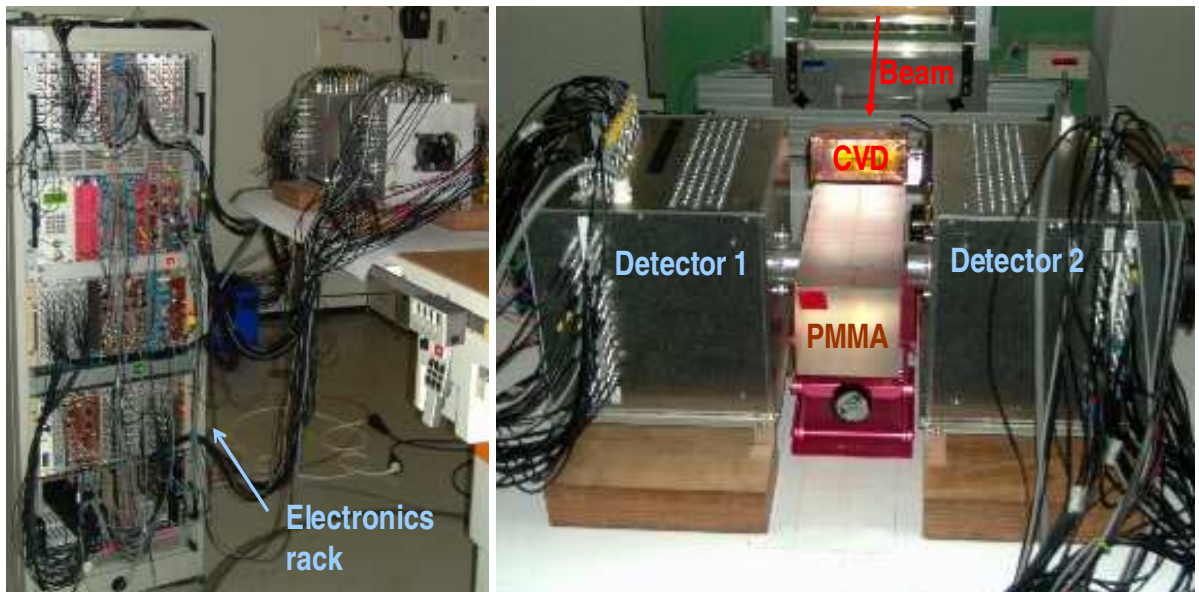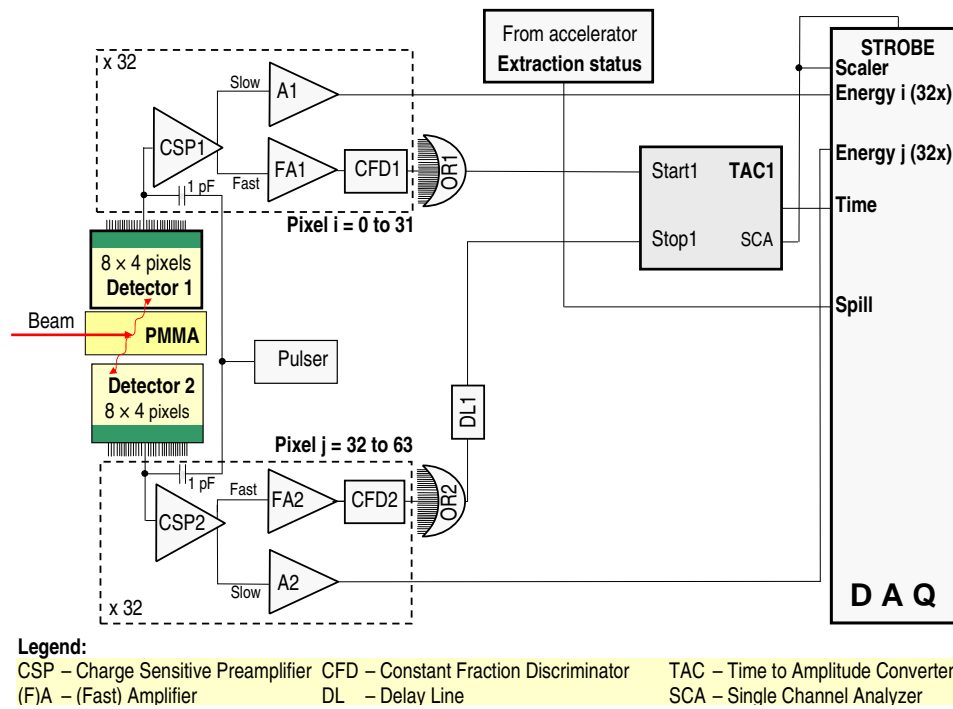
Figure 5.2: Fast-slow coincidence setup for all in-beam imaging experiments. The photographs show the electronics and detector setup positioned at the isocenter of the medical cave at GSI. The chemical vapor deposition diamond detector (CVD, bottom-right) was only used in the experiments described in chapter 6.

slow electronics readout that was implemented. The splitting of the signal from each pixel into a fast (timing) and a slow (energy) shaping electronics chain allowed using conventional, modular nuclear electronics for both time and energy measurements. After splitting the signal at the output of each charge sensitive preamplifier (chapter 4, section 4.5), the slow (energy) signal of each pixel was fed into an 8-input, MA8000 spectroscopy amplifier from Stelzer Physikalische Messgeräte, with 0.5 μs shaping constant and adjustable gain ($G \geq 10$). The 64 amplified energy signals were then delivered to four PS7164 CAMAC analog-to-digital converters (ADC) from Phillips Scientific, with 16 inputs each. On the timing chain, each fast signal of each preamplifier was delivered to a PS779 32-channel, fast DC amplifier from Phillips Scientific with gain 10 and, from there, fed into a CF8000 8-input constant fraction discriminator (CFD) from Ortec with 30 ns internal delay. The disjunctively connected outputs of all the CFD of detector 1, implemented with a 429A logic fan-in/fan-out from Lecroy, were then fed into the start input of a TAC/SCA 567 time-to-amplitude converter (TAC) from Ortec, while the disjunctively connected ouputs of detector 2 were delayed with an N108 dual delay unit from CAEN to form the TAC stop signal. A time window of about 20 ns was set at the TAC and its single channel analyzer (SCA) digital ouput gated all CAMAC[1] analog-to-digital converters (ADC) and started the CAGE[2] data acquisition system (appendix B). The TAC output was fed into an AD811 CAMAC ADC from Ortec.

For every detected coincidence, all 64 energy channels were read, together with the coincidence time between the two detectors and, in addition, one channel containing a digital signal provided by the synchrotron (high for spill on, i.e. beam extraction, ~ 2 s, low for spill off, i.e. pause between extractions, ~ 3 s). This synchrotron signal allows, as necessary during in-beam imaging, to discriminate data acquired during the pauses between the extractions from data acquired during particle extraction. This separation is necessary because of the high background occurring during beam extractions, arising from prompt γ-rays and particles emitted after nuclear reactions between the projectiles and target nuclei (chapter 6). All data generated by each coincidence were recorded in list mode format by means of the data acquisition (DAQ) system described in appendix B. This system also reads a C257 16-input scaler from CAEN that counts all the incoming coincident events, even if not processed by the acquisition electronics, which allows an off-line dead time correction to be performed. Finally, it must be stated that a single pixel threshold was implemented, i.e. an energy threshold of about 250 keV was set individually at each CFD of each pixel. Consequently, the energy spectra present low energy events below the threshold due to noise, interpixel crosstalk and, in the case of spectra acquired during beam extraction, due to the acceptance of low energy events imposed by higher energy events triggering pixels elsewhere in the detectors.

5.3   In-Beam Imaging Performance

This first set of experiments aimed at testing the performance of the detectors under irradiation conditions. Such study was necessary since their imaging capability was expected to be mostly influenced by the particle [Gun04a, Gun04b] and photon [Paw97, Par05b, Cre05d] flux generated by nuclear reactions as the beam penetrates the target.

5.3.1   Setups

The setups depicted in Fig. 5.3 were applied to compare the imaging performance of the detectors when acquiring under and without irradiation of a phantom positioned upstream and downstream from the detectors. The parameters compared were the energy, time and spatial

---

[1] CAMAC, a backplane electronics bus, stands for computer automated measurement and control.
[2] CAGE, a C/C++ software/hardware data acquisition solution for CAMAC, stands for CAMAC acquisition through GPIB and ethernet. GPIB stands for general purpose interface bus.
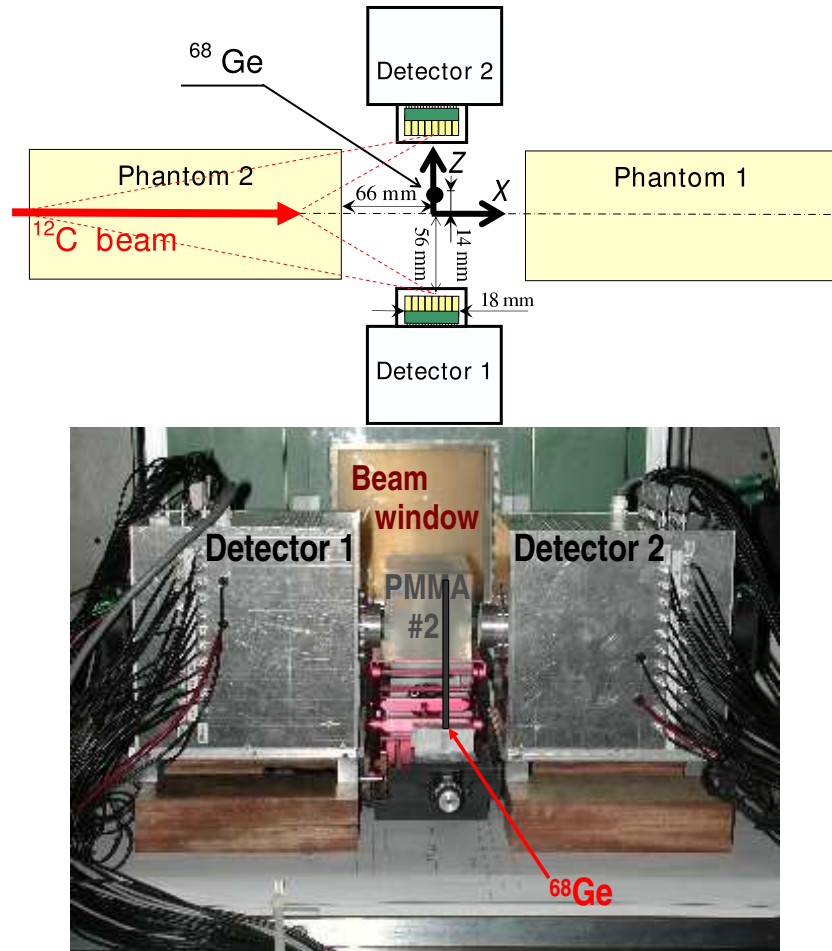
Figure 5.3: Arrangements for the first in-beam PET imaging with LSO/APDA detectors. The photograph shows the setup used for irradiating phantom 2. A ^{68}Ge line source was positioned vertically (along the Y axis), 14 mm apart from the isocentre in order not to be hit during the irradiation. The two phantoms were used alternatively to stop the carbon ion beam upstream (PMMA 2) and downstream (PMMA 1) from the FOV of the detectors.

resolution obtained in each setup. The phantoms were used alternatively and the distances between the irradiated phantom and the detectors were chosen so that the geometry of the edge positioned detectors (dotted circles in Fig. 5.1) of a high acceptance tomograph could be simulated at a scale of approximately $1:3$ (Fig. 5.1 versus Fig. 5.3). A ^{68}Ge line source with 3 mm diameter, 14.5 cm length and 17.3 MBq activity was positioned vertically between the detectors, with a shift of 14 mm to detector 2 in order not to be hit by the beam when phantom 1 was used. Imaging of this line source was performed before, during and after the irradiation of the phantoms, each with $9 \times 9 \times 20 \, cm^3$. For that, a pencil-like beam with 3.7 mm diameter (FWHM) and 341.9 AMeV energy penetrated 18.0 cm into each phantom. These were positioned outside the field-of-view (FOV) of the LSO/APDA detectors. The beam intensity was 2×10^8 ions per spill which, after the 1400 spills requested for each irradiation, yields a fluence about $1\,000$ times higher than for a typical daily treatment fraction ($\sim 3 \times 10^8$ ions).

5.3.2 Data acquisition dead-times and event rates

By making use of the accelerator status signal the data acquired could be separated into events collected during beam extractions and during pauses between the beam extractions. The present section summarizes the event rates measured in both regimes after an analysis of the

dead-times η of the data acquisition system (DAQ).
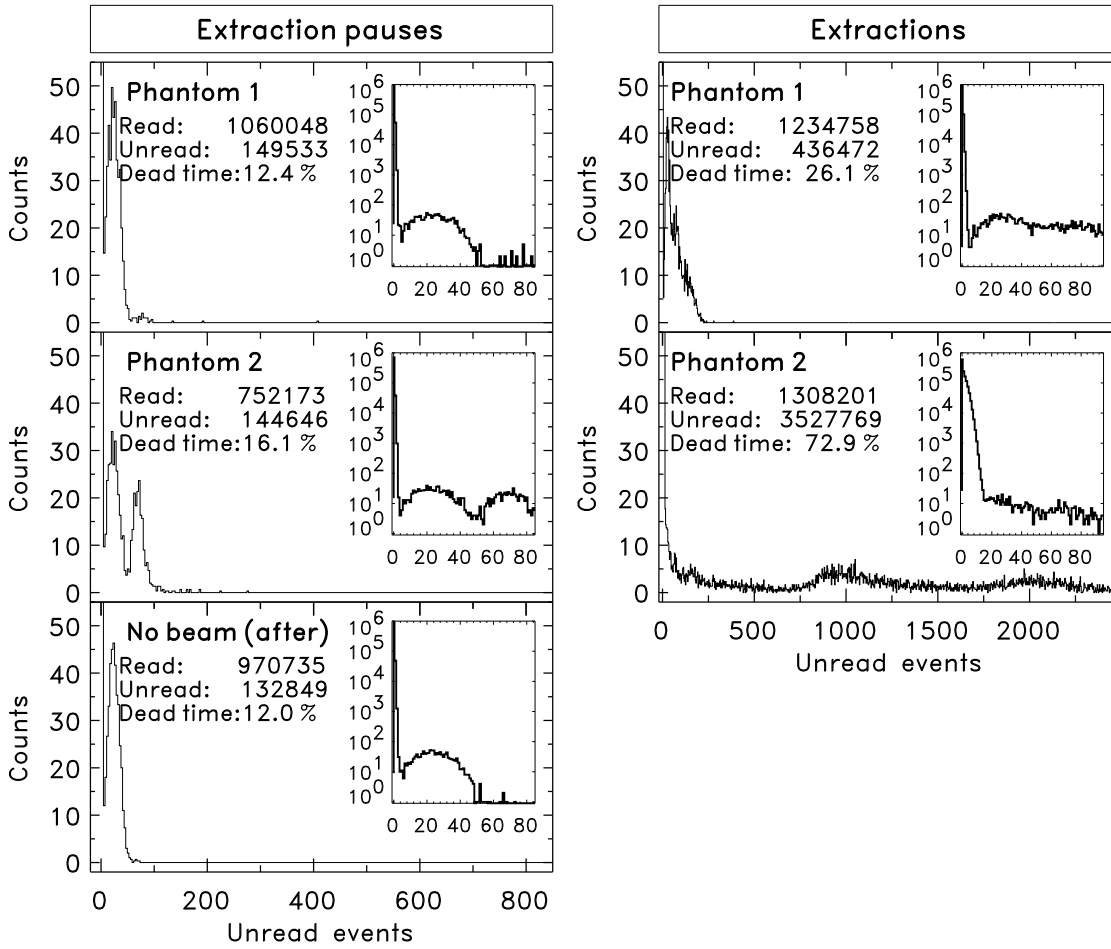
Figure 5.4: Histograms of unread events, with the corresponding data acquisition (DAQ) dead-times, during the extraction pauses and beam extractions.

Fig. 5.4 shows the histograms of unread events obtained during the several imaging setups described in the previous section. The plots were obtained by sampling, from event-to-event, the difference in the scaler values in each event subtracted by unity. That means that the counts in bin 0 correspond to the number of read events where there were no DAQ dead time losses, or the number of counts in bin 20, for example, corresponds to the number of occurrences where 20 events were lost between two consecutive DAQ readouts. The histogram of unread events for the setup without beam, performed before the irradiation of phantoms 1 and 2, is not shown in Fig. 5.4 since it is very similar to the histogram corresponding to the setup without beam but performed after the irradiation of the phantoms (Fig. 5.4, bottom). All histograms of unread events have their maximum at the first bin (unread events = 0, i.e. $\eta = 0$ %) and fall off rapidly from a value above 10^5 to a minimum valley with about 10 counts in bin 10 ($\eta = 90.9$ %), indicating the good performance of the DAQ system with respect to dead time. After bin 10 ($\eta = 90.9$ %), a single peak (double peak for the setup with the detectors positioned downbeam, phantom 2) is observed, corresponding most probably to situations where the data acquisition suffered a buffer overload generating a timeout signal due to the inability of the DAQ system to transfer all its stored events to the acquisition computer in synchronization with the incoming events (appendix B). In such situations an automatic synchronization reset between the several electronics modules driving the acquisition is performed with, consequently,

no data taking during the handshake of the several modules. At all times the scaler implemented continues counting the lost events so that the dead-time can be quantified, as shown in Fig. 5.4. The ratio of events within the first peak in all histograms (bin $\leq$ 10) to the number of events with bin $\geq$ 10 is remarkably high, indicating the good capability of the DAQ system to handle the high rates encountered. It must be stated that the input rates handled by CAGE were tested before the experiments to a limit of 100 kcps[1], which was the maximum impulse rate delivered by the pulser available (appendix B). During beam extractions, the extension to higher bins of the histogram of unread events with the detectors positioned downbeam from the irradiated phantom (phantom 2, middle row, right in Fig. 5.4) indicates that the CAGE acquisition system was operating close to its limit in that particular setup, with a high number of buffer overloads generating timeout signals and, consequently, a high number of unread events between readouts.

Table 5.1 summarizes the measured DAQ dead-time η as well the η-corrected event rates. These rates refer to those impinging onto the detectors operated in coincidence and not to the event rate within the FOV of the detectors, i.e. they were calculated taking into account the beam delivery macrostructure for this experiment, namely 2.2 s during beam extractions and 2.3 s during extraction pauses, a time of irradiation of 105 minutes and the DAQ dead-time. No detection efficiency and solid angle corrections were considered at this stage due to the high spatial anisotropy of the incoming events during beam extractions [Gun04a, Gun04b]. A clear asymmetry between the setup with the detectors positioned upbeam and downbeam from the irradiated phantom can be seen, with an event rate about 3 times higher measured with the detectors positioned downbeam from the target.

Table 5.1: Data acquisition dead-times η and event rates measured with the setups of Fig. 5.3.

Experiment	Before irradiation	Detectors up-beam	Detectors down-beam	After irradiation
^{12}C beam	No	342.0 AMeV	342.0 AMeV	No
Phantom	No	Phantom 1	Phantom 2	No
$\eta_{extractions}$ (%)	-	26.1	72.9	-
Event rates$_{extractions}$ (cps)	-	542	1570	-
η_{pauses} (%)	11.7	12.4	16.1	12.0
Event rates$_{pauses}$ (cps)	332	376	310	343

cps = counts per second

5.3.3   Energy, time and spatial resolutions during extraction pauses

In the present section the energy, time and spatial resolutions achieved during the extraction pauses are summarized. Fig. 5.5 shows one energy channel and the coincidence time spectrum measured for a ^{68}Ge line source placed between the detectors (section 5.3.1). The top row shows the results acquired under irradiation of the phantom positioned downbeam from the detectors, whereas the bottom row shows the results obtained with the phantom irradiated upbeam from the detectors. A slight degradation of the energy resolution during the irradiation with the detectors situated in the forward cone of light nuclear fragments (bottom row, beam stopped in phantom 2) is observed, together with an indication for a slight worsening of the time resolution. The energy and time spectra (not shown) acquired before and after the irradiation of phantoms 1 and 2 are very similar to the spectra acquired during the irradiation of phantom 1 (extraction pauses, Fig. 5.5, top row). The results are evidenced in Table 5.2, which shows

---

[1] Kilo counts per second (kcps).
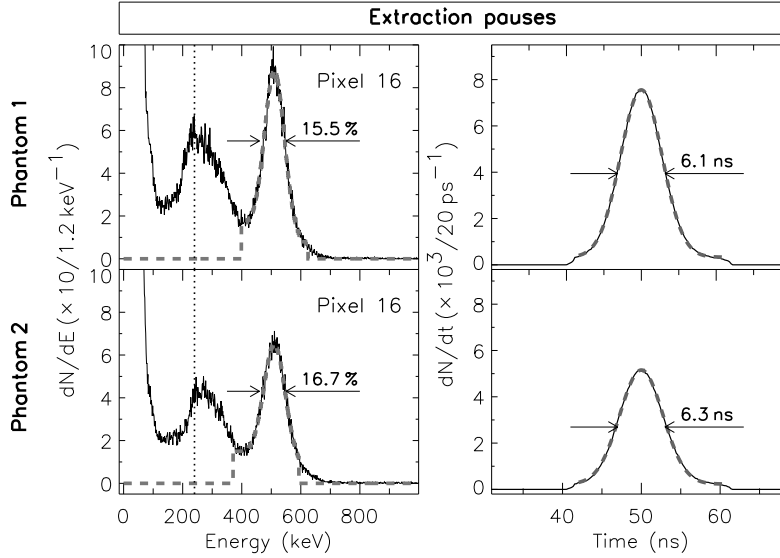
Figure 5.5: Comparison of energy and time resolution measured during the extraction pauses. A ^{68}Ge line source was positioned in the FOV of the two detectors (Fig. 5.3). The beam stopped downstream (top row) and upstream (bottom row) from the detectors. The dotted and dashed lines show the hardware threshold and the Gaussian fit to the full-energy peak, respectively.
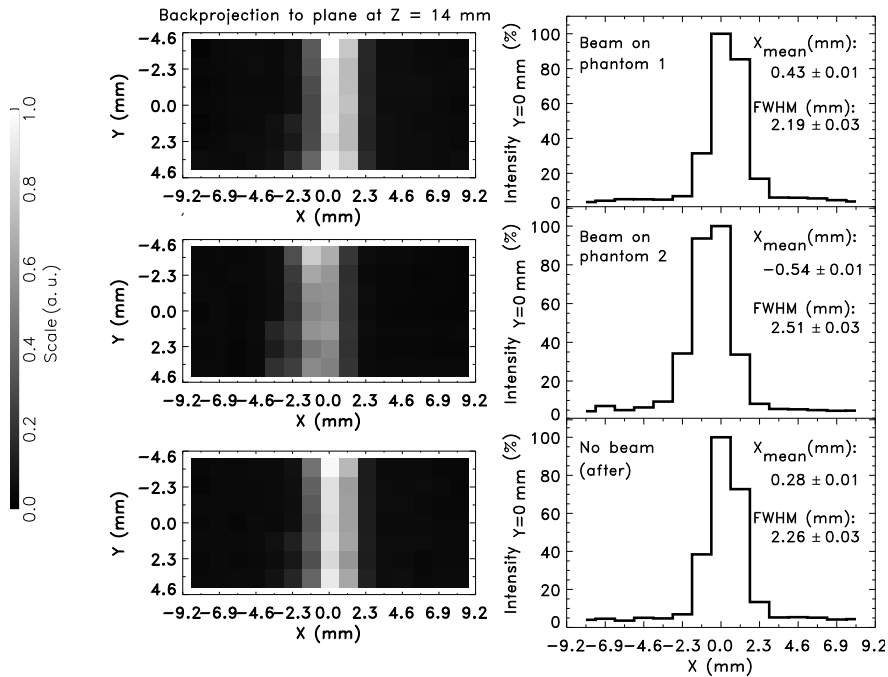
Figure 5.6: Comparison of spatial resolution from in-beam images of a ^{68}Ge line source (Fig. 5.3). The measured datasets were backprojected onto the perpendicular plane between the detectors at $Z = 14$ mm (left column). The images in the right column show the normalized linear profiles through the middle of the backprojected plane on the left column.

both the mean energy resolution for all 64 channels as well as the coincidence time resolution obtained in all measurements with the ^{68}Ge line source.

In Fig. 5.6 it can be seen that the spatial resolution is also slightly worsened for the detectors

Table 5.2: Imaging a ^{68}Ge line source (setup of Fig. 5.3).

Experiment	Before irradiation	Detectors up-beam	Detectors down-beam	After irradiation
^{12}C beam	No	342.0 AMeV	342.0 AMeV	No
Phantom	No	Phantom 1	Phantom 2	No
$\Delta E/E$ (FWHM, %)	15.5 ± 0.5	15.5 ± 0.3	16.4 ± 0.6	15.5 ± 0.3
Δt (FWHM, ns)	6.2 ± 0.2	6.1 ± 0.2	6.3 ± 0.2	6.2 ± 0.2

positioned in the forward cone of the stopped beam. The images of the line source obtained before any phantom irradiation are not shown in Fig. 5.6. They are very similar to those obtained after the irradiation. The backprojection onto the plane between the detectors containing the ^{68}Ge line source is shown and allows to see a slightly worse spatial resolution, quantified for the linear profile of the line source. More importantly, in all the in-beam experiments it has been observed that after finishing the irradiation the time, energy and the spatial resolution returned back to the initial values.

5.3.4 Energy and time spectra during beam extractions

The analysis of the energy and time spectra measured during beam extractions clearly reveals a much higher random contamination for the detectors positioned downbeam from the beam stopping region. Fig. 5.7 shows energy and time spectra collected for the two setups stopping the beam in Fig. 5.3. In the energy spectra corresponding to the setup of phantom 1 a drop in the number of events below the hardware threshold is observed, as shown for pixel 16 in Fig 5.7. This behaviour, described in section 5.2, is expected due to the lower count rates measured in this configuration (Table 5.1). In the setup receiving higher event rates (phantom 2, bottom row) no discontinuity is observed at the threshold value due to the increased background events
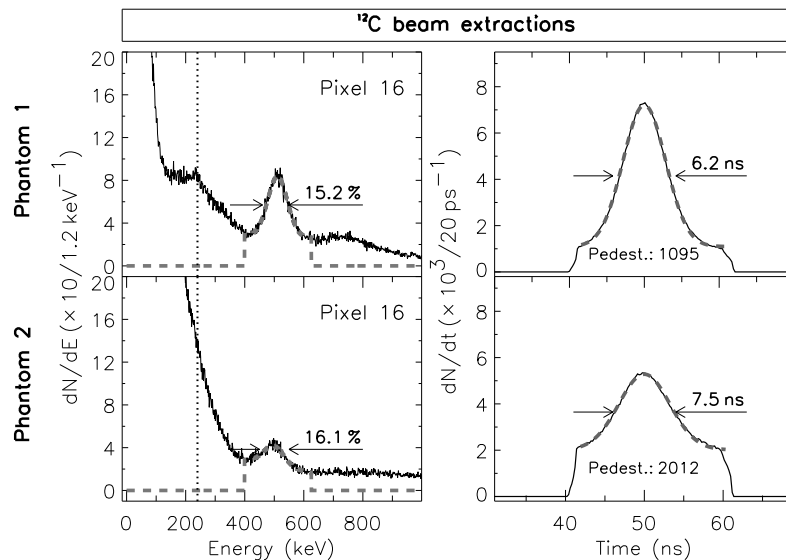
Figure 5.7: Energy and time spectra obtained during beam extractions. A ^{68}Ge line source was positioned in the FOV of the two detectors (Fig. 5.3). Results show the beam stopped downstream (top row) and upstream (bottom row) from the detectors. The dotted and dashed lines show the hardware threshold and the Gaussian fit to the full-energy peak, respectively.

being imaged. Fig. 5.7 shows clearly that in the setup with the detectors positioned downstream from the irradiation (phantom 2) a much higher background is present, resulting in a lower height of the 511 keV peak and worse energy resolution. In addition, the time spectrum also shows a resolution deterioration, with a twofold increase in the pedestal value revealing the presence of a higher number of random events. For the present experiments a separation of the events collected during beam extractions and during the extraction pauses was enough to image successfully the ^{68}Ge line source positioned in the FOV of the detectors. But this high event yield must be further carefully studied if in-beam PET imaging during beam extractions will be implemented, as necessary for future heavy ion therapy installations, where a higher accelerator duty factor in comparison to the GSI medical machine is expected (chapter 6).

5.4   Imaging ^{12}C Beam Induced Positron Emitter Distributions

This set of experiments was devoted to the imaging of the positron emitter depth distribution generated by a pencil-like ^{12}C beam stopping in a phantom. Such an imaging experiment is of importance since it simulates the application of the detectors under study for monitoring the ^{12}C patient tumor irradiation. These β^+ activity measurements check, furthermore, the imaging capability of the detectors after being exposed to the irradiation of two phantoms with high fluences (about 1000 times higher than for a typical daily treatment fraction) and with the detectors positioned up and downbeam from the irradiated phantom.

5.4.1   Setup

As shown in Fig. 5.8, the FOV of the longitudinal positron camera formed by the two detectors is much smaller than the beam range in PMMA (18 mm versus 74 mm, respectively, with a beam energy of 200.3 AMeV). Therefore, the phantom ($9 \times 9 \times 20$ cm^3) was moved through the FOV in 9 steps of 9 mm each (half the axial length of one LSO/APDA detector), thus
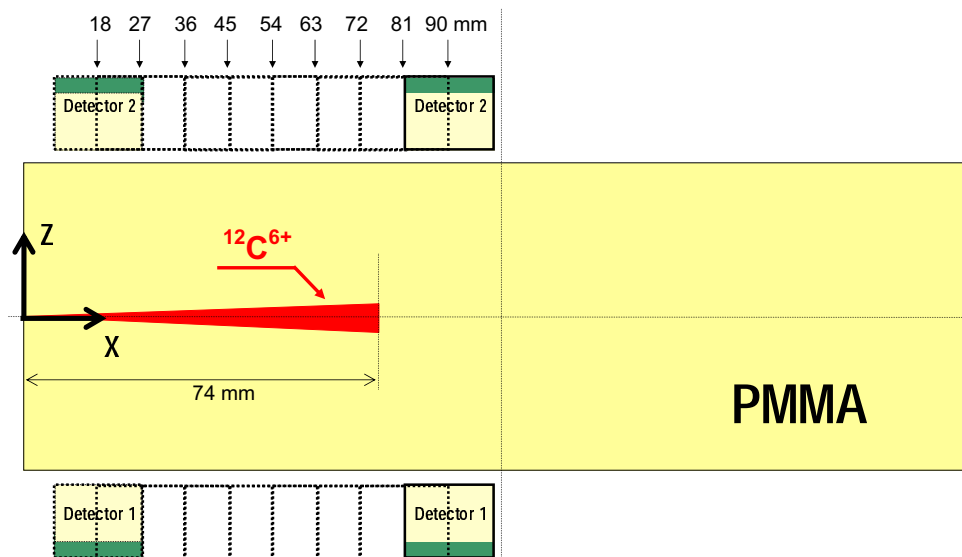
Figure 5.8: Arrangement for the second set of in-beam PET imaging experiments. Nine phantoms were irradiated subsequently in order to image the β^+ activity resulting from stopping the carbon ion beam. The position of the centre of the detectors relative to the front face of each phantom is shown by the arrows at the top.

covering 99 mm parallel to the beam track (Fig. 5.8). For each detector position one new phantom was used in order to avoid the remaining activity from the previous irradiation to be detected. The photograph in Fig. 5.2 shows one such phantom exactly positioned between the LSO/APDA detectors. The chemical vapor deposition (CVD) diamond particle detector shown in the photograph was not used at this stage, but at a later stage for implementing random suppression during beam extractions, described in chapter 6.

5.4.2 Data acquisition dead-times and event rates

In order to perform quantitative imaging of the ^{12}C beam induced positron emitter distribution, presented in the next section, three items must be known: the solid angle of the FOV formed by the two detectors, the overall photon detection efficiency and the acquisition dead time η. This section evaluates the latter, divided into $\eta_{extractions}$ and η_{pauses}. Fig. 5.9 shows the histograms of unread events obtained for the whole scan described in section 5.4.1. The corresponding DAQ dead-times are also shown. By considering both the beam delivery macrostructure for the used ion energy, with beam extractions taking 2 s and extraction pauses 3 s, as well as the irradiation time of 20 minutes, the mean coincidence event rate impinging onto the detectors and forming a signal above threshold in both detectors could be calculated, yielding 20 cps and 652 cps during extraction pauses and beam extractions, respectively.
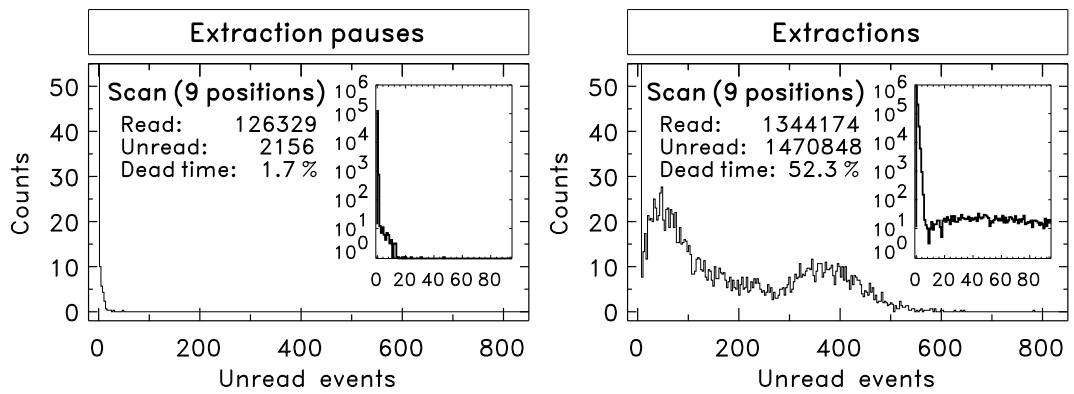
Figure 5.9: Histograms of unread events, with the corresponding data acquisition (DAQ) dead-times, during the scanned measurements depicted in Fig 5.8.

5.4.3 Depth-profile and 2D longitudinal tomogram

Fig. 5.10 shows the measured β^+-activity distribution obtained by shifting the irradiated phantoms along the beam direction, as described in section 5.4.1. Both the depth-profile and the longitudinal tomogram were obtained by backprojecting the coincidence data onto the central plane between the detectors. Only events leaving a signal within an energy window of 300 to 850 keV in the triggered pixels of both detectors were selected.

The shape of the measured distribution is in agreement with the expectations from the kinematics of the nuclear fragmentation reactions leading to the positron emitters [Eng92]. Onto a plateau of activity formed by target fragments (^{11}C, ^{10}C, ^{15}O and ^{13}N), a pronounced activity maximum due to the projectile fragments (^{11}C, ^{10}C) is superimposed (Fig. 1.17).

For quantification of the image acquired during the extraction pauses, the parameters shown in Table 5.3 were used, namely the DAQ dead time η_{pauses}, the geometrical solid angle at the image center $\Omega_\odot$, the image fill factor Π, described in section 4.6.2, the probability for escape
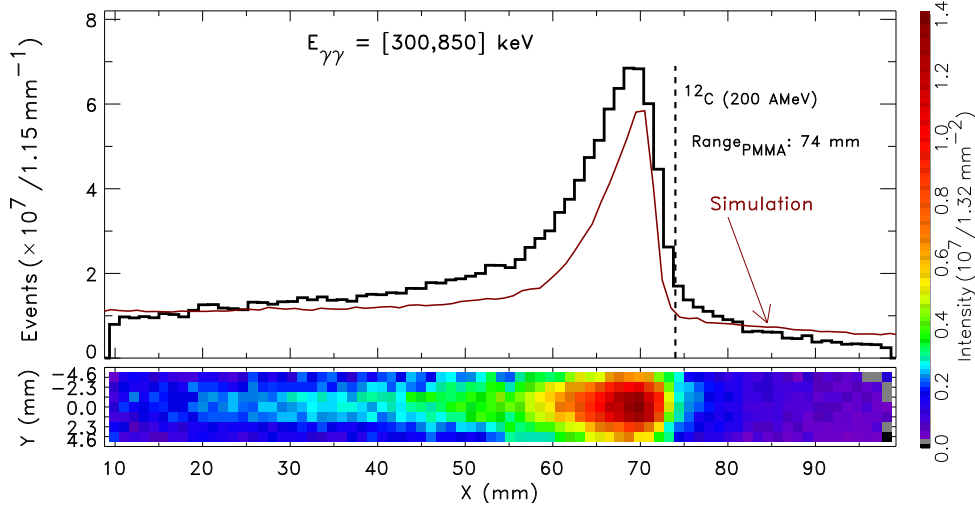
Figure 5.10: Depth-profile and longitudinal tomogram of the β^+ activity induced by stopping the carbon beam within the field of view (FOV) of the LSO/APDA detectors.

of the two unscattered annihilation γ-rays from the phantom, $P_{\gamma\gamma\,esc}$, and the efficiency for detecting a photon coincidence in two opposing LSO crystals within the considered energy window ε'_{LOR}.

Table 5.3: Parameters used for image quantification (extraction pauses).

Name	Symbol	Value
Detected coincidences	N_d	87705
Dead time	η_{pauses}	1.7 %
Solid angle (32 LOR)	$\Omega_\odot = 32 \cdot \Omega_{LOR}$	$32 \cdot 2.3 \times 10^{-4}$
Image fill factor	Π	30.5 %
Double γ-ray escape from phantom	$P_{\gamma\gamma\,esc}$	15.2 %
LOR efficiency (photopeak, no phantom)	ε_{LOR}	4.9 % (Eq. 4.11)
LOR efficiency (300 to 850 keV, no phantom)	ε'_{LOR}	$3.7 \cdot \varepsilon_{LOR}$
Corrected coincidences	N_c	1.44×10^9
Expected coincidences	N_e	1.41×10^9

The value of η_{pauses} was presented in section 5.4.2. To obtain Ω_{LOR} a simulation routine similar to that described in section 4.6.3 was written. This routine considered 10 million events at the isocenter annihilating isotropically and counted those events impinging onto the surfaces of two opposing pixels. The overall geometrical solid angle at the isocenter $\Omega_\odot$ follows by multiplication with the number of LOR (32). This method was preferred instead of taking into account the full frontal area of the LSO matrix detectors because of the non-negligible dead area surrounding each LSO crystal. This area is filled with air and teflon tape. In order to account for the smaller geometrical solid angle of image voxels positioned elsewhere than the isocenter, the flood source measurement with exactly the same detector geometry, studied in section 4.6.2, was used to correct on a voxel-by-voxel base the number of events backprojected into the mid-plane image. This correction represents the mean relative geometrical solid angle of each image voxel with respect to the central one and is given by the mean image fill factor Π, defined in section 4.6.2. Since neither $\Omega_\odot$ nor Π account for the absorption of photons in the phantom, the probability for escape of the two unscattered annihilation γ-rays from the phantom, $P_{\gamma\gamma\,esc}$, was

calculated based on the absorption value for 511 keV photons in PMMA (9.32×10^{-2} cm^2 g^{-1}, with $\rho_{PMMA} = 1.18$ g cm^{-3}) obtained from [Xco99]. The efficiency for detecting a photon coincidence in two opposing LSO crystals with photon energy values between 300 and 850 keV (ε_{LOR}) was measured to be 3.7 times higher than the same efficiency calculated for two photons with energy values lying within the FWHM of the photopeaks (Table 4.2).

The simulation of the expected number of counts N_e was achieved with the PosGen Monte-Carlo code [Has96, Pön04], with its output confirmed in appendix C. The code yields a total of 1.98×10^7 β^+-decaying nuclei produced per each spill with 2×10^8 carbon ions with 200.2 AMeV energy. The expected total number of counts $C^{(j)}$ from the decay of isotope j with half-life $T_{1/2}^{(j)}$ followed by integrating the initial activity $A_0^{(j)}$, induced per spill, over the 240 spills used (5 s spill period):

$$C^{(j)} = A_0^{(j)} \, \frac{T_{1/2}^{(j)}}{\ln 2} \, \sum_{i=0}^{239} \left[1 - \exp\left(\frac{-i \cdot 5\,\mathrm{s}}{T_{1/2}^{(j)} / \ln 2} \right) \right]. \tag{5.1}$$

The simulation curve in Fig. 5.10 regards acquisitions in the extraction pauses and, consequently, considers only isotopes with half-lives larger than a second (^{11}C, ^{10}C, ^{15}O and ^{13}N) weighted with the timing fraction of the extraction pauses: 3/5, so that

$$N_e = \frac{3}{5} \cdot \left[\sum_j C^{(j)} - C_{8.8\,mm}^{(j)} \right], \quad j = \, ^{11}\mathrm{C}, \, ^{10}\mathrm{C}, \, ^{15}\mathrm{O}, \, ^{13}\mathrm{N}, \tag{5.2}$$

with $C_{8.8\,mm}^{(j)}$ being the number of coincidences expected to have been measured if the phantom length between 0 and 8.8 mm would have been imaged (cf. Figs. 5.8 and 5.10). By taking into account the irradiation time of 1200 s, a beam penetration depth of 65 mm and its circular, Gaussian cross section with 1 cm FWHM[1], the measured β^+-activity density created by the incoming carbon ion fluence amounts to 5.3×10^5 Bq cm^{-3}. This corresponds to 98 and 350 Bq cm^{-3} Gy^{-1} if the maximum and average[2] dose of 5.4 kGy and 1.5 kGy, respectively, is considered.

5.5 LSO Activation Studies

The pioneering work at the Lawrence Berkeley National Laboratory (LBNL) between 1971 and 1992 [Pet94], where the first steps towards using heavy ions for radiotherapy were done (section 1.2.3), included a great amount of research with positron emission tomography [Tob71, Tob77, Lla88]. Nevertheless, the clinical implementation of in-beam PET had to be abandoned at LBL since the scintillator material (BGO) was activated. The reason for this was assumed to arise from the light particles produced by the use of passive beam shaping [Lla88]. At GSI, the use of the rasterscan technique [Hab93] made possible the successful implementation [Paw97] and clinical use [Eng04b] of the in-beam positron tomograph BASTEI (chapter 1, section 1.4.2). With the studies summarized in chapter 2 indicating a great improvement in the quality of in-beam PET images if the gap between the dual-head tomograph is made smaller, it became important to study whether the scintillator material for the next-generation in-beam PET detector (LSO) becomes activated by the flux of light particles leaving the patient downbeam [Gun04a, Gun04b].

---

[1] For the dose calculation the beam cross section is given by $\pi\sigma^2$, with $\sigma = $ FWHM/2.35.

[2] Calculated between 0.9 and 8 cm with the PosGen code.

5.5.1   Method

In order to maximize the amount of particles hitting the scintillators under study, two patients with only one irradiation portal were selected. A small matrix of nine LSO crystals with a total volume of about 0.6 cm^3 was placed at their masks downbeam, following the beam direction with maximum penetration depth in order to meet the expected maximum light particle flux leaving the irradiated patient. Fig. 5.11 depicts the positioning of the irradiated LSO crystals
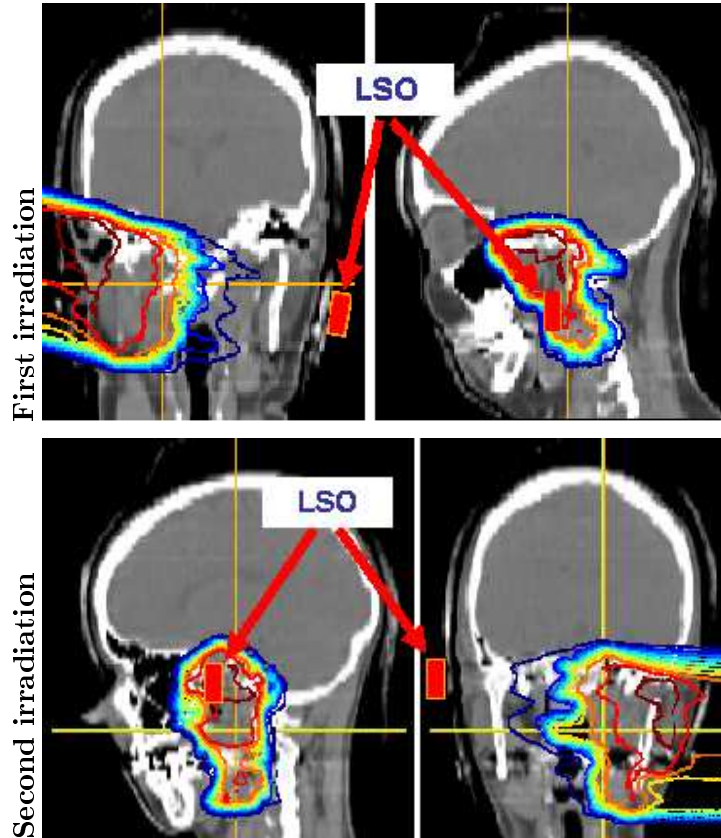
Figure 5.11: Dose distributions (frontal and sagittal views) of the two single-portal treatments in the skull base showing the irradiated LSO outside the masks. The dose distributions, plotted with iso-dose lines from 5% (dark blue) to 95% (red) of the maximum dose, are overplotted on the patient CT (grey image).

outside both patient masks. The maximum dose imparted in the field of the first irradiated patient was 1.02 Gy delivered with 1.23×10^9 ^{12}C ions with energies ranging from 126 to 258 AMeV. The second patient received a fluence of 1.29×10^9 ^{12}C ions with 113 to 255 AMeV, corresponding to a dose maximum of 1.05 Gy.

5.5.2   High-resolution γ-ray spectra and their interpretation

Spectroscopic measurements of the irradiated crystals, performed with a high-purity germanium (HPGe) detector, were compared with measured spectra acquired before the irradiation (one overnight measurement was made before the crystals were irradiated). The spectroscopic measurement of the irradiated crystals started aproximately 2 minutes after finishing the dose delivery to the second patient. The spectrum was saved after 1, 2, 4, 8, 16, 45 minutes and after 4 hours and 21 minutes. Finally, several measurements of 6 hours each were taken during

the following 4 days. Figs. 5.12 and 5.13 show the spectra obtained. The top spectrum in each row shows the overnight measurement sampled before irradiating the crystals (53 800 s). The bottom spectrum in each row was started 2 minutes after the crystals were irradiated and acquired during 15 700 s. When evaluating the photon lines shown, only peak heights greater or equal than 3σ above the background were considered. In order to attribute the energy values to the lines found the HPGe detector had been previously calibrated (Deutscher Kalibrierdienst DKD) with a radioactive homogeneous mixture and the corresponding calibration files were used (energy only). Since the calibration source (1 liter volume with $1\,\mathrm{g\,cm^{-3}}$ density) did not have the same shape and density as the crystal matrix, the efficiency calibration could not be used and, consequently, a quantitative analysis (number of decays in the crystal matrix itself) was not possible. Nevertheless, the crystals were positioned in exactly the same position before and after the irradiation so the comparison of the corresponding spectra in quantitative terms is valid. For isotope identification both the table of isotopes [Fir96] as well as its database available online [TOI04] were used.

Natural decay chains from ^{232}Th and ^{238}U

The comparison of the lines present before and after irradiating the crystals shows some peak enhancement for selected energies. In order to quantify this enhancement the count rates at the detector were calculated by considering, for each line in each measurement, the peak area above the background level. Fig. 5.14 shows two stable (top) and two enhanced (bottom) γ-ray lines which were identified to arise from the decay of isotopes belonging to the natural decay chains of ^{232}Th and ^{238}U, respectively (Fig. 5.15).

The reason for the different behaviour of the two natural decay chains lies on the presence of ^{222}Rn, a gas at normal pressure and temperature, in the ^{238}U series. While the ^{232}Th series shows no sign of activity enhancement (Fig. 5.14, top), the bottom images clearly show an increase in count rate after the measurement performed after the crystal matrix irradiation was started. It is a know fact that the presence of ^{222}Rn and its decay products constitutes a major part of airborne radioactivity [Par77]. This gaseous element must have drifted into the container surrounding the HPGe detector, which was not totally closed to the atmosphere. More importantly, the removal and later re-introduction of the crystal matrix after the irradiation changed the air conditions in the measuring container. Due to this dynamic behaviour, the decay curves shown in the bottom images of Fig. 5.14, despite clearly showing an increase in activity in respect to the activity value registered before irradiating the crystals, do not exhibit the typical decrease of activity proportional to the lifetime of the original element.

Decay of ^{176}Lu into ^{176}Hf and the 511 keV line

Fig. 5.16 shows two γ-ray lines characteristic of the decay of ^{176}Lu to ^{176}Hf. As it can be seen, no activity enhancement significantly above the measured error bars is observed. More importantly, no new γ-ray lines arise at an energy equal or close to 511 keV (Fig. 5.12) thus, from the point of view of LSO activation, the flux of particles leaving the patient downbeam do not pose a problem to in-beam PET imaging even for the detectors positioned at small angles with respect to the beam direction.

5.6 Influence of the Natural Radioactivity of LSO

Despite its many advantages as a scintillator for PET, the lutetium in LSO contains approximately 2.6 % ^{176}Lu, a naturally occurring radioisotope with a half-life in the order of 3.8×10^{10} years. The decay of ^{176}Lu leads to a measured background rate density of ap-
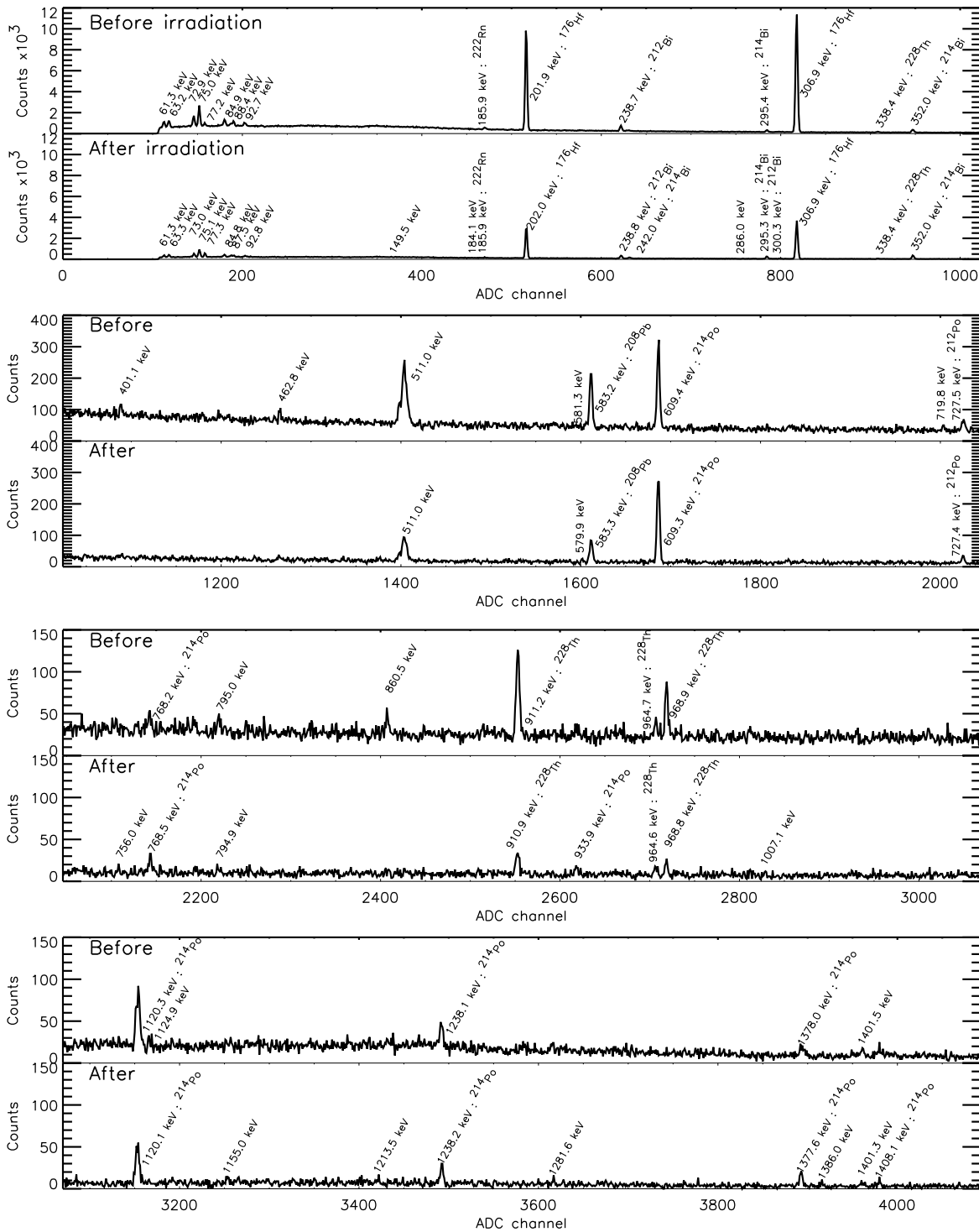
Figure 5.12: LSO activation studies with a high purity germanium (HPGe) detector. Spectra show lines of lower energy. The acquisition times are 53 800 s and 15 700 s for the spectrum measured before and after the crystal irradiation, respectively.
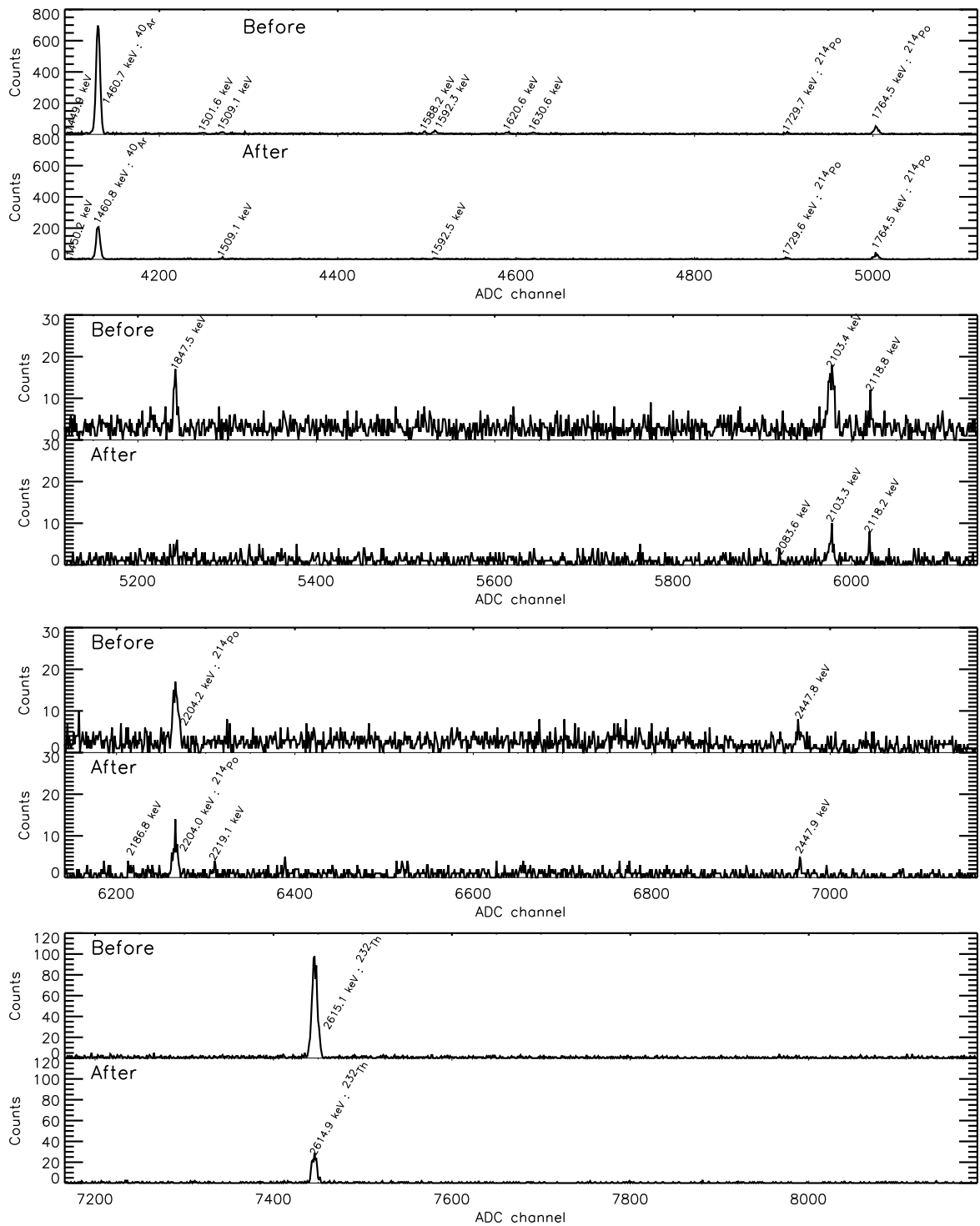
Figure 5.13: LSO activation studies with a high purity germanium (HPGe) detector. Spectra show lines of higher energy. The acquisition times are 53 800 s and 15 700 s for the spectrum measured before and after the crystal irradiation, respectively.
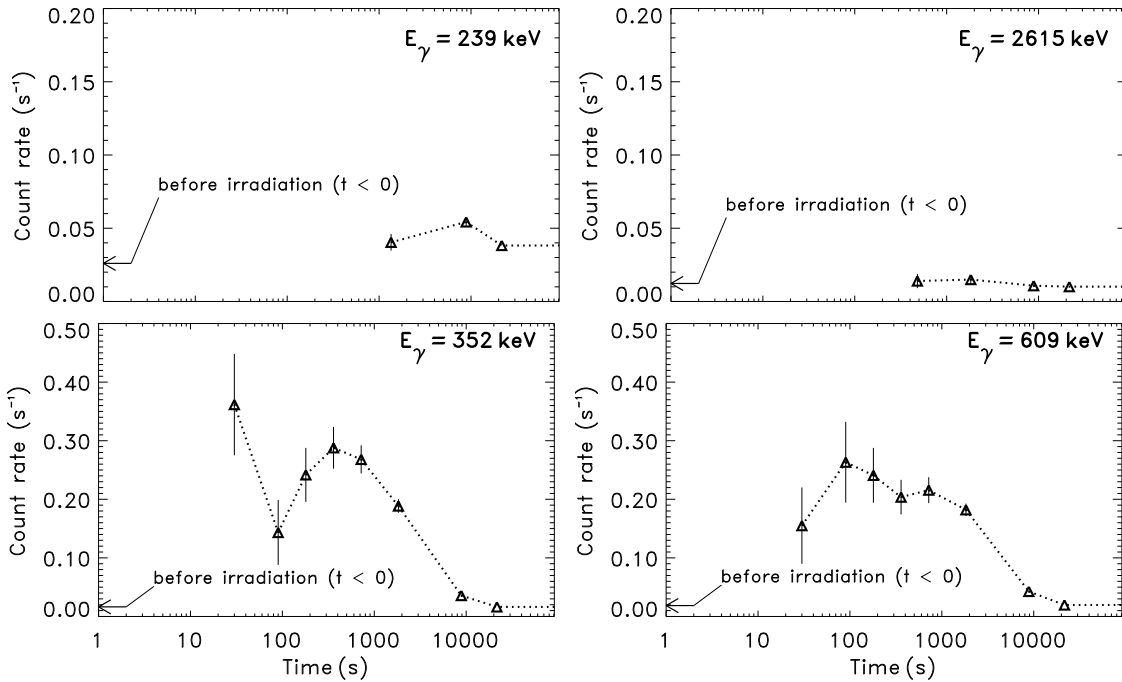
Figure 5.14: Count rates from the two stronger γ-ray lines from the ^{232}Th (top) and ^{238}U (bottom) series.
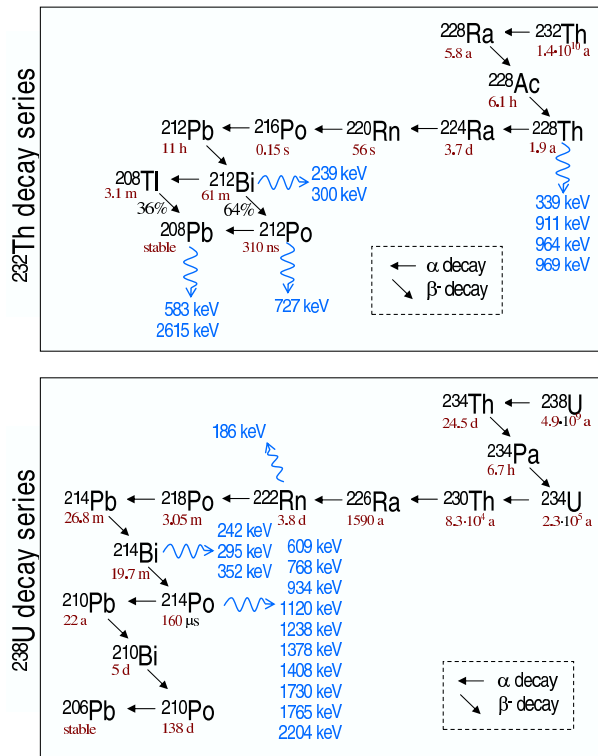
Figure 5.15: Decay chains of the natural elements ^{232}Th (top) and ^{238}U (bottom), with the half lives of each isotope shown below it.
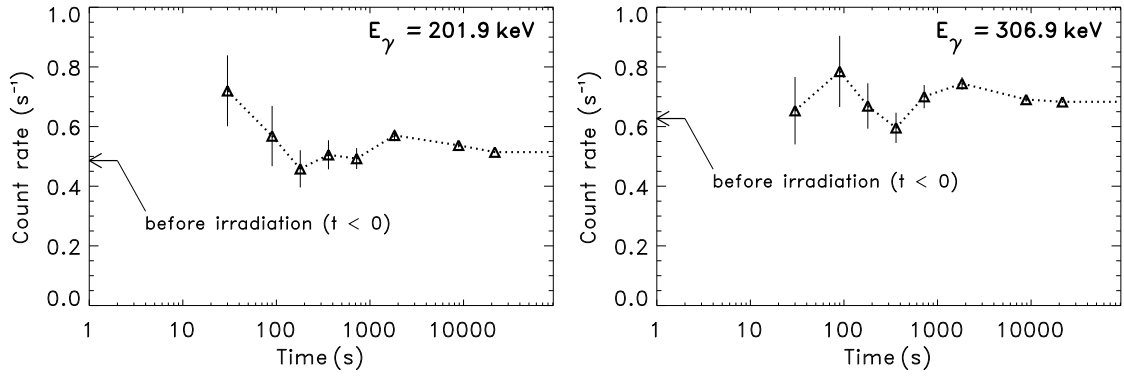
Figure 5.16: Count rates from two γ-ray lines from the decay of ^{176}Lu to ^{176}Hf.

proximately 240 Bq cm^{-3} of scintillator material [Hub02]. Its decay scheme is shown in Fig. 5.17, together with the resulting natural radioactivity measured in an LSO crystal with $10.5 \times 10.7 \times 13.7$ mm^3 [Hub02]. Also shown is the kinetic energy spectrum of the β^--decay, calculated with a non-relativistic approximation according to [Mar66].

The shape of the background spectrum from LSO is thought to arise from γ-ray absorption within the crystal itself, mostly by photoabsorption but also by Compton scattering. This results in a shift to higher energies of the background spectrum in respect to the β^- energy curve. The peak at aproximately 700 keV results most probably from the simultaneous detection of the β^- particle, with a most probable energy value of about 400 keV, as shown, together with the γ-lines with energies of 202 and 88 keV.

In order to estimate the random coincidence rate expected with the LSO/APDA detectors two energy windows typically installed in PET systems were considered and are depicted in Fig. 5.17 with vertical lines. These are 400 - 600 keV (dot-dashed) and 350 - 650 keV (dotted), corresponding to a selection of events within 511 keV $\pm \frac{17\%}{22\%}$ and 511 keV $\pm \frac{27\%}{31\%}$, respectively. Within the narrower energy window the activity density is 66 cps cm^{-3}, whereas the wider energy window yields 97 cps cm^{-3}.
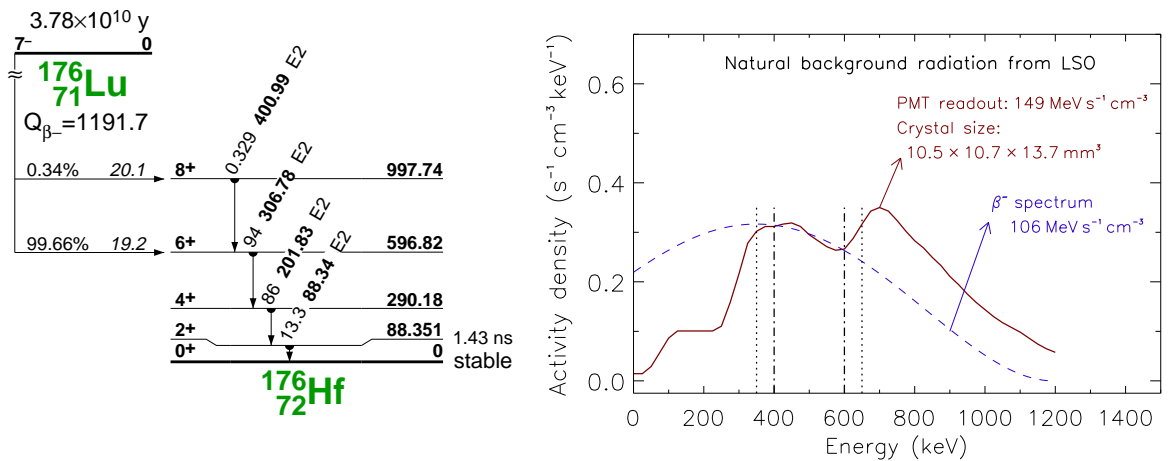
Figure 5.17: Decay scheme of ^{176}Lu into ^{176}Hf by β^- emission (left), taken from [Fir96], and measured natural radioactivity from LSO (right), taken from [Hub02]. Also shown is the calculated kinetic energy spectrum of the β^--decay.

5.6.1 Extrinsic and intrinsic true and random coincidences

The random coincidence rate R_i that results from the activity density calculated in the previous section arises from the intrinsic activity of LSO. In a PET measurement, the total random coicidence rate is the sum of R_i with the extrinsic random coincidence rate R_e, with R_e arising from the physics processes inherent to the sampling of annihilation radiation. Fig. 5.18 illustrates the contribution of the intrinsic and extrinsic event rates to both the true and the random rates measurable in an LSO-based PET scanner.
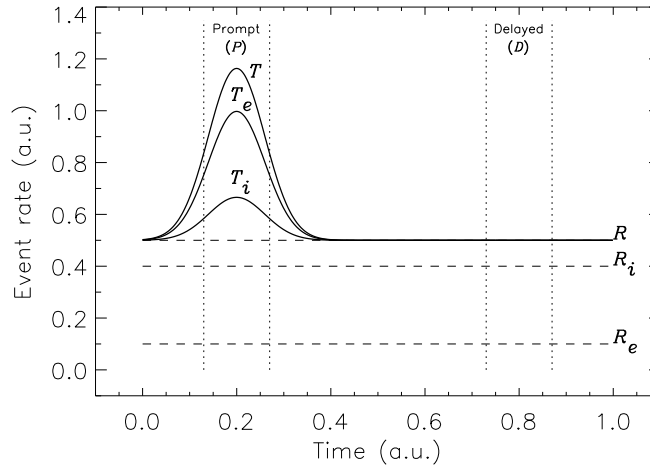
Figure 5.18: Illustration of the intrinsic and extrinsic true and random coincidence rates in LSO-based PET scanners. The intrinsic contribution arises from the natural radioactivity of LSO and is fixed for a given tomograph. It can be quantified with a simple blank scan. The extrinsic rates depend on the intensity and geometrical distribution of the β^+ activity being measured.

The prompt P and delayed D time windows plotted in Fig. 5.18 with vertical dotted lines represent the basis of the so-called delayed coincidence random suppression method, currently implemented in most modern PET scanners [Bad96]. In summary, this method calculates the true event rate T occurring in each LOR by subtracting D from P, with D being the event rate measured in a time window arbitrarily delayed in respect to the prompt coincidence time window. For random coincidence rates stationary in time $D = R$. The intrinsic true coincidence rate T_i shown in Fig. 5.18 arises from events where a ^{176}Lu nuclide undergoes β^--decay in one detector and emits a prompt γ-ray that is absorbed in a second detector.

The delayed coincidence random suppression method is sufficient for PET systems without intrinsic detector radioactivity or for PET measurements where the intrinsic detector radioactivity is much smaller than the signal activity being sampled [Wat04]. For in-beam PET, though, the measured activity density lies orders of magnitude below that sampled in human PET studies (section 6.1) and a detailed analysis of both T_i and R_i is necessary in order to compare their values with the expected in-beam PET signal T_e at future planned tomographs. The influence of T_i onto realistic in-beam PET images acquired with BASTEI was studied in [Lau00] by assuming the BGO material substituted with LSO in that tomograph. In the following section that study is complemented by calculating the value of T_i expected for a closed-ring and a dual-head tomograph with narrow gaps (Fig. 5.1), and extended by comparing the expected intrinsic random coicidence rate R_i with the in-beam PET signal T_e.

5.6.2 Extrapolation to tomographs with intrinsic radioactivity

Influence of the intrinsic random coincidence rate R_i

The influence of the measured natural background from LSO on the PET images obtained by a given tomograph can be quantified by means of the so-called randoms-to-trues ratio RTR [Wat04]. In the present background considerations the RTR measured in a given LOR between two opposed pixels of a tomograph is given by

$$RTR = \frac{R_i}{T_e} = \frac{2\,\Delta t\,(a_i\,V_{pix})^2}{a_e V_{vox}\,\Omega_{vox}\,P_{\gamma\gamma\,esc}\,\epsilon_{scint}^2\,\epsilon_{ph}^2}, \tag{5.3}$$

with symbols and values defined in Table 5.4. An intrinsic activity density a_i of 66 Bq cm^{-3}, expected for an energy window from 400 to 600 keV (section 5.6), was considered.

Table 5.4: Parameters for quantifying the randoms-to-trues ratio RTR in an LSO-based tomograph with 45 cm inner radius.

	Name	Symbol	Value	Unit
R_i	Coincidence time resolution	$2\,\Delta t$	4	ns
	Intrinsic activity density[a]	a_i	66[a]	Bq cm^{-3}
	Volume of pixel looking at LOR	V_{pix}	$1 \times 1 \times$crystal depth	cm^3
T_e	Extrinsic activity density (PET signal)[b]	a_e	200[b]	Bq cm^{-3} Gy^{-1}
	Volume of image voxel	V_{vox}	$1 \times 1 \times 1$	cm^3
	Double γ-ray escape from object	$P_{\gamma\gamma\,esc}$	not considered	
	Solid angle of image voxel	Ω_{vox}	2.3×10^{-3}	%
	Double detection efficiency for 511 keV	ϵ_{scint}^2	68 (2 cm), 86 (3 cm depth)	%
	Double photoelectric effect fraction	ϵ_{ph}^2	32 (LSO)	%

[a]Energy window: 400 - 600 keV   [b]Typical for fractionated, carbon ion tumor treatments

The RTR dependence on the activity density of the object being imaged is plotted in Fig. 5.19 for LSO, LYSO with 50 % yttrium in respect to lutetium (elemental abundance) and LGSO
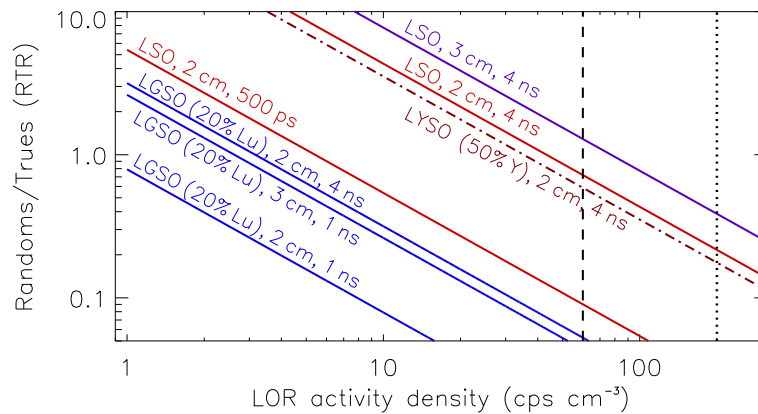
Figure 5.19: Randoms-to-trues-ratio RTR versus activity density in the object. Calculations were performed for one LOR formed by three different lutetium-based scintillators. For LSO the parameters of Table 5.4 were followed. The physical properties of LYSO and LGSO were taken from Table 4.1. The dashed and dotted vertical lines show the typical activity density for a dose maximum of 0.3 and 1 Gy, respectively, delivered with fractionated, carbon ion tumor treatments.

with 20 % lutetium in respect to gadolinium. By considering the maximum dose delivered at fractionated carbon ion tumor treatments, lying between 0.3 and 1 Gy, and a typical activity density per maximum dose unit of 200 Bq cm^{-3} Gy^{-1}, a minimum and maximum activity density of 60 and 200 Bq cm^{-3} are obtained and are shown in Fig. 5.19 with a vertical, dashed and vertical, dotted line, respectively. These lines delimit, therefore, the region of interest to analyze for fractionated, carbon ion tumor treatments[1].

The analysis of Fig. 5.19 allows to see that an RTR close to unity is expected for low dose portals if LSO crystals with radial depth of 2 cm, or greater, and a coincidence time resolution of 4 ns are implemented. If the time resolution obtained with the detectors is decreased by about one order of magnitude, down to 500 ps, than Fig. 5.19 shows that the maximum RTR expected does not exceed 0.1. A coincidence time resolution of 500 ps is expected with LSO/APDA detectors under development[2] for PEM [San04], and has been measured [Ver05] by applying digital signal processing techniques to the timing signals of one pixel of the LSO/APDA detectors described in chapter 4. If the tomograph consists of crystals of LGSO with 2 cm radial depth, the maximum RTR expected reduces to approximately 5 %.

A value of RTR = 1 means that the PET signal is immersed in an activity background with the same intensity. The effects onto in-beam PET images of an RTR = 1 and RTR = 0.1 scenarios were simulated for the head and neck treatment studied in section 2.6.1, with the results displayed in Figs. 5.20 and 5.21, respectively. Table 5.5 shows the simulation details regarding the statistics considered for two tomographs, with $\phi = 0\,^\circ$ and $\phi = 46\,^\circ$ denoting a closed ring and a dual head tomograph (Fig. 2.1), respectively.

Table 5.5: Simulation of in-beam PET imaging with intrinsic detector activity (Fig. 5.20).

	~ 1.0		~ 0.1	
Randoms-to-trues ratio RTR				
Tomograph geometry	$\phi = 0\,^\circ$	$\phi = 46\,^\circ$	$\phi = 0\,^\circ$	$\phi = 46\,^\circ$
Total extrinsic true events simulated ($\times 10^6$)	2.5	2.5	2.5	2.5
Target volume (dm^3)	1.3	1.3	1.3	1.3
Average event density ($\times 10^6$ events dm^{-3})	1.9	1.9	1.9	1.9
Total extrinsic true events detected ($\times 10^3$)	237	174	237	174
Total intrinsic randoms simulated ($\times 10^6$)	7.5	7.5	0.75	0.75
Volume of image space with randoms (dm^3)	4.1	4.1	4.1	4.1
Average randoms density ($\times 10^6$ randoms dm^{-3})	1.8	1.8	0.18	0.18
Total intrinsic randoms detected ($\times 10^3$)	815	544	81	54

The images in Figs. 5.20 and 5.21 can be directly compared with the background-free reconstructions shown in Fig. 2.11. This comparison allows to conclude that an RTR = 1 scenario is clearly unacceptable since the positron annihilation signal is immersed in a sea of activity which disturbs image evaluation. This observation compromises the application of LSO-based detectors for in-beam PET (Fig. 5.19) if a coincidence time resolution at the nanosecond scale is applied. Nevertheless, the application of modern readout schemes allowing digital signal processing techniques to be implemented has proven to be able to lower the coincidence time resolution obtained with conventional nuclear electronics. Such techniques are mandatory for future, LSO-based, in-beam PET readout schemes since only a coincidence time resolution of 500 ps yields an acceptable RTR of 0.1 (Fig. 5.21). An alternative to reduce the background activity from the scintillator is to make use of recently available LGSO crystals [Shi04], containing

---

[1] For the same dose, a higher signal activity is expected for ion species with lower atomic number than ^{12}C due to their lower stopping power.

[2] This 500 ps coincidence time resolution will be achieved within the PEM project by means of digital pulse processing and with a double scintillation light readout per crystal [Lec02], with crystals of 20 cm depth.
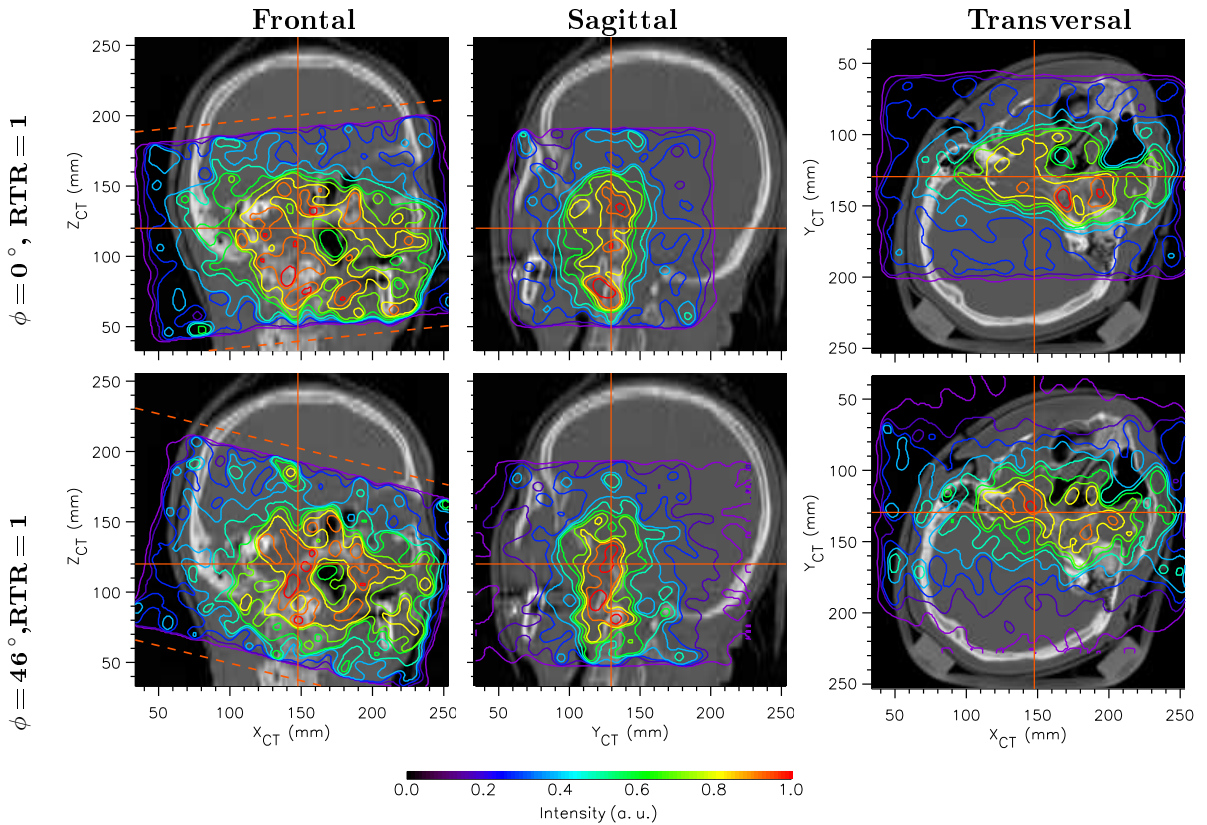
Figure 5.20: Influence of a high LSO background activity (RTR = 1) onto reconstructed images of a head and neck simulated treatment. The dashed lines in the frontal views show the limits (top view) of the dual-head tomograph considered.
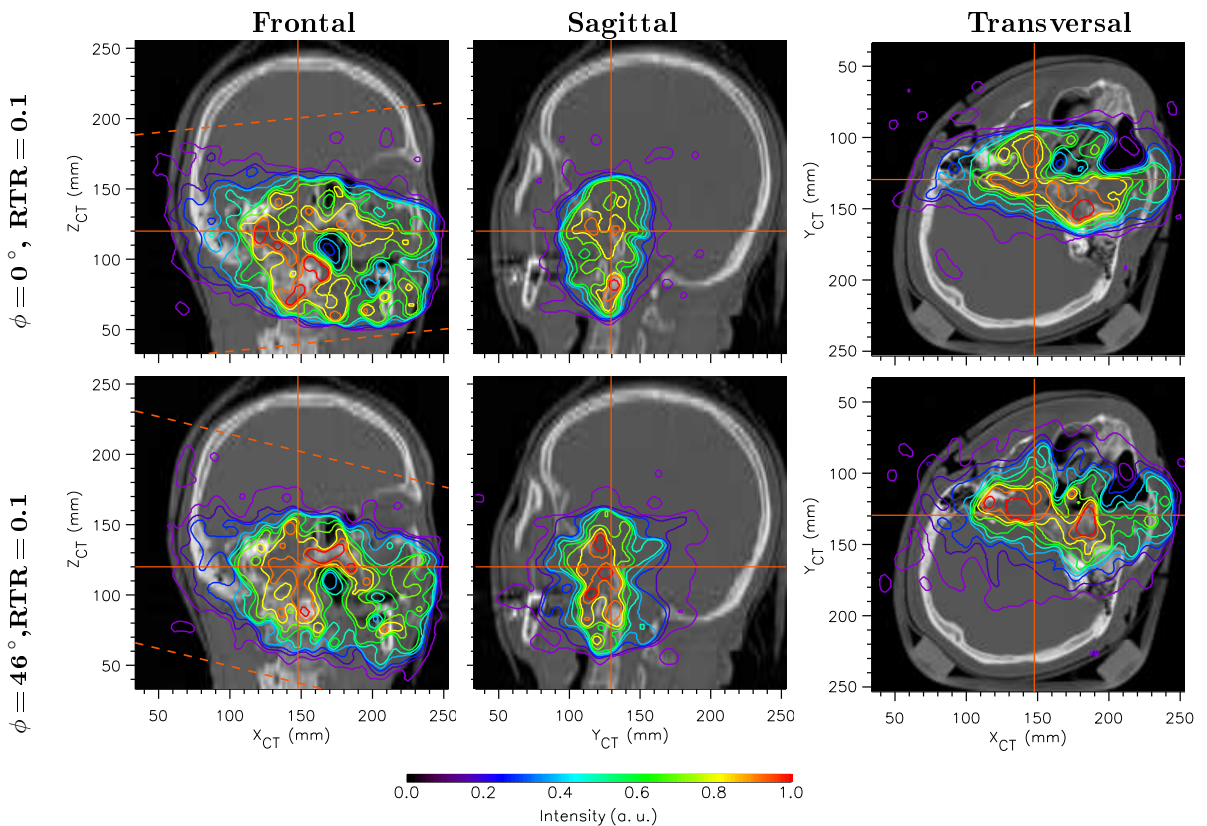
Figure 5.21: Influence of a low LSO background activity (RTR = 0.1) onto reconstructed images of a head and neck simulated treatment. The dashed lines in the frontal views show the limits (top view) of the dual-head tomograph considered.

80 % less lutetium but providing less detection efficiency than LSO, as shown in Table 5.6.

Table 5.6: Coincidence detection efficiencies[a] (%) of several modern scintillators.

Scintillator	BGO	LSO	LGSO	GSO	LaBr$_3$
2 cm radial depth	11.9	7.0	4.0	3.6	0.6
3 cm radial depth	14.4	8.8	5.4	4.8	1.0

[a]Only double photoelectric events are considered.

Influence of the intrinsic true rate T_i

As illustrated in Fig. 5.18, not only R_i contributes to the background measured in the total true coincidence rate T. The intrinsic true rate T_i, arising from events where a ^{176}Lu nuclide undergoes β^--decay in one detector and emits a prompt γ-ray that is absorbed in a second detector, also contributes to the background measured. In order to estimate T_i, a blank scan performed with the ACCEL LSO-based tomograph [Wat04], yielding $T_i = 600$ cps measured with an energy window of 350-650 keV, was extrapolated to the dual-head tomograph with small gaps depicted in Fig. 5.1. This extrapolation takes into account the different volumes of the tomographs only and yields $T_i = 750$ cps and $T_i = 1134$ cps for 20 and 30 mm crystal depths, respectively. The obtained values were then normalized to the mid-plane between the detector heads and further attenuated by 46 % due to the presence of the patient[1] in the FOV of the tomograph [Lau00]. In the same publication the ratio of the intrinsic-to-extrinsic true coincidences, T_i/T_e, was estimated to be about 3.3 % for a narrower energy window of 400-600 keV and for a crystal depth of 20 mm [Lau00].

The value of T_i per unit area can now be directly compared with the extrinsic true coincidence rate T_e per unit area expected for this tomograph when imaging tumor treatments with carbon ion irradiation. For that, the average size of all clinical in-beam PET images acquired with BASTEI during carbon ion irradiation up to this date was considered: $22.3 \times 14.0 \times 15.1$ cm^3. To this volume corresponds an area in the midplane between the two detector heads of about 312 cm^2. By taking into account a detection efficiency of approximately 4 % for BASTEI at the isocenter versus the 10 % covered also at the isocenter with the dual-head tomograph in Fig. 5.1, the typical 100 cps event rate measured with BASTEI scales up to 250 cps if a crystal depth of 20 mm is assumed. This corresponds to an expected signal activity density T_e normalized to the mid-plane between the detector heads of 0.8 cps cm^{-2}, which increases to 1.0 cps cm^{-2} if the LSO crystal depth is extended to 30 mm. The values estimated are

Table 5.7: True coincidence rates due to the natural background from LSO. A dual-head tomograph with 90 cm diameter, 30 cm axial length, 2 or 3 cm radial depth and an opening angle of about 40° (Fig. 5.1) was considered in the calculations.

Energy window	400-600 keV		350-650 keV	
Crystal depth	20 mm	30 mm	20 mm	30 mm
Intrinsic true coincidences T_i (cps)	-	-	750	1134
in mid-plane (cps cm^{-2})	-	-	0.30	0.45
attenuated (cps cm^{-2})	-	-	0.14	0.21
Extrinsic true rate T_e[a]				
in mid-plane (cps cm^{-2})	-	-	0.8	1.0
T_i/T_e (%)	3.3[b]	$\geq$ 3.3	17.5	26

[a]Extrapolated from BASTEI, energy window 250-850 keV   [b]From [Lau00]

---

[1] Calculated for head and neck treatments only. Pelvis treatments yield a larger number of attenuated photons and, therefore, a further reduced T_i.

shown in Table 5.7. Its analysis allows to conclude that, as with the intrinsic randoms rate R_i, a better ratio of the intrinsic-to-extrinsic true coincidences, T_i/T_e, is obtained with a crystal depth of 20 mm if an energy window of 350 - 650 keV is considered. This ratio amounts to 17.5 %, which is a background value to be added to the RTR ratio. Although an estimation of T_i can be made by performing a blank scan and computing the photon attenuation on the basis of the patient CT, the noise inherent to very low statistics data sets is difficult to remove. Therefore, a minimum energy window of 400 - 600 keV is an important condition to take into account for a lutetium-based tomograph imaging low intensity β^+-activity distributions.

In summary, the best in-beam PET performance with LSO/APDA detectors is expected with an energy window smaller or equal to 400 - 600 keV and with a coincidence time resolution of 500 ps. An undesirable RTR close to unity is expected if lower dose portals are imaged with LSO crystals with a radial depth of 20 mm and 4 ns coincidence time resolution. This fact has been confirmed experimentally in [Cre05c]. Although random correction can be applied online to yield true counts in high-statistics human PET applications [Boe03], the low statistics sets of in-beam PET result in high variations of T_e and R_i due to noise, which may yield unsatisfactory random suppression. More importantly, recent accelerator developments to be implemented at future heavy ion therapy units, e.g. in Heidelberg, will compress the treatment duration by decreasing the time windows between beam extractions. The random suppression solutions described in chapter 6, allowing in-beam PET data taking during particle extractions, are not suited for subtracting an activity background stationary in time. In other words, the intrinsic true coincidence rate T_i arising from the natural background activity of LSO was estimated in [Lau00] to be about 3.3 % of the in-beam PET signal[1], which does not influence significantly in-beam PET images acquired with BASTEI. This fact is confirmed for a next-generation, closed ring or dual-head tomograph but, the impossibility of efficiently suppressing the intrinsic random coincidences R_i suggests that digital signal processing techniques [Lec02, Ver05], decreasing the coincidence time resolution to 500 ps, are a main requisite for an LSO-based, in-beam PET tomograph. A modern, fast, high light-yield, radiation hard scintillator [Tan98] like LGSO [Shi04], containing 80 % less lutetium than LSO, is also a choice if conventional nuclear electronics are to be used. With slightly higher detection efficiency[2] (ϵ_{det}^2) in respect to GSO (Table 5.6), a lutetium-free scintillator, the eventual choice of LGSO relies on its two times larger light yield (Table 4.1), which is an important factor for achieving optimum timing. This, in turn, is an important parameter in order to apply random suppression during particle extraction, as described in chapter 6.

5.7 Time-of-Flight for In-Beam PET

Recent developments have resulted in scintillators with high light yield and very fast fluorescence time constant. Best examples, shown in Table 4.1, are lanthanum bromide, $LaBr_3$, and the very recently discovered cerium bromide, $CeBr_3$, with light yields twice that of LSO and decay times of 35 and 17 ns, respectively. Together with LSO, these scintillators offer the possibility of using the time difference between the moment of detection of the two opposed γ-rays. This so-called time-of-flight (TOF) difference allows to restrict the location of the positron annihilation point within the LOR formed by the two hit detectors, as shown in section 5.7.1. For LSO-based detectors, it has long been foreseen that improvements in the readout electronics that could lead to a coincidence time resolution of 500 ps FWHM would reduce the noise variance in conventional PET imaging by a factor of 5 [Mos99a], i.e. for the same image quality the scan time may be 5 times shorter. Recently, a coincidence time resolution of 165 ps

---

[1] With an energy window of 400 - 600 keV and a scintillator depth of 20 mm.
[2] For a given tomograph, the scintillator-dependent ϵ_{det}^2 is multiplied by the scintillator-independent coincidence solid angle Ω_{coinc} in order to obtain the total coincidence detection efficiency.

FWHM has been measured between LaBr$_3$ and BaF$_2$ crystals, which can be extrapolated down to 73 ps FWHM if two LaBr$_3$ are used [Glo04]. Nevertheless, a slightly higher value of 313 ps FWHM has been reported [Kuh04a] betwen two LaBr$_3$-based detectors with an Anger-logic-based readout scheme [Kuh04b], i.e. with the reduced electronics channels typically installed in commercial PET scanners. These values could be reduced if a data readout allowing digital signal processing techniques to be applied would be implemented, as verified with LSO-based detectors [Var05, Ver05].

With the current trend in the coincidence time resolution of PET detectors pointing towards hundreds or even tens of picoseconds, it seems to be reasonable to analyze the impact of such developments for in-beam PET. In addition to reduce the noise background of PET images, TOF techniques gain much importance for dual-head, in-beam PET scanners due to the capability of the TOF information to reduce the longitudinal image elongation studied in chapter 2. Equally important, both for closed-ring as well as for dual-head, in-beam positron tomographs, is the immense decrease in data processing time if the TOF information is used, making in-beam TOF-PET images available even during the irradiation for tomographs with a coincidence time resolution below 200 ps FWHM [Cre05a].

5.7.1 Principles of the time-of-flight technique

Fig. 5.22 illustrates the physics principle inherent to TOF-PET. If the detectors and readout electronics of a given PET scanner provide a coincidence time resolution below the nanosecond scale, then the time difference between the arrival of the photons to each detector may be used to restrict the location of the annihilation point within the LOR formed by the two detectors. For any given LOR formed by detectors a and b, the coordinate x which gives the distance from the center of the LOR to the point where the positron annihilated, is given by $x = (t_b - t_a) \cdot c / 2$, with c being the speed of light. The spatial resolution that can be obtained for x corresponds to half the coincidence time resolution between detectors a and b. Such mechanism reduces greatly the contribution of Compton scattered and random photons arriving from outside the FOV of a 3D tomograph, therefore enhancing the signal to noise ratio of TOF-PET images [Mos04]. This makes TOF-PET attractive when imaging large objects, as is the case of tracer imaging in conventional human PET.
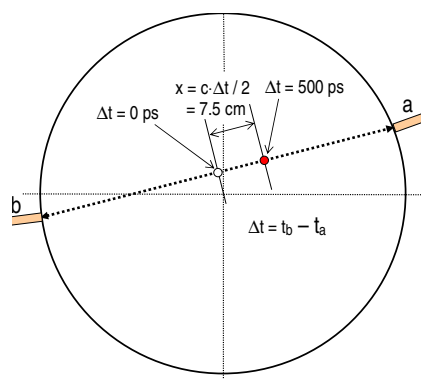
Figure 5.22: Principle of the time of flight technique in tomography. The color-filled circle depicts an annihilation located 7.5 cm from the middle of the LOR between two given detectors. This corresponds to a photon path difference of 15 cm. Therefore, the spatial resolution obtained with TOF-PET is half the coincidence time resolution of its detectors times the speed of light.

5.7.2 Time-of-flight reconstructions of real treatment simulations

During heavy ion treatments, a considerable amount of activity is transported to locations outside the FOV of the in-beam positron tomograph. In these situations, the use of TOF information may decrease the number of background events registered. But the most important advantages of an eventual in-beam TOF-PET arise if the time difference between the arrival of the photons is used to directly compute, on an event-by-event basis, the location where the positron annihilation occurred. Not only the computing time is immensely reduced, as shown in Table 5.8, but also the limitations arising from limited-angle tomography vanish if the coincidence time resolution is better than 200 ps FWHM, as shown in Figs. 5.23 and 5.24, obtained with a simulated dual head tomograph with wide gaps ($\phi = 100°$, cf. Fig. 2.1). The
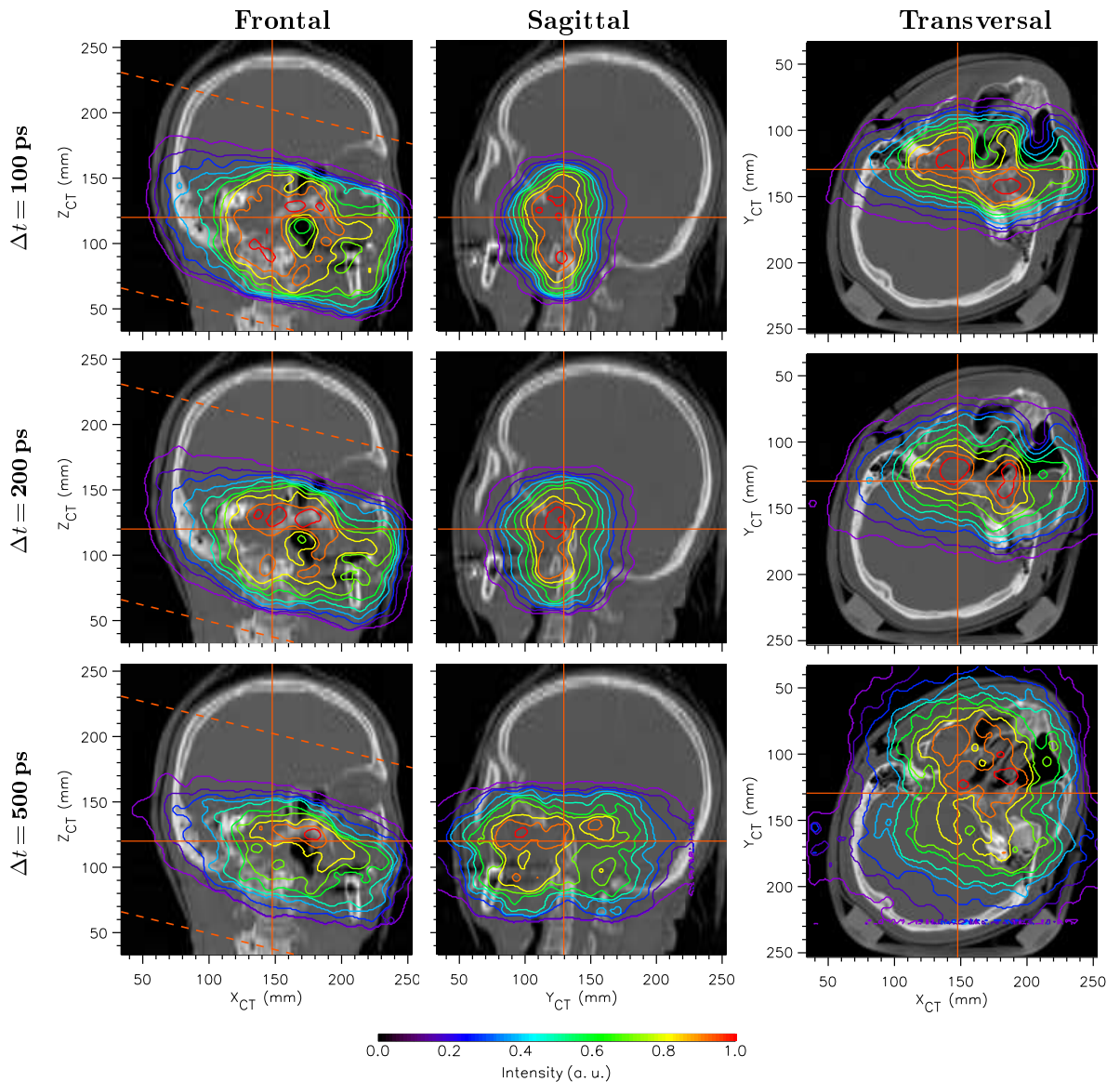
Figure 5.23: Head and neck irradiation: direct TOF reconstruction for different coincidence time resolutions Δt given in ps FWHM. All images correspond to a dual head tomograph with wide gaps ($\phi = 100°$, cf. Fig. 2.1). The dashed lines in the frontal views show the limits (top view) of the dual-head tomograph considered.

minimum coincidence time resolution mentioned, 200 ps FWHM, although not far from being achieved [Var05, Ver05, Mos04], is still a technological challenge for commercial PET systems.

The analysis of Figs. 5.23 and 5.24 allows a minimum, useful coincidence time resolution to be estimated at 200 ps FWHM, as mentioned. This corresponds to a spatial resolution of 3 cm FWHM in the Y_{PET} axis, along which the gap with missing detectors lies (cf. Fig. 2.1). This spatial resolution is enough, as observed in the middle row in Figs. 5.23 and 5.24, to refrain the image elongation observed in Figs. 2.10 and 2.13, respectively, yielding therefore in-beam PET images that can be directly compared with the β^+-activity distribution produced in the target volume (Figs. 2.9 and 2.12 for head-and-neck and pelvis irradiation, respectively).

The most impressive results expected if TOF-PET detectors with very high coincidence time resolution, below 200 ps FWHM, would be commercialy available, are the speed with which the image becomes available to the radiotherapist after the irradiation of each portal: below 2 minutes as demonstrated in Table 5.8. This increase in image processing speed arises from the possibility to calculate at once the point of positron annihilation as soon as the coordinates of the hit detectors and the TOF information are known. Such algorithm needs to process one single iteration through the collected data only, in opposition to the 50 iterations necessary with the MLEM algorithm which, in addition, needs to cross the full image space for every pair of detectors that was triggered. Due to this last detail the processing speed of the direct
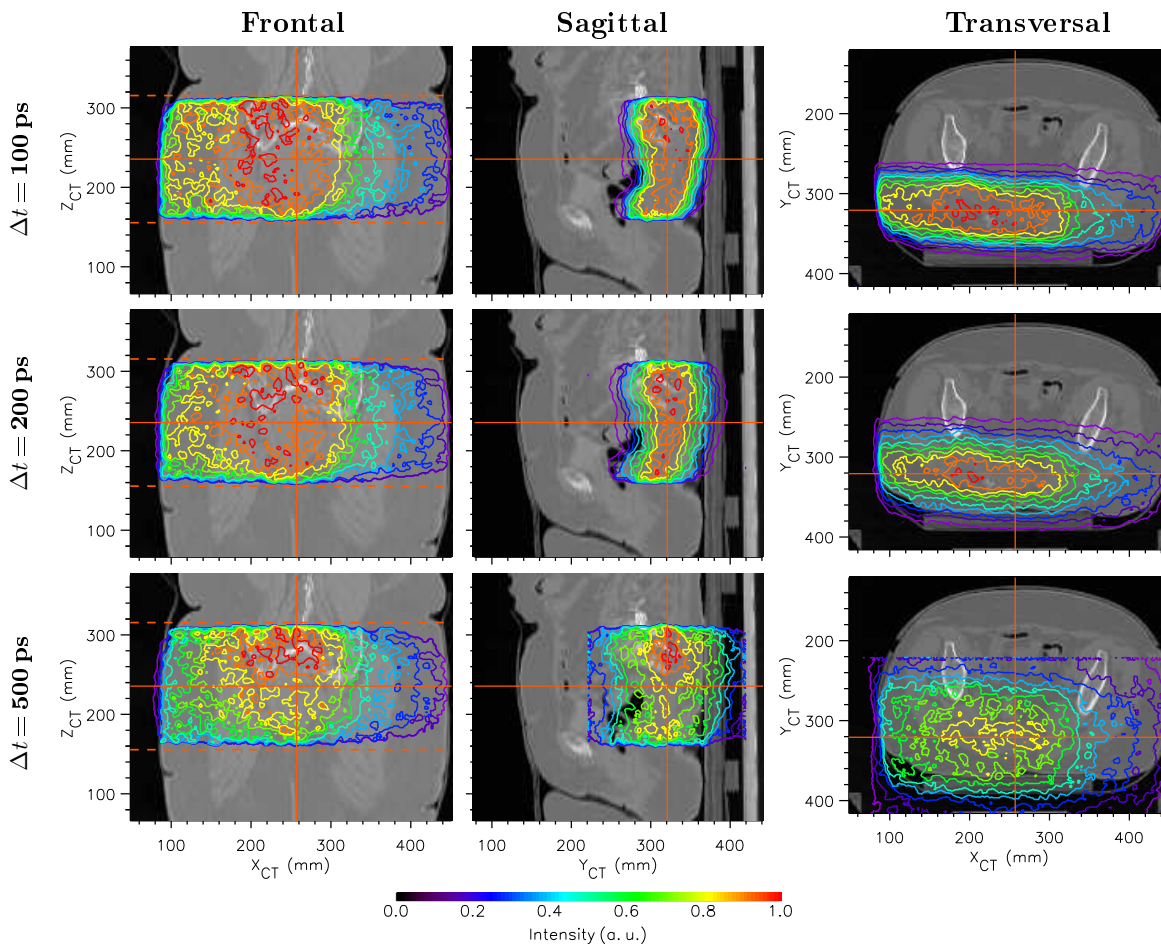
Figure 5.24: Pelvis irradiation: direct TOF reconstruction with different coincidence time resolutions Δt given in ps FWHM. All images correspond to a dual head tomograph with wide gaps ($\phi = 100°$, cf. Fig. 2.1). The dashed lines in the frontal views show the limits (top view) of the dual-head tomograph considered.

Table 5.8: Comparison of times required for image availability: direct-TOF versus MLEM-based PET imaging. Computations executed on an Intel(R) Xeon(TM) CPU 3.20 GHz dual-processor. All reconstructions regard a dual head tomograph with wide gaps ($\phi = 100°$, Fig. 2.1).

Treatment	Image size (cm^3)	Number of events	Run time TOF[a]	MLEM (50 iterations)
Head and neck	$22 \times 20 \times 20$	1.3×10^6	45 s	5 h 40 m
Pelvis	$40 \times 25 \times 25$	5.3×10^6	103 s	> 5 days

[a] The image is ready after a single iteration through the data

TOF algorithm is expected to stay below that of fast, expectation maximization algorithms like OSEM.

Since the time to obtain an image is smaller than the typical irradiation time, TOF-PET would allow the image to be processed and shown to the oncologist during the course of the irradiation, i.e. in-beam PET could be called for the first time *on-line*, in-beam PET. Moreover, a coincidence time resolution of 50 ps FWHM, i.e. 7.5 mm FWHM, would allow an image of each single pencil-like beam being delivered with the rasterscan technique [Hab93] to be obtained at once.

5.8 Summary and Outlook

The performance and in-beam imaging capabilities of two position sensitive γ-ray detectors consisting of Hamamatsu avalanche photodiode arrays (S8550) individually coupled to crystals of cerium-doped lutetium oxyorthosilicate (LSO) were presented. In a first set of experiments the imaging performance of the detectors was tested before, during and after the irradiation of phantoms of polymethylmethacralate with carbon ion beams with fluences equivalent to 1 000 typical daily therapeutic fractions. Only minor energy, time and spatial resolution deterioration was observed, with the initial values being recovered after stopping the irradiation. The line source, placed in the FOV of the detectors, was imaged as the detectors were positioned in the backward or forward cone of phantoms bombarded with the high energy ^{12}C ion beam with the mentioned characteristics. The line source images obtained revealed that it is possible, from the point of view of detector hardness, implementing a dual-head, in-beam positron camera with these detectors forming two small gaps for (1) the entrance of the therapeutic beam and (2) the escape of the light nuclear fragments produced in the patient. Thus, a double-head positron camera of large solid angle covered becomes feasible, allowing limited angle artifacts in in-beam PET images to be minimized (chapter 2). However, it must be noted that, from the point of view of in-beam PET imaging with low statistics, a more realistic experiment with decreased activity within the FOV of the detectors could also provide useful information since the activity of the line source was orders of magnitude higher than that of typical in-beam PET measurements.

In the second set of experiments, an image of the β^+-activity depth distribution created in a phantom stopping the high energy carbon ion beam was successfully performed. This was an important achievement since it demonstrated (1) the in-beam imaging capability of this detector type and (2) the sufficient radiation hardness of such detectors to be operated at a radiotherapy treatment site.

In another experiment the activation of the scintillator material LSO under therapeutical ir-radiation was investigated. An LSO crystal matrix was submitted to the flux of light particles leaving two, single-portal patients treated with carbon ions. The absence of either new γ-ray

lines or an enhancement of existing lines in the high-resolution spectroscopic measurements performed before and after irradiating the LSO crystal matrix reveals that scintillator activation does not take place in realistic therapeutic conditions.

Due to the small amount of ^{176}Lu, a natural radioactive isotope, in LSO, the influence of the natural background activity of LSO onto the random and true coincidences expected for an LSO-based tomograph was addressed. It was seen that the random coincidences count rates arising from this background can compromise the use of LSO for in-beam PET scanners due to the low-intensity in-beam PET signal. Conventional random suppression techniques applied in nuclear medicine PET imaging fail for in-beam PET measurements during particle extraction, which is a mandatory requisite for next-generation in-beam positron tomographs due to the optimized usage of ion accelerators (chapter 6). This means that, in order not to compromise the quality of the low-statistics in-beam PET images, a modern readout with digital signal processing, providing a coincidence time resolution of 500 ps, is mandatory.

Finally, the impact of recent developments in ultra-fast timing detectors, potentially allowing the implementation of the time-of-flight technique onto commercial PET scanners, was extrapolated to in-beam PET. It was seen that TOF techniques gain much importance for dual-head, in-beam PET scanners due to the capability of the TOF information to reduce the image elongation that characterizes limited-angle tomography. Equally important, both for closed-ring as well as for dual-head, in-beam positron tomographs, is the immense decrease in data processing time if the TOF information is used, making in-beam PET images available even during the irradiation for tomographs with a coincidence time resolution below 200 ps FWHM.

In summary, the obtained results indicate that LSO, a fast, high light-yield scintillator material, is best suitable for in-beam PET when its time output is read with digital signal processing techniques achieving 500 ps coincidence time resolution. With this constraint satisfied, its combination with APDA forms a feasible concept for the compact, magnetic field resistant detectors required for in-beam PET applications. There may be an increased interest in such dedicated PET systems in the future since several clinical heavy ion facilities are planned [Hea98, Sie04] and, furthermore, the in-beam PET method has also the potential to monitor the precision of ion therapy with lighter species [Par04, Par05a, Fie05].

Chapter 6

Suppression of Random Coincidences during Particle Extraction

6.1 Motivation

The counting statistics of in-beam PET is generally low with consequences to the signal-to-noise ratio of the reconstructed images. The reasons for this are twofold. First, the counting statistics are limited by the dose applied to the patient, delivered mostly in 20 fractions[1] [Sch02b] with usually two beam portals. Typical activity densities induced at the tumor therapy irradiation reach about $200\,\mathrm{Bq\,cm^{-3}\,Gy^{-1}}$, with the dose per portal ranging between 0.3 and 1 Gy. This contrasts with activity density values of 10^4 to $10^5\,\mathrm{Bq\,cm^{-3}}$ in human PET tracer imaging and even $10^6\,\mathrm{Bq\,cm^{-3}}$ in animal PET studies. In addition, current limitations arise from the fact that in-beam PET data, measured at beams with a sub-μs time structure due to the accelerator radiofrequency (RF), are highly corrupted by random coincidences. These arise from prompt γ-rays following nuclear reactions of the projectiles with the atomic nuclei of the tissue. As outlined in section 6.2, they cannot be suppressed with random-correction techniques from conventional PET [Paw97, Par02b]. Therefore, in-beam PET images are reconstructed taking into account merely events registered in the pauses (~ 2-$4\,\mathrm{s}$) between the beam macropulses ($\leq 2\,\mathrm{s}$, Fig. 1.19). For a given detector geometry, the only way for improving image quality is the efficient utilization of the annihilation photons available.

Furthermore, and more important than improving image quality, is the fact that recent accelerator developments implementing optimized beam extraction techniques result in a much reduced timing window for in-beam PET data taking if the presently installed acquisition technique is applied. The synchrotron proposed for the clinic in Heidelberg will use the RF knock-out[2] extraction method [Hir92] with variable extraction time between 1 and 10 s and multiple beam extraction at the same flat top [Dol00]. This yields great advantages [Eic03] both for respiration-gated treatments as well as for reducing the treatment duration using the rasterscan beam delivery technique [Hab93]. With injection and acceleration times of about 30 μs and 1 s, respectively, this results in a beam delivery duty factor[3] D_f between 8 and 93 %,

---

[1] The less frequent treatment of locally advanced adenoid cystic carcinomas [Sch03d] or spinal chordomas [Sch03a] applies 6 fractions with carbon ion irradiation complemented with photon irradiation by means of intensity modulated radiation therapy (IMRT).

[2] In summary, the RF knock-out method consists in applying a transverse electric radio-frequency-field (RF) with a frequency synchronous to the betatron frequency of the particles in the ring [Dol00]. Due to this excitation the particles are moved from the inner, stable region of their trajectories to outer, unstable ones. After a few turns in the ring the particles are driven through electrostatic and magnetic septa into a trajectory leading them out of the ring (extraction).

[3] Duty factor D_f of an accelerator is the ratio $D_f = \Delta t_M / T_M$, with Δt_M being the macropulse duration (beam extraction, $\sim 2\,\mathrm{s}$ at the present GSI therapy unit) and T_M being the time of a synchrotron acceleration cycle, comprising beam injection, acceleration and extraction (presently 5 s at GSI).

i.e. extreme cases of accelerator optimization could yield only 7 % of the (reduced) irradiation time available for in-beam PET data taking, making in-beam PET unfeasible if a method for random suppression during particle extraction [Eng05c] is not implemented.

One immediate consequence of the implementation of such a method, also mentionable as a motivation, is the applicability of in-beam PET to cyclotron-delivered therapeutic ion beams [Cre05d], not possible without random suppression during particle extraction because of the continuous particle delivery behaviour of cyclotrons (i.e. $D_f \sim 100\,\%$).

For these reasons, two methods for suppressing the micropulse-induced random coincidences have been proposed [Eng05c] and were tested at the GSI medical beam line [Cre05d] with results described below.

6.2 Methods for Random Correction

It has been shown that the noise introduced by random coincidences is an important limiting factor of count-rate performance for PET cameras operating in 3D mode [Bad96, Spi98]. The number of random coincidences may be reduced by altering the camera geometry to restrict the FOV for single events [Spi98] or by reducing the coincidence resolving time of the system. Once these factors have been minimized, the number of random coincidences on a particluar line-of-response (LOR) can be corrected in conventional PET following either the delayed coincidence method or the singles count rates method. The delayed coincidence method is more common in the current generation of cameras. It assumes the measured prompt count rate C_m at a given LOR to be the sum of the true coincidence count rate C_t with the random count rate C_r, provided C_r is stationary in time. C_r is measured at a time significantly greater than the coincidence resolving time of the detectors and subtracted from C_m for each LOR. In the singles count rates method, singles rates from each individual detector element are collected and used to account for the random count rate of each LOR with the relation

$$C_r = 2\,\Delta t\,C_i\,C_j, \tag{6.1}$$

where C_i and C_j are the singles count rates in detectors i and j forming LOR ij and $2\,\Delta t$ is the time resolution of the system. The application of both methods to in-beam PET fails because during particle extraction C_r is not constant in time due to the existence of a microstructured beam delivery [Par02b].

6.2.1 The time microstructure of the beam

During beam extraction, a correlation between the moment of arrival of the carbon ions and a given phase of the RF-signal from the accelerator has been found [Par05b]. This correlation is depicted in Fig. 6.1 for a given beam energy and intensity (10^7 ions/s). During each RF period T_{RF} the ions arrive within a time window Δt_{bunch}. The width of Δt_{bunch} depends on the beam energy and, therefore, on T_{RF}, and is independent from the beam intensity up to the maximum therapy value of 2×10^8 ions/spill, which is orders of magnitude below the incoherent charge space limit of 10^{11} carbon ions/spill of the heavy ion synchrotron SIS[1] at GSI.

At the tumor therapy at GSI, the ^{12}C beam energy ranges from 88.83 to 430.10 AMeV, corresponding to T_{RF} from 480 down to 250 ns, respectively. The correlation between T_{RF} and the beam relativistic kinetic energy K is given by

$$T_{RF} = \frac{P_{SIS} \cdot f(E)}{n_{SIS} \cdot c} \cdot \frac{K + m_o c^2}{\sqrt{K^2 + 2K m_o c^2}}\,, \tag{6.2}$$

---

[1] Schwerionensynchrotron.
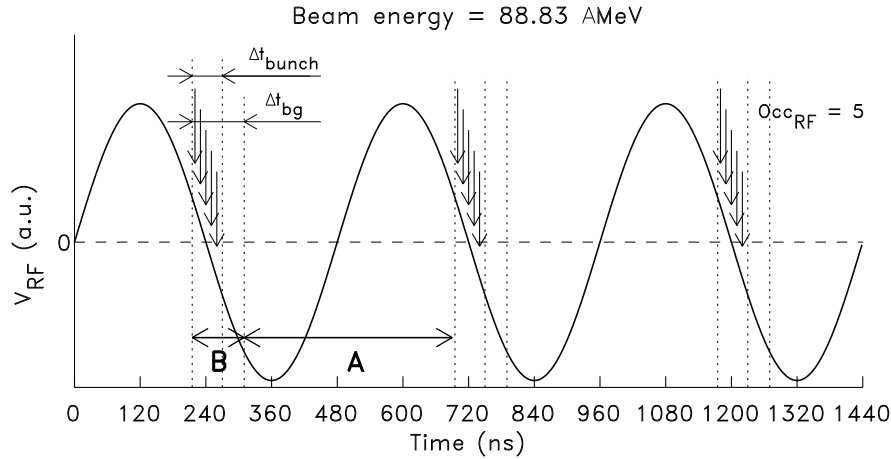
Figure 6.1: Correlation between the time of particle arrival, illustrated schematically with arrows, and RF-phase (arbitrarily set to π), depicted for a given beam energy and intensity (10^7 ions/s). The RF-occupancy occ_{RF} in the example displayed is 5, with $occ_{RF} = I \cdot T_{RF}$ and I the beam intensity. The letters A and B refer to the time windows outside the microbunch (A) and inside the microbunch with the corresponding high photon yield (B, bunch).

with values and units described in Table 6.1. The particle trajectory factor $f(K)$ arises from the different oscillations about the synchrotron perimeter that the particles undergo for a given energy, with $f(K)$ decreasing with increasing energy.

Table 6.1: Parameters correlating beam energy and RF-period.

Name	Symbol	Value
Perimeter of synchrotron	P_{SIS}	216 m
Particle trajectory factor	$f(E)$	1.091 to 1.008
Number of concomitant bunches	n_{SIS}	4
Speed of light in vacuum	c	2.998×10^8 m/s
Energy per nucleon	E	88.8 to 430.1 AMeV
Total kinetic energy	$K = 12 \cdot E$	1.1 to 5.2 GeV
Rest mass of ^{12}C	m_o	11 178 MeV/c^2

The time window Δt_{bunch} comprises the time slot in which the ions arrive at each RF cycle. During this time, and shortly after it (Δt_{bg} in Fig. 6.1), a high flux of γ-rays arising from nuclear reactions is emitted [Par05b]. This sub-μs periodic flux constitutes the source of the high, in-beam random rate and any in-beam random suppression method must be able to discard it.

6.2.2   The methods for in-beam PET random correction

Two methods have been proposed which allow for identifying coincident events occuring within the time window Δt_{bg} [Eng05c] and are depicted in Fig. 6.2. From timing considerations only, and accounting for the accelerator duty factor presently implemented at GSI ($\sim 40\,\%$ during patient irradiation), an increase in image statistics of up to $65\,\%$ is expected if coincidences acquired during the macropulse, but out of the micropulses, can be taken into account. The two methods rely on the synchronization of the $\gamma\gamma$-coincidences measured by the positron camera with the time microstructure of the beam, either by using the RF-signal from the accelerator

or the signal of a thin, fast particle detector placed in the beam path immediately in front of the target.
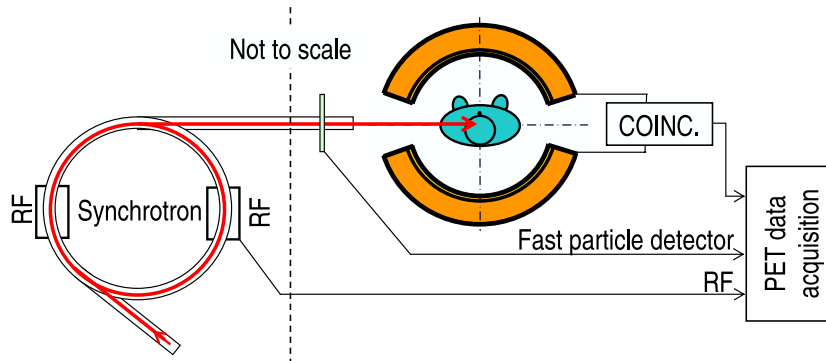
Figure 6.2: Implementation of the methods proposed for in-beam PET random suppression. Each detected $\gamma\gamma$-coincidence is correlated with the incoming ion by using either a fast particle detector or the RF signal from the accelerator.

Using the RF-signal from the accelerator

If each $\gamma\gamma$ coincidence detected with the positron camera is correlated with the phase of the RF-signal, those events occuring within Δt_{bg} can either be labeled for posterior elimination or immediately discarded by the acquisition electronics (DAQ). In this first proof-of-principle approach, the readout of all events was performed with a multi-channel, zero-suppression free, list mode data acquisition (appendix B) that allowed off-line data processing. This was necessary in order to implement a proper timing selection around Δt_{bg} since coincidence measurements between $\gamma\gamma$ events and the RF-phase had not been performed before. Furthermore, the width of Δt_{bg} depends on the time resolution of the scintillation detectors used.

For the detection of a given RF-phase a fast peak detector NIM module (phase-trigger) was developed at FZR [Hei04]. A peak detector was chosen, instead of the leading edge circuit proposed in [Eng05c], because the RF signal delivered to the medical cave where the experiment was performed has about 30 % amplitude variation [For03] depending on the signal frequency. Although the present experiment was performed at a fixed beam energy, the phase trigger was seen to be a good first solution since the long cabling between the synchrotron and the medical cave introduced low frequency base-line oscillations of $\pm\,10\,\%$ of the RF amplitude. A time measurement between RF-periods randomly separated revealed that the phase-trigger used is nearly insensitive to these oscillations with measured deviations being less than $1\,\%$ in all cases. Despite its phase detection ability independent of the pulse amplitude, this capacitor-based peak detector introduces frequency dependent delays resulting in a non-constant phase detection when used as a phase-trigger at consecutively changing beam energies, as is the case during therapeutic irradiation by means of the GSI rasterscan beam delivery [Hab93]. A phase-trigger independent of signal amplitude, frequency and base line oscillations, based on the leading edge circuit mentioned but preceeded by a high-pass passive filter and built in zero-crossing mode is proposed in [Eng05c].

Using a fast particle detector

A second method of labeling coincidences arriving during the microbunches makes use of a thin, fast particle detector (FD) placed in the beam path in front of the target. In principle, and for RF-occupancies close to unity, this approach should allow the implementation of narrower

time windows around Δt_{bg} when compared to the RF-method, as depicted in Fig. 6.3. As it can be seen, the FD method does not trigger a gate unless a particle arrives, leading to higher readout available time in the case of low occ_{RF}.
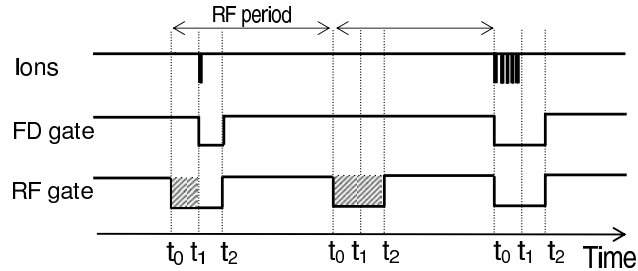
Figure 6.3: Different timing windows, automatically adjusting to the RF occupancy, are implementable with a fast particle detector FD, in contrast to the fixed-length, RF-generated windows.

For ion arrival detection a 300 μm thick, chemical vapor deposition (CVD) diamond detector [Fra04] was used. The detector was developed and optimized at the Forschungs- und Technologietransfer GmbH (FOTEC), Wiener-Neustadt, Austria. Fig. 6.4 shows its in-beam performance when 200.2 AMeV carbon ions trespass it at a beam intensity of 10^8 ions/s, corresponding to an occ_{RF} of about 32 ions/bunch. The analog signal in Fig. 6.4 shows that the CVD detector is capable of identifying single ions but, due to the 3 MHz low cutoff frequency [Fra04] introduced by the 1 nF capacity placed between the fast amplifiers reading the diamond detector (Fig. 6.5), the shaping electronics deliver a signal with undershoot and pulse pileup. Furthermore, saturation of the last amplifying stage also occurred due to the high current induced by the high ion flux in the middle of the microbunch. For these reasons, the measurements obtained with the CVD detector present noisier time spectra and spatial profiles, as described in section 6.6. Besides this fact, the results with the diamond detector are identical in all aspects to those obtained with the phase-trigger.
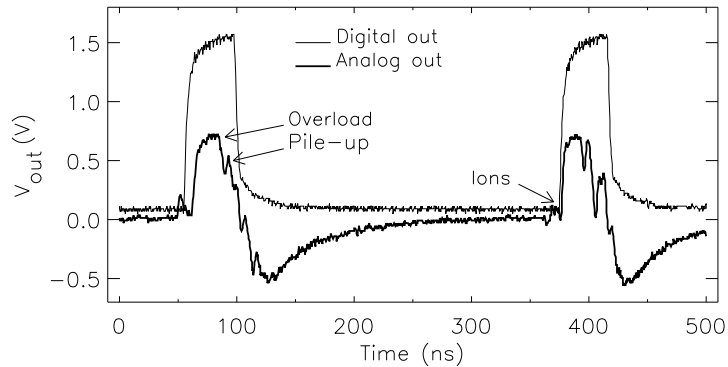
Figure 6.4: Analog and digital outputs of the diamond detector during two microbunches with an RF-occupancy of about 32. The analog signal is shown after three amplification stages with 3 MHz bandwidth each and total amplification gain of 60 dB.

6.3   Implementation and Electronics

The two methods described were simultaneously implemented with the system depicted in Fig. 6.5, partially identical to that described in section 5.2 except for two extra timing channels. Two position sensitive scintillation detectors, each consisting of 32 crystals of cerium-doped

lutetium oxyorthosilicate with $2.1 \times 2.1 \times 15\,\mathrm{mm}^3$, coupled to the 4×8 pixels of an avalanche photodiode array [Kap04], were operated in coincidence. Limited angle in-beam tomographic imaging was performed following the method summarized in [Cre04] and described in more detail in section 5.4.1. This allowed to retrieve 2D images and linear profiles of the positron emitter depth distribution under several regimes, e.g. during the extraction pauses or during the beam extractions, inside and outside the microbunches.

For every detected $\gamma\gamma$ coincidence a readout of the energy signal in all imaging pixels (64) is performed, which allows for applying energy selection during off-line data evaluation. Further, the time differences between the detected $\gamma\gamma$ coincidence and the RF-phase (TAC 3: $\gamma\gamma$-RF) were recorded, as well as the particle crossing the diamond detector (TAC 2: $\gamma\gamma$-ion). The accelerator status was also recorded by sampling the extraction signal. Finally, all detected $\gamma\gamma$ coincidences signaled by the SCA output of TAC1 were fed into a scaler that counted all hits, even if the acquisition was busy processing a previous event. This allowed correcting the measured event rates with the corresponding DAQ dead time.

The timing diagram corresponding to the front-end and processing electronics during beam extraction is depicted in Fig. 6.6. Although the experiment was performed at $occ_{RF} = 32$, the
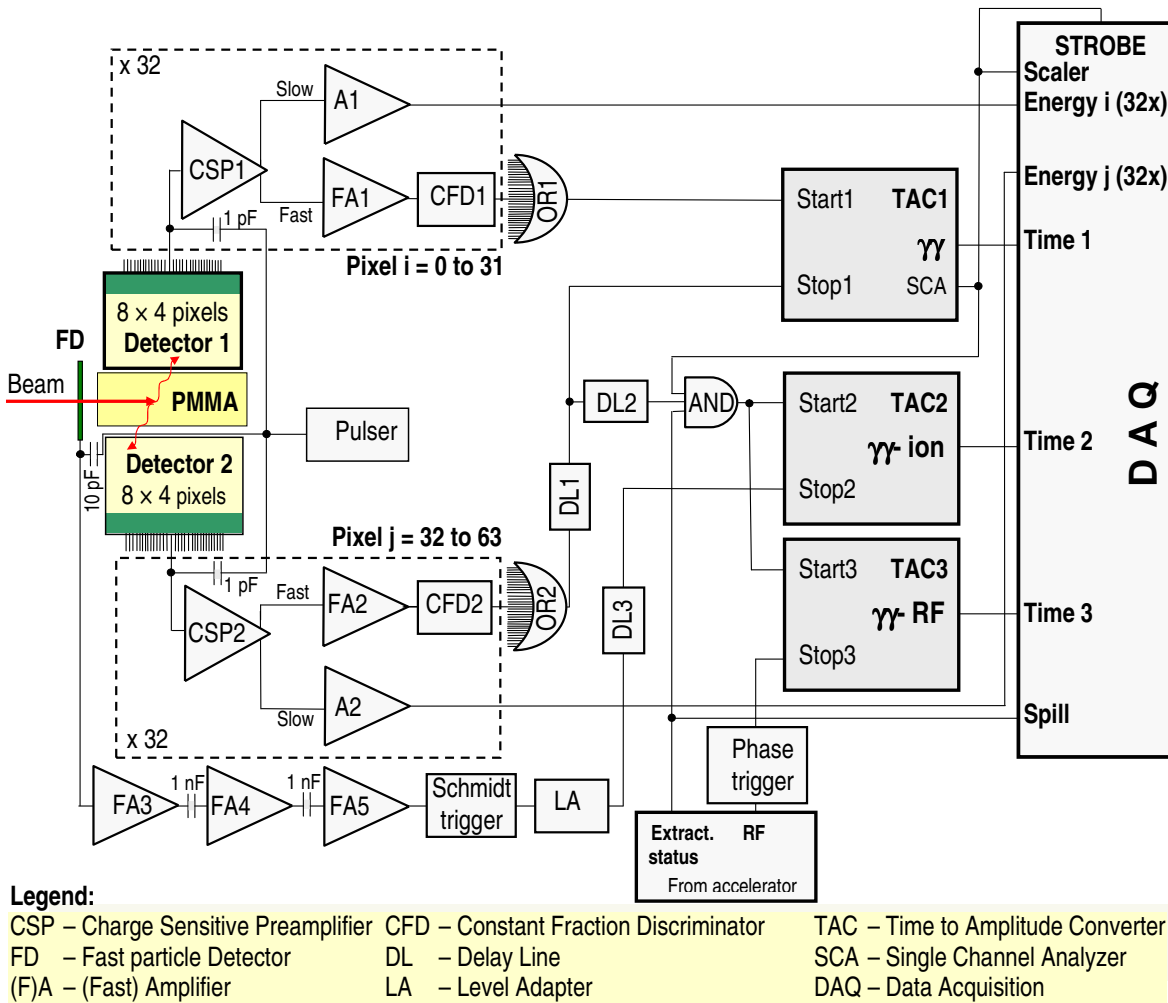
Figure 6.5: Scheme of the experimental setup, the event trigger, front-end and signal processing electronics implemented for the random suppression experiment.

figure displays $occ_{RF} = 4$ for simplicity. The output of the fast particle detector FD is depicted with the desired ultra-fast detector timing, i.e. without undershoot, pileup-free and able to perform single particle detection.
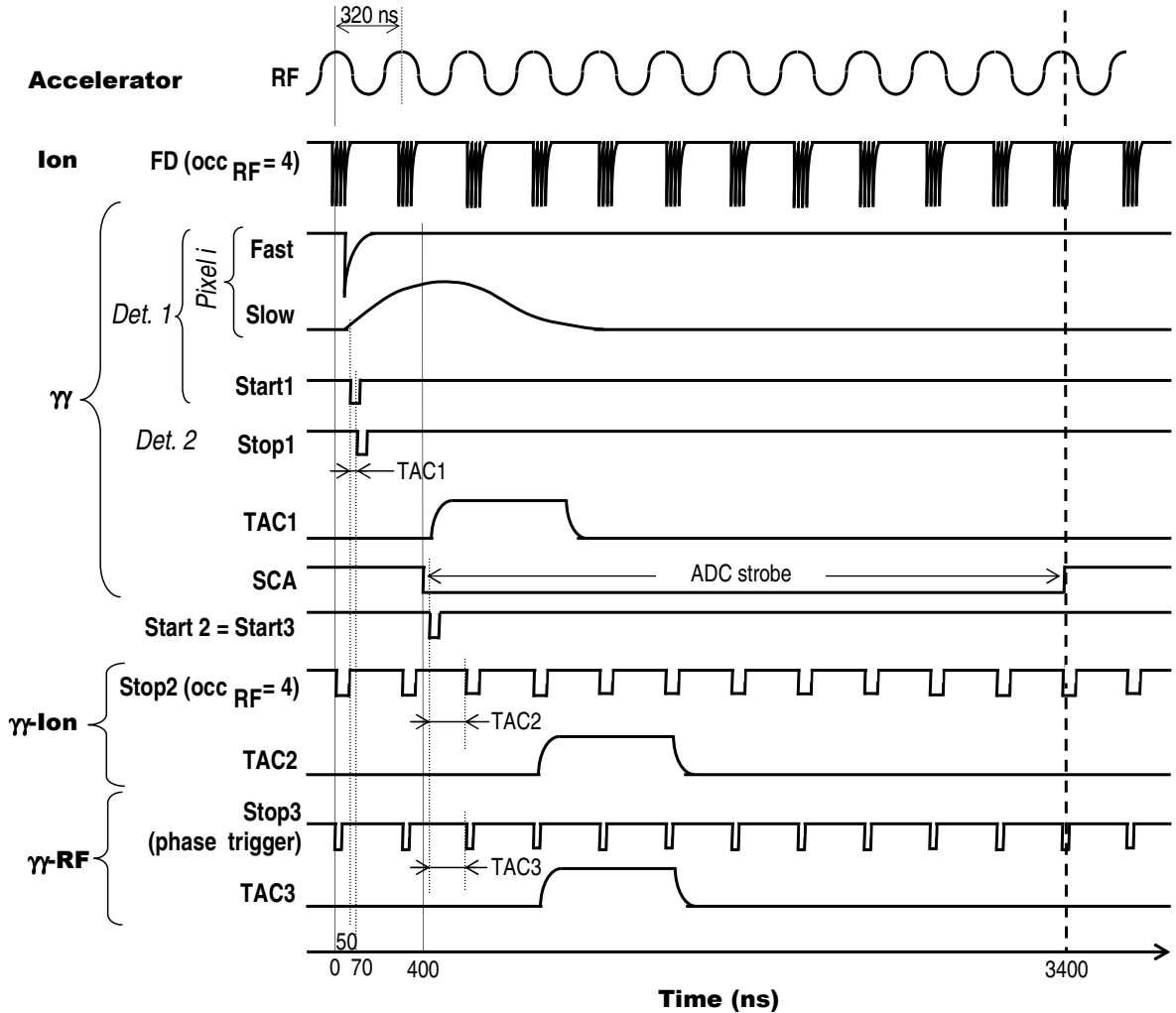
Figure 6.6: Timing diagram of the electronics in Fig. 6.5 during beam extraction depicted with $occ_{RF} = 4$ for simplicity.

6.4 Data Acquisition Dead-Time

In order to quantify the real event count rate hitting the detectors, together with the gain in image statistics, the dead time η of the DAQ must be known. For that, every event triggered increased a scaler that counted all hits, even if the DAQ was busy processing a given event. Fig. 6.7 shows the histograms of unread events obtained during the whole scan for all beam delivery regimes: extraction pauses and extractions. A detailed explanation of the plots and their meaning was presented in section 5.4.2. The extraction regime was further divided into the timing windows A and B of Fig. 6.1, i.e. outside and during the microbunches, respectively, as detailed in section 6.5.1. The ratio of total unread events during the extraction pauses and beam extractions, with the total number of events generated during the scan, yields a system total dead time η_{tot} of 57.4 %. This value includes the dead times of two different measuring regimes that can be clearly separated (Fig. 1.19): the extraction pauses with low count rate
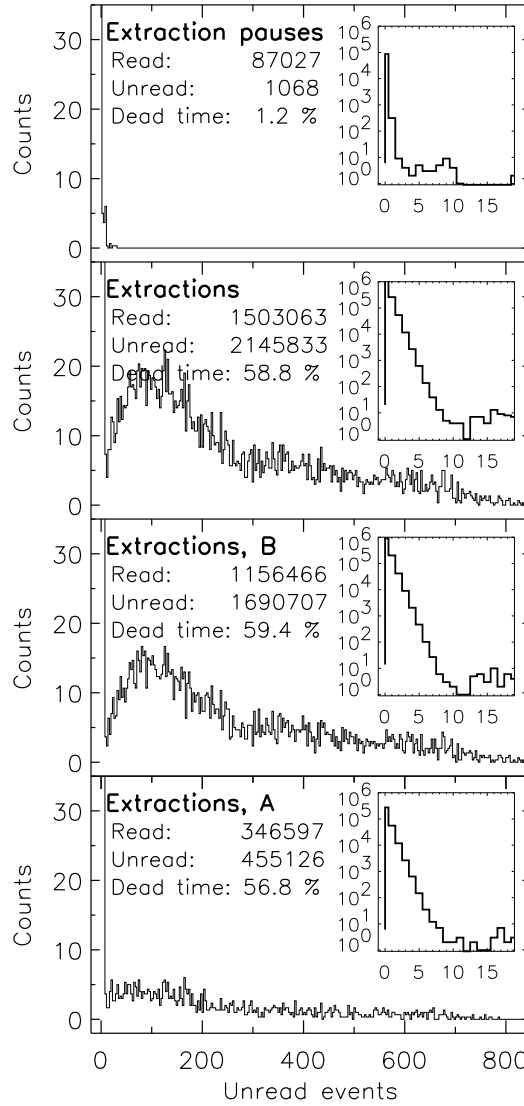
Figure 6.7: Histograms of unread events during all beam delivery regimes, with corresponding system dead times. The letters A and B refer to the time windows outside and inside the microbunches, respectively (Fig. 6.1).

and, consequently, low DAQ dead time, with $\eta_{pause} = 1.2\,\%$, and events aquired during beam extraction with higher DAQ dead time $\eta_{ext} = 58.8\,\%$. The relation between η_{tot}, η_{ext} and η_{pause} must follow

$$\frac{M_{tot}}{1 - \eta_{tot}} = \frac{M_{ext}}{1 - \eta_{ext}} + \frac{M_{pause}}{1 - \eta_{pause}}, \tag{6.3}$$

with M_{tot}, M_{ext} and M_{pause} the number of measured events in total, during beam extractions and pauses, respectively. These values are given in Fig. 6.7, namely $M_{tot} = 3\,736\,991$, $M_{ext} = 3\,648\,896$ and $M_{pause} = 88\,095$. The correlation between η_{ext} and η_{pause} is plotted with the solid curve in Fig. 6.8, obtained by fixing η_{tot} in Eq. 6.3. The diamond symbol shows the readout dead times achieved during particle extraction and in the pauses. The same relation given by Eq. 6.3 is valid during beam extraction with its two sub-regimes: timing windows A and B. This relation is plotted with the dashed curve in Fig. 6.8, with η_A and η_B related to the top and right axes, respectively, and $\eta_{ext} = 58.8\,\%$. As expected, the values obtained for

η_A and η_B are very similar to that of η_{ext}, i.e. a separation of the two sub-regimes could not be achieved. This happens because during beam extraction the signals and the readout of each event overlay several RF periods (Fig. 6.6) and count rate regimes. For this reason, even the low rate events taking place outside Δt_{bg} (A) present a high dead time close to 58.8 %.

In summary, the dead times taken into account to correct image intensities in the next sections, $\eta_{pause} = 1.2\,\%$ and $\eta_{ext} = 58.8\,\%$, are understood and justified.
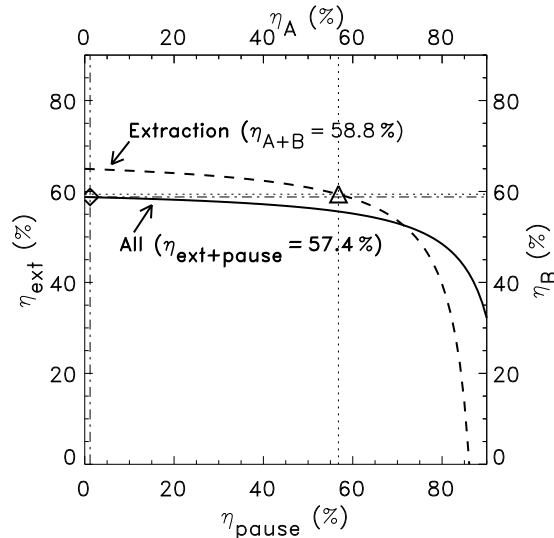
Figure 6.8: Relation between the dead times of several beam delivery regimes following Eq. 6.3. The bottom and left axes correspond to the solid curve, whereas the dashed curve is plotted against the right and top axes.

6.5 Results with the $\gamma\gamma$-RF Method

For off-line data evaluation the routines developed to analyze the first in-beam imaging experiment with LSO/APDA detectors (chapter 5) were extended in order to handle two extra timing channels. An event selection based on the accelerator status signal and detailed in section 5.2 discriminated coincidences occuring within the beam extractions from those sampled during the extraction pauses. In addition, the present analysis further separated events acquired during beam extractions, as described in the next section.

6.5.1 Time and energy correlation between $\gamma\gamma$ and $\gamma\gamma$-RF

A clear correlation between the $\gamma\gamma$ coincidences and the beam microstructure was observed and is shown in Fig. 6.9 for the RF measurements. This correlation can first be seen in column 1 where all events arriving within a time window of about 20 ns are plotted. The energy threshold was set by hardware individually for each pixel at about 300 keV. The $\gamma\gamma$ time spectrum is deteriorated by randoms in comparison to the same spectrum in the extraction pauses (column 4) and the $\gamma\gamma$-RF time spectrum shows a peak above a constant plateau, indicating the elevated event rate during the microbunches [Par05b]. After setting an energy window for the photon detectors (column 2), the peak-to-plateau ratio in the $\gamma\gamma$-RF time spectrum decreases more than one order of magnitude. The $\gamma\gamma$-RF peak almost vanishes if only photopeak coincident photons within two times the full width at half maximum, i.e 511 keV $\pm$ FWHM, are considered (column 3). The energy spectra displayed in column 2 and 3, with software-imposed energy windows, show only events corresponding to the maximum
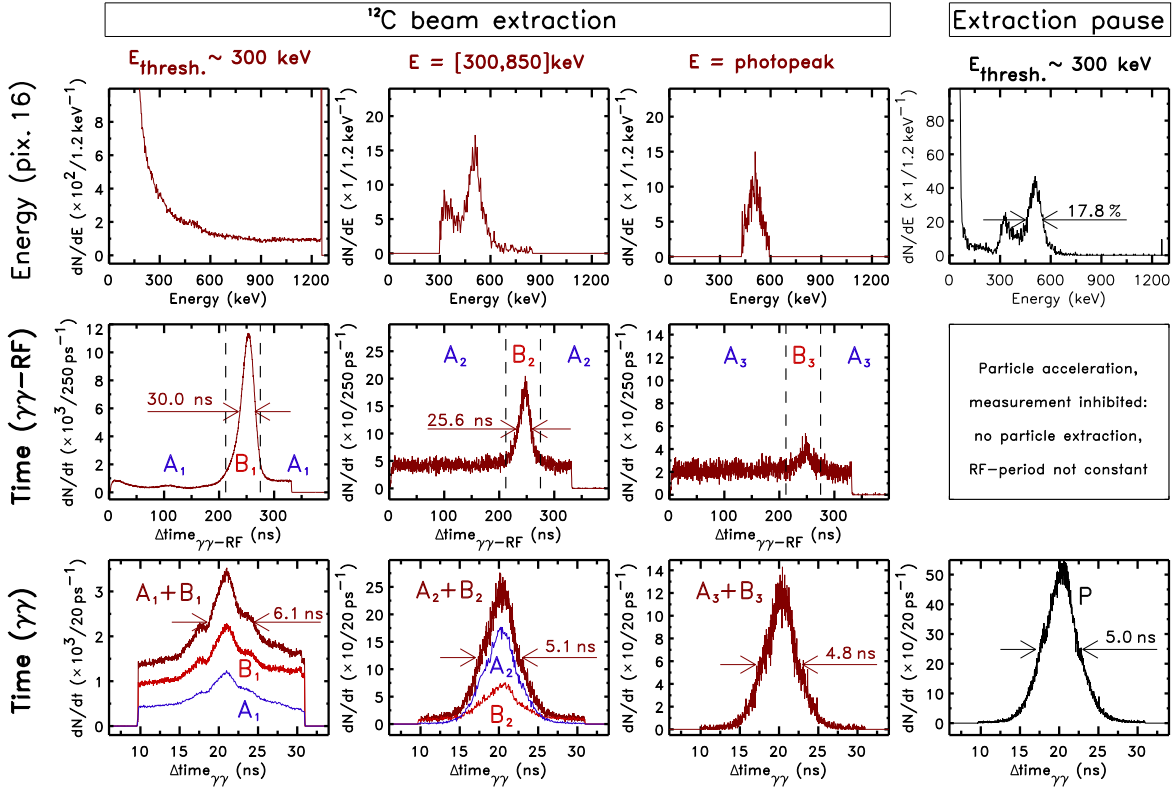
Figure 6.9: Results of $\gamma\gamma$-RF triple coincidence measurements during ^{12}C beam extraction. The $\gamma\gamma$ coincidence time spectra (lower row) have been constructed by setting different sorting conditions in the γ-ray energy spectra (upper row) and the $\gamma\gamma$-RF time distributions (middle row). As reference, γ-ray energy and coincidence time spectra acquired in the beam extraction pauses are additionally shown (column 4).

energy in both detectors. In contrary, columns 1 and 4 display spectra with a hardware imposed threshold of about 300 keV, which consequently allows low energy events below the threshold to be seen. These arise due to noise, inter-pixel crosstalk and, more importantly, due to the acceptance of low energy events imposed by higher energy events triggered in pixels elsewhere in the detectors. This behaviour was expected and allowed at this stage in order to be able to analyze low energy events due to the single-pixel threshold implemented. Evaluation of crosstalk is described in section 6.9.3. In conclusion, the $\gamma\gamma$ time spectra in columns 2 (curve A_2) and 3 (curve A_3+B_3) approach the shape seen in the extraction pauses. This indicates that the large peak in the $\gamma\gamma$-RF time spectra originates indeed from prompt nuclear decay and not from positron annihilation.

6.5.2 Tomographic imaging and quantification of image gain

A broad energy window is normally implemented in commercial PET systems in order to cope with the detector energy resolution, together with detector gain variations with time and temperature between system calibrations. Therefore, the following section presents random suppression results achieved by applying an energy window at each read event of 300 to 850 keV, similar to that of BASTEI (250 to 850 keV) despite the different detector energy resolutions.

Broad energy window: 300 to 850 keV

The activity distributions obtained with a photon energy window betweeen 300 and 850 keV are plotted in Figs. 6.10 and 6.11 for three beam delivery regimes: extraction pauses (P), during extractions but out of Δt_{bg} (A$_2$), and during extractions but inside Δt_{bg} (B$_2$). In both figures it can be seen that the events acquired within the microbunch (B$_2$) exhibit a typical random behavior, presenting a nearly constant spatial distribution (Fig. 6.10, top) corresponding to a plateau (Fig. 6.11, curve B$_2$) declining beyond the primary particle range, i.e. outside the region where the nuclear reactions predominantly take place. In contrast, events acquired outside Δt_{bg} reproduce well the characteristic β^+ distribution (Fig. 6.10, middle) and depth profile (Fig. 6.11, curve A$_2$) of the irradiation-induced activity rather well (Fig. 6.10, bottom and Fig. 6.11, curve P).
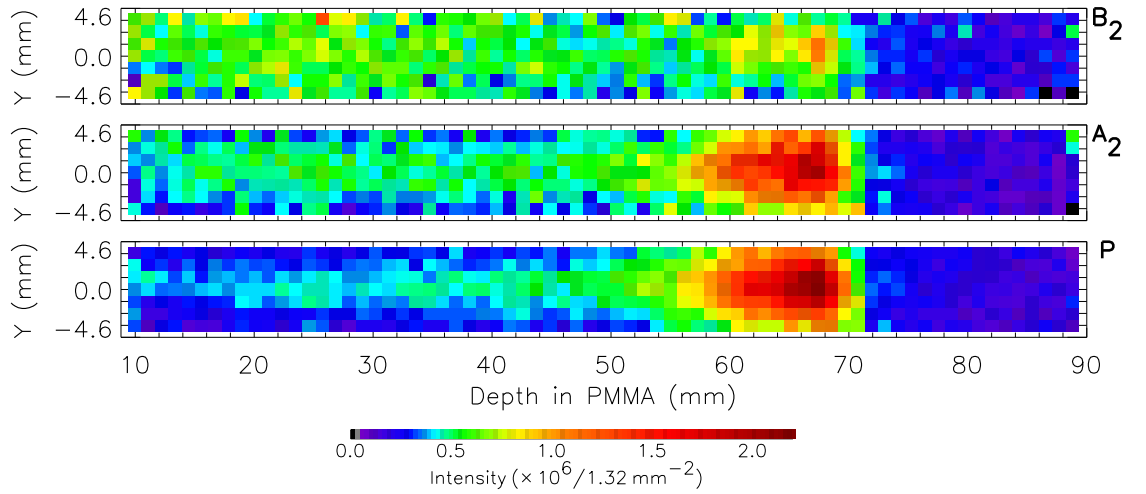
Figure 6.10: Longitudinal tomograms of the activities generated by stopping the beam in a phantom of Lucite and obtained with the γγ-RF method (top and middle only). The γ-ray energy window is 300 to 850 keV. The symbols P, A$_2$ and B$_2$, also described in the text, refer to Fig. 6.9.
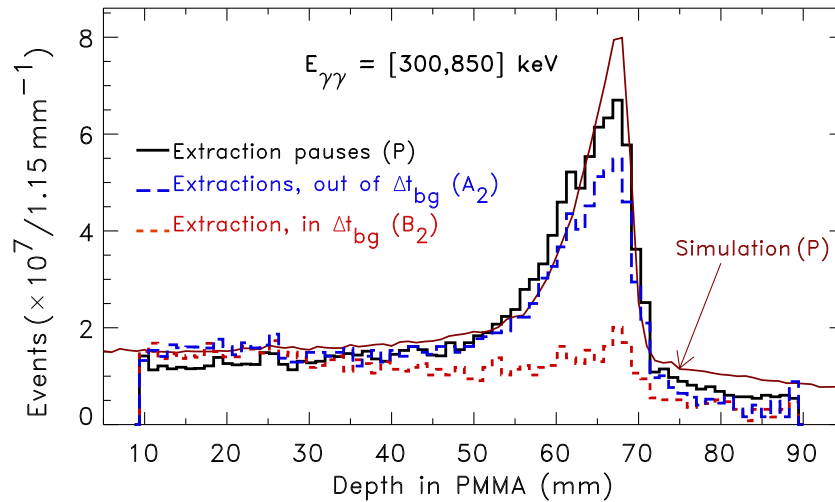
Figure 6.11: Depth profiles obtained with the γγ-RF method. The simulation (extraction pauses only) curve was shifted 4 mm to the left in an attempt to compensate for the ion energy loss in the diamond detector (300 μm thick) and its copper housing.

For image quantification the correction factors mentioned in Table 5.3 were used. These included the solid angle of the two coincident detectors, simulated by starting 10 million events at the isocenter annihilating isotropically and registering the fraction of events detected along one line-of-response (LOR) of two opposing crystals, yielding $\Omega_{LOR} = 2.3 \times 10^{-4}$. Due to the much longer distance between detectors (112 mm) in respect to detector size (18.4×9.2 mm^2 front face), the central solid angle $\Omega_{\odot}$ follows by multiplication with the total number of LOR (32). The total coincidence detection efficiency ε'_{tot} of the two opposing detectors is given by

$$\varepsilon'_{tot} = \Omega_{\odot} \cdot \varepsilon'_{LOR} \cdot \Pi \cdot (1 - \varepsilon_{PMMA})^2, \tag{6.4}$$

with ε'_{LOR} the efficiency of coincidence photon detection for one LOR. With the photon energy window implemented ε'_{LOR} amounts to 18.1 %. The value of ε'_{LOR} is higher than ε_{LOR}, obtained in section 4.6.3, due to the inclusion of photons from outside the photopeak arising mostly from the lower threshold of 300 keV. The value was calculated by considering the ratio of events measured within the photopeak (FWHM) in both detectors to the events measured within a wide energy window of 300 to 850 keV also in both detectors. This ratio was found to be 3.7, i.e. $\varepsilon'_{LOR} = 3.7 \cdot \varepsilon_{LOR}$. The image fill factor Π was calculated in section 4.6.2 and represents the mean relative solid angle of each image voxel with respect to the central voxel (30.5 %), as determined by flood source measurements. The term $(1-\epsilon_{PMMA})^2$ quantifies the probability for double escape of the 511 keV γ-rays from the phantom: 15.2 %.

The simulation of the expected number of counts was achieved with the PosGen Monte-Carlo code [Has96, Pön04], yielding a total of 1.98×10^7 β^+-decaying nuclei produced per spill (2×10^8 carbon ions with 200.2 AMeV energy). The expected total number of counts $C^{(j)}$ from the decay of isotope j with half-life $T_{1/2}^{(j)}$ follows by integrating the initial activity $A_0^{(j)}$ induced per spill over the 300 spills used (5 s spill period):

$$C^{(j)} = A_0^{(j)} \frac{T_{1/2}^{(j)}}{\ln 2} \sum_{i=0}^{299} \left[1 - \exp\left(\frac{-i \cdot 5\,\text{s}}{T_{1/2}^{(j)}/\ln 2} \right) \right] \tag{6.5}$$

For the calculation of the simulation curve in Fig. 6.11, and because it regards acquisitions in the extraction pauses only (short lived nuclei not imaged), only isotopes with half-lives greater than a few seconds were considered (^{11}C, ^{10}C, ^{15}O and ^{13}N) and the total events detected were multiplied by 3/5 (timing weight of the extraction pauses). Table 6.2 shows the relative production of the most abundant nuclei and its relative decay in a 25 minute measurement due to the effects of the different lifetimes and the fluence delivery throughout 300 spills. In Fig. 6.12 the time evolution of the event rate and the corresponding number of total decaying events is shown for the most abundant isotopes created in PMMA. It was calculated taking into

Table 6.2: Production and decay of positron emitter nuclei after stopping $6 \cdot 10^{10}$ carbon ions with 200.2 AMeV in PMMA. The ions were delivered throughout 300 spills, corresponding to a 25 minute irradiation. Calculated with the PosGen Monte-Carlo code and weighted with Eq. 6.5.

Nucleus	Lifetime	Total generated	Total decaying	Endpoint energy
^{11}C	20.4 min	$4.0 \cdot 10^9$ (68 %)	$2.1 \cdot 10^9$ (55.7 %)	1.98 MeV
^{10}C	19.3 s	$2.8 \cdot 10^8$ (4.7 %)	$2.8 \cdot 10^8$ (7.2 %)	3.65 MeV
^{15}O	2.0 min	$9.2 \cdot 10^8$ (15.6 %)	$8.8 \cdot 10^8$ (22.7 %)	2.75 MeV
^{13}N	10 min	$1.2 \cdot 10^8$ (2 %)	$9.2 \cdot 10^7$ (2.4 %)	2.2 MeV
^{12}N	11 ms	$3.8 \cdot 10^8$ (6.5 %)	$3.8 \cdot 10^8$ (9.9 %)	16.6 MeV
^{8}B	770 ms	$8.3 \cdot 10^7$ (1.4 %)	$8.3 \cdot 10^7$ (2.1 %)	3.3 MeV

account the formalism described in appendix C. Fig. 6.12 allows to see that the relative weight of short-lived isotopes, measurable only by making use of randoms suppression, increases if the irradiation time is made smaller, which is the current trend due to the accelerator developments mentioned in section 6.1.
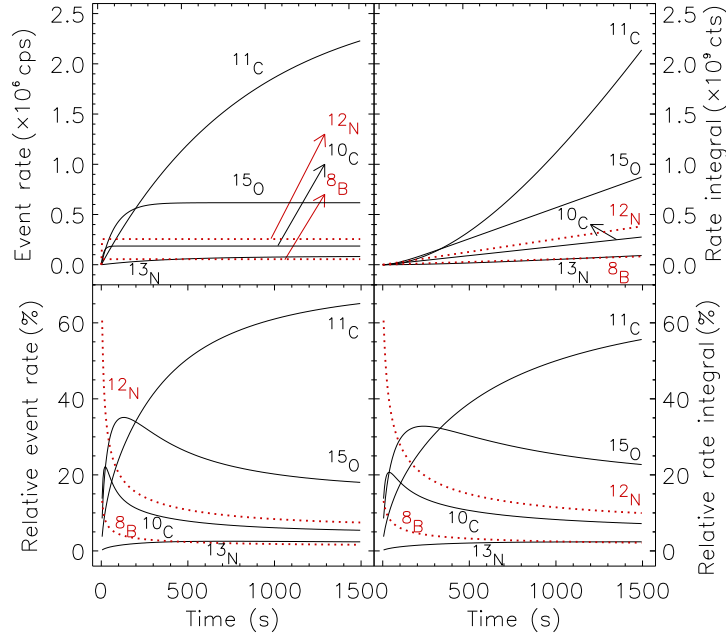
Figure 6.12: Event rate (top left), rate time integral (top right, right y axis), and corresponding relative isotope abundance (bottom) during carbon irradiation of a phantom of Lucite. Only the most abundant products are considered. Beam energy and intensity are 200.2 AMeV and 2×10^8 ions per spill, respectively. The dotted lines plot isotopes with half-lives shorter than a second.

The relative improvement in image counts, ΔC_r, was $\leq 90\%$. It was calculated by dividing the number of coincidences measured during beam extraction, outside the microbunches (image A_2, Fig. 6.10), by the number of events measured during the extraction pauses (image P, Fig. 6.10). This ratio is dependent on the width of the energy window applied, as well as on the beam energy. Table 6.3 summarizes results.

Table 6.3: Increase in image statistics deduced from the β^+-activity distributions.

Energy window	ΔC_r (peak-to-peak)	ΔC_r (8.8 - 90 mm)	ΔC_r (0 - 90 mm)
300 - 850 keV	78 %	88 %	90 %
Photopeak ($2\times$FWHM)	73 %	75 %	78 %

The values of ΔC_r peak-to-peak, shown in Table 6.3 in the first column with results, correspond to the ratio of the maxima in the two β^+-activity profiles described in the previous paragraph. For the values of ΔC_r corresponding to a depth in PMMA of 0 to 90 mm, shown in the last column, a constant plateau of activity was assumed to exist between the point at 8.8 mm (beginning of image) down to the point at 0 mm (beginning of phantom, not imaged). The higher relative increase in image statistics obtained with respect to the 65 % estimated in [Eng05c] is suspected to originate from the contribution of short lived, β^+-decaying isotopes that are detected with high efficiency during the beam extractions for the first time. According to the simulation, and correcting for the measuring time of 25 minutes by using Eq. 6.5, the most

abundant are ^{12}N and ^{8}B, contributing 9.9 % and 2.1 % to the total number of annihilation events, respectively (Table 6.2). Note also the higher image blurring at the entrance plateau of activity in Fig. 6.10 (middle, A_2) due to the higher β^+ endpoint energy of these isotopes.

Narrow energy window: photopeak

The random suppression results obtained by selecting events that deposited its energy fully within the photopeak in both detectors are discussed in the present section. The corresponding relative increase in image statistics was already included in Table 6.3.

Figs. 6.13 and 6.14 show the longitudinal tomograms and depth-profiles obtained in the beam extraction regimes under consideration. The measured data in both figures were corrected taking into account Eq. 6.4 but, due to the different energy window, a new value for the efficiency of coincidence photon detection for one LOR (ε''_{LOR}) was used. This value was calculated to be 8.3 %, corresponding to $\varepsilon''_{LOR} = 1.7 \cdot \varepsilon_{LOR}$.
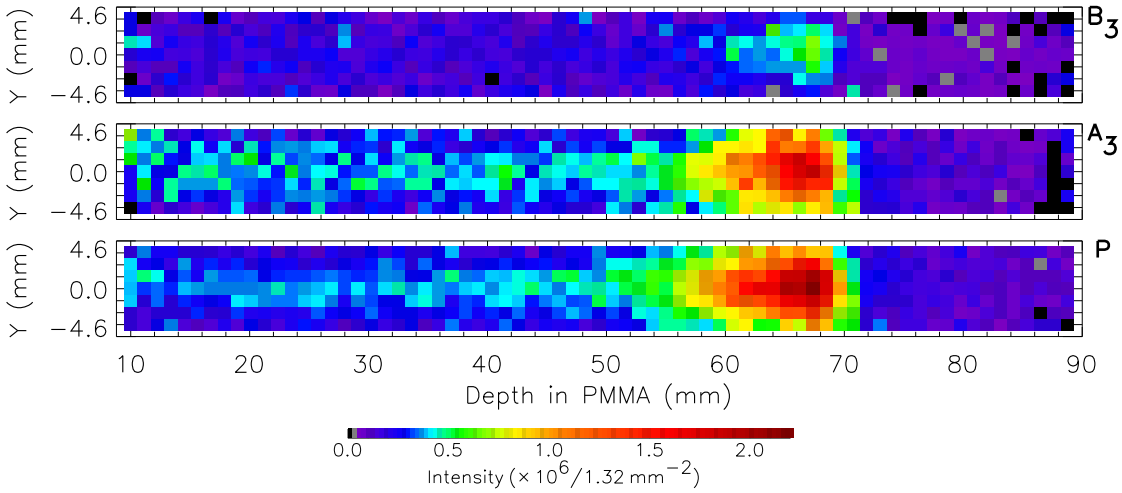
Figure 6.13: Longitudinal tomograms obtained with a narrow energy window (other details as in Fig. 6.10). The symbols P, A_3 and B_3 refer to Fig. 6.9.
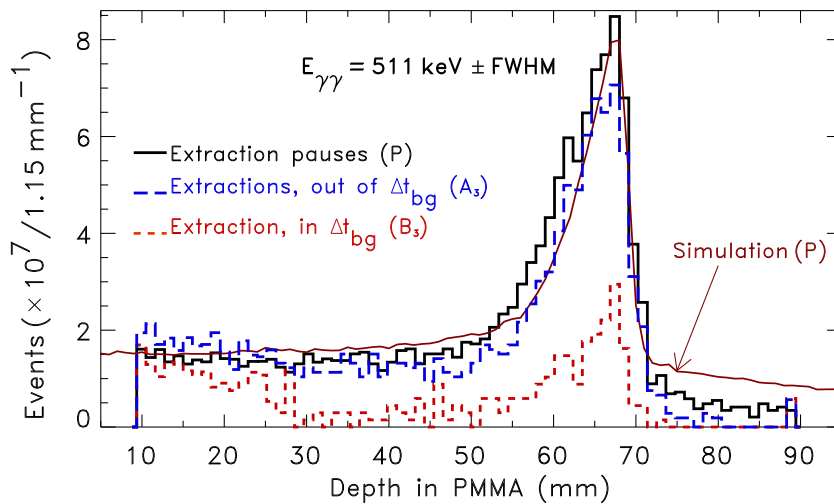
Figure 6.14: Depth profiles obtained with a narrow energy window and the $\gamma\gamma$-RF method. Simulation and other details as in Fig. 6.11.

From the top image in Fig. 6.13 and curve B$_3$ in Fig. 6.14 it can be seen that the implementation of a narrow energy window around the photopeak in both detectors filters a great part, but not all, of the events arriving during the macrobunches. This is in agreement with the corresponding $\gamma\gamma$-RF time spectrum in Fig. 6.9, column 3, where a slight peak above the plateau is still observable. Also observable in the middle image in Fig. 6.13 is the higher image blurring at the entrance plateau of activity due to the higher β^+ endpoint energy of the short-lived isotopes imaged, as pointed out in the last section.

6.6 Results with the $\gamma\gamma$-Ion Method

The results obtained with the diamond detector are similar to those presented in the previous section ($\gamma\gamma$-RF) if proper energy selection is applied. Fig. 6.15 compares triple-coincidence time spectra obtained with both methods. In addition to the worse time resolution achieved with the diamond detector, it can be seen that for a relatively high amount of events this measurement was not achieved, which can be quantified by the number of hits in channel zero of the TAC (overload). The amount of unread events with the CVD detector represents 48 % of all events measured during particle extractions. This is thought to originate on the too low threshold implemented on the electronics of the diamond detector, resulting in noise detection and the consequent over-extension of the timing signals. For this reason, the $\gamma\gamma$-ion analysis has considered only events occurring between 1 and 350 ns in the $\gamma\gamma$-ion triple-time spectrum, since only these events have physical significance.
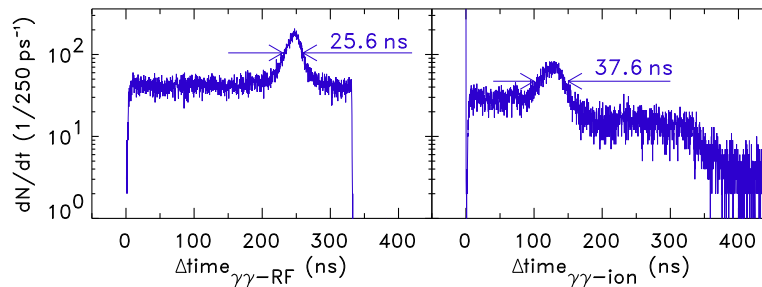
Figure 6.15: Triple-coincidence time spectra: $\gamma\gamma$-RF (left) and $\gamma\gamma$-ion (right, measured with the diamond detector). Both spectra correspond to $\gamma\gamma$ events within an energy window of 300 to 850 keV.

6.6.1 Time and energy correlation between $\gamma\gamma$ and $\gamma\gamma$-ion

A clear correlation between the $\gamma\gamma$ coincidences and the beam microstructure measured with the $\gamma\gamma$-ion was also observed and is shown in Fig. 6.16. The energy spectra displaying the implemented energy windows, as well as the energy and time measurements performed during extraction pauses, were already shown in Fig. 6.9. Fig. 6.16 shows the time window implemented on the $\gamma\gamma$-ion spectra in order to separate events collected inside (B') and outside (A') the microbunches. As mentioned, this separation could not be so well achieved as with the $\gamma\gamma$-RF method due to the too low threshold implemented on the diamond detector that allowed noise measurements to be performed, yielding a low number of events collected in the spectra. Despite this fact, the curves show the same correlations described in section 6.5.1 which allow the suppression of coincident events during beam extraction and the construction of the tomographic images and depth profiles shown in the next section.
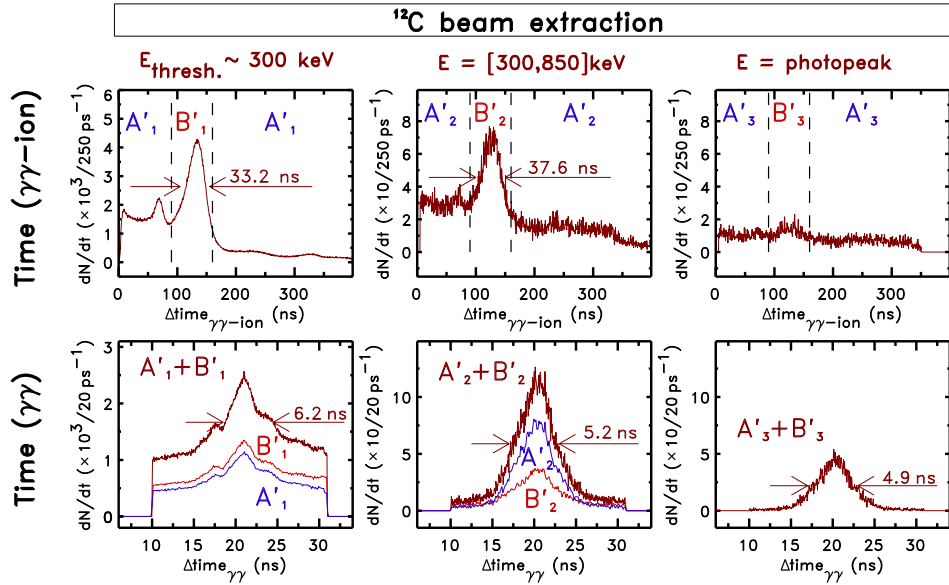
Figure 6.16: Results of $\gamma\gamma$-ion coincidence measurements during ^{12}C beam extraction with 200.2 AMeV. The time and energy correlations are the same as those described in Fig. 6.9.
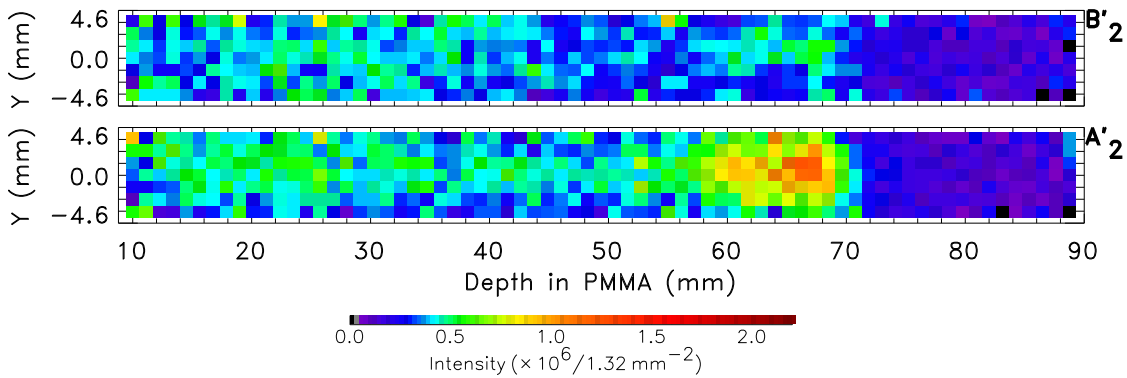
Figure 6.17: Longitudinal tomograms obtained with the $\gamma\gamma$-ion method. The symbols A'$_2$ and B'$_2$ refer to Fig. 6.16.
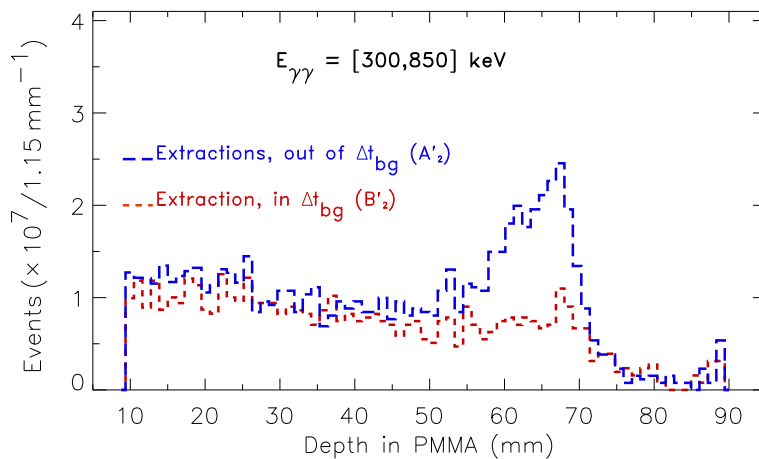
Figure 6.18: Depth profiles obtained with the $\gamma\gamma$-ion method.

6.6.2 Tomographic imaging

Figs. 6.17 and 6.18 show the activity distributions obtained with a broad energy window from 300 to 850 keV for the two beam delivery regimes collected during beam extractions: inside (B') and outside (A') the microbunches. The activity distributions collected in the extraction pauses were already shown in section 6.5.2 and are not displayed here. In both figures it can be seen that the separation of events collected inside and outside the microbunches is also achieved but with much lower statistics due to the reasons described. The same factors for quantification of image statistics acquired within the energy window of 300 to 850 keV were applied, namely $\Omega_{LOR} = 2.3 \times 10^{-4}$, $\Omega_{\odot} = 7.36 \times 10^{-3}$, $\varepsilon_{LOR} = 18.1\,\%$, $(1\text{-}\varepsilon_{PMMA})^2 = 15.2\,\%$ and $\Pi = 30.5\,\%$. Therefore, Figs. 6.17 and 6.10, as well as Figs. 6.18 and 6.11, can be compared directly.

6.7 Time Correlation between RF-Phase and Ion Arrival

As it can be seen in Figs. 6.5 and 6.6, the start signal for both the $\gamma\gamma$-RF as well as the $\gamma\gamma$-ion time measurements was exactly the same. Care was taken so that the same cable length was used after the AND gate in Fig. 6.5. This allows to combine, by subtraction on an event-by-event basis, the time information of both measurements to obtain the time correlation between the moment of ion arrival, triggered by the diamond detector, and a given RF-phase, given by the phase-trigger. Eqs. 6.6, 6.7 and 6.8 put in evidence the physical processes inherent to each time distribution acquired, with $*$ denoting the convolution operation in the time domain:

$$\Delta t_{\gamma\gamma-RF} = \Delta t_{RF-det} * \Delta t_{bunch} * \Delta t_{\gamma-emiss} * \Delta t_{\gamma\gamma-det}, \qquad (6.6)$$

$$\Delta t_{\gamma\gamma-ion} = \Delta t_{ion-det} * \Delta t_{bunch} * \Delta t_{\gamma-emiss} * \Delta t_{\gamma\gamma-det} \qquad (6.7)$$

$$\Delta t_{ion-RF} = \Delta t_{ion-det} * \Delta t_{RF-det}. \qquad (6.8)$$

The measured $\Delta t_{\gamma\gamma-RF}$ time distribution in Eq. 6.6 is the result of the convolution of Δt_{RF-det} with Δt_{bunch}, $\Delta t_{\gamma-emiss}$ and $\Delta t_{\gamma\gamma-det}$. The distribution Δt_{RF-det} represents the time resolution achieved by the phase trigger in detecting a fixed RF phase, which was seen in section 6.2.2 to be less than 1 ns; Δt_{bunch} is the time distribution of the ions in the microbunch; $\Delta t_{\gamma-emiss}$ describes the photon or particle emission after the nuclear reaction during the microbunch (section 6.8); and $\Delta t_{\gamma\gamma-det}$ is the time resolution of the the two photon detectors operated in coincidence, shown to be approximately 5 ns in Figs. 6.9 and 6.16. The time distribution $\Delta t_{\gamma-emiss}$ describes all the event emission processes: the events promptly emitted at the nanosecond scale during the microbunch as well as the delayed γ-rays resulting from the several β^+-decays induced. The $\Delta t_{\gamma\gamma-ion}$ time distribution in Eq. 6.7 results from the same processes except for Δt_{RF-det}, which is substituted with $\Delta t_{ion-det}$ given by the time resolution achieved with the diamond detector in reading the moment of ion arrival. By subtracting (6.6) from (6.7), on an event-by-event basis as mentioned, the dependence on all processes, except those shown in Eq. 6.8, is eliminated[1]. This correlation is shown in Fig. 6.19. The double peak structure observed, separated by about one RF-period, was expected due to the different electronics components and cabling implemented on the two stopping channels. Besides the small, slightly peaked continuum observable on the left of each main peak, arising most probably from the noisy conditions at the diamond detector described in section 6.6.1, the packing of

---

[1] It is important to emphasize that the subtraction of the variables of Eq. 6.6 from those of Eq. 6.7 was done on an event-by-event basis, i.e. from the list mode data and still within the time domain.
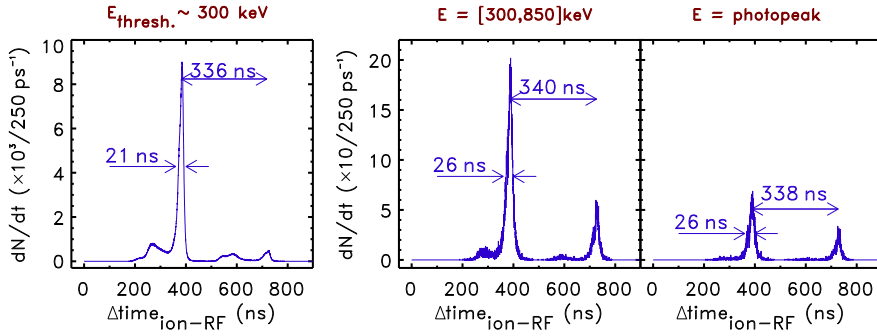
Figure 6.19: Time correlation between RF-phase and ion arrival for different energy windows imposed on the $\gamma\gamma$ events. The spectra were obtained by subtracting (event by event) the diamond detector time value (TAC 3, Fig. 6.5) from the RF time measurement (TAC 2), with a bias of 500 ns to avoid negative values in the spectra.

all events into a single RF-phase is remarkable. Due to the leading edge trigger implemented with the diamond detector (Fig. 6.4) and to the high occ_{RF} of 32 ions per bunch during these measurements, the values obtained for the time resolution between ion arrival and RF phase in Fig. 6.19 ($\Delta t_{\text{ion-RF}}$) do not correspond to the bunch width Δt_{bunch} (Fig. 6.9), but to the time correlation between the arrival of the first ion in the bunch and a given RF-phase so that $\Delta t_{\text{ion-RF}} \leq \Delta t_{bunch}$. If occ_{RF} were of the order of unity or smaller, than $\Delta t_{\text{ion-RF}} = \Delta t_{bunch}$ would hold. Table 6.4 summarizes the results obtained for $\Delta t_{\text{ion-RF}}$ and compares them to the measured $\gamma\gamma$-RF and $\gamma\gamma$-ion measurements, taken from row 2 in Fig. 6.9 and row 1 in Fig. 6.16, respectively.

Table 6.4: Measured time resolution for ion-RF, $\gamma\gamma$-RF and $\gamma\gamma$-ion coincidences.

Energy window	ion-RF	$\gamma\gamma$-RF	$\gamma\gamma$-ion
	Time resolution (FWHM, ns)		
$\geq$ 300 keV	21	30	33
300-850 keV	26	26	38

The worse results obtained with the $\gamma\gamma$-ion method, due to the noise accepted at the diamond detector, were discussed in section 6.6.1. Nevertheless, important information can be drawn by comparing the values of $\Delta t_{\text{ion-RF}} = 21$ ns and $\Delta t_{\gamma\gamma\text{-RF}} = 30$ ns, measured with an energy threshold of 300 keV, with the value of $\Delta t_{bunch} = 32$ ns FWHM, measured in [Par05b] for the same beam energy. The value of Δt_{bunch} mentioned was measured with a plastic scintillator used as a particle detector and at lower occ_{RF} in order to avoid pulse pileup: the beam intensity was $5 \cdot 10^5$ ions/s which corresponds to $occ_{RF} = 0.16$. Despite the lower value obtained for $\Delta t_{\text{ion-RF}}$, expected and justified above, the similar time resolutions observed between Δt_{bunch} and $\Delta t_{\gamma\gamma\text{-RF}}$ are remarkable and indicate a negligible delay between the moment of particle arrival and single photon emission[1]. As a consequence, the application of a time window for random suppression needs to consider only the time distribution of the ions in respect to the RF-phase, i.e. Δt_{bunch}.

---

[1] This is valid at the nanosecond time scale under discussion, with instrumentation of interest for in-beam PET. Faster timing techniques applied to a narrower beam microbunch, or to the present microbunch time structure but with $occ_{RF} \leq 1$, will off course be able to detect the delay between ion arrival and single photon emission (section 1.2.1).

6.8   Events with Higher Energy

Due to its influence on the system dead time and on the count rates achieved, the depth profiles and detector hit patterns of coincidences with energy values above 300 keV and above 1200 keV (ADC overload) were analyzed. This information is necessary since commercial PET systems, including BASTEI, applying energy discrimination for coincident events do not apply it on the channels processing the singles rates [Lub04]. Consequently, dead time estimations on these systems do include the full energy spectrum of detected events and, therefore, this knowledge for quantitative in-beam PET is of high importance.

6.8.1   Depth profiles and event hit multiplicity

Fig. 6.20 shows the depth profiles obtained with the higher energy events mentioned. It can be seen that the typical random or β^+-activity profiles of Fig. 6.11 are substituted by profiles with counts increasing with the penetration depth, suggesting the detection of events emitted preferentially in the forward direction, as noted in [Par05b] for a single detector and described in section 5.3 for these multi-pixel detectors. Although it is known that a flux of particles of mainly protons and neutrons, but also other light nuclei, escapes the target volume in the forward direction [Gun04a, Gun04b], it is not clear whether the profiles observed in Fig. 6.20 arise from γ-rays, particles or both. In order to gain some insight into this quest, the event hit multiplicity, i.e. the number of triggered pixels in each detected coincidence, was analyzed.
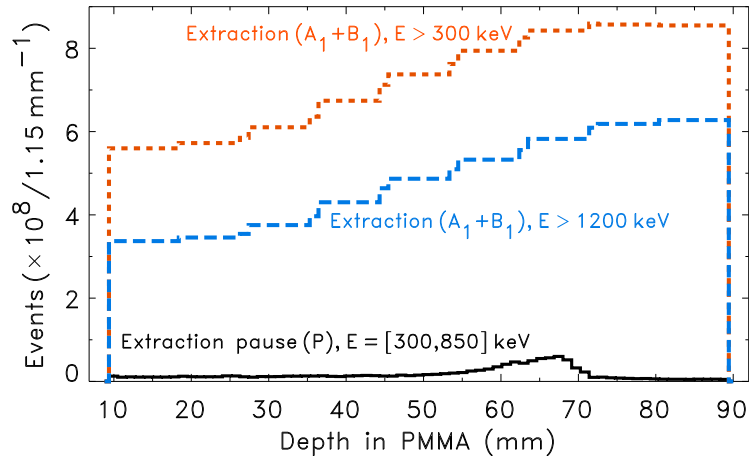
Figure 6.20: Depth profiles of coincident events with higher energy values registered during beam extractions. The profiles show the average of the events seen by the full detector rather than a pixel-based backprojection due to the impossibility of energy discrimination above 1200 keV (ADC overload, Fig. 6.9). The β^+-activity profile measured during the extraction pauses is also shown for comparison.

Fig. 6.21 shows the hit multiplicities obtained during beam extraction, separated by different event energies and plotted for the full scan of the detectors as depicted in Fig. 5.8 (except detectors positioned at 90 mm), as well as for the first and last positions of the detectors in these random suppression measurements. It can be seen that the hit multiplicities obtained for the low energy events (photopeak and energy window from 300 to 850 keV) decrease monotonically and continuously, presenting low mean multiplicity values close to unity (Table 6.5) as expected from the single hit characteristic of photons in such small detectors. The only phenomenon expected to contribute to higher multiplicity at these energies is multiple Compton scattering in the LSO crystals. Interpixel crosstalk (measured to be about 10 %, section 6.9.3), whith higher energy events creating a false low energy trigger in neighbouring pixels, is ruled out since the
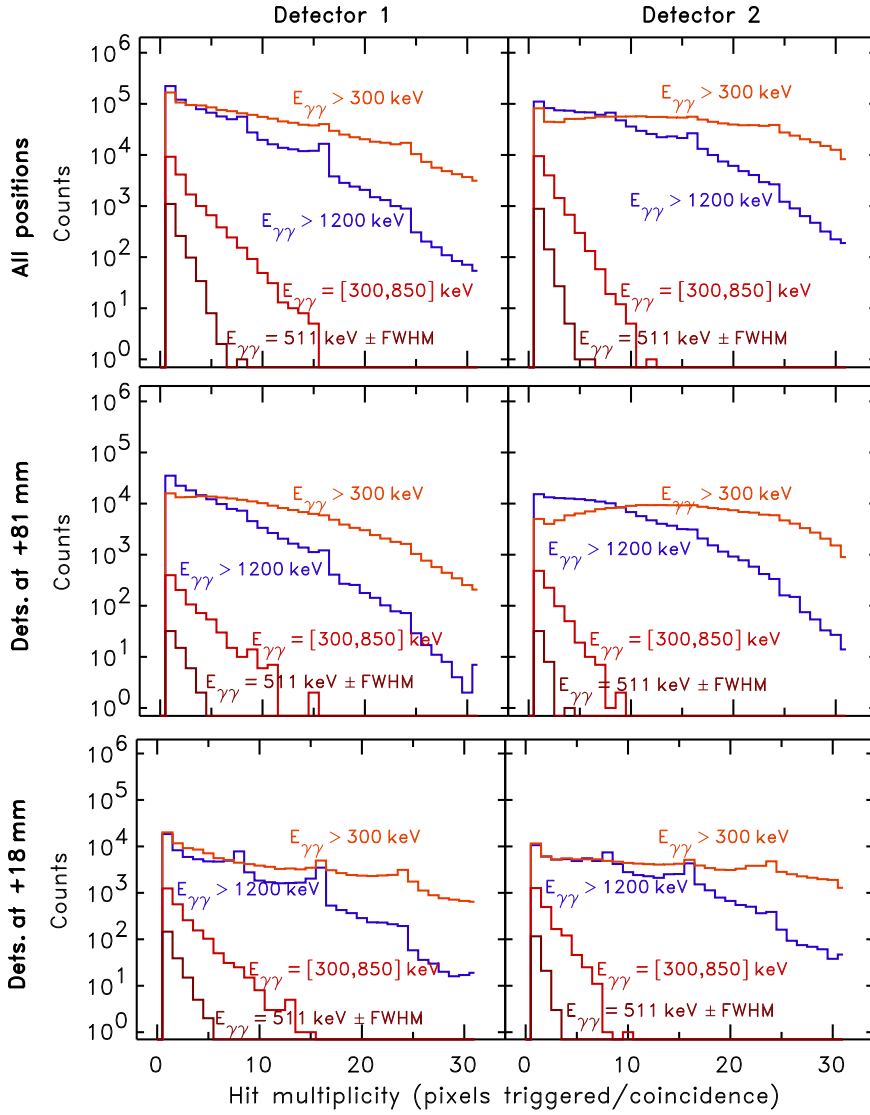
Figure 6.21: Histograms with the event hit multiplicity for different energy windows. The detector positions refer to Fig. 5.8. The analysis of all the events corresponding to the full scan with the detectors is signed as **All positions**.

Table 6.5: Mean hit multiplicity per coincidence. Detector positions after Fig. 5.8.

| | Extr. pauses | | Extractions | | | | | |
| | All positions | | All positions | | Dets. at $+18$ mm | | Dets. at $+81$mm | |
Energy window	Det. 1	Det. 2	Det. 1	Det. 2	Det. 1	Det. 2	Det. 1	Det. 2
$511\,\mathrm{keV} \pm \mathrm{FWHM}$	1.0	1.0	1.4	1.0	1.4	1.0	1.6	1.0
300-850 keV	1.3	1.2	2.1	1.0	2.2	1.0	2.6	1.0
≥ 300 keV	1.1	2.0	8.9	12.5	9.5	12.0	9.0	13.5
≥ 1200 keV	1.1	1.0	4.9	5.2	6.1	5.3	4.5	5.6

signal with maximum amplitude in each detector was requested to be within the specified energy window. If the number of photons detected per coincidence increases, e.g. by considering wider energy windows in the detected data, the curves showing the hit multiplicity are expected to decrease their slope (absolute value), but conserving the continuous behaviour described. This is observed in the multiplicity curves of Fig. 6.21 corresponding to events detected with energy

above 300 keV, remarkably continuous for the detectors positioned at 81 mm. On the contrary, coincidences with energy values above 1200 keV present discontinuous multiplicity curves, with sharp falls occurring precisely at every eight pixels and, therefore, strongly suggesting the passage of charged particles through the detectors in a logitudinal direction along the beam (each 8×4 pixels detector was positioned with the 8 pixel rows aligned horizontally, parallel to the beam direction). These particles could have their origin both inside the phantom stopping the beam as well as on the diamond detector and its housing, trespassed upbeam.

The asymmetry in mean hit multiplicity between detector 1 and 2 (Table 6.5) can be explained based on the slightly higher threshold implemented on detector 2 (therefore smaller hit multiplicity at lower energies) as well as based on the malfunctioning of two pixels (one per detector, section 6.9.1) that were shut off. Since the malfunctioning pixel of detector 1 was positioned closer to its center (maximum solid angle), the hit rejection was higher on this detector and, consequently, its average hit multiplicity lower.

Although these results do not suffice to prove the nature of the particles creating the high energy event profiles of Fig. 6.20, they do indicate the necessity of setting an upper energy threshold close to 511 keV during in-beam PET measurements.

6.8.2 Event rates

The increase in image statistics obtained is valid for the present beam delivery system with a duty factor D_f of 40 %, with $D_f = \Delta t_M / T_M$, Δt_M being the macropulse duration (beam extraction, 2 s) and T_M being the time of a synchrotron acceleration cycle, comprising beam injection, acceleration and extraction (5 s). In order to estimate the gain in collected events for therapeutic beams delivered with other accelerators with different D_f and microstructure timings, the knowledge of the event count rates is necessary. This is shown in Fig. 6.22, where
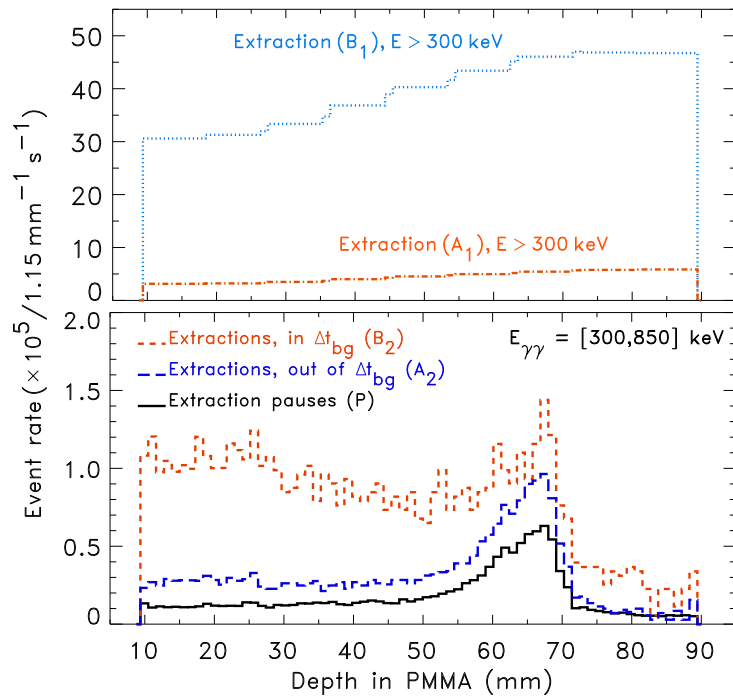
Figure 6.22: Event rate profiles in different beam delivery regimes. Rates were corrected for the solid angle of the detectors assuming isotropic event emission. The high event rate during beam extraction is remarkable.

the number of events collected in each regime was divided by the total length of the time window in which it was collected. It must be noted that an extrapolation of these results to a PET system with larger solid angle is only feasible in the case of the curves showing the isotropic, β^+-decaying events (P and A_2). The remaining curves regard anisotropic fluxes and will of course yield count rates and image deterioration dependent on the position of the detectors, as described in section 5.3 as well as in [Par05b, Cre04].

6.9   Detector Performance

The results obtained in the present chapter are related to the properties of the imaging detectors used which, in turn, differ slightly from those described in chapter 5, section 5.3, due to different operation parameters implemented, such an increased high voltage in order to achieve better timing performance. Since any in-beam PET to be implemented a posteriori must carefuly consider these properties, the main performance parameters of the detectors used are summarized below.

6.9.1   Longterm stability

The present experiment required operating the detectors one year after their last in-beam experiment (chapter 5), and one and a half year after their initial setup. Two pixels were found working inappropriately: correct energy spectra could only be acquired at the expense of extreme amplifier gain and timing with these two pixels was not possible. This is thought to arise from an insufficient coupling of the scintillators to the surface of the APD due to exposure of the detectors to the vibrations during long traveling. Therefore, it can be concluded that silicon glue and teflon tape (chapter 4, section 4.5, and [Kap04]) provide a good, long-lasting solution for manufacturing these detectors.

6.9.2   Energy and time resolution

Because time resolution was an important issue during the present measurements, the APDA were operated with an internal gain of 70 instead of gain 50, section 5.2 and [Cre03]. As expected, the timing performance of the two LSO/APDA detectors improved to 5.0 ns FWHM from 6.2 ns FWHM at the cost of worse energy resolution: $16.5 \pm 0.3 \%$ FWHM versus the $15.5 \pm 0.3 \%$ FWHM presented in section 5.2 and [Cre03].

6.9.3   Inter-pixel crosstalk

An inter-pixel crosstalk of about 10% was observed, meaning that a 511 keV photon fully depositing its enegy in a given pixel leaves a signal of ~ 50 keV in its neighboring pixels due to optical crosstalk only. The reasons for this are the incomplete light isolation of the teflon tape surrounding the LSO crystals and the light sharing at the LSO-diode coupling mostly due to the common, thick expoxy layer covering all diodes (section 4.4.3). Inter-pixel crosstalk plays a role in estimating count rates since high energy events (e.g. a 5 MeV signal from a crossing particle) may leave in its neighbor a false signal (500 keV). In the present data evaluation all pixels were read and analyzed and the pixel with maximum energy was selected in each detector for energy windowing followed by image processing, thus crosstalk events are automatically rejected since their signals have less amplitude than that of the pixel where the real event took place. Future applications must apply either the same principle or a hardware energy selection that is able to reject a full cluster of pixels once a high energy event is detected in one of them. In summary, applying energy windows is sufficient for event selection for tomographic imaging but image quantification requires considering all events impinging the detectors. These findings may be

of importance in conventional nuclear medicine PET [Lub04] and are of utmost importance for random suppression and image quantification during in-beam PET measurements.

6.10 Application to Radiotherapeutic Beams

The applicability and usefulness of the methods presented depend on the timing characteristics of the therapeutic beam where the methods are to be applied. The importance of random suppression during in-beam PET measurements increases as the accelerator duty factor D_f increases. For example, linear accelerators for electron, photon and even ion [Ama04] radiotherapy have extremely small duty factors ($\sim 0.1\%$) and, consequently, the random suppression method summarized in section 1.4.2 and detailed in [Paw97, Eng04b] suffices for in-beam PET at these machines. In contrary, isochronous and superconducting cyclotrons used for ion radiotherapy [Ros00, PSI99, Kim01] deliver continuous wave (CW) beams ($D_f \cong 100\%$), which render in-beam PET implementable only with the present random suppression methods. Synchrotron-delivered radiotherapeutic beams have duty factors between 10 and 90 % [Hab93, Eic03, Fur03, Cou04], meaning that such facilities can considerably profit from the application of the random suppression techniques presented here. Table 6.6 emphasizes these conclusions by summarizing the timing characteristics of several radiotherapy facilities worldwide. The values given for Δt_{bg} represent the FWHM of the bunch. All random suppression results presented in this chapter reserved a time window of $2 \times$ FWHM about the microbunch.

Table 6.6: Time characteristics of some therapeutic beams worldwide. The symbol T_M refers to the period of the macropulses of the accelerator, D_F refers to its duty cycle, T_{RF} is the period of the RF signal, Δt_{bg} is the typical bunch width, and $\overline{occ_{RF}}$ the mean RF occupancy.

Facility	Acc. type	Ion(s)	T_M (s)	D_f (%)	T_{RF} (ns)	Δt_{bg} (ns)	$\overline{occ_{RF}}$ (ppb)	Ref.
Catania	Cycl.	p	n.a.	CW	30	4-6	300	[Cir04]
GSI	Sync.	C	5	~ 40	480-250	~ 30	13.9	[Hab93]
Heidelberg	Sync.	p-O	2-12	8-92	284-148	n.k.	8.0	[Eic03]
HIMAC	Sync.	C	3.3	61	151	n.k.	n.k.	[Fur03]
Loma Linda	Sync.	p	2.2	82	109-10³	n.k.	1471	[Cou04]
NPTC	Cycl.	p	n.a.	CW	9.4	0.8	118	[Ros00]
PSI	Cycl.	p	n.a.	CW	19.75	0.3	n.k.	[PSI99]
TERA	Sync.	p	1	65	80	n.k.	n.k.	[Buc96]
TERA	Linear	p	5 ms	0.06	0.33	0.03	n.k.	[Ama04]

Catania:	Laboratori Nazionali del Sud, Catania, Italy.
Heidelberg:	Heavy Ion Cancer Therapy Facility, Heidelberg, Germany.
HIMAC:	Heavy Ion Medical Accelerator in Chiba, Japan.
Loma Linda:	Loma Linda Univ. Proton Treatment Center, Loma Linda, USA.
NPTC:	Northeastern Proton Treatment Center, Boston, USA.
PSI:	Paul Scherrer Institute, Villigen, Switzerland.
TERA:	TErapia con Radiazioni Adroniche, Novara, Italy.

n.a.: not applicable   n.k.: not known   ppb: particles per bunch   CW: continuous wave

6.10.1 Implementation at GSI and at the Heidelberg clinics

A mean RF occupancy of 13.9 carbon ions per bunch was calculated for the GSI facility by considering all combinations of beam energies and intensities used to treat all patients to this date (Fig. 6.23). Extrapolating these values to the synchrotron parameters at the future ion
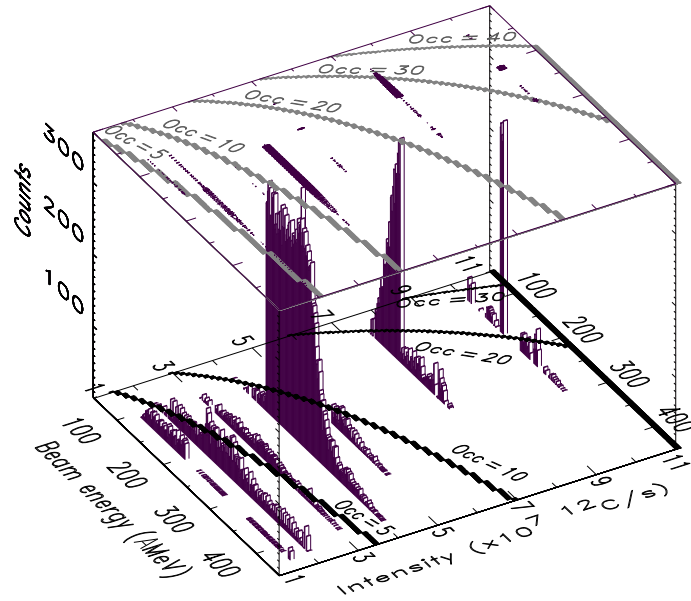
Figure 6.23: Histogram with the combined beam energies and intensities used to treat 240 patients at GSI between January 1998 and August 2004. Overplot are several RF occupancy curves at GSI (top, grey) and at the future synchrotron in Heidelberg (bottom, dark).
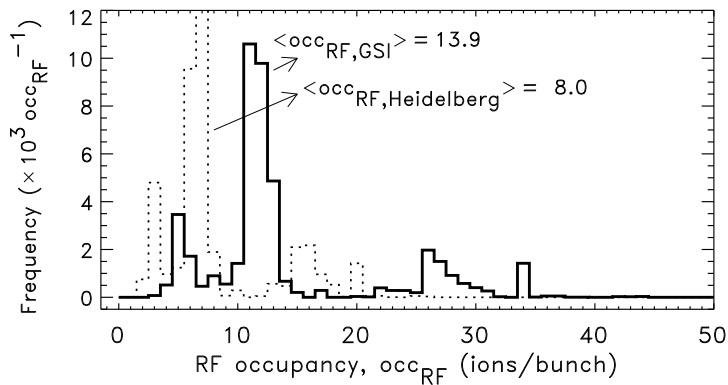
Figure 6.24: Histograms with the RF occupancies at GSI (solid curve) and expected for Heidelberg (dashed curve), corresponding to Fig. 6.23.

therapy facility in Heidelberg, with an even higher duty factor, yields $\overline{occ_{RF}} = 8.0$ ^{12}C ions per bunch. This value indicates that there may be an advantage, from the point of view of timing (Fig. 6.3), in using the $\gamma\gamma$-ion in respect to the $\gamma\gamma$-RF method for this facility. Nevertheless, the smaller stopping power of ion species with lower atomic number than carbon, and the lower relative biological effectiveness of these species, require the beam intensity to be magnified if the same dose is to be applied. Consequently, a higher RF occupancy is to be expected for ions lighter than carbon, which renders, apart from carbon and oxygen ions, the $\gamma\gamma$-RF and $\gamma\gamma$-ion methods identical in this aspect.

Despite the noise problems presented in section 6.6 for the diamond detector, arising from normal first-attempt experiments, the $\gamma\gamma$-ion method is easier to implement in real therapeutic situations since it does not require a correction for the transit time of the ions in the beam pipeline (which is dependent on beam energy). Nevertheless, its has the drawback of requiring

additional material in the beam path. This would become an advantage if the fast particle detector could be used also as a beam monitor [Per04, Ber01], which is not a trivial task since a large area, position sensitive detector covering the whole beam delivery portal (20×20 cm^2 at GSI) would have to be assembled. In addition, the very high mean occ_{RF} for proton treatments, e.g. 1479 particles per bunch at the Loma Linda synchrotron (Table 6.6), requires the eventual beam monitor to be able of performing charge integration in order to detect ions overlapping in time. In summary, an ultra-fast, particle counter detector with a large dynamic range would be required, which is indeed a technological challenge. One possible alternative to the large size of the beam monitor would be to position a small area, fast particle detector at the last beam focus in the accelerator pipeline. Nevertheless, this again would require a correction for the ion transit time in the beam pipe.

6.10.2   Cyclotron-delivered therapeutic ion beams

In-beam PET implementation at cyclotron-based facilities seems to be non-trivial because of the small time differences between Δt_{bg} and T_{RF}, with Δt_{bg} ranging from 0.3 ns [PSI99] to about 6 ns [Cir04] and T_{RF} from about 10 ns [Ros00] to 30 ns [Cir04]. On the accelerator side, two methods to increase T_{RF} are possible [Bra99]. One makes use of single turn extraction, which allows delivering an arbitrary pattern of beam pulses produced with a combination of bunching and chopping at the injection level (more difficult for heavy ions). The second uses multi turn extraction followed by a subharmonic buncher that reduces the beam repetition rate to the orbital frequency [Bra99]. Nevertheless, in order not to disturb the optimal operation of the cyclotron, the best solution should arise from the use of fast scintillators combined with appropriate very fast signal processing electronics, e.g. as proposed [Lec02] and already achieved [San04] with LSO/APDA used for positron emission mammography (PEM).

6.11   Summary and Outlook

Two methods for suppressing the high-yield, micropulse-induced random coincidences during beam extraction have been tested successfully at the medical beam line at GSI. With the accelerator duty cycle of 40 % installed there, the increase in image statistics was measured to be between 70 and 90 %. Both random suppression methods are based on the synchronization of the $\gamma\gamma$-coincidences measured in-beam by the positron camera with the time microstructure of the beam, either by using the RF-signal from the accelerator or the signal of a thin diamond detector placed in the beam path in front of the target. Energy and triple-coincidence time correlated spectra and tomographic images of the β^+-activity induced by the beam in a plastic phantom, first-measured during beam extraction, have clearly confirmed the feasibility of the proposed random suppression methods. In addition, tomographic imaging of short-lived β^+-decaying isotopes that could not be discriminated so far due to the high event flux within the microbunches, could be performed. Both methods indicate that in-beam PET random suppression can be achieved by applying narrow energy windows about the 511 keV photopeak on each pair of detectors. Nevertheless, since such narrow windowing is unfeasible with the current electronics implemented in commercial PET tomographs, a broader energy window was applied at the detectors, providing the same level of random suppression if the moment of coincidence arrival was time correlated with the beam microstructure. The methods provide a solution for implementing in-beam PET in hadrontherapy facilities with synchrotron and cyclotron delivered beams with high duty factors or continuous wave, respectively. Namely, and more importantly, they provide a solution for applying in-beam PET at synchrotron-based, heavy ion radiotherapy facilities [Hea98, Sie04] with an optimized beam delivery duty factor where in-beam PET data taking can be compromised if none of these random suppression

methods is applied.

Despite the positive first results, the random suppression methods presented still require a system that corrects for the transit time of the ions in the beam pipeline (ion transit time is energy dependent) before being applied to a therapeutic system either with the $\gamma\gamma$-RF method or with the $\gamma\gamma$-ion method, with the fast particle detector positioned at the last focus of the accelerator. If a fast particle detector capable of performing beam monitoring is developed (detector size, speed and energy proportionality are an issue), then such a position sensitive detector must have an area of 20×20 cm^2 and a disjunctively connected output of all its pixels must be made available to the in-beam PET data acquisition system.

Chapter 7

Conclusions and Outlook

Several objectives pursued within the present work, optimization of in-beam positron emission tomography applied for the monitoring of heavy ion tumor irradiation, have been met. In some issues a first, important step towards an optimization has been given, but future work is still needed, as detailed below.

The most important limitation of in-beam PET firstly addressed in this work was the problem of image artifacts arising from limited angle tomography. The present reconstruction routine applies a penalization factor at image voxels located far from the isocenter, preserving image proportionality at the isocenter, where the tumor is located. In order to understand the source of these artifacts, and in order to be able to propose a detector configuration that minimizes them, two software tools were constructed. The first was a tomograph simulation capable of handling variable detector configurations, simulating the detection of the annihilation radiation and providing a versatile detector encoding scheme. The second consists of a flexible reconstruction routine able of reading and treating mathematically the ouput of this simulation. This reconstruction routine extends the mathematical data treatment already implemented for the in-beam tomograph at GSI. It presents a novel approach for 3D data histograming and allows, therefore, real 3D tomographic reconstruction. Although this routine provides a reconstruction solution for next-generation, optimized in-beam positron emission tomographs, it presents two limitations. These are the large processing time and large memory size required if very large data sets are handled, as is the case with irradiation in the pelvis region. In order to reduce the processing time the routine must be adapted to the ordered subsets estimation algorithm (OSEM), which reduces the number of iterations from the present fifty to only a few. Concerning the large memory size, modern computers already provide a working solution. This can be seen by the pelvis irradiation images presented throughout this work. They correspond to a large image volume and data size, and were processed with normal, commercial computers. Nevertheless, the development of a 3D system matrix exploiting the symmetries existing in the processes of emmission tomography will greatly reduce both time and memory demands in PET reconstruction algorithms.

Using the simulation and reconstruction routines mentioned, the origin of several artifacts was identified to be dependent on the gaps between the two heads in a dual-head detector system. Two detector configurations for next-generation, improved in-beam PET were proposed: a dual-head tomograph with small gaps, allowing the incoming beam to arrive to the tumor, and a closed ring tomograph. The closed ring tomograph must be positioned, during patient irradiation, tilted in respect to the direction of the incoming beam. In order to evaluate the optimum detector configuration with real patient data another simulation code, previously developed by past members of this team, was used. This code, named PosGen, generates β^+-activity distributions based on the computed tomogram of a patient and on a given irradiation plan. Within this work the PosGen code was slightly modified in order to be coupled with

the routine simulating the several tomographs. The images obtained after reconstruction show a clear advantage for closed ring tomographs if large irradiation fields, like irradiation in the pelvis region, are to be monitored with in-beam PET.

Integrating either proposed detector configuration into future heavy ion treatment facilities was also studied. For horizontal, fixed beam lines it was seen that both configurations can be implemented with slight modifications in respect to the solution presently installed at GSI. For isocentric, rotating beam deliveries several proposals were analyzed. It was seen that implementing in-beam PET in the beam gantry, a solution developed at GSI, offers the most advantages. This GSI solution was further extended, within this work, in order to allow for a closed ring tomograph to be implemented.

The limitations imposed by the low statistics data sets of in-beam PET images were also addressed in this work. Three reasons exist for this. First, the amount of nuclear reactions inducing β^+-decaying isotopes is, per se, relatively small in comparison to the incoming ion fluence. The statistics of in-beam PET images will improve if the number of treatment fractions is reduced (higher dose per fraction). This item was not addressed in the present work. Second, a high number of annihilating events is lost due to biological mechanisms like washout, or due to the low detection efficiency provided by a dual-head tomograph with large gaps. This loss of events is reduced with the detector configurations proposed for next-generation tomographs: a closed ring, or a dual-head tomograph with small gaps. And third, data taking during particle extraction is presently vetoed due to the presence of a high background that overlaps the annihilation signal.

The problem of high noise during particle extractions was first addressed by other members of the in-beam PET team. A demanding research work, envisaged at understanding the mechanism originating the high background noise existing during particle extractions, was put forward. A correlation existing between the moment of arrival of background events with the arrival of the carbon ions, synchronized with the radiofrequency (RF) signal from the accelerator, was found and exploited. This provided the knowledge for developing a technical solution, within this work, in order to allow in-beam PET data taking during particle extractions. Such solution was required for two reasons. First, in order to increase the statistics of the presently acquired images. Second, and more importantly, in order to allow in-beam PET to be implemented at future facilities using optimized synchrotron or cyclotron accelerators. This is because recent developments in accelerator technology result in beam extraction times occupying close to 100 % of the accelerator duty cycle. Two technological solutions for suppressing the high noise background of in-beam PET were proposed in a patent, and verified experimentally at the GSI medical beam line within this work. This verification, using a triple coincidence technique, allowed for the first time to readout, and image, double-γ-ray events correlated with the moment of ion arrival during particle extraction. Two γ-ray, position sensitive detectors, with 32 pixels each, were assembled and used. A very thin diamond detector, positioned in the beam path as an ion detector, was used to signal the moment of ion arrival. A fast, RF-trigger electronics module, developed in house, was used to time a given phase of the RF-signal from the accelerator. A pencil-like beam was stopped in a phantom and the 2D images and depth profiles, obtained for the first time during particle extraction, clearly show the feasibility of the two technical solutions proposed in the patent. These images and profiles allowed also to gather evidence about the influence of short-lived, β^+-decaying isotopes with higher endpoint energies. These short lived isotopes could not be discriminated so far due to the high event flux within particle extractions. Nevertheless, a measurement of their lifetimes could not be performed, meaning that a clear proof of their detection is still lacking.

But the positive background suppression results were obtained with a fixed beam energy. Sev-

eral challenges must be addressed before either of the random suppression methods is applied onto a therapeutic site equipped with in-beam PET. One random suppression method correlates the incoming γ-rays with the moment of ion arrival based on a fast particle detector positioned in the beam path. If this method is used, than a fast particle detector capable of performing beam monitoring must be developed. Detector size, speed and energy proportionality are an issue. Furthermore, such a position sensitive detector must have an area of 20×20 cm^2 and a disjunctively connected output of all its pixels must be made available to the in-beam PET DAQ system.

Another random suppression method correlates the incoming γ-rays with a given phase of the RF-signal from the accelerator. Since the transit time of the ion in the beam pipeline depends on its energy, the RF-phase that properly vetoes the high background noise will also depend on the beam energy. Therefore, a system that corrects for the transit time of the ions in the beam pipeline is necessary in this situation. In addition, the RF-phase trigger must provide a digital output with constant delay in respect to any input frequency, i.e. it must not depend on beam energy. One possible solution verified experimentally is described in appendix D.

Concerning detector development, a great effort was put in this work onto assembling and testing state-of-the-art technology specially adapted to the requisites of in-beam PET. Two position sensitive, γ-ray detectors consisting of finger-like crystals of lutetium oxyorthosilicate (LSO) coupled to two avalanche photodiode arrays (APDA) were assembled. The substitution of the conventional photomultiplier tube (PMT) by APDA provides the magnetic field resistance needed for the next-generation, in-beam PET detectors. Such fields, generated by the last beam bending magnet, will be present if in-beam PET is installed onto isocentric, rotating beam deliveries. In addition, the more than ten times smaller dimensions of APDA in respect to PMT will allow a huge volume reduction of positron emission tomographs built with such detectors. Furthermore, the energy and time resolutions measured with the new detectors, better than those obtained with the presently installed detectors, are directly related to the quality of PET images. The in-beam imaging capability of these LSO/APDA detectors were tested under or after harsh irradiation conditions. In one experiment the detectors were positioned up and downbeam from a target irradiated with a fluence equivalent to 1000 typical daily therapeutic fractions. A line source positioned between the detectors was imaged, allowing parameters like time, energy and spatial resolution to be compared before, during and after irradiating the target. A second experiment imaged the β^+-activity distribution generated by a monoenergetic beam in a target of Lucite. In addition, a third experiment exposed a scintillator block of LSO to the flux of light particles leaving two single-portal patient treatments. Germanium-detector-based, spectroscopic γ-ray measurements showed no scintillator activation. These combined results prove the feasibility of using an LSO/APDA detector for next-generation, improved in-beam PET scanners with high detection efficiency and reduced image artifacts.

But, due to the small amount of ^{176}Lu, a natural radioactive element, in LSO, the influence of the natural background activity density of LSO onto an LSO-based tomograph had to be estimated. It was seen that, in order not to compromise the quality of the low-statistics in-beam PET images, modern, digital data acquisition techniques are necessary in order to reduce the coincidence time resolution of the detectors to a full width at half maximum (FWHM) of 1 ns or below.

Finally, the impact of recent developments in ultra-fast timing detectors, potentially allowing the implementation of the time-of-flight technique onto commercial PET scanners, was extrapolated to in-beam PET. Very promising results can be achieved if future PET detectors with a coincidence time resolution below 200 ps FWHM can be built.

Appendices

Appendix A

A Factorization Scheme for 3D Tomographic Data

In order to be able to optimize the detector geometry for in-beam PET scanners, a set of simulation and reconstruction routines capable of handling a high number of coincidence channels, corresponding to a high resolution, closed ring tomograph, was needed. If the ECAT® EXACT™ HR$^+$ tomograph (CTI PET Systems Inc.) is considered, containing 32 complete detector rings, the total number of single detector channels is 18 432. Since in-beam PET is characterized by low statistics data-sets sampled with a limited angle tomograph, rebinning the 3D collected data into 2D sets disturbs the spatial information of the few lines-of-response (LOR) existing, which vetoes the application of already existing rebinning algorithms. Therefore, a fully 3D implementation of the maximum likelihood expectation maximization (MLEM) algorithm was done [Cre02, Cre05b] by making use of the system symmetries and coincidence channel possibilities illustrated in Figs. A.1 and A.2.

Fig. A.1 shows the pixel numbering scheme implemented both in the simulation and in the reconstruction routines. For every detected coincidence the simulation registers, in list mode, two numbers corresponding to the pixels hit. It is up to the reconstruction routine to histogram the incoming list mode data appropriately before proceeding with the iterations of the MLEM algorithm. In order to handle the enormous amount of crystal combinations possibilities, close to 170 million, dynamic memory allocation was necessary together with a factorization scheme that allowed the reconstruction to handle only non-empty coincidence channels. For that, all possible coincidence possibilities were analyzed, as depicted in Fig. A.2. It can be seen that a total of 5 299 200 and 164 275 200 crystal combinations can occur within intra-ring and inter-ring
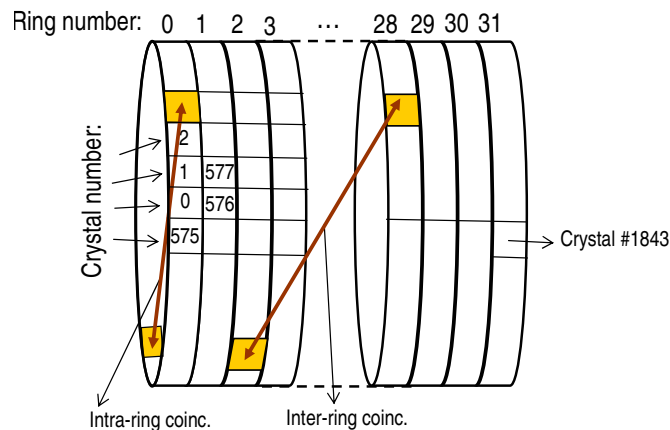

Figure A.1: Intra- and inter-ring coincidences and ring and pixel numbering adopted for the reconstruction routine. The image shows a closed ring detector geometry. If a dual head tomograph is considered pixels that should be absent are simply ignored.
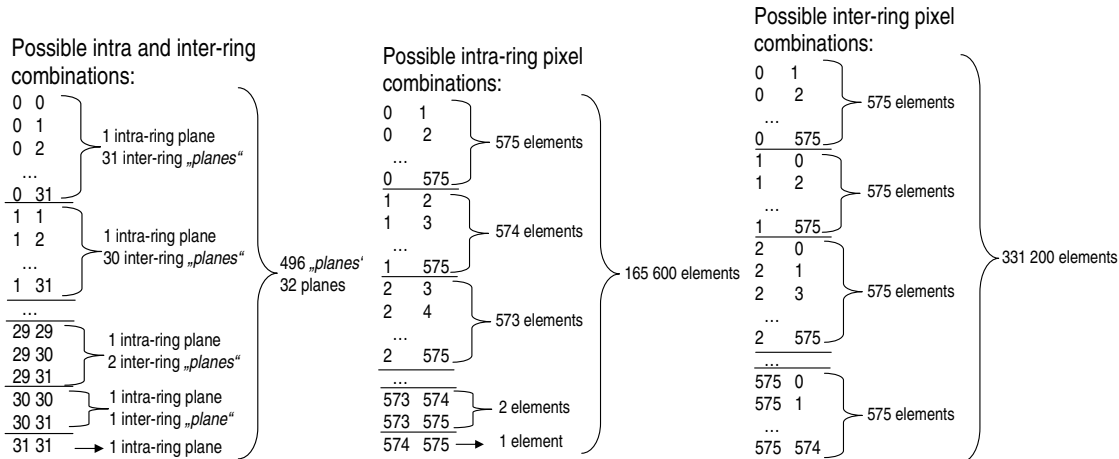
Figure A.2: Scheme showing possible intra-ring, inter-ring and pixel combinations.

coincidences, respectively, yielding a total number of coincidence possibilities of $169\,574\,400$. In order to facilitate the histograming of any given set of coincidences, measured or simulated, the asymmetry between intra-ring and inter-ring pixel combinations was broken by assuming a factorization scheme that considers inter-ring pixel combinations only. The asymmetry is again restored if during the factorization all pixels triggered in an intra-ring coincidence, and only those, are histogramed taking into account the pixel with inferior number in first place. For example, if pixels 100 and 200 are hit in the same ring, than the histogram combination with pixels 200 and 100 must not exist since it regards the same coincidence channel, which is not true if two different rings are hit. The next paragraph exemplifies the C code that, respecting the constraints mentioned, generates a triangle-shaped histogram (Fig. A.2, left column) with a unique channel existing for every coincidence occuring in any given `rowA`, `ringA` and `rowB`, `ringB` of the tomograph, with `rowA` and `rowB` denoting the number of the pixel triggered within the ring (0 to 575, cf. Fig. A.1).

```
if (rowA > rowB && ringA == ringB) { // smaller pixel goes first
    aux = rowB,  rowB  = rowA,  rowA  = aux; }


// smaller ring goes first except for detections in same ring
if (ringA > ringB) { aux = rowB,  rowB  = rowA,  rowA  = aux;
                     aux = ringB, ringB = ringA, ringA = aux; }


hitPlane= ringA * axialCH + ringB;    // hit plane (axialCH=32 for exact-hr+)
chINpl  = rowA * crPERri + rowB;      // channel within plane (crPERri=576)
channel = hitPlane * chPERpl + chINpl;// unique channel number (chPERpl=331200)
```

In addition to the factorization algorithm described, dynamical allocation for new histogram channels appearing during the building of the histogram was implemented by means of a linked list scheme, where each histogram channel points to its immediately inferior, non-empty, non-adjacent channel and, at the same time, to its immediately superior, non-empty, non-adjacent channel. This allows the histogram to contain only non-empty channels and to grow only when a new, nonexisting channel is triggered. In order to save computer memory and increase the processing speed the histograms used during later iterations loose the linked list character since new histogram channels cannot appear during the iterations of the MLEM reconstruction algorithm. Finally, both the simulation and the reconstruction routines are versatile concerning the number of pixels considered, i.e. they are able to handle a larger number of pixels in the tomograph, e.g. by increasing the radius of the tomograph as studied in section 2.6.2.

Appendix B

CAGE - A Multi-Parameter Data Acquisition at CAMAC Speed

A data acquisition system performing multi parameter readout of electronic modules operating under the CAMAC[1] standard was developed in order to readout the two position sensitive γ-ray detectors studied in chapters 4, 5 and 6. Each detector provides 32 energy outputs resulting in 65 and 67 analog channels to be read if the additional coincidence time spectra are taken into account (chapters 4 and 5, and chapter 6, respectively). This numbers increase further if the extraction status from the accelerator is also sampled, as well as a scaler allowing to read the number of events lost by the system during data readout. Four CAMAC peak sensing ADC from Phillips Scientific, model PS7164, were used, each providing 16 channels input. A CAMAC/GPIB[2] crate controller from Kinetic Systems, model 3988, reads the ADC and sends the data through the GPIB protocol to a GPIB/Ethernet converter from National Intruments, model GPIB-ENET/100. The GPIB/Ethernet converter can be accessed by any linux-running machine logged to the local network. For that, a C/C++ based application named CAGE (Camac Acquisition through GPIB and Ethernet) was developed [Cre03]. It allows the user to control the CAMAC acquisition and to see, on-line, the spectra being collected. The GPIB/ENET driver software for linux is publicly available [Nat05] and the control routines for the display are based on the Qt open-source package [Tro05].

CAGE is prepared to automatically perform and display single spectrum acquisitions with rates above 40 kcps[3] (Table B.1), two simultaneous spectra (Fig. B.1) reaching rates of approximately 30 kcps, 16 spectra, 64, 66 and 69 spectra. When acquiring 16 spectra or less, the 65 kiloword buffer of the crate controller, with 24-bit long words, is used to maximize speed throughput by reading one ADC in the so-called Q-repeat mode. In this mode, a CAMAC read function can be repeatedly executed at CAMAC-bus speed (~ 1 MHz, 24 bit, parallel) and the result is stored in the buffer only when the ADC delivers a CAMAC Q-signal, i.e. a valid read cycle. CAGE starts the connection protocol only when the buffer is full and, once the hand-shake between the host computer and the crate controller is performed, the full buffer is transferred in direct memory access (DMA) mode at the maximum speed of the intervening buses (8 Mbit, parallel, for the GPIB bus and 10 to 100 Mbit, serial, for the TCP/IP[4]).

If the number of spectra exceeds 16, than more than one ADC is needed and one repeated read function does not suffice. In this case, an auxilliary crate controller from Kinetic Systems, model 3982, is used which has two internal buffers: one for function storage and one for data, with 8 kiloword each. CAGE first stores in the 3982 function buffer the CAMAC operations to be performed every time an event arrives. An ADC from Ortec, model 811, with the slowest

---

[1] Computer Automated Measurement And Control.
[2] General Purpose Interface Bus.
[3] Kilo counts per second.
[4] Transmission Control Protocol / Internet Protocol.

conversion time, asserts its look-at-me (LAM) signal when it has finished conversion and with this starts the 3982 acquisition cycle. The 3982 runs in standalone mode, handling the arriving events and storing them in the data buffer at CAMAC speed. CAGE checks the data buffer and only reads it, in DMA mode as mentioned, after it is more than half-full, again optimizing the buses transfer capabilities.
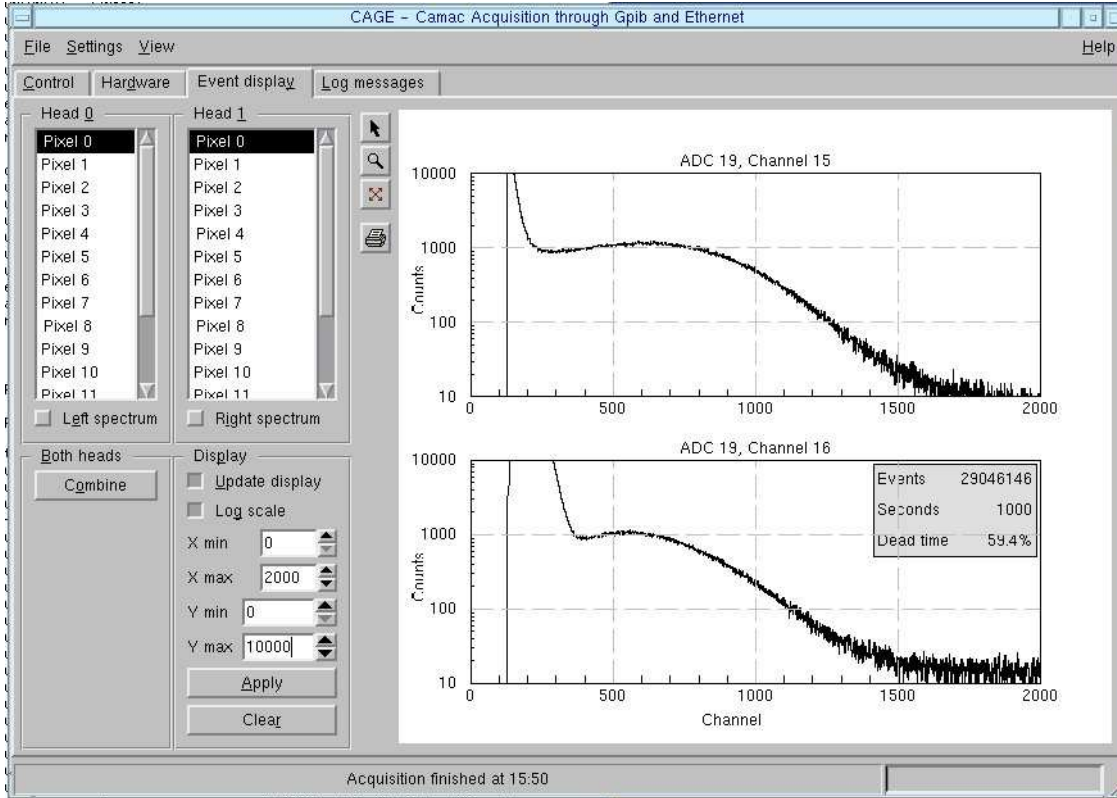
Figure B.1: CAGE user interface displaying two single photoelectron spectra. The spectra were simultaneously acquired with two Phillips PMT: an XP2020Q at -2650 V (top) and an XP3312B at -1300 V (bottom).

Table B.1: CAGE performance for several input rates and readout channels. All values obtained with a comb-shape spectrum generator.

In	Out											
Input rate (cps)	1 ch.		2 ch.		16 ch.		32 ch.		64 ch.		66 ch.	
	RR (cps)	DT (%)	RR (cps)	DT (%)	RR (cps)	DT (%)	RR (cps)	DT (%)	RR (cps)	DT (%)	RR (cps)	DT (%)
100	98.7	1.3	98.4	1.6	96	4	92	8	87	13	86	14
1 k	977	2.3	974	2.6	900	10	624	37	446	55	398	60
10 k	9 k	9.8	9.1 k	9.5	4.4 k	56	1.4 k	86	745	93	611	94
100 k	43 k	57	29 k	71	6 k	94	1.6 k	98.4	794	99.2	650	99.4

RR = Readout rate (counts per second),   DT = Dead time (%).

Appendix C

Generated and Detected Positron Activity during Irradiation

The present appendix summarizes the method used to estimate the number of positron emitting nuclei detected within a given irradiation, e.g. as plotted in the simulation curve in Figs. 6.11 and 6.14, and detailed in Table 6.2 and Fig. 6.12. The number $N_0^{(j)}$ of each isotope species j produced by an incoming beam with fluence F and target range R was extrapolated from the output of the Monte-Carlo code PosGen [Has96, Pön04] shown in Fig. 1.17. The simulated value of $N_0^{(j)}$ must agree with that expected for thick targets

$$N_0^{(j)} = F \cdot \rho \cdot \frac{N_A}{A} \cdot R \cdot \sigma^{(j)}, \tag{C.1}$$

with $\rho \cdot \frac{N_A}{A}$ being the target molecular density and $\sigma^{(j)}$ the partial cross section containing all the reactions yielding isotope j. The term $\sigma^{(j)}$ is given by

$$\sigma^{(j)} = \sum_i^M f_i \cdot \sigma_{PT_i}^{(j)}, \tag{C.2}$$

with M the number of chemical elements composing the target, f_i the stoichiometric coefficient for element i in the target molecule and $\sigma_{PT_i}^{(j)}$ the partial cross section for the reactions $T_i(P,j)T_i'$ and $T_i(P,P')j$, i.e. the cross section for the reactions creating the projectile or target fragment j by impinging projectile P on target element T_i, respectively.

Eq. C.1 holds for a beam kinetic energy E between 500 down to 100 AMeV, where $\sigma^{(j)}$ is approximately constant [Sih93]. For smaller beam energies $\sigma^{(j)}$ depends on E and must be substituted with $\sigma^{(j)}(E)$, with $\sigma^{(j)}(E)$ presenting a first steep rise with decreasing E, followed by a sharp drop to zero for $E \leq 30$ AMeV [Has96, Sih93].

If the irradiation conditions used to build Table 6.2 are considered, i.e. a total of 6×10^{10} carbon ions are delivered onto a PMMA target with a kinetic energy of 200.2 AMeV, corresponding to $R = 74$ mm, together with e.g. $\sigma_{^{12}C^{16}O}^{(^{15}O)} = 84$ mb taken from [Sih93], than the total number of ^{15}O target fragments produced following Eq. C.1 is 8.06×10^8, which lies 12 % below the number simulated with the PosGen code (9.2×10^8, Table 6.2) most probably because the Monte Carlo code takes into account the steep increase in the cross section for producing ^{15}O at low beam kinetic energy. The same is verified for the production of ^{11}C, both target and projectile, by considering $\sigma_{^{12}C^{12}C}^{(^{11}C)} = 53$ mb [Sih93], $\sigma_{^{12}C^{16}O}^{(^{11}C)} = 26.5$ mb [Sih93], and $\sigma_{^{12}C^1H}^{(^{11}C)} = 57$ mb [Bee03]. In this case Eq. C.1 yields 3.7×10^9 ^{11}C ions versus a total of 4.0×10^9 generated with the PosGen code. This again is a good agreement due to the same argument: the Monte Carlo code must consider the higher cross sections verified when the beam energy decreases, therefore yielding 7.2 % more ^{11}C isotopes than the simpler approach given by Eq. C.1.

Once the number $N_0^{(j)}$ of isotopes j produced per spill is known, and assuming it is created at time instant $t_0 = 0$, the activity value at a later time instant t_1, $A_{t_1}^{(j)}$, is given by

$$A_{t_1}^{(j)} = \frac{N_0^{(j)}}{T_{1/2}^{(j)}/\ln 2} \cdot \sum_{i=0}^{N_s-1} \exp\left(\frac{-i \cdot T_M}{T_{1/2}^{(j)}/\ln 2}\right), \qquad (C.3)$$

with N_s the number of spills delivered between t_0 and t_1, T_M the macropulse (spill) period and $T_{1/2}^{(j)}$ the half-life of isotope j. The number of isotopes j decaying within the time window $(t_0 = 0, t_1)$ of a PET measurement, $C^{(j)} = N^{(j)}(t_0 = 0, t_1)$, is given by the time integral of Eq. C.3:

$$C^{(j)} = N^{(j)}(t_0 = 0, t_1) = \int_{t_0}^{t_1} A^{(j)}(t)\, \mathrm{d}t = N_0^{(j)} \cdot \sum_{i=0}^{N_s-1} \left[1 - \exp\left(\frac{-i \cdot T_M}{T_{1/2}^{(j)}/\ln 2}\right)\right]. \qquad (C.4)$$

Eq. C.4 shows that isotopes with half-lives $T_{1/2}^{(j)}$ much shorter than T_M yield

$$C_{short-lived}^{(j)'} = A_0^{(j)} \cdot \frac{T_{1/2}^{(j)}}{\ln 2} \cdot N_s, \qquad (C.5)$$

i.e. the induced activity nearly completely decays within any PET measurement. This mechanism explains the increasing relative weight of short-lived, β^+-decaying isotopes, e.g. ^{12}N and ^{8}B, with decreasing measuring time. Due to their fast decay, this fact can only be observed when data taking during particle extraction is implemented (Table 6.2 and Fig. 6.12). By weighting Eq. C.5 with the proper time window for data taking during particle extraction, the number of short-lived isotopes detected slightly reduces to

$$C_{short-lived}^{(j)} = A_0^{(j)} \cdot \frac{T_{1/2}^{(j)}}{\ln 2} \cdot N_s \cdot \left[\frac{\Delta t_{bg}}{T_{RF}} - 1\right], \qquad (C.6)$$

with Δt_{bg} and T_{RF} defined in Fig. 6.1 and Eq. 6.2, respectively.

If the same time window is applied for isotopes with $T_{1/2}^{(j)} > T_M$, and adding the proper weight resulting from the duty factor D_f of the accelerator, defined in section 6.1, the number of long-lived isotopes detected is given by

$$C_{long-lived}^{(j)} = C^{(j)} \cdot \left[1 - D_f\right] + C^{(j)} \cdot D_f \cdot \left[\frac{\Delta t_{bg}}{T_{RF}} - 1\right] = C^{(j)} \cdot \left[1 + D_f \cdot \left(\frac{\Delta t_{bg}}{T_{RF}} - 2\right)\right]. \quad (C.7)$$

Finally, both $C_{long-lived}^{(j)}$ and $C_{short-lived}^{(j)}$ must be multiplied by the geometrical acceptance and coincidence detection efficiency of the detectors measuring the decaying β^+-activity.

Appendix D

A Random Suppression Solution for BASTEI

The results obtained with the phase trigger described in section 6.2.2 allowed to perform random suppression during particle extraction with the two LSO/APDA detectors (section 6.5). The phase trigger utilized [Hei04] showed excellent performance for a fixed beam energy, being independent from the amplitude of the RF signal, as necessary for all results presented in sections 6.5, 6.7 and 6.8.2. Nevertheless, its digital output presents frequency dependent delays, described in section 6.2.2, which veto its application during the consecutive changing beam energies utilized during therapeutic irradiation by means of the GSI rasterscan beam delivery [Hab93]. For this reason, the experimental results obtained with a phase trigger independent of the amplitude, frequency and baseline oscillations of its input signal are presented here. The proposed phase trigger [Eng05c] is based on a leading edge circuit, preceeded by a high-pass passive filter and built in zero-crossing mode (Fig D.1). Its performance is shown in Fig. D.2, obtained by feeding into an assembled phase-trigger several signals from a waveform generator. The timings of the input signals covered the range of frequencies used at the GSI rasterscan delivery system, was well as the timings to be used at the synchrotron in the Heildelberg clinics (Table 6.6). It can be seen that a negligible oscillation (inferior to 2 %) exists between the output of the phase trigger in respect to the moment of zero-crossing of all input signals. The input frequencies covered the accelerator RF timings from the GSI facility as well as from the hospital facility planned in Heidelberg. Input frequencies ranged between 2.08 MHz (Fig. D.2, top) up to 7.1 MHz (Fig. D.2, bottom), with the signal amplitudes varying between 0.5 and 2 V in all cases, which is well above the 30 % maximum amplitude variation of the RF signal at GSI [For03]. In addition to the tests described, a low frequency signal (not shown), simulating an oscillating baseline, was added to the input of the phase-trigger and it
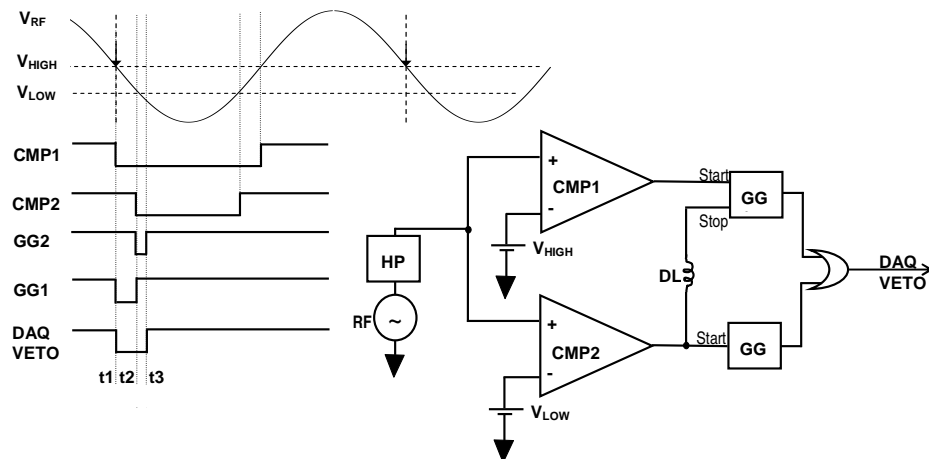

Figure D.1: Timing diagram (left) of a zero-crossing, phase trigger concept (right). The high-pass filter HP brings the DC component of the RF signal to zero, i.e. it eliminates slow moving baseline oscillations. By setting V_{HIGH} to ground the remaining electronics acts like a zero-crossing detector insensitive to amplitue and frequency variations of the input signal (cf. Fig. D.2).
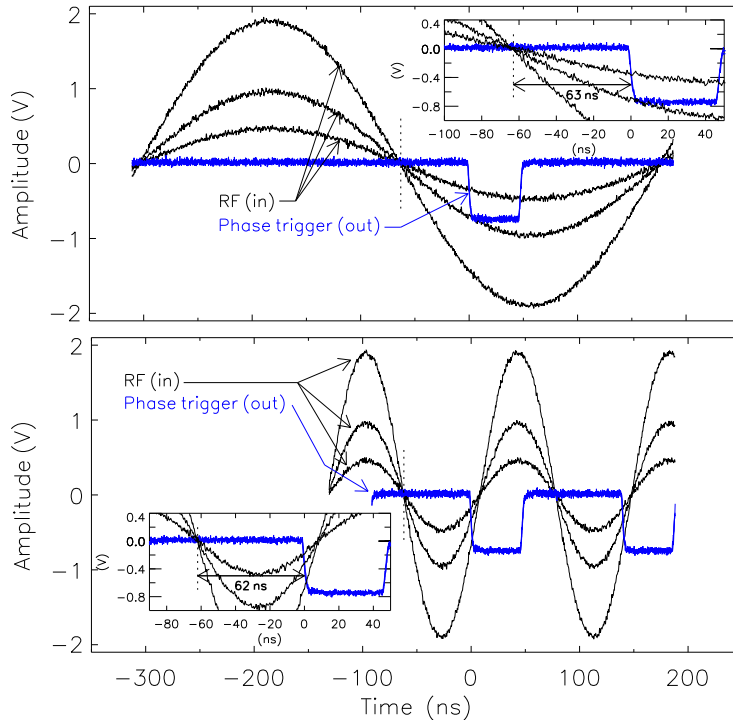
Figure D.2: Results measured with the phase trigger proposed. The three output signals in each image overlap perfectly (text has details).

was seen that a simple passive, double stage, high-pass filter (HP in Fig. D.1) provided enough attenuation of the slow oscillations, enabling the phase-trigger to perform without restrictions.

The output of the phase trigger, DAQ VETO, can be implemented onto the electronics of BASTEI following the scheme in Fig. D.3. An analog multiplexer sets the connection from the anode signal of each PMT to ground (through a $50\,\Omega$ resistor) only when the DAQ VETO signal is asserted. This disables the data acquisition from BASTEI to read the high yield event background during the microbunches (Δt_{bg}, Fig. 6.1). This setup still lacks a time correction for the ion transit time in the beam pipeline, which is a parameter dependent on the beam energy that can be calibrated once and written on an electronic look-up table. Together with this look-up table, the whole assembly would provide a low-cost random suppression solution for BASTEI based on one phase-trigger circuit, already assembled at FZR, together with 256 (or 64 Quad) fast analog multiplexers installed between the anode outputs of the 256 PMT and the electronics boards from BASTEI, as shown in Fig. D.3.
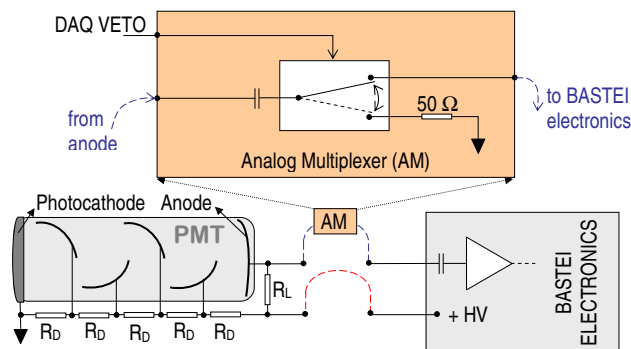

Figure D.3: Implementation of the phase trigger output onto BASTEI. The dashed, curved lines denote the two cables connecting the data acquisition electronics from BASTEI to each PMT.

Bibliography

[Ada01] L.E. Adam, J.S. Karp, M.E. Daube-Witherspoon, R.J. Smith. Performance of a whole-body PET scanner using curve-plate NaI(Tl) detectors. *J. Nucl. Med.*, 42:1821–1830, 2001.

[Ahl80] S.P. Ahlen. Theoretical and experimental aspects of the energy loss of relativistic heavily ionizing particles. *Rev. Mod. Phys.*, 52:121–173, 1980.

[Alk56] D.G. Alkhazov, D.S. Andreyev, A.P. Greenberg, I.N. Lemberg. Investigation of Coulomb excitation of nuclei by nitrogen ions. *Nucl. Phys.*, 2(1):65–80, 1956.

[Ama04] U. Amaldi, P. Berra, K. Crandall, D. Toet, M. Weiss, R. Zennaro, E. Rosso, B. Szeless, M. Vretenar, C. Cicardi, C. De Martinis, D. Giove, D. Davino, M. R. Masullo, V. Vaccaro. LIBO - a linac-booster for proton therapy: construction and tests of a prototype. *Nucl. Instrum. Meth. A*, 521:512–529, 2004.

[Ang58] H.O. Anger. Scintillation camera. *Rev. Sci. Instrum.*, 29:27–33, 1958.

[Bad96] R.D. Badawi, P.K. Marsden, B.F. Cronin, J.L. Sutcliffe, M.N. Maisey. Optimization of noise-equivalent count-rates in 3D PET. *Phys. Med. Biol.*, 41:1755–1776, 1996.

[Bad97] E. Badura, H. Eickhoff, H. Essel, Th. Haberer, J. Hoffmann, U. Krause, W. Ott, K. Poppensieker, M. Richter, D. Schardt, R. Steiner, B. Voss. Safety and control system for the GSI therapy project. In *ICALEPCS97*, pages 555–558, Beijing, November 1997.

[Bar56] W.H. Barkas, W. Birnbaum, F.M. Smith. Mass-ratio method applied to the measurement of L-meson masses and the energy balance in pion decay. *Phys. Rev.*, 101(2):778–795, 1956.

[Bee03] J. Beebe-Wang, P. Vaska, F.A. Dilmanian, S.G. Peggs, D.J. Schlyer. Simulation of proton therapy treatment verification via PET imaging of induced positron-emitters. In *Proc. IEEE 2003 Med. Ima. Conf.*, Portland, OR, USA, Oct. 2003. M8-6.

[Ber01] E. Berdermann, K. Blasche, P. Moritz, H. Stelzer, B. Voss. The use of CVD-diamond for heavy-ion detection. *Diam. Relat. Mater.*, 10:1770–1777, 2001.

[Bir64] J.B. Birks. *The Theory and Practice of Scintillation Counting*. Pergamon Press, London, 1964.

[Bob84] G.J. Bobbink, A. Engler, R.W. Kraemer, J. Nash, R.B. Sutton. Study of radiation damage to long BGO crystals. *Nucl. Instrum. Meth. A*, 227:470–477, 1984.

[Boe03] R. Boellaard, F. Buijs, H.W.A.M. de Jong, M. Lenox, T. Gremillion, A.A. Lammertsma. Characterization of a single LSO crystal layer High Resolution Research Tomograph. *Phys. Med. Biol.*, 48:429–448, 2003.

[Boh15] N. Bohr. The penetration of atomic particles through matter. *Philos. Mag.*, 30:581, 1915.

[Bou00]   P. Bourgeois, M. Karolak, G. Vasseur. Performance of the photomultiplier tubes used in the DIRC of BABAR: effect of a magnetic field and of helium. *Nucl. Instrum. Meth. A*, 442:105–112, 2000.

[Bra99]   S. Brandenburg, L. de Vries. A subharmonic buncher for the AGOR-cyclotron. In E. Baron and M. Lieuvin, editors, *Cyclotrons and Their Applications 1998: XV International Conference*, pages 193–195, Caen, France, 1999. IoP Publishing, Bristol.

[Bra03]   A. Brahme. Biologically optimized 3-dimensional in vivo predictive assay-based radiation therapy using positron emission tomography-computerized tomography imaging. *Acta Oncol.*, 42(2):123–136, April 2003.

[Bre56]   G. Breit, M.E. Ebel. Nucleon transfer and virtual coulomb excitation. *Phys. Rev.*, 104(4):1030–1046, 1956.

[Bro76]   R.A. Brooks and G. DiChiro. Principles of computer assisted tomography (CAT) in radiographic and radioisotopic imaging. *Phys. Med. Biol.*, 21(5):689–732, 1976.

[Buc96]   D. Bucin, M. Conte, O. Ferrando, A. Ratti, V. Tamburini. Conventional protron synchrotron. In U. Amaldi, M. Grandolfo, and L. Picardi, editors, *The RITA Network and the Design of Compact Proton Accelerators*. INFN-LNF Divisione Ricerca, Frascati, 1996.

[Buh03]   P. Buhzan, B. Dolgoshein, L. Filatov, A. Ilyin, V. Kantzerov, V. Kaplin, A. Karakash, F. Kayumov, S. Klemin, E. Popova, S Smirnov. Silicon photomultiplier and its possible applications. *Nucl. Instrum. Meth. A*, 504:48–52, 2003.

[Cas86]   M.E. Casey, R. Nutt. A multicrystal two dimensional BGO detector for positron emission tomography. *IEEE T. Nucl. Sci.*, 33:460–463, 1986.

[Cha98]   Y. Charon, P. Lanièce, H. Tricoire. Radio-imaging for quantitative autoradiography in biology. *Nucl. Med. Biol.*, 25:699–704, 1998.

[Che83]   V.Yu. Chepel. A new liquid xenon scintillation detector for positron emission tomography. *Nucl. Tracks Radiat. Meas.*, 21(1):47–51, 1983.

[Che04a] V. Chepel, F. Neves, V. Solovov, A. Pereira, M.I. Lopes, J. Pinto da Cunha, P. Mendes, A. Lindote, C.P. Silva, R. Ferreira Marques, A.J.P.L. Policarpo. Performance of a chamber for studying the liquid xenon response to nuclear recoils. In *Proc. IEEE 2004 Nucl. Sci. Symp.*, Rome, Italy, Oct. 2004. N16-28.

[Che04b] S.R. Cherry. *In vivo* molecular genomic imaging: new challenges for imaging physics. *Phys. Med. Biol.*, 49:13–48, 2004.

[Chu99]   W.T. Chu. Hadron therapy. In W.R. Hendee, editor, *Biomedical Uses of Radiation*, pages 1055–1131. Wiley-VCH Publishers, New York, April 1999.

[Cir04]   G.A.P. Cirrone, Laboratori Nazionali del Sud - INFN, Catania, November 2004. Personal communication.

[Col00]   J. Collot, S. Jan, E. Tournefier. A liquid xenon PET camera for neuro-science. In B. Aubert and J. Colas, editors, *CALOR2000 Proc. 9th Int. Conf. on Calorimetry in High Energy Physics*, pages 305–313. Frascati Phys. Ser., 2000.

[Con03]   M. Conti, B. Bendriem, M. Casey, M. Chen, F. Kehren, C. Michel, V. Panin. Imple-
          mentation of time-of-flight on CPS HiRez PET scanner. In *Proc. IEEE 2003 Med.
          Ima. Conf.*, Portland, OR, USA, Oct. 2003. M3-1.

[Coo99]   D.W. Cooke, B.L. Benneth, R.E. Muenchausen, K.J. McClellan, J.M. Roper,
          M.T. Whittaker. Intrinsic trapping sites in rare-earth and yttrium oxyorthosilicates.
          J. Appl. Phys., 86(9):5308–5310, 1999.

[Coo00]   D.W. Cooke, K.J. McClellan, B.L. Bennett, J.M. Roper, M.T. Whittaker,
          R.E. Muenchausen, R.C Sze. Crystal growth and optical characterization of cerium-
          doped $Lu_{1.8}Y_{0.2}SiO_5$. *J. Appl. Phys.*, 88(12):7360–7362, 2000.

[Cou04]   G. Coutrakon, J. Hubbard, J. Johanning, G. Maudsley, T. Slaton, P. Morton. A
          performance study of the Loma Linda proton medical accelerator. *Med. Phys.*,
          21(11):1691–1701, 2004.

[Cre98]   P. Crespo, V. Chepel, M.I. Lopes, L. Janeiro, R. Ferreira Marques, A.J.P.L. Poli-
          carpo. Pulse shape analysis in the liquid xenon multiwire ionisation chamber for
          PET. *IEEE T. Nucl. Sci.*, 45(3):561–567, 1998.

[Cre00]   P. Crespo, J. van der Marel, V. Chepel, M.I. Lopes, D. Santos, L. Janeiro, V. Solovov,
          R.F. Marques, A.J.P.L. Policarpo. Pulse processing for the PET multiwire liquid
          xenon ionisation chamber. *IEEE T. Nucl. Sci.*, 47(6):2119–2126, 2000.

[Cre02]   P. Crespo, K. Lauckner, W. Enghardt. A new fully 3D maximum likelihood PET
          reconstruction applicable to different detector arrangements. *GSI Rep. 2002-1 (Ann.
          Rep. 2001)*, pages 173–174, 2002.

[Cre03]   P. Crespo, J. Pawelke, W. Enghardt. A CAMAC data acquisition system for multi pa-
          rameter measurements. *Wiss.-Tech. Ber. FZR-372 (Ann. Rep. 2002)*, page 82, 2003.

[Cre04]   P. Crespo, M. Kapusta, J. Pawelke, M. Moszyński, W. Enghardt. First in-beam PET
          imaging with LSO/APD-array detectors. *IEEE T. Nucl. Sci.*, 51(5):2654–2661, 2004.

[Cre05a] P. Crespo, G. Shakirin, W. Enghardt. Direct time-of-flight for online, in-beam PET:
          concept and feasibility study. *Phys. Med. Biol.*, 2005. To be submitted.

[Cre05b] P. Crespo, G. Shakirin, W. Enghardt. On the detector arrangement for in-beam PET
          for hadron therapy monitoring. *Phys. Med. Biol.*, 2005. Submitted.

[Cre05c] P. Crespo, N. Abolmaali, R. Bergmann, E. Will, W. Enghardt. Low-activity PET
          measurements with LSO- and BGO-based positron tomographs. *Phys. Med. Biol.*,
          2005. To be submitted.

[Cre05d] P. Crespo, T. Barthel, H. Frais-Kölbl, E. Griesmayer, K. Heidel, K. Parodi,
          J. Pawelke, W. Enghardt. Suppression of random coincidences during in-beam PET
          measurements at ion beam radiotherapy facilities. *IEEE T. Nucl. Sci.*, 52(5):980–987,
          2005.

[Cry00]   The Crystal Clear Collaboration. Crystal data. `http://crystalclear.web.cern.`
          `ch/`, available Jun. 2005. Last update: Dec. 2000.

[Dat97]   C.P. Datema, I.P. Pleasents, D. Ramsden. Hybrid photodiodes in scintillation counter
          applications. *Nucl. Instrum. Meth. A*, 387:100–103, 1997.

[Deb00]   J. Debus, Th. Haberer, D. Schulz-Ertner, O. Jäkel, F. Wenz, W. Enghardt,
          W. Schlegel, G. Kraft, M. Wannenmacher. Bestrahlung von Schädelbasistumoren
          mit Kohlenstoffionen bei der GSI. *Strahlenther. Onkol.*, 176(5):211–216, 2000.

[Dei00]   K. Deiters, Y. Musienko, S. Nicol, B. Patel, D. Renker, S. Reucroft, R. Rusack,
          T. Sakhelashvili, J. Swain, P. Vikas. Properties of the most recent avalanche photodi-
          odes for the CMS electromagnetic calorimeter. *Nucl. Instrum. Meth. A*, 442:193–197,
          2000.

[Der82]   S.E. Derenzo, T.F. Budinger, R.H. Huesman, J.L. Cahoon. Dynamic positron emis-
          sion tomography in man using small bismuth germanate crystals. In *Proc. of the
          Sixth Int. Conf. on Positron Annihilation*, pages 1–11, Fort Worth, TA, April 1982.

[dG94]   T.R. de Grado, T.G. Turkington, J.J. Williams, C.W. Stearns, J.M. Hoffman,
          R.E. Coleman. Performance characteristics of a whole-body PET scanner. *J. Nucl.
          Med.*, 35:1398–1406, 1994.

[Dol00]   A. Dolinskii, H. Eickhoff, B. Franczak. The synchrotron of the dedicated ion beam
          facility for cancer therapy, proposed for the clinic in Heidelberg. In *Proceedings of
          the 2000 Particle Accelerator Conf.*, pages 2509–2511, Vienna, Austria, 2000.

[Eic03]   H. Eickhoff, R. Bär, A. Dolinskii, Th. Haberer, B. Schlitt, P. Spiller, U. Weinrich.
          HICAT - the German hospital-based light ion cancer therapy project. In *Proceedings
          of the 2003 Particle Accelerator Conf.*, pages 694–698, Portland, OR, USA, 2003.

[Eng92]   W. Enghardt, W.D. Fromm, H. Geissel, H. Keller, G. Kraft, A. Magel, P. Manfraß,
          G. Münzenberg, F. Nickel, J. Pawelke, D. Schardt, C. Scheidenberger, M. Sobiella.
          The spatial distribution of positron-emitting nuclei generated by relativistic light-ion
          beams in organic matter. *Phys. Med. Biol.*, (11):2127–2131, 1992.

[Eng00]   W. Enghardt, R. Hinz, K. Lauckner, J. Pawelke, F. Pönisch, B.G. Hasch. In-situ
          positron emission tomography for dose localisation at the tumour therapy with ^{12}C.
          GSI Rep. 2000-1 (Ann. Rep. 1999), pages 164–165, 2000.

[Eng03]   W. Enghardt, P. Crespo, W. Bourgeois, A. Winter. A technical feasibility study
          for a PET therapy monitor combined with a rotating ion beam delivery. *Wiss.-
          Tech. Ber. FZR-372 (Ann. Rep. 2002)*, pages 83–84, 2003.

[Eng04a] W. Enghardt, K. Parodi, P. Crespo, F. Fiedler, J. Pawelke, F. Pönisch. Dose quantifi-
          cation from in-beam positron emission tomography. *Radiother. Oncol.*, 73(2):96–98,
          2004.

[Eng04b] W. Enghardt, P. Crespo, F. Fiedler, R. Hinz, K. Parodi, J. Pawelke, F. Pönisch.
          Charged hadron tumour therapy monitoring by means of PET. *Nucl. Instrum.
          Meth. A*, 525:284–288, 2004.

[Eng05a] W. Enghardt. Positronen-Emissions-Tomographie für die Qualitätssicherung der
          Ionenstrahl-Therapie von Tumoren, Habilitationsschrift, Dresden University of Tech-
          nology, Dresden, 2005.

[Eng05b] W. Enghardt, H. Müller. In-beam PET at high-energy photon beams: a feasibility
          study. *Phys. Med. Biol.*, 2005. Submitted.

[Eng05c] W. Enghardt, P. Crespo, K. Parodi, J. Pawelke. Verfahren zur Korrektur der beim Monitoring der strahlentherapeutischen Behandlung mittels in-beam PET erhaltenen Messwerte. *Deutsches Patent- und Markenamt München*, (DE 10 2004 009 784 A1), Sept. 2005.

[Fie03]   C. Field, T. Hadig, M. Jain, D.W.G.S. Leith, G. Mazaheri, B.N. Ratcliff, J. Schwiening, J. Va'vra. Timing and detection efficiency properties of multi-anode PMTs for a focusing DIRC. In *Proc. IEEE 2003 Nucl. Sci. Symp.*, Portland, OR, USA, Oct. 2003. N38-8.

[Fie05]   F. Fiedler, P. Crespo, K. Parodi, M. Sellesk, W. Enghardt. The feasibility of in-beam PET for therapeutic beams of ^{3}He. In *IEEE 2005 Nucl. Sci. Symp.*, Puerto Rico, Oct. 2005. Accepted.

[Fir96]   R.B. Firestone and V.S. Shirley, editor. *Table of Isotopes*. John Wiley & Sons, Inc., New York, 8th edition, 1996.

[For03]   P. Forck, GSI Darmstadt, December 2003. Personal communication.

[Fra04]   H. Frais-Kölbl, E. Griesmayer, H. Kagan, H. Pernegger. A fast low-noise charged-particle CVD diamond detector. *IEEE T. Nucl. Sci.*, 51(6):3833–3837, 2004.

[Fur03]   T. Furukawa, K. Noda, E. Urakabe, M. Muramatsu, M. Kanazawa, K. Maeda. Characteristics of fast beam switching for spot scanning. *Nucl. Instrum. Meth. A*, 503:485–495, 2003.

[Gar00]   N. Garnier, C. Dujardin, A.N.C. Belsky, J.P. Moy, H. Wieckzorek, P. Chevallier, A. Firsov. Spectroscopy of CsI(Tl). In *SCINT99 Proc. of the 5th Int. Conf. on Inorganic Scintillators and their Applications*, pages 379–384, M. V. Lomonosov State University, Moscow, 2000.

[Glo04]   J. Glodo, W.W. Moses, W.M. Higgins, E.V.D. van Loef, P. Wong, S.E. Derenzo, M.J. Weber, K.S. Shah. Effects of Ce concentration on scintillation properties of LaBr$_3$:Ce. In *Proc. IEEE 2004 Nucl. Sci. Symp.*, Rome, Italy, Oct. 2004. N19-5.

[Got93]   B. Gottschalk, A.M. Koehler, R.J. Schneider, J.M. Sisterson, M.S. Wagner. Multiple Coulomb scattering of 160 MeV protons. *Nucl. Instrum. Meth. B*, 74:467–490, 1993.

[Gro98a] D.E. Groom. Particle detectors. *The European Physical Journal C*, 3(1-4):154–162, 1998.

[Gro98b] D.E. Groom. Photon and electron interactions with matter. *The European Physical Journal C*, 3(1-4):152–153, 1998.

[GSI99a] Proposal for a dedicated ion beam facility for cancer therapy. *GSI Nachrichten*, 1:14–16, 1999.

[GSI99b] Tumour therapy, first results from the clinical study. *GSI-Nachrichten*, 3:8, 1999.

[Gun04a] K. Gunzert-Marx. *Nachweis leichter Fragmente aus Schwerionenreaktionen mit einem BaF$_2$-Teleskop-Detektor*. PhD thesis, Darmstadt University of Technology, Darmstadt, Feb. 2004.

[Gun04b] K. Gunzert-Marx, D. Schardt, R.S. Simon. Fast neutrons produced by nuclear fragmentation in treatment irradiations with ^{12}C beam. *Radiat. Prot. Dosim.*, 110(1-4):595–600, 2004.

[Hab93] Th. Haberer, W. Becher, D. Schardt, G. Kraft. Magnetic scanning system for heavy ion therapy. *Nucl. Instrum. Meth. A*, 330:296–305, 1993.

[Hab01] Th. Haberer, H. Eickhoff, P. Spiller, GSI Darmstadt, 2001. Personal communication.

[Hag02] K. Hagiwara et al. Review of Particle Physics. *Phys. Rev. D*, 66:010001+, 2002. `http://pdg.lbl.gov`, available Jun. 2005.

[Hal94] E.J. Hall. *Radiobiology for the radiobiologist*. J.B. Lippincott Company, Philadelphia, 4th edition, 1994.

[Has96] B.G. Hasch. *Die physikalischen Grundlagen einer Verifikation des Bestrahlungsplanes in der Schwerionen-Tumortherapie mit der Positronen-Emissions-Tomographie*. PhD thesis, Dresden University of Technology, Dresden, Dec. 1996.

[Hea98] The Heavy Ion Collaboration. *Proposal for a dedicated ion beam facility for cancer therapy*. K.D. Groß, M. Pavlovic, editors, GSI Darmstadt, 1998.

[Hei04] K. Heidel. Ableitung eines VETO-Signals aus der Beschleuniger HF an der GSI, FZ-Rossendorf, March 2004. Internal communication.

[Hel00] E. Hell, W. Knüpfer, D. Mattern. The evolution of scintillating medical detectors. *Nucl. Instrum. Meth. A*, 454:40–48, 2000.

[Hig75] V.L. Highland. Some practical remarks on multiple scattering. *Nucl. Instrum. Meth.*, 129:497, 1975.

[Hig79] V.L. Highland. Some practical remarks on multiple scattering. *Nucl. Instrum. Meth.*, 161:171, 1979.

[Hir92] K. Hiramoto, M. Nishi. Resonant beam extraction scheme with constant separatrix. *Nucl. Instrum. Meth. A*, 322:154–160, 1992.

[Hof48] R. Hofstadter. Alkali halide scintillator counters. *Phys. Rev.*, 74:100–101, 1948.

[Hof00] S. Hofmann, G. Münzenberg. The discovery of the heaviest elements. *Rev. Mod. Phys.*, 72(3):733–767, July 2000.

[Hub02] J.S. Huber, W.W. Moses, W.F. Jones, C.C. Watson. Effect of ^{176}Lu on singles transmission for LSO-based PET cameras. *Phys. Med. Biol.*, 47:3535–3541, 2002.

[Hug79] W.L. Hughes, G.H. Nussbaum, R. Connolly, B. Emami, P. Reilly. Tissue perfusion rate determined from the decay of oxygen-15 after photon activation in situ. *Science*, 204:1215–1217, 1979.

[Huh93] M. Huhtinen, P.A. Aarnio. Pion induced displacement damage in silicon devices. *Nucl. Instrum. Meth. A*, 335:580–582, 1993.

[Hum03] J.L. Humm, A. Rosenfeld, A. Del Guerra. From PET detectors to PET scanners. *Eur. J. Nucl. Med. Mol. I.*, 30:1574–1597, 2003.

[ICR70] *Linear energy transfer*. ICRU Report No. 16, Washington, 1970.

[ICR84] *Stopping powers for electrons and positrons*. ICRU Report No. 37, Washington, 1984.

[ICR93] *Stopping powers and ranges for protons and alpha particles*. ICRU Report No. 49, Washington, 1993.

[Iva98]   D.Yu. Ivanov, E.A. Kuraev, A. Schiller, V.G. Serbo. Production of e^+e^- pairs to all orders in $Z\alpha$ for collisions of high-energy muons with heavy nuclei. *Phys. Lett. B*, 442:453–458, 1998.

[Jäk00]   O. Jäkel, J. Debus. Selection of beam angles for radiotherapy of skull base tumours using charged particles. *Phys. Med. Biol.*, 45:1229–1241, 2000.

[Jäk01]   O. Jäkel, M. Krämer, C.P. Karger, J. Debus. Treatment planning for heavy ion radiotherapy: clinical implementation and application. *Phy. Med. Biol.*, 46:1101–1116, 2001.

[Jäk02]   O. Jäkel. Bestrahlungsplanung für die Schwerionentherapie. In *Berichte aus der Medizinischen Physik*. Shaker Verlag GmbH, Aachen, 2002. ISBN 3-8322-0350-8.

[Jan02]   S. Janek. 3-dimensional patient dose delivery verification based on PET-CT imaging of photonuclear reactions in 50 MV scanned photon beams, Master thesis, Karolinska Institute and Royal Institute of Technology, Stockholm, 2002.

[Joy74]   A.R. Joy. A standard system of coordinates for radiotherapy apparatus. *Phys. Med. Biol.*, 19:213–219, 1974.

[Kap00]   M. Kapusta, M. Moszyński, M. Balcerzyk, J. Pawelke. Comparison of the scintillation properties of LSO:Ce and YSO:Ce as the detectors for high resolution PET. *Acta Phys. Pol. B*, 31(1):101–106, 2000.

[Kap02]   M. Kapusta, P. Crespo, M. Moszyński, W. Enghardt, M. Szawlowski, B.L. Zhou, D. Wolski. Evaluation of LAAPD arrays for high-resolution scintillator matrices readout. *IEEE T. Nucl. Sci.*, 44(4):1693–1698, 2002.

[Kap03]   M. Kapusta, P. Crespo, D. Wolski, M. Moszyński, W. Enghardt. Hamamatsu S8550 APD arrays for high-resolution scintillator matrices readout. *Nucl. Instrum. Meth. A*, 504:139–142, 2003.

[Kap04]   M. Kapusta, P. Crespo, D. Wolski, K. Heidel, L. Heinrich, J. Hutsch, J. Pawelke, M. Sobiella, A. Trzcińska, M. Moszyński, W. Enghardt. The LSO/APD array as a possible detector for in-beam PET in hadron therapy. *IEEE T. Nucl. Sci.*, 51(4):1389–1394, 2004.

[Kar03]   C.P. Karger, D. Schulz-Ertner, B.H. Didinger, J. Debus, O. Jäkel. Influence of setup errors on spinal cord dose and treatment plan quality for cervical spine tumors: a phantom study for photon IMRT and heavy charged particle radiotherapy. *Phys. Med. Biol.*, 48:3171–3189, 2003.

[Kau61]   R. Kaufmann, R. Wolfgang. Nucleon transfer reactions in grazing collisions of heavy ions. *Phys. Rev.*, 121(1):192–205, 1961.

[Kau02]   C. Kausch, W. Enghardt. The evaluation of carbon ion therapy PET data within the time domain. *Wiss.-Tech. Ber. FZR-341 (Ann. Rep. 2001)*, page 102, 2002.

[Kim01]   J. Kim, F. Marti, H. Blosser. Design study of a superconducting cyclotron for heavy ion therapy. In F. Marti, editor, *Cyclotrons and Their Applications 2001: XVI International Conference*, pages 324–326, East Lansing, MI, USA, 2001. AIP Conference Proceedings, New York.

[Kim02] T. Kimble, M. Chou, B.H.T. Chai. Scintillation properties of LYSO crystals. In *Proc. IEEE 2002 Med. Ima. Conf.*, Norfolk, VI, USA, Nov. 2002. M10-34.

[Kno89] G.F. Knoll. *Radiation Detection and Measurement*. John Wiley & Sons, New York, 2nd edition, 1989.

[Kob83] M. Kobayashi, K. Kondo, H. Hirabayashi, S.-I. Kurokawa, M. Taino, A. Yamamoto. Radiation damage of BGO crystals due to low energy γ rays, high energy protons and fast neutrons. *Nucl. Instrum. Meth.*, 206:107–117, 1983.

[Kop04] U. Kopf, P. Heeg, P. Emde. The gantry irradiation room at the Heidelberg irradiation facility. *GSI Rep. 2004-1 (Ann. Rep. 2003)*, page 183, 2004.

[Kra90] G. Kraft. Radiobiological and physical basis for radiotherapy with protons and heavier ions. *Strahlenther. Onkol.*, 166:10, 1990.

[Kra99] G. Kraft, M. Scholz, U. Bechthold. Tumor therapy and track structure. *Radiat. Environ. Biophys.*, 38(4):229–237, 1999.

[Kra00] G. Kraft. Tumor therapy with heavy charged particles. *Prog. Part. Nucl. Phys.*, 45:473–544, 2000.

[Krä94] M. Krämer, G. Kraft. Calculations of heavy ion track structure. *Radiat. Environ. Bioph.*, 33(2):91–109, 1994.

[Krä00] M. Krämer, O. Jäkel, T. Haberer, G. Kraft, D. Schardt, U. Weber. Treatment planning for heavy ion radiotherapy: physical beam model and dose optimization. *Phys. Med. Biol.*, 45:3299–3317, 2000.

[Kuh04a] A. Kuhn, J.S. Karp, G. Muehllehner, F.W. Newcomer, R. VanBerg. Performance assessment of pixelated LaBr$_3$ detector modules for TOF PET. In *Proc. IEEE 2004 Med. Ima. Conf.*, Rome, Italy, Oct. 2004. M9-059.

[Kuh04b] A. Kuhn, S. Surti, J.S. Karp, P.S. Raby, K.S. Shah, A.E. Perkins, G. Muehllehner. Design of a lanthanum bromide detector for time-of-flight PET. *IEEE T. Nucl. Sci.*, 51:2550–2557, 2004.

[Kyu94] H. Kyushima, Y. Hasegawa, A. Atsumi, K. Nagura, H. Yokota, M. Ito, J. Takeuchi, K. Oba, H. Matsuura, S. Suzuki. Photomultiplier tube of new dynode configuration. *IEEE T. Nucl. Sci.*, 41(4):725–729, 1994.

[Lar63] B. Larsson, L. Leksell, B. Rexed. The use of high energy protons for cerebral surgery in man. *Acta. Chir. Scand.*, 125:1–7, 1963.

[Lau99] K. Lauckner. *Entwicklung eines iterativen 3D Rekonstruktionsverfahrens für die Kontrolle der Tumorbehandlung mit Schwerionen mittels der Positronen-Emissions-Tomographie*. PhD thesis, Dresden University of Technology, Dresden, 1999.

[Lau00] K. Lauckner, P. Crespo, J. Pawelke, W. Enghardt, G. Kraft. An LSO-based scanner for in-beam PET: a feasibility study. In *Proc. IEEE 2000 Med. Ima. Conf.*, Lyon, France, Oct. 2000. M14-289.

[Lav83] M. Laval, M. Moszyński, R. Allemand, E. Cormoreche, P. Guinet, R. Odru, J. Vacher. Barium fluoride - inorganic scintillator for subnanosecond timing. *Nucl. Instrum. Meth.*, 206:169–176, 1983.

[Lec02]   P. Lecoq, J. Varela. A dedicated PET camera for mammography. *Nucl. Instrum. Meth. A*, 486:1–6, 2002.

[Leo94]   W.R. Leo. *Techniques for nuclear and particle physics experiments*. Springer-Verlag, 1994.

[Lin05]   http://learntech.uwe.ac.uk/radiography/RScience/linac/ beamshapingcomponents.htm, available in Jun. 2005.

[Lit68]   J. Litton, J.T. Lyman, C.A. Tobias. Penetration of high-energy heavy ions with the inclusion of Coulomb, nuclear and other stochastic processes, Lawrence Berkeley Laboratory, UCLA 17392 rev., UC-34 Physics, TID 4500 (2nd. edition), 1968.

[Lla88]   J. Llacer. Positron emission medical measurements with accelerated radioactive ion beams. *Nucl. Sci. Appl.*, 3:111–131, 1988.

[Lom99]   A.J. Lomax, T. Bortfeld, G. Goitein, J. Debus, C. Dykstra, P.A. Tercier, P.A. Coucke, R.O. Mirimanoff. A treatment planning inter-comparison of proton and intensity modulated photon radiotherapy. *Radiother. Oncol.*, 51(3):257–271, 1999.

[Lub04]   M. Lubberink, H. Schneider, H. Lundqvist. Modified dead time correction for prompt gamma radiation emitting PET isotopes. In *Proc. IEEE 2004 Med. Ima. Conf.*, Rome, Italy, Oct. 2004. M5-322.

[Lyn91a] G.R. Lynch, O.I. Dahl. Approximations to multiple Coulomb scattering. *Nucl. Instrum. Meth. B*, 58(1):6–10, 1991.

[Lyn91b] D.E. Lyndstadt, J.R. Castro, T.L. Phillips. Neon ion radiotherapy: results of the phase I-II clinical trial. *Int. J. Radiat. Oncol.*, 20:761–769, 1991.

[Maj85]   S. Majewski, D. Anderson. Radiation damage test of barium fluoride scintillator. *Nucl. Instrum. Meth. A*, 241:76–79, 1985.

[Mar66]   P. Marmier, E. Sheldon. *Physics of Nuclei and Particles*, volume 1. Academic Press, New York, 1966.

[McI60]   M.C. McIntyre, T.L. Watts, F.C. Jobes. Neutron transfer and the tunneling mechanism in the bombardment of gold by nitrogen. *Phys. Rev.*, 19(3):1331–1339, 1960.

[Mel91]   C.L. Melcher. Lutetium orthosilicate single crystal scintillation detector. *U.S. Patent*, (4 958 080 /5 025 151), 1990/1991.

[Mel92]   C.L. Melcher, J.S. Schweitzer. Cerium-doped lutetium oxyorthosilicate: a fast, efficient new scintillator. *IEEE T. Nucl. Sci.*, 39(4):502–505, 1992.

[Min94]   B.I. Minkov. Promising new lutetium based single crystals for fast scintillation. *Functional Materials*, 1:103–105, 1994.

[Mol48]   G. Molière. Theorie der Streuung schneller geladener Teilchen II, Mehrfach- und Vielfachstreuung. *Z. Naturforschung A*, 3:78–97, 1948.

[Mos83]   M. Moszyński, R. Allemand, M. Laval, R. Odru, J. Vacher. Recent progress in fast timing with CsF scintillators in application to time-of-flight positron tomography in medicine. *Nucl. Instrum. Meth.*, 205:239–240, 1983.

[Mos93]   W.W. Moses, S.E. Derenzo. Empirical observation of resolution degradation in
          positron emission tomographs utilizing block detectors. *J. Nucl. Med.*, 34:101–102,
          1993.

[Mos94]   W.W. Moses, S.E. Derenzo, T.F. Budinger. PET detector modules based on novel
          detector technologies. *Nucl. Instrum. Meth. A*, 353:189–194, 1994.

[Mos95]   W.W. Moses, S.E. Derenzo, A. Fyodorov, M. Korzhik, A. Gektin, B. Minkov,
          V. Aslanov. $LuAlO_3$:Ce - a high density, high speed scintillator for gamma detection.
          IEEE T. Nucl. Sci., 42:275–279, 1995.

[Mos96]   W.W. Moses, S.E. Derenzo. Scintillators for positron emission tomography. In
          SCINT95 Proc. of the Int. Conf. on Inorganic Scintillators and their Applications,
          pages 9–16, Delft, The Netherlands, 1996. Delft University Press.

[Mos99a] W.W. Moses, S.E. Derenzo. Prospects for time-of-flight PET using LSO scintillator.
          IEEE T. Nucl. Sci., 46:474–478, 1999.

[Mos99b] M. Moszyński, M. Balcerzyk, M. Kapusta, D. Wolski, C.L. Melcher. Large size
          LSO:Ce and YSO:Ce scintillators for 50 MeV range γ-ray detector. In *Proc. IEEE
          1999 Nucl. Sci. Symp.*, Seattle, WA, USA, Oct. 1999. N20-18.

[Mos00]   W.W. Moses. Scintillator requirements for medical imaging. In *SCINT99 Proc. of
          the 5th Int. Conf. on Inorganic Scintillators and their Applications*, pages 11–21, M.
          V. Lomonosov State University, Moscow, 2000.

[Mos01]   M. Moszyński, M. Kapusta, M. Szawlowski, D. Wolski, I. Wegrzecka, M. Wegrzecki.
          Comparative study of avalanche photodiodes with different sctructures in scintillation
          detection. *IEEE T. Nucl. Sci.*, 48:1205–1210, 2001.

[Mos02]   W.W. Moses.   Synergies between electromagnetic calorimetry and PET.
          Lawrence Berkeley National Laboratory, July 2002.   Paper LBNL-51197, `http:
          //repositories.cdlib.org/lbnl/LBNL-51197`, available in Jun. 2005.

[Mos03]   J.-B. Mosset, S. Saladino, J.-F. Loude, C. Morel. Characterisation of arrays of
          avalanche photodiodes for small animal positron emission tomography. *Nucl. In-
          strum. Meth. A*, 504:325–330, 2003.

[Mos04]   W.W. Moses. Factors influencing timing resolution in a commercial LSO PET cam-
          era. In *Proc. IEEE 2004 Nucl. Sci. Symp. and Med. Ima. Conf.*, Rome, Italy, Oct.
          2004. JNM2-1.

[Mue02]   G. Muehllehner, J.S. Karp, S. Surti. Design considerations for PET scanners.
          Q. J. Nucl. Med., 46(1):16–23, 2002.

[Nat05]   `http://www.ni.com/linux/ni488dl.htm`, available in Jun. 2005.

[Nik04]   A. Nikoghosyan, D. Schulz-Ertner, B. Didinger, O. Jäkel, I. Zuna, A. Höss, M. Wan-
          nenmacher, J. Debus. Evaluation of therapeutic potential of heavy ion therapy for
          patients with locally advanced prostate cancer. *Int. J. Radiat. Oncol.*, 58(1):89–97,
          2004.

[Nör80]   W. Nörenberg. Basic concepts in the description of collisions between heavy nuclei.
          In R. Bock, editor, *Heavy Ion Collisions*, pages 1–43. North-Holland, 1980.

[Oel96]   U. Oelfke, G.K.Y. Lam, M.S. Atkins. Proton dose monitoring with PET: quantitative studies in Lucite. *Phys. Med. Biol.*, 41:177–196, 1996.

[Oli79]   L.F. Oliveira, R. Donangelo, J.O. Ràsmussen. Abrasion-ablation calculations of large fragment yields from relativistic heavy ion reactions. *Phys. Rev. C*, 19(3):826–833, 1979.

[Org02]   G. Organtini. The CMS electromagnetic calorimeter. In *Proc. IEEE 2002 Nucl. Sci. Symp.*, Norfolk, VI, USA, Nov. 2002. N19-1.

[Ort05]   Ortec 142AH preamplifier. Users manual. `http://www.ortec-online.com/electronics/preamp/142ah.htm`, available in Jun. 2005.

[Pac00]   E. Pace, R. Di Benedetto, S. Scuderi. Fast stable visible-blind and highly sensitive CVD diamond UV photodetectors for a laboratory and space applications. *Diam. Relat. Mater.*, 9:987–993, 2000.

[Par77]   K.S. Parthasarathy. Concentrations of the decay products of ^{222}Rn in a basement laboratory. *Phys. Med. Biol.*, 22(2):341–347, 1977.

[Par02a] K. Parodi, W. Enghardt. An interactive approach for local dose quantification from in-beam PET data. *Wiss.-Tech. Ber. FZR-341 (Ann. Rep. 2001)*, page 98, 2002.

[Par02b] K. Parodi, W. Enghardt, T. Haberer. In-beam PET measurements of β^+ radioactivity induced by proton beams. *Phys. Med. Biol.*, 47:21–36, 2002.

[Par04]   K. Parodi. *On the feasibility of dose quantification with in-beam PET data in radiotherapy with ^{12}C and proton beams.* PhD thesis, Dresden University of Technology, Dresden, Nov. 2004.

[Par05a] K. Parodi, F. Pönisch, W. Enghardt. Experimental study on the feasibility of in-beam PET for accurate monitoring of proton therapy. *IEEE T. Nucl. Sci.*, 52(3):778–786, 2005.

[Par05b] K. Parodi, P. Crespo, H. Eickhoff, T. Haberer, J. Pawelke, D. Schardt, W. Enghardt. Random coincidences during in-beam PET measurements at microbunched therapeutic ion beams. *Nucl. Instrum. Meth. A*, 545:446–458, 2005.

[Pau00]   D. Pauwels, N. Le Masson, B. Viana, A. Kahn-Harari, E.V.D. van Loef, P. Dorenbos, C.W.E. van Eijk. A novel inorganic scintillator: $Lu_2Si_2O_7:Ce^{3+}$ (LPS). *IEEE T. Nucl. Sci.*, 47:1787–1790, 2000.

[Paw95]   J. Pawelke. *Methodische Untersuchungen zum Einsatz der Positronen-Emissions-Tomographie in der Leichtionen-Tumortherapie.* PhD thesis, Dresden University of Technology, Dresden, June 1995.

[Paw96]   J. Pawelke, L. Byars, W. Enghardt, W.D. Fromm, H. Geissel, B.G. Hasch, K. Lauckner, P. Manfraß, D. Schardt, M. Sobiella. The investigation of different cameras for in-beam PET imaging. *Phys. Med. Biol.*, 41:279–296, 1996.

[Paw97]   J. Pawelke, W. Enghardt, Th. Haberer, B.G. Hasch, R. Hinz, M. Krämer, K. Lauckner, M. Sobiella. In-beam PET imaging for the control of heavy-ion tumour therapy. *IEEE T. Nucl. Sci.*, 44(4):1492–1498, 1997.

[Ped95]   E. Pedroni, R. Bacher, H. Blattmann, T. Böhringer, A. Coray, A. Lomax, S. Lin,
          G. Munkel, S. Scheib, U. Schneider, A. Tourovsky. The 200 MeV proton therapy
          project at the Paul Scherrer Institute: conceptual design and practical realisation.
          Med. Phys., 22(1):37–53, 1995.

[Per04]   H. Pernegger, H. Frais-Kölbl, E Griesmayer, H. Kagan. Design and test of a high-
          speed single-particle beam monitor. *Nucl. Instrum. Meth. A*, 535:108–114, 2004.

[Pet89]   M.D. Petroff, M.G. Stapelbroek. Photon-counting solid-state photomultiplier. *IEEE
          T. Nucl. Sci.*, 36(1):158–162, 1989.

[Pet94]   P. Petti, A.J. Lennox. Hadronic radiotherapy. *Ann. Rev. Nucl. Part. S.*, 44:155–197,
          1994.

[Phe75]   M.E. Phelps, E.J. Hoffman, N.A. Mullani, M.M. Ter-Pogossian. Application of an-
          nihilation coincidence detection to transaxial reconstruction tomography. *J. Nucl.
          Med.*, 16:210–224, 1975.

[Pic01]   B.J. Pichler, F. Bernecker, G. Boning, M. Rafecas, W. Pimpl, M. Schwaiger,
          E. Lorenz, S.I. Ziegler. A 4×8 APD array, consisting of 2 monolithic silicon wafers,
          coupled to a 32-channel LSO matrix for high-resolution PET. *IEEE T. Nucl. Sci.*,
          48(2):1391–1396, 2001.

[Pic04]   B.J. Pichler, B.K. Swann, J. Rochelle, R.E. Nutt, S.R. Cherry, S.B. Siegel. Lutetium
          oxyorthosilicate block detector readout by avalanche photodiode arrays for high res-
          olution animal PET. *Phys. Med. Biol.*, 49:4305–4319, 2004.

[Pid03]   L. Pidol, A. Kahn-Harari, B. Viana, E. Virey, B. Ferrand, P. Dorenbos,
          J.T.M de Haas, C.W.E. van Eijk. High efficiency of lutetium silicate scintillators,
          Ce-doped LPS and LYSO crystals. In *Proc. IEEE 2003 Nucl. Sci. Symp.*, Portland,
          OR, USA, Oct. 2003. N27-4.

[Pit05]   `http://www.pituitary.com`, available in Jun. 2005. Last update: May. 2005.

[Pön03a] F. Pönisch. *Optimierung der Positronen-Emmissions-Tomographie bei der Schwerio-
          nentherapie auf der Basis von Röntgentomogrammen.* PhD thesis, Dresden University
          of Technology, Dresden, 2003.

[Pön03b] F. Pönisch, W. Enghardt, K. Lauckner. Attenuation and scatter correction for in-
          beam positron emission tomography monitoring of tumour irradiations with heavy
          ions. *Phys. Med. Biol.*, 48:2419–2436, 2003.

[Pön04]   F. Pönisch, K. Parodi, B.G. Hasch, W. Enghardt. The modelling of positron emitter
          production and PET imaging during carbon ion therapy. *Phys. Med. Biol.*, 49:5217–
          5232, 2004.

[Pre97]   K. Prelec. Ions and accelerators for cancer treatment. *Fizika B*, 6:177–206, 1997.

[PSI99]   `http://abe.web.psi.ch/accelerators/ringcyc.html`, available in Jun. 2005.,
          Last update: Jan. 1999.

[Reg02]   M. Regler, M. Benedikt, K. Poljanc. Medical accelerators for hadron therapy with
          protons and carbon ions. In *CERN Accelerator School*, Seville, Oct. 2002. Hephy-
          PUB-757/02.

[Rei98]   C.O. Reinold, D.R. Schultz, U. Bechthold, G. Kraft, S. Hagman H. Schmidt-Böcking. Ternary ridge of ejected electrons from fast ion-atom collisions. *Phys. Rev. A.*, 58(3):2611–2614, 1998.

[Rey56]   H.L. Reynolds, A. Zucker. Nuclear reactions produced by nitrogen on nitrogen. *Phys. Rev.*, 101(1):166–171, 1956.

[Ros00]   A.B. Rosenfeld, P.D. Bradley, I. Cornelius, G. I. Kaplan, B.J. Allen, J.B. Flanz, M. Goitein, A. van Meerbeeck, J. Schubert, J. Bailey, Y. Tabkada, A. Maruhashi, Y. Hayakawa. New silicon detector for microdosimetry applications in proton therapy. *IEEE T. Nucl. Sci.*, 47(4):1386–1394, 2000.

[San04]   A.I. Santos, A. Trindade et al. Design and evaluation of the clear-PEM detector for positron emission mammography. In *Proc. IEEE 2004 Med. Ima. Conf.*, Rome, Italy, Oct. 2004. M10-28.

[Sch89]   W. Schimmerling, J. Miller, M. Wong, M. Rapkin, J. Horward, H. Spieker, B.V. Jarret. The fragmentation of 670 AMeV neon as a function of depth in water. *Radiat. Res.*, 120:36–71, 1989.

[Sch91]   T. Schwab. *Transport von Schwerionen durch Materie innerhalb ionenoptischer Systeme.* PhD thesis, University of Gießen, Gießen, 1991. GSI report 91-10.

[Sch92]   P. Schotanus, P. Dorenbos, V.D Ryzhikov. Detection of CdS(Te) and ZnSe(Te) scintillation light with silicon photodiodes. *IEEE T. Nucl. Sci.*, 39(4):546–550, 1992.

[Sch96a] I. Schall, D. Schardt, H. Geissel, H. Irnich, E. Kankeleit, G. Kraft, A. Magel, M.F. Mohar, G. Münzenberg, F. Nickel, C. Scheidenberger, W. Schwab. Charge changing nuclear reactions of relativistic light ion beams ($5 \leq Z \leq 10$) passing through thick absorbers. *Nucl. Instrum. Meth. B*, 117:221–234, 1996.

[Sch96b] D. Schardt, I. Schall, H. Geissel, H. Irnich, G. Kraft, A. Magel, M.F. Mohar, G. Münzenberg, F. Nickel, C. Scheidenberger, W. Schwab, L. Sihver. Nuclear fragmentation of high-energy heavy-ion beams in water. *Adv. Space Res.*, 17(2):287–294, 1996.

[Sch96c] W.H. Scharf, O.A. Chomicki. Medical accelerators in radiotherapy: past, present and future. *Phys. Medica*, XII(4):199–226, 1996.

[Sch96d] M. Scholz, G. Kraft. Track structure and the calculation of biological effects of heavy charged particles. *Adv. Space Res.*, (1-2):5–14, 1996.

[Sch02a] D. Schulz-Ertner, T. Haberer, M. Scholz, C. Thilmann, F. Wenz, O. Jäkel, G. Kraft, M. Wannenmacher, J. Debus. Acute radiation-induced toxicity of heavy ion radiotherapy delivered with intensity modulated pencil beam scanning in patients with base of skull tumors. *Radiother. Oncol.*, 64:189–195, 2002.

[Sch02b] D. Schulz-Ertner, T. Haberer, O. Jäkel, C. Thilmann, M. Krämer, W. Enghardt, G. Kraft, M. Wannenmacher, J. Debus. Radiotherapy for chordomas and low-grade chondrosarcomas of the skull base with carbon ions. *Int. J. Radiat. Oncol.*, 53(1):36–42, 2002.

[Sch03a] D. Schulz-Ertner, A. Nikoghosyan, B. Didinger, C.P. Karger, O. Jäkel, M. Wannenmacher, J. Debus. Treatment planning intercomparison for spinal chordomas using intensity-modulated photon radiation therapy (IMRT) and carbon ions. *Phys. Med. Biol.*, 48:2617–2631, 2003.

[Sch03b] D. Schulz-Ertner, A. Nikoghosyan, C. Thilmann, T. Haberer, O. Jäkel, C. Karger, M. Scholz, G. Kraft, M. Wannenmacher, J. Debus. Carbon ion radiotherapy for chordomas and low grade chondrosarcomas of the skull base. *Strahlenther. Onkol.*, 179:598–605, 2003.

[Sch03c] D. Schulz-Ertner, A. Nikoghosyan, O. Jäkel, T. Haberer, G. Kraft, M. Scholz, M. Wannenmacher, J. Debus. Feasibility and toxicity of combined photon and carbon ion radiotherapy for locally advanced adenoid cystic carcinomas. *Int. J. Radiat. Oncol.*, 62(2):391–398, 2003.

[Sch03d] D. Schulz-Ertner, B. Didinger, A. Nikoghosyan, O. Jäkel, I. Zuna, M. Wannenmacher, J. Debus. Optimization of radiation therapy for locally advanced adenoid cystic carcinomas with infiltration of the skull base using photon intensity-modulated radiation therapy (IMRT) and a carbon ion boost. *Strahlenther. Onkol.*, 179(5):345–51, 2003.

[Sch04] D. Schulz-Ertner, J. Debus, A. Nikoghosyan, C. Thilmann, M. Wannenmacher, O. Jäkel,C. Karger, P. Heeg, T. Haberer, D. Schardt, M. Scholz, M. Krämer, E. Rietzel, G. Kraft. Heavy ion therapy at GSI. *GSI Rep. 2004-1 (Ann. Rep. 2003)*, page 172, 2004.

[Sha04] K.S. Shah, J. Glodo, W. Higgins, E.V.D. van Loef, W.W. Moses, S.E. Derenzo, M.J. Weber. $CeBr_3$ scintillators for gamma-ray spectroscopy. In *Proc. IEEE 2004 Room Temp. Sem. Det.*, Rome, Italy, Oct. 2004. R04-1.

[She82] L.A. Shepp and Y. Vardi. Maximum likelihood reconstruction for emission tomography. *IEEE T. Med. Imaging*, 1(2):113–122, 1982.

[Shi04] S. Shimizu, K. Kurashige, T. Usui, N. Shimura, K. Sumiya, N. Sengutttuvan, A. Gunji, M. Kamada, H. Ishibashi. Scintillation properties of LGSO crystal. In *Proc. IEEE 2004 Med. Ima. Conf.*, Rome, Italy, Oct. 2004. M5-414.

[Sho84] M.D. Short. Gamma camera systems. *Nucl. Instrum. Meth.*, 221:142–149, 1984.

[Sie04] Siemens Medical Solutions. Particle therapy, getting to the point, Siemens AG, Medical Solutions, Erlangen, Germany, 2004. Order No. A91100-M2600-C689-2-7600.

[Sih93] L. Sihver, C.H. Tsao, R. Silberberg, T. Kanai, R.F. Barghouty. Total reaction and partial cross section calculations in proton-nucleus ($Z_t \leq 26$) and nucleus-nucleus reactions (Z_p and $Z_t \leq 26$). *Phys. Rev. C*, 47(3):1225–1236, 1993.

[Smi96] K.M. Smith. GaAs detector status. *Nucl. Instrum. Meth. A*, 383:75–80, 1996.

[Spi98] T.J. Spinks, M.P. Miller, D.L. Bailey, P.M. Bloomfield, L. Livieratos, T. Jones. The effect of activity outside the direct field of view in a 3D-only whole-body positron tomograph. *Phys. Med. Biol.*, 43:895–904, 1998.

[Suz93] S. Suzuki, T. Nakaya, A. Suzuki, H. Suzuki, K. Yoshioka, Y. Yoshizawa. PMTs of superior time resolution, wide dynamic range, and low cross-talk multi-anode PMTs. *IEEE T. Nucl. Sci.*, 40(4):431–433, 1993.

[Sve98] R. Svensson, M. Åsell, P. Näfstadius, A. Brahme. Target, purging magnet and electron collector design for scanned high-energy photon beams. *Phys. Med. Biol.*, 43:1091–1112, 1998.

[Tak83]   K. Takagi, T. Fukazawa. Cerium-activated Gd_2SiO_5 single crystal scintillator. *Appl. Phys. Lett.*, 42:43–45, 1983.

[Tan98]   M. Tanaka, K. Hara, S. Kim, K. Kondo, H. Takano, M. Kobayashi, H. Ishibashi, K. Kurashige, K. Susa, M. Ishii. Applications of cerium-dopped gadolinium silicate Gd_2SiO_5:Ce scintillator to calorimeters in high-radiation environment. *Nucl. Instrum. Meth. A*, 404:283–294, 1998.

[Tob52]   C.A. Tobias, H.O. Anger, J.H. Lawrence. Radiological use of high energy deuterons and alpha particles. *Am. J. Roentgenol. Radiat. Ther. Nucl. Med.*, 67:1–27, 1952.

[Tob71]   C.A. Tobias, A. Chatterjee, A.R. Smith. Radioactive fragmentation of N^{7+} ion beam observed in a beryllium target. *Phys. Lett. A*, 37:119–120, 1971.

[Tob77]   C.A. Tobias, E.V. Benton, M.P. Capp, A. Chatterjee, M.R. Cruty, R.P. Henke. Particle radiography and autoactivation. *Int. J. Radiat. Oncol.*, 3:35–44, 1977.

[TOI04]   Table of Radioactive Isotopes online. `http://ie.lbl.gov/toi`, available Jun. 2005. Last update: Jan. 2004.

[Tom03]   T. Tomitani, J. Pawelke, M. Kanazawa, K. Yoshikawa, K. Yoshida, M. Sato, A. Takami, M. Koga, Y. Futami, A. Kitagawa, E. Urakabe, M. Suda, H. Mizuno, T. Kanai, H. Matsuura, I. Shinoda, S. Takizawa. Washout studies of ^{11}C in rabbit thigh muscle implanted by secondary beams of HIMAC. *Phys. Med. Biol.*, 48:875–889, 2003.

[Tro05]   `http://www.trolltech.com`, available in Jun. 2005.

[Ura01]   E. Urakabe, T. Kanai, M. Kanazawa, A. Kitagawa, K. Noda, T. Tomitani, M. Suda, Y. Iseki, K. Hanawa, K. Satoh, M. Shimbo, H. Mizuno, Y. Hirata, Y. Futami, Y. Iwashita, A. Noda. Spot scanning using radioactive ^{11}C beams for heavy-ion radiotherapy. *Jpn. J. Appl. Phys. A*, 40:2540–2548, 2001.

[Var05]   J. Varela. Clear PEM, a dedicated PET camera for mammography, LIP Lisbon, Portugal and CERN, Geneva, Switzerland, March 2005. Personal communication.

[vE02]   C.W.E. van Eijk. Inorganic scintillators in medical imaging. *Phys. Med. Biol.*, 47:85–106, 2002.

[Ver05]   P.E. Vert, G. Bohner, M. Boutemeur, J. Lecoq, P. Le Du, G. Mathez, P. Mangeot, G. Montarou. Contribution of HEP electronics technics to the medical imaging field. In *Proc. IEEE-NPSS Real Time Conf. 2005*, Stockholm, Sweden, Jun. 2005. S9-3.

[vL00]   E.V.D. van Loef, P. Dorenbos, C.W.E. van Eijk, K. Krämer, H.U. Güdel. High-energy-resolution scintillator: Ce^{3+} activated $LaCl_3$. *Appl. Phys. Lett.*, 77:1467–1468, 2000.

[vL01]   E.V.D. van Loef, P. Dorenbos, C.W.E. van Eijk, K. Krämer, H.U. Güdel. High-energy-resolution scintillator: Ce^{3+} activated $LaBr_3$. *Appl. Phys. Lett.*, 79:1573–1575, 2001.

[Vyn89]   S. Vynckier, F. Vanneste, F. Richard, A. Bol, C. Michel, A. Wambersie. Control of patient positioning for fast neutron therapy using positron emission tomography. *Brit. J. Radiol.*, 62:1031–1032, 1989.

[Wat04]   C.C. Watson, M.E. Casey, L. Eriksson, T. Mulnix, D. Adams, B. Bendriem. NEMA NU 2 performance tests for scanners with intrinsic radioactivity. *J. Nucl. Med.*, 45:822–826, 2004.

[Web73]   M.J. Weber, R.R. Monchamp. Luminescence of $Bi_4Ge_3O_{12}$: spectral and decay properties. *J. Appl. Phys.*, 44:5495–5499, 1973.

[Web90]   S. Webb, editor. *The Physics of Medical Imaging*. Adam Hilger, Bristol, 1990.

[Web96]   U. Weber. *Volumenkonforme Bestrahlung mit Kohlenstoffionen zur Vorbereitung einer Strahlentherapie*. PhD thesis, University of Kassel, Kassel, 1996.

[Wey03]   W.K. Weyrather, J. Debus. Particle beams for cancer therapy. *Clin. Oncol.*, 15:23–28, 2003.

[Wie94]   K. Wienhard, M. Dahlbom, L. Eriksson, C. Michel, T. Bruckbauer, U. Pietrzyk, W.-D. Heiss. The ECAT EXACT HR: performance of a new high resolution positron camera. *J. Comput. Assist. Tomo.*, 18:110–118, 1994.

[Wil46]   R.R. Wilson. Radiobiological use of fast protons. *Radiology*, 47:487–491, 1946.

[Wil83]   J. Wilson, J.F.B. Hawkes. *Optoelectronics: An Introduction*. Prentice-Hall International, London, 1983.

[Won90]   M. Wong, W. Schimmerling, M.H. Phillips, B.A. Ludewigt, D.A. Landis, J.T. Walton, S.B. Curtis. The multiple Coulomb scattering of very heavy charged particles. *Med. Phys.*, 17(2):163–171, 1990.

[Won94]   C.Y. Wong. *Introduction to high-energy heavy-ion collisions*. World Scientific, Singapore, 1994.

[Xco99]   XCOM: Photon cross sections database. `http://physics.nist.gov/PhysRefData/Xcom/Text/XCOM.html`, available Jun. 2005. Last update: Nov. 1999.

[Zhu97]   R.-Y. Zhu. Precision crystal calorimetry in future high energy colliders. *IEEE T. Nucl. Sci.*, 44(3):468–476, 1997.

[Zhu98]   R.-Y. Zhu. Radiation damage in scintillating crystals. *Nucl. Instrum. Meth. A*, 413:297–311, 1998.

[Zie85]   J.F. Ziegler, J.F. Biersack, U. Littmark. *The stopping and range of ions in solids*. Pergamon Press, 1985.

[Zie99]   J.F. Ziegler. Stopping of energetic light ions in elemental matter. *J. Appl. Phys.*, 85(3):1249–1272, 1999.

Acknowledgements

modules and knowledge and Mr. Berlin for preparing more than 150 meters of cabling. A special acknowledgment must be made to Eng. Klaus Heidel, from the same division, without whom this thesis would not have been possible. This acknowledgment extends from the preparation of the motherboards for the preamplifiers reading the LSO/APDA detectors, to the testing of the preamplifiers, their optimization with hints to their designers, as well as many other issues: power supply assembling, the simulation of several readout electronic components with PSPICE, and inumeral discussions about power consumption, timing, cabling and other optimizations. Klaus, thank you for the many hours out there on the field. I thank also Eng. Andreas Steinbrecher, then at the Institut für Energetik und Umwelt GmbH, Rossendorf, for his personal involvement in the study with PET on a separate gantry, and for sharing the images that were adapted to Fig. 3.4. I acknowledge Dr. Waldemar Neubert, Dr. Wolfgang Wagner, Dr. Bärbel and Dr. Lothar Naumann, Jenny Philipp, Elisabeth Leßmann, Krassimir Kossev, Martin Erhard, Alexander Sadovski, Kalliopi Kanaki, Manfred Beckers, Christoph Klein, Dr. Schlett, Mrs. Schneidereit and Jens Steiner for the relaxed working atmosphere inside and outside the division of radiation physics. I thank particularly Dr. Enghardt, Fine Fiedler and Martin Erhard for the great help in writing the German summary of this thesis.

- From Heidelberg, the whole medical personnel and the team of medical physicists. Their dedication to the tumor therapy project is a motivation on the professional and personal levels.

- From the ASINS, Poland, Prof. Dr. Marek Moszyński for a fruitful collaboration with his institute and for sharing his time and knowledge on scintillators and solid state detectors, his former PhD student Dr. Maciej Kapusta for the many hours spent together in the laboratory and for useful suggestions, Eng. Dariusz Wolski for the design and production of the preamplifiers that read the LSO/APDA, and Prof. Dr. Zbigniew Guzik for interesting discussions on other levels of physics.

- From MedAustron, Austria, Prof. Dr. Helmut Frais-Kölbl, for the fruitful co-work before and during the randoms suppression experiments, including sharing his expertise and suggestions on the field of nano-second (and below) timing, together with the operation of the CVD detector, and the shared data resulting in Fig. 6.4, and Prof. Dr. Erich Griesmayer for participating in the collaboration, providing the means so that we could use the diamond detector.

- From the LIP-Lisbon, Portugal, Prof. Dr. João Varela, Andreia Trindade and Pedro Rodrigues, for the useful discussions and exchange of information concerning the avalanche photodiode from Hamamatsu, the LSO scintillator and for sharing their knowledge regarding their fast and advanced acquisition technology.

I thank all my teachers at the University of Coimbra, Portugal, for the shared knowledge in the fields of physics and instrumentation during my under-graduate studies. I thank particularly Prof. Dr. Policarpo, Dr. Isabel Lopes, Dr. Vitaly Chepel, Dr. van der Marel and Luís Janeiro for the productive atmosphere within the liquid xenon team at the LIP-Coimbra. I thank also Prof. Dr. Mário Pimenta, Dr. Fernando Barão and Dr. Patrícia Gonçalves, from LIP-Lisbon, for their help and shared knowledge in the field of data evaluation and simulation for astroparticle physics detectors before I joined the German Heavy Ion Therapy Collaboration.

On the personal level, I thank the true friendship of Miguel, Chiqui, Faouzi, Fairouz, Farouk, Christiane, Andrea, Lutz, Isabel, P. Nuno, Aga, Iwona, family Colvenbach and family West. I thank in a very special way D. Alice Carvalho for the dedication put into teaching and forming human beings.

To my American host family, with whom I studied one year in the United States: Mom, Dad (always present), Kyle and Jenna, the opening of your family to a newcomer, the sharing of your family laces in that year and after, the time and dedication you've put forward have always been present in my memory. Thank you. Together with my real-blood family, your share the dedication of this work.

Finally, most importantly and not chronologically, my family. Para além de vos dedicar todo este trabalho, Mã, Pá, e Lena, agradeço-vos a todos pela família unida que somos: Mã, sempre presente, Pá, Guida, Lena, Artur e cunhada Tai, Ricardo e cunhada Carla, o mano mais velho Fabrizio e os meus queridos sobrinhos Micaela, Sofia, Guido e Gift. Que todos juntos, com os nossos pequenos erros mas sobretudo com os nossos esforços, preparemos e usufruemos de um mundo melhor.

Curriculum Vitæ

Personal data

Name: Paulo Alexandre Vieira Crespo
Date of birth: 9 May 1971
Place of birth: Beira, Mozambique
Nationality: Portuguese

Education

Since Oct. 1999   PhD student with the in-beam PET team of the German Heavy Ion
                  Therapy Collaboration

1997   University of Coimbra; graduation in Physics Engineering, specialization in
                  Instrumentation, average 16/20

1994 – 1995   University of Milan and Politechnic of Milan; ERASMUS scholarship,
                  - Optoelectronics (Polytechnic of Milan): 28/30
                  - Applied electronics (Dep. of Physics, University of Milan): 28/30
                  - Laboratory of instrumentation and electronics (idem): 30/30

1991   Beginning of Physics Engineering studies, Dep. of Physics, University of Coimbra

1989   Beginning of Economy studies, Faculty of Economy, University of Coimbra

1987 – 1988   N.Y. State Attica Junior-Senior High School, NY, USA; exchange student,
                  average 90/100

Post-graduate research

1998 – 1999   LIP-Lisbon; within the Alpha Magnetic Spectrometer experiment at CERN
1997 – 1998   LIP-Coimbra; development of a liquid xenon detector for PET
Aug/Sept 1997   CERN; within the tracker system team of the CMS experiment

Patents

2004   W. Enghardt, **P. Crespo**, K. Parodi, J. Pawelke, *Verfahren zur Korrektur der beim Monitoring der strahlentherapeutischen Behandlung mittels in-beam Positronen-Emissions-Tomographie erhaltenen Messwerte*, no. 10 2004 009 784.4, Deutsches Patent- und Markenamt, Feb. 2004. Patent from FZR

Publications in refereed journals

2005   **P. Crespo**, T. Barthel, H. Frais-Kölbl, E. Griesmayer, K. Heidel, K. Parodi, J. Pawelke, W. Enghardt, *Suppression of random coincidences during in-beam PET measurements at ion beam radiotherapy facilities*, IEEE Trans. Nucl. Sci., vol. 52, no. 5, pp. 980–7

      P. Crespo, G. Shakirin, W. Enghardt, *On the detector arrangement for in-beam PET for hadron therapy monitoring*, Phys. Med. Biol., submitted

      P. Crespo, G. Shakirin, W. Enghardt, *Direct time-of-flight for online, in-beam PET: concept and feasibility study*, Phys. Med. Biol., to be submitted

      P. Crespo, N. Abolmaali, R. Bergmann, E. Will, W. Enghardt, *Low-activity PET measurements with LSO- and BGO-based positron tomographs*, Phys. Med. Biol., to be submitted

      K. Parodi, **P. Crespo**, H. Eickhoff, T. Haberer, J. Pawelke, D. Schardt, W. Enghardt, *Random coincidences during in-beam PET measurements at microbunched therapeutic ion beams*, Nucl. Instr. Meth. A, vol. 545, pp. 446-58

2004   **P. Crespo**, M. Kapusta, J. Pawelke, M. Moszyński, W. Enghardt, *First in-beam PET imaging with LSO/APD-array detectors*, IEEE Trans. Nucl. Sci., vol. 51, no. 5, pp. 2654–61

      M. Kapusta, **P. Crespo**, D. Wolski, K. Heidel, L. Heinrich, J. Hutsch, J. Pawelke, M. Sobiella, A. Trzcińska, M. Moszyński, W. Enghardt, *The LSO/APD array as a possible detector for in-beam PET in hadron therapy*, IEEE Trans. Nucl. Sci., vol. 51, no. 4, pp. 1389–94

Publications in refereed journals, cont'd

2004   W. Enghardt, **P. Crespo**, F. Fiedler, R. Hinz, K. Parodi, J. Pawelke, F. Pönisch, *Charged hadron tumour therapy monitoring by means of PET*, Nucl. Instr. Meth. A, vol. 525, pp. 284–8

2003   M. Kapusta, **P. Crespo**, D. Wolski, M. Moszyński, W. Enghardt, *Hamamatsu S8550 APD arrays for high resolution scintillation readout*, Nucl. Instr, Meth. A, vol.504, pp. 139–42

2002   M. Kapusta, **P. Crespo**, M. Moszyński, W. Enghardt, M. Szawlowski, B. Zhou, D. Wolski, *Evaluation of LAAPD arrays for high resolution scintillator matrices readout*, IEEE Trans. Nucl. Sci., vol. 49, no. 4, pp. 1693–8

2001   **P. Crespo**, J. Debus, W. Enghardt, Th. Haberer, O. Jäkel, M. Krämer, G. Kraft, *Tumour therapy with carbon ion beams*, Phys. Medica, vol. XVII, no. 4, pp. 1–3

2000   **P. Crespo**, J. van der Marel, V. Chepel, M.I. Lopes, D. Santos, L. Janeiro, V. Solovov, R.F. Marques, A.J.P.L. Policarpo, *Pulse processing for the PET multiwire liquid xenon ionisation chamber*, IEEE Trans. Nucl. Sci., vol. 47, no. 6, pp. 2119–26

      With the AMS collaboration, *Cosmic protons*, Phys. Lett. B, vol. 490, pp. 27–35

      With the AMS collaboration, *Leptons in near earth orbit*, Phys. Lett. B, vol. 484, pp. 10–22

      With the AMS collaboration, *Protons in near earth orbit*, Phys. Lett. B, vol. 472, pp. 215–26

1999   V. Chepel, M.I. Lopes, J. van der Marel, **P. Crespo**, D. Santos, L. Janeiro, V. Solovov, R. Ferreira Marques, A.J.P.L. Policarpo, *The liquid xenon detector for PET: recent results*, IEEE Trans. Nucl. Sci., vol. 46, pp. 1038–44

      With the AMS collaboration, *Search for anti-helium in cosmic rays*, Phys. Lett. B, vol. 461, pp. 387–96

1998   **P. Crespo**, V. Chepel, M.I. Lopes, L. Janeiro, R. Ferreira Marques, A.J.P.L. Policarpo, *Pulse shape analysis in the liquid xenon multiwire ionisation chamber for PET*, IEEE Trans. Nucl. Sci., vol. 45, no. 3, pp. 561–7

Conference contributions and proceedings

2005   F. Fiedler, **P. Crespo**, K. Parodi, M. Sellesk, W. Enghardt, *The feasibility of in-beam PET for therapeutic beams of ^3He*, IEEE 2005 Nucl. Sci. Symp. and Med. Imag. Conf., Puerto Rico, USA, Oct. 2005. Talk and proceedings (accepted)

2004   **P. Crespo**, T. Barthel, H. Frais-Kölbl, E. Griesmayer, K. Heidel, K. Parodi, J. Pawelke, W. Enghardt, *Suppression of random coincidences during in-beam PET measurements*, IEEE 2004 Nucl. Sci. Symp., Rome, Italy, Oct. 2004. Talk and proceedings

2003   **P. Crespo**, M. Kapusta, J. Pawelke, M. Moszyśnki, W. Enghardt, *First in-beam PET imaging with LSO/APD-array detectors*, IEEE 2003 Med. Imag. Conf., Portland, OR, USA, Oct. 2003. Poster and proceedings

      M. Kapusta, **P. Crespo**, D. Wolski, K. Heidel, L. Heinrich, J. Hutsch, J. Pawelke, M. Sobiella, A. Trzcinska, M. Moszyński, W. Enghardt, *The LSO/APDA array as a possible detector for in-beam PET in hadron therapy*, IEEE 2003 Nucl. Sci. Symp., Portland, OR, USA, Oct. 2003. Talk

2002   M. Kapusta, **P. Crespo**, D. Wolski, M. Moszyński, W. Enghardt, *Hamamatsu S8550 APD arrays for high resolution scintillator matrices radout*, Third Beaune Conf. on New Developments in Photon Detection, Beaune, France, June 2002. Talk

2001   M. Kapusta, **P. Crespo**, M. Moszyński, W. Enghardt, M. Szawlowski, B Zhou, D. Wolski, *Evaluation of LAAPD arrays for high resolution scintillator matrices readout*, IEEE 2001 Nucl. Sci. Symp., San Diego, CAL, USA, Nov. 2001. Talk

2000   **P. Crespo**, J. Debus, W. Enghardt, Th. Haberer, O. Jäkel, M. Krämer, G. Kraft, *Tumour therapy with carbon ion beams*, MeRPE: Meeting on Medical Radiation Physics and Engineering, Lisbon, Portugal, Nov. 2000. Talk

       K. Lauckner, **P. Crespo**, W. Enghardt, J. Pawelke, G. Kraft, An LSO-based scanner for in-beam PET: a feasibility study, IEEE 2000 Nucl. Sci. Symp., Lyon, France, Oct. 2000. Poster and proceedings

1998   **P. Crespo**, J. van der Marel, V. Chepel, M.I. Lopes, L. Janeiro, V. Solovov, R Ferreira Marques, A.J.P.L. Policarpo, *Pulse processing for the PET liquid xenon multiwire ionisation chamber*, IEEE 1998 Nucl. Sci. Symp., Toronto, CAN, Nov. 1998. Poster

       V. Chepel, M.I. Lopes, J. van der Marel, **P. Crespo**, L. Janeiro, V. Solovov, R Ferreira Marques, A.J.P.L. Policarpo, *The liquid xenon chamber for PET: recent results*, IEEE 1998 Nucl. Sci. Symp., Toronto, CAN, Nov. 1998. Poster

1997   **P. Crespo**, V. Chepel, M.I. Lopes, L. Janeiro, R Ferreira Marques, A.J.P.L. Policarpo, *Pulse shape analysis in the liquid xenon multiwire ionisation chamber for PET*, IEEE 1997 Med. Imag. Conf., Orlando, NM, USA, Nov. 1997. Poster

Other communications

2004   **P. Crespo**, *In-beam PET for handrontherapy using LSO/APD-array detectors*, 41th Crystal Clear General Meeting, CERN, Sept. 2004. Invited talk

       P. Crespo, *Optimization of an in-beam positron emission tomograph for monitoring carbon ion radiotherapy with a rotating beam line*, PhD students seminars, Inst. of Nuclear and Hadron Physics, FZR, Dresden, July 2004. Talk

       P. Crespo, W. Enghardt, J. Pawelke, *CAGE - a CAMAC based DAQ for radiation physics*, Data Acquisition Meeting at the Inst. of Nuclear and Hadron Physics, FZR, Dresden, July 2004. Talk

       P. Crespo, M. Kapusta, J. Pawelke, M. Moszyński, W. Enghardt, *First in-beam PET imaging with LSO/APD-array detectors*, Internal evaluation of the Inst. of Nuclear and Hadron Physics, FZR, Dresden, March 2004. Poster

2003   **P. Crespo**, W. Enghardt, A. Winter, Th. Haberer, W. Bourgeois, *The combination of a PET scanner with a rotating ion beam delivery*, ENLIGHT Workpackage 5, Inst. of Nuclear and Hadron Physics, FZR, Dresden, Jan. 2003. Talk

2002   **P. Crespo**, *Photon detection with avalanche photodiodes*, Inst. of Radiation Protection Physics, Dresden University of Technology, May 2002. Talk

2001   **P. Crespo**, *The search for super heavy nuclei: has the top been reached?*, PhD students seminars, GSI Darmstadt, June 2001. Talk

       P. Crespo, *Tumour therapy with carbon ion beams*, Heavy Ion Laboratory, Warsaw, Mar. 2001. Invited talk

       P. Crespo, *Latest results and the motivations for the AMS experiment: search for dark matter, anti-matter and cosmic ray composition*, PhD students seminars, GSI Darmstadt, Jan. 2001. Talk

2000   **P. Crespo**, *Tumour therapy with carbon ion beams*, Portuguese Research Reactor, Sacavém, Portugal, Dec. 2000. Invited talk

1999   **P. Crespo**, *The astrophysics motivations of the AMS experiment and the motivations for a RICH detector: search for dark matter, anti-matter and cosmic ray composition*, Inst. of Nuclear and Hadron Physics, FZR, Dresden, Oct. 1999. Talk

       P. Crespo, *A liquid xenon multiwire drift chamber for γ-ray detection with 3D information*, Div. of Radiation Physics, Inst. of Nuclear and Hadron Physics, FZR, Dresden, Aug. 1999. Talk

       P. Crespo, F. Barão, *Cerenkov angle reconstruction algorithm with an aerogel radiator*, AMS RICH detector collaboration, CERN, June 1999. Talk

Annual reports

2004   **P. Crespo**, T. Barthel, H. Frais-Kölbl, E. Griesmayer, K. Heidel, K. Parodi, J. Pawelke, W. Enghardt, *Suppression of random coincidences during in-beam PET measurements*, Wiss.-Tech. Ber., FZR-423, pp. 79

2003   **P. Crespo**, M. Kapusta, J. Pawelke, M. Moszyński, W. Enghardt, *In-beam PET imaging with LSO/APD-array detectors: first results*, Wiss.-Tech. Ber., FZR-401, pp. 65

2002   **P. Crespo**, J. Pawelke, W. Enghardt, *A CAMAC data acquisition system for multi parameter measurements*, Wiss.-Tech. Ber., FZR-372, pp. 82

       P. Crespo, M. Kapusta, K. Heidel, L. Heinrich, J. Hutsch, J. Pawelke, M. Sobiella, D. Wolski, W. Enghardt, M. Moszyński, *Position sensitive photon detectors of lutetium oxyorthosilicate crystals coupled to avalanche photodiode arrays*, Wiss.-Tech. Ber., FZR-372, pp. 81

       M. Kapusta, **P. Crespo**, M. Moszyński, W. Enghardt, , D. Wolski *Hamamatsu S8550 APD arrays for high resolution scintillator matrices readout*, Wiss.-Tech. Ber., FZR-372, pp. 80

       W. Enghardt, **P. Crespo**, W. Bourgeois, A. Winter, *A technical feasibility study for a PET therapy monitor combined with a rotating ion beam delivery*, Wiss.-Tech. Ber., FZR-372, pp. 83–4

2001   **P. Crespo**, M. Kapusta M. Moszyński, W. Enghardt, J. Pawelke, M. Szawlowski, *Evaluation of avalanche photodiode arrays for the readout of high granularity scintillation matrices*, GSI Rep. 2002-1, pp. 170

       P. Crespo, W. Enghardt, K. Lauckner, *A new fully 3D maximum likelihood PET reconstruction applicable to different detector arrangements*, GSI Rep. 2002-1, pp. 173–4

2000   **P. Crespo**, K. Lauckner, W. Enghardt, *The combination of an in-beam PET scanner with a rotating beam delivery for ion tumour therapy*, Wiss.-Tech. Ber., FZR-319, pp. 100–1

       K. Lauckner, **P. Crespo**, W. Enghardt, J. Pawelke, *Feasibility study for an LSO-based in-beam PET scanner*, Wiss.-Tech. Ber., FZR-319, pp. 99

       W. Enghardt, K. Parodi, J. Pawelke, F. Pönisch, M. Sobiella, **P. Crespo**, T. Haberer, C. Kausch, K. Lauckner, D. Schardt, *Positron emission tomography (PET) for ion therapy quality assurance*, GSI Rep. 2001-1, pp. 161

Attended schools and workshops

1999   1999 CERN Summer Student School, CERN, Aug. 1999, as volunteer

1998   1998 CERN School of Computing, Funchal, Portugal, Sept. 1998

1997   CERN Workshop on Field Buses, CERN, Sept. 1997

Languages

       Portuguese, English, Italian, Spanish; fluent conversation, reading and writing

       French; medium conversation, reading and writing

       German; basic conversation and reading

Computer

Analysis	PAW 2.10/09 (Physics Analysis Workstation, CERN)
	IDL (Interactive Data Language, CREASO, Gilching, Germany)
Simulation	Geant 3.21 (detector description and simulation tool, CERN)
	Electro (electrostatic modeller, Integrated Engineering Software Inc., Canada)
Acquisition	LabWindows/CVI (National Instruments Corp., Austin, TX, USA)
	C/C++ code interfaced with Qt (Trolltech AS, Oslo, Norway) and Qplotter (CERN)
Programming	C, C++, Fortran, Pascal, Assembler (Texas Instruments TMS)